# Finite-rate combustion models for Large Eddy Simulation of non-premixed combustion; An a priori DNS analysis

Shamooni Pour Dezfouli, Ali

(2020)

# Finite-rate combustion models for Large Eddy Simulation of non-premixed combustion; An a priori DNS analysis

Am Fachgebiet Maschinenbau
der Technischen Universität Darmstadt
zur Erlangung des akademischen Grades eines
Doktor-Ingenieurs (Dr.-Ing.)
genehmigte

Dissertation

vorgelegt von

**Ali Shamooni Pour Dezfouli, M.Sc.**

aus Ahvaz (Iran)

| | |
|---|---|
| Berichterstatter: | Prof. Dr.-Ing C. Hasse |
| Mitberichterstatter 1: | Assoc. Prof. A. Cuoci (Politecnico di Milano) |
| Mitberichterstatter 2: | Prof. Dr. rer. nat. A. Sadiki |
| Tag der Einreichung | 20. Mai. 2019 |
| Tag der mündlichen Prüfung | 06. Dez. 2019 |

Darmstadt 2019
D17

Shamooni Pour Dezfouli, Ali: Finite-rate combustion models for Large Eddy Simulation of non-premixed combustion; An a priori DNS analysis,
Darmstadt, Technische Universität Darmstadt,
Year thesis published in TUprints: 2020
Date of the viva voce: 06.12.19

# Erklärung /Statement

Hiermit erkläre ich, dass ich die vorliegende Arbeit, abgesehen von den in ihr ausdrücklich genannten Hilfen, selbständig verfasst habe. Ich erkläre außerdem, dass ich bisher noch keinen Promotionsversuch unternommen habe.

**English translation for information purposes only:**

I herewith declare that I have written the submitted dissertation independently, expect for explicitly quoted sources. I furthermore declare that I have not applied for a PhD before.

_____

Milan, 4. April 2019 Ali Shamooni Pour Dezfouli, M.Sc.


POLITECNICO DI MILANO
DEPARTMENT OF CHEMISTRY, MATERIALS, AND CHEMICAL ENGINEERING
DOCTORAL PROGRAMME IN CHEMICAL ENGINEERING

---

# FINITE-RATE COMBUSTION MODELS FOR LARGE EDDY SIMULATION OF NON-PREMIXED COMBUSTION; AN A PRIORI DNS ANALYSIS

Doctoral Dissertation of:
**Ali Shamooni Pour Dezfouli**

Supervisors:
**Prof. Alberto Cuoci (Politecnico di Milano)**
**Prof. Amsini Sadiki (Technische Universität Darmstadt)**

Tutor:
**Prof. Enrico Tronconi**

The Chair of the Doctoral Program:
**Prof. Alessio Frassoldati**

2019 – XXXI

# Acknowledgment

The doctoral program is a double degree doctorate program under Marie-Curie Actions (CLEAN-Gas project) in collaboration with EKT institute in Mechanical Eng. Dep. of TU-Darmstadt, Germany. Professor Amsini Sadiki is the co-supervisor. The PhD. candidate carried out one-year research in the mentioned institute.

This project has received funding from the European Union's Horizon 2020 research and innovation program under the Marie Sklodowska-Curie grant agreement No. 643134.

I would like to express my sincere gratitude to my supervisors, Professors Alberto Cuoci from PoliMi and Amsini Sadiki from TU-Darmstadt, and also Professor Tiziano Faravelli, who gave me the chance to be part of the CleanGas project, a great opportunity in my career. I would like to thank our project coordinator in PoliMi, Mrs. Isabella Branca, who helped me, even beyond her defined tasks, to overcome all the issues during this period.

I would also like to thank the reviewers of my thesis, Professor Nilanjan Chakraborty from Newcastle University and Professor Alessandro Parente from Université Libre de Bruxelles, for their valuable comments. I also wish to show my appreciation to the rest of my dissertation committee from TU-Darmstadt, Prof. Dr.-Ing. Christian Hasse and Prof. Dr.-Ing. Heinz-Peter Schiffer.

I also wish to thank Professor Evatt Hawkes from the University of New South Wales for providing me the DNS validation data.

Last but not least, I would like to thank my wife, Keihaneh, for all her love and support throughout this period.

# Zusammenfassung

Die Beschreibung der Turbulenz-Chemie-Wechselwirkung (TCW) bleibt in der Verbrennungswissenschaft trotz vielen Bemühungen noch eine offene Fragestellung. Es werden Modelle benötigt, um die nicht geschlossenen chemischen Quellterme zu schliessen, wenn die Reynolds-gemittelten oder gefilterten Navier-Stokes-Gleichungen für chemische Spezies in reaktiven Strömungen gelöst werden. “Finite-Rate” (FR) Modelle sind diejenigen, bei denen keine Annahmen hinsichtlich der Strömung oder der Flamme getroffen werden. Es wird dann versucht, die tiefpassgefilterten Produktions- / Verbrauchsraten (im Fall von Large Eddy Simulation (LES)) direkt zu modellieren. In der Direkten Numerischen Simulation (DNS) werden jedoch alle Skalen der Strömung und der Chemie aufgelöst, und es ist keine TCW-Modellierung erforderlich. Die DNS-Daten reaktiver Strömungen mit relativ detaillierter Chemie, die dank großer paralleler Superrechner und Programmcodes mittlerweile verfügbar sind, können verwendet werden, um entweder grundlegende Einblicke in turbulente reaktive Strömungen zu erhalten oder TCW-Modelle direkt zu formulieren bzw. bewerten. Die Beurteilung erfolgt entweder durch *a priori* oder *a posteriori* DNS-Analysen.

In dieser Arbeit wurden unter Verwendung von DNS-Datenbank von nicht vorgemischten Jet-Flammen grundlegende Analysen der spektralen Eigenschaften (Geschwindigkeit und Dissipation der kinetischen Energiespektren) der Flamme und der inneren Intermittenz in dieser Flammenart durchgeführt. Die gewonnenen Erkenntnisse wurden anschließend zur Entwicklung neuer FR-Verbrennungsmodelle für LES verwendet. Insbesondere wurde das Eddy-Dissipation-Konzept (EDC) durch Modifikation der Koeffizienten und des Intermittenzfaktors im Modell verbessert. Einerseits geht diese Modifikation aus einer theoretischen Basis hervor, die neuen Kenntnisse der spektralen Eigenschaften beinhaltet. Andererseits ergibt sich die Modifikation des Intermittenzfaktors von EDC aus einer direkten Anwendung der beobachteten Skalierung von Dissipationsschwankungen. Es wurde festgestellt, dass die Statistik der Geschwindigkeitsgradienten in der Nähe der Mittelebene der reaktiven Jets derjenigen von den nichtreaktiven Jets auf der Mittellinie einer Nachlaufströmung, einer gittererzeugten Turbulenz oder auch einer erzwungenen Box-Turbulenz folgt. Darüber hinaus wurden

existierende “Scale Similarity” (SS) Modelle für LES anhand der DNS-Daten *a priori* bewertet und neue dynamische SS Modelle, die auf der Germano Identität basieren, entwickelt und anhand der *a priori* DNS-Analyse weiter bewertet.

# Abstract

TURBULENCE and chemistry interaction (TCI) is still an open problem in the combustion science. Models are needed to account for the unclosed chemistry source terms when the averaged or filtered Navier-Stokes governing equations are solved for chemical species in reactive flows. Finite-rate (FR) combustion models attempting to model the low-pass filtered production/consumption rates (in the case of Large Eddy Simulation or LES) directly. The Eddy Dissipation Concept (EDC) and Scale Similarity (SS) models are two types of FR combustion models for LES. The aim of the study is to assess and improve the performance of the two mentioned models using Direct Numerical Simulation (DNS) databases. In DNS all flow and chemistry scales are resolved and no TCI modeling is required. The DNS databases of reactive flows with relatively detailed chemistry, which are now available thanks to massively large parallel computational tools and codes, can be utilized to both gain fundamental insights on the turbulent reactive flows and directly assess TCI models. The assessment can be through *a priori* and *a posterior* DNS analyses. In the current work, fundamental analyses are carried out, using DNS databases of non-premixed jet flames, on the spectral behavior (velocity and dissipation of kinetic energy spectra) and the internal intermittency phenomenon in this type of flames. The physical findings are applied to develop new FR combustion models for LES. In particular, Eddy Dissipation Concept (EDC) is improved by the modifications on the coefficients and the intermittency factor of the model. The modification on the coefficients follows a theoretical basis in which the new findings on spectral behavior have been applied to reduce the degree of freedom of the model by relating the two free coefficients of the model. On the other hand, the modification in the intermittency factor of EDC is the direct application of the observations in the scaling of dissipation fluctuations. The new EDC models are then *a priori* assessed using the DNS databases. Besides, the existing Scale Similarity (SS) models for LES are *a priori* assessed using the DNS databases and new dynamic SS models are developed based on Germano's identity for LES and further assessed using the *a priori* DNS analysis.

# Contents


**1 Introduction** **1**

**2 Turbulence** **9**
2.1 Introduction . . . . . 9
2.2 The Theory: Statistical Approach . . . . . 9
2.2.1 Probability Density Functions . . . . . 10
2.2.2 Joint Statistics . . . . . 14
2.2.3 Favre Variables and Statistics . . . . . 16
2.2.4 Structure Functions . . . . . 17
2.2.5 The Kolmogorov 1941 Theory . . . . . 18
2.2.6 Turbulent Scales . . . . . 19
2.2.7 Turbulent Kinetic Energy and its Dissipation Spectra . . . . . 23
2.3 The Modelling: Navier-Stokes Equations . . . . . 28
2.3.1 Favre Averged Navier-Stokes . . . . . 30
2.3.2 Favre Filtered Navier-Stokes . . . . . 34

**3 Turbulence-Chemistry Interactions: Finite-Rate Combustion Models** **39**
3.1 Introduction . . . . . 39
3.2 Eddy Dissipation Concept (EDC) . . . . . 40
3.2.1 EDC for RANS . . . . . 41
3.2.2 EDC for LES . . . . . 45
3.2.3 Evaluation of EDC Model Coefficients . . . . . 46
3.2.4 Volume Fraction of Fine Structures: Internal Intermittency Factor 53
3.2.5 Residence Time in Fine Structures . . . . . 56
3.2.6 Summary . . . . . 57
3.3 Non-Dynamic Scale Similarity Combustion Models for LES . . . . . 63
3.4 New Dynamic Scale Similarity Models for LES . . . . . 65
3.4.1 DA: Dynamic formulation of SSRRRM (model A) . . . . . 65
3.4.2 DB: Dynamic formulation of SSFRRM (model B) . . . . . 67
3.4.3 DC: Dynamic formulation of model C . . . . . 68
3.4.4 Summary . . . . . 70

**4 Methodology** **73**
4.1 Introduction . . . 73
4.2 Model Assessments Using DNS Data: *A Priori* and *A Posteriori* Analysis 73
4.3 Explicit Filters . . . 74
4.4 Assessment Metrics . . . 79
4.5 DNS Databases . . . 79
4.6 *A priori* Analysis Code . . . 81

**5 Results: The *A Priori* DNS Analysis** **83**
5.1 Introduction . . . 83
5.2 Intermittency in Reactive Flows . . . 84
5.2.1 Large Scale (External) Intermittency . . . 84
5.2.2 Small Scale (Internal) Intermittency . . . 93
5.2.3 Summary and Conclusions . . . 105
5.3 Velocity Spectra For Reactive Flows . . . 107
5.3.1 Normalized Spectra Using Favre Averaged Kolmogorov's Scales 109
5.3.2 Normalized Spectra Using Cut-off Length Scales From Velocity Dissipation Spectra . . . 116
5.3.3 Normalized Spectra in Different Combustion Regimes . . . 119
5.3.4 The Model Spectrum for Reactive Flows . . . 124
5.3.5 Summary and Conclusions . . . 132
5.4 *A Priori* Analysis of FR-TCI-LES Moldels . . . 133
5.4.1 Eddy Dissipation Concept (EDC) Model . . . 133
5.4.2 Non-Dynamic Scale Similarity Models . . . 145
5.4.3 New Dynamic Scale Similarity Models . . . 158

**6 Conclusions and Future Works** **169**
6.1 Summary and Conclusions . . . 169
6.2 Future Works . . . 172
6.2.1 Proposals for Future Works on the Theory . . . 172
6.2.2 Proposals for Future Works on the Applications . . . 174

**Bibliography** **175**

**Glossary** **185**

**Appendices** **191**

**A Extra Results for Spectral Analysis** **193**

**B Extra Results for Dynamic SS models** **203**

# List of Figures


2.1 Turbulent water jet, adapted from [61]. . . . 20
2.2 From [77]; Decomposition of the energy spectrum by different solution methods. (**a**) Reynolds Average Navier-Stokes Simulation (RANS); (**b**) Unsteady Reynolds Average Navier-Stokes Simulation (URANS); (**c**) Large Eddy Simulation (LES). . . . 31

3.1 The EDC cascade. Left side shows the cascade in physical space, the right side is in wavenumber space. . . . 42
3.2 The EDC cascade in sub-grid scales. . . . 45
3.3 The 3D model dissipation spectrum of Pope for non-reacting (NR) flows and the proposed 3D model dissipation spectrum for rective (R) flows. . . . 51

4.1 1D graphical illustration of fits filtering level (simple filter) of the DNS data and the sampling on a coarse grid. It is assumed that $N$ is 4 for simplicity . . . 78
4.2 (**a**) Locations of the cutoff filter with the corresponding filter widths on log-log plot of compensated energy spectrum computed on the central plane; (**b**) Fraction of the Favre averaged resolved TKE using different filter widths at $t = 20t_j$. . . . 78
4.3 Schematic of the temporal jet Direct Numerical Simulation (DNS) case, including the contours of heat release rate (colored from black to white) and the mass fraction of OH radical (colored from blue to red) at the maximum extinction time ($20t_j$). Local extinction events on the shear layers are observed with low OH mass fraction and the corresponding low heat release rate . . . 80
4.4 (**a**) Maximum of Favre averaged temperature during the simulation for three DNS cases. The vertical red dashed line show the time instants with maximum local extinction; (**b**) Favre averaged mixture fraction in the whole simulation time colored by Favre averaged temperature, the vertical red lines are the time instants analyzed in the current study . . . 80
4.5 Normalized energy spectrum on the center plane of the H case DNS at t=20$t_j$ (black line) and -5/3 scaling law shown by red dashed line. . . . 82
4.6 Schematic of the *a priori* analysis codes. . . . 82

5.1 Data extracted from case H at t=20$t_j$ on the central $Oxy$ plane: (**a**) OH mass fraction, with the green lines the T/NT interfaces and the red lines the stoichiometric mixture fraction isolines; (**b**) Temperature, with white dashed line the location of the central $Oxz$ plane, black dashed line an $Oxz$ plane corresponding to the Favre mean stoichiometric mixture fraction and the gray dashed line $Oxz$ a plane corresponding to the maximum of Favre mean density fluctuations. . . . 86
5.2 Logarithm of the vorticity magnitude in three different planes across the jet at t=20$t_j$ for case H. (**a**) On the central plane; (**b**) On the plane corresponding to Favre mean stoichiometric mixture fraction; (**c**) On the plane corresponding to the maximum Favre mean density fluctuations. The black lines are the stoichiometric mixture fraction isolines. . . . 87
5.3 The same as Fig. 5.2 but the dark blue color shows the non-turbulent regions detected by the threshold. 88

5.4 The external intermittency factor, $\gamma_{ext}$, computed at t=20$t_j$ using the threshold of $w_{threshold} = 0.1 \times mean\, centerline\, vorticity\, magnitude$, for case (**a**) L; (**b**) M; (**c**) H. The vertical lines show the crosswise locations, $y$, of selected $Oxz$ planes used to extract the statistics. . . . . 90
5.5 Probability density functions (PDF) of the normalized velocity fluctuations in turbulent and the whole region compared with the Gaussian PDF extracted from case H at t=20$t_j$ on (**a**) the central $Oxz$ plane; (**b**) the plane corresponding to the mean stoichiometric mixture fraction; (**c**) the plane corresponding to the maximum of density fluctuations RMS. . . . . 90
5.6 The statistics of streamwise velocity fluctuation, $u'$, extracted from case H at t=20$t_j$ across the reacting shear layer, (**a**) skewness ; (**b**) flatness. . . . . 91
5.7 Probability density function (PDF) of normalized velocity fluctuations in turbulent region detected by different magnitude of vorticity thresholds extracted from case H at t=20$t_j$ on the plane corresponding to the maximum of density fluctuations RMS. Arrows show the direction of increasing $w_{threshold}$. . . . . 92
5.8 The statistics of streamwise velocity fluctuation in turbulent regions, $u_t'$, using different magnitude of vorticity thresholds extracted from case H at t=20$t_j$ across the reacting shear layer, (**a**) skewness ; (**b**) flatness. Arrows show the direction of increasing threshold. . . . . 92
5.9 From [103], the schematic of Tennekes Model for dissipative structures. . . . . 95
5.10 Flatness of streamwise velocity fluctuation gradient computed in full zone (green dashed line) and only turbulent zones (black line), extracted at t=20$t_j$ across the reacting shear layer of case H. Upper half of the data have been used, from the center plane ($y/H = 0$) to a plane where the external intermittency factor, $\gamma_{ext} = 0.1$. . . . . 97
5.11 Flatness of streamwise and crosswise velocity fluctuation gradients (conditioned on turbulent regions) compared with the fluctuation of dissipation rate (conditioned on turbulent regions), extracted at $t = 20t_j$ across the reacting shear layer for case H. . . . . 98
5.12 Different Taylor Reynolds numbers extracted at t=20$t_j$ across the reacting shear layer for case H. Upper half of the statistics are plotted, from the center plane ($y/H = 0$) to a plane where the external intermittency factor, $\gamma_{ext} = 0.1$. . . . . 99
5.13 The flatness factor of longitudinal gradient of streamwise velocity fluctuations versus longitudinal Taylor scale Reynolds number defined in Eq. 5.15. The inverse of intermittency factor is also shown on the lower half of the diagram. The black markers (also mentioned in the legend) are from figure 3 of [35] (the data compilation in different types of flows with low $Re_\lambda$, $Re_\lambda < 300$ ). The solid line is the fit to these reference data, $\exp(0.373)Re_{\lambda_u}^{0.281}$. The color markers are plotted on top of the diagram. These are the data extracted from the central plane of current DNS databases. Downward-pointing triangle: the low Reynolds (L) case. Diamonds: the medium Reynolds (M) case. Upward-pointing triangle: the high Reynolds (H) case. Each color refers to an instant of time. Blue: t=20$t_j$ corresponding to the maximum local extinction event in all three DNS cases. Green: t=30$t_j$. Red: t=35$t_j$. The two latter time instants are corresponding to re-ignition events where the re-ignition mainly occurs around central plane in the jet core region. Filled color markers are flatness factors. Unfilled color markers are the inverse of the intermittency factor. The dashed line is a line with the same slope in logarithmic scale as the fitted solid line. . . . . 100
5.14 Second moment of local dissipation (the inverse of internal intermittency factor) versus Reynolds number. Reynolds in defined as $Re = u_{rms}L/\nu$, with $u_{rms} = \sqrt{2TKE}$, $L$ the scale representative of large scales and $\nu$ the viscosity. The filled circles are from the HIT data compilation in [32], where $H$ was taken to be the the length of cube in DNS of HIT. The solid line is the theoretical prediction by Yakhot [36] for HIT, $Re^{0.152}$. The color markers are the data extracted from the central plane of current DNS databases. For the current reactive DNS jet data, $H$ is the initial width of the fuel jet, $Re = u_{rms,t}H/\nu_t$ is used instead of $Re$, where the subscript $t$ refers to conditional data conditioned on turbulent zones only. Downward-pointing triangle: the low Reynolds (L) case. Diamonds: the medium Reynolds (M) case. Upward-pointing triangle: the high Reynolds (H) case. Each color refers to an instant of time. Blue: t=20$t_j$ corresponding to the maximum local extinction event in all three DNS cases. Green: t=30$t_j$. Red: t=35$t_j$. The two latter time instants are corresponding to re-ignition events where the re-ignition mainly occurs around central plane in the jet core region. . . . . 101
5.15 The second moment of local dissipation against the Reynolds number ($Re = u_{rms}L/\nu$) across the reactive jets. (Top) t=20$t_j$; (Middle) t=30$t_j$; (Bottom ) t=35$t_j$; (Left) case H; (Right) case M. . . 103
5.16 The second moment of local dissipation computed in full zone (green dashed line) and only turbulent zones (black line), extracted at t=20$t_j$ across the reacting shear layer of the H case DNS. Upper half of the statistics are plotted, from the center plane ($y/H = 0$) to a plane where the external intermittency factor, $\gamma_{ext} = 0.1$. . . . . 104

5.17 Data from M case DNS at t=35$t_j$ corresponding to the re-ignition mode of flame, on an $Oxz$ plane at $y/H = 2.625$ in the intermittent region of flow, corresponding to the location where a peak of normalized second moment of local dissipation occurs (see also Fig. 5.15f), (**a**) the logarithm of vorticity magnitude; (**b**) the logarithm of inverse of normalized second moment of local dissipation. Yellow arrows show the occurrence of very high vortical structure and the correspondingly, high second moment of local dissipation. . . . . 104
5.18 Normalized second moment of local dissipation, extracted at t=20$t_j$ and t=30$t_j$ across the reacting shear layers for cases H and M, (**a**) against Taylor scale Reynolds number computed in turbulent zones only; (**b**) against large scale Reynolds number, $Re = u_{rms}L/\nu$ with $u_{rms} = \sqrt{2TKE}$ and $L$ the initial width of the jet, showing only case H; (**c**) against large scale Reynolds number showing only case M. The data are color coded. The black markers refer to the data in intermittent flow where external intermittency factor is below 0.99. The colored data are the data in turbulent region. The upper triangles are the H case data while diamonds are the Mcase data. . . . . 105
5.19 From [165], $\mathcal{F}_{\frac{\partial u'}{\partial x}}$ against $Re_{\lambda_u}$ from experiments and DNS of different types of wall bounded flows. Consider the colored markers which are the data of smooth wall boundary layer and note how flatness is changing with Taylor Reynolds number. Three regions were highlighted, the near-wall region (red, $y/\delta \leq 0.04$), inertia-dominated region (yellow, $0.04 \leq y/\delta \leq 0.2$), and outer region (green, $0.2 \leq y/\delta \leq 0.6$), with $\delta$ the boundary layer thickness. . . . . 106
5.20 Normalized quantities across the shear layer for case H at t=20$t_j$. . . . . 110
5.21 The 1D longitudinal spectra on different planes across the reacting shear layer at maximum extinction time, t=20$t_j$ for case H, (**a**) Non-normalized; (**b**) Normalized using Favre averaged $\eta$ and $\varepsilon$. . . . . 112
5.22 1D compensated spectra on different planes across the reacting shear layer at maximum extinction time, t=20$t_j$ extracted from H case DNS, (**a**) 1D compensated energy spectra; (**b**) 1D compensated longitudinal spectra. . . . . 113
5.23 1D compensated longitudinal spectra on different planes across the reacting shear layer at maximum extinction time, t=20$t_j$ for case H with the slopes of the exponential drop-off. . . . . 114
5.24 1D compensated spectra across the reacting shear layer at the maximum extinction time, t=20$t_j$ for case H, (**a**) Extracted from the Favre mean Stoichiometric mixture fraction plane; (**b**) Extracted from the central plane. . . . . 115
5.25 1D longitudinal dissipation spectra across the reacting shear layer at t=20$t_j$ for case H, (**a**) Non-normalized spectra; (**b**) Normalized using Favre averaged $\eta$ and $\varepsilon$. . . . . 116
5.26 1D longitudinal velocity spectra across the reacting shear layer at t=20$t_j$ for case H; (**a**) Normalized using the Favre averaged $\eta$ and $\varepsilon$; (**c**) Normalized using the Batchelor length scale and Favre averaged $\varepsilon$. . . . . 117
5.27 1D longitudinal dissipation spectra across the reacting shear layer at maximum extinction time, t=20$t_j$ for case H; (**a**) Normalized using the Favre averaged $\eta$ and $\varepsilon$; (**c**) Normalized using the Batchelor length scale and Favre averaged $\varepsilon$. . . . . 118
5.28 1D longitudinal velocity spectra across the reacting shear layer at the maximum extinction, t=20$t_j$ and re-ignition times t=30,35$t_j$ for case H on the central plane and the mean stoichiometric plane, (**a**) Non-normalized spectra; (**b**) Normalized using the Favre averaged $\eta$ and $\varepsilon$; (**c**) Normalized using the Batchelor length scale and $\varepsilon$. . . . . 120
5.29 1D longitudinal dissipation spectra across the reacting shear layer at the maximum extinction, t=20$t_j$ and re-ignition times t=30,35$t_j$ for case H on the central plane and the mean stoichiometric plane, (**a**) Non-normalized spectra; (**b**) Normalized using the Favre averaged $\eta$ and $\varepsilon$; (**c**) Normalized using the Batchelor length scale and $\varepsilon$. . . . . 121
5.30 1D longitudinal velocity spectra across the reacting shear layer at maximum extinction, t=20$t_j$ and re-ignition times t=30$t_j$ for cases H and M on the mean stoichiometric plane, (**a**) Non-normalized spectra; (**b**) Normalized using the Favre averaged $\eta$ and $\varepsilon$; (**c**) Normalized using the Batchelor length scale and $\varepsilon$. . . . . 122
5.31 1D longitudinal dissipation spectra across the reacting shear layer at maximum extinction, t=20$t_j$ and re-ignition times t=30$t_j$ for cases H and M on the mean stoichiometric plane, (**a**) Non-normalized spectra; (**b**) Normalized using the Favre averaged $\eta$ and $\varepsilon$; (**c**) Normalized using the Batchelor length scale and $\varepsilon$. . . . . 123
5.32 1D longitudinal dissipation spectra across the reacting shear layer at the maximum extinction, t=20$t_j$ and re-ignition, t=30$t_j$, times for cases H and M on the mean stoichiometric plane compare with the modified model spectrum of Pope, (**a**) Non-normalized spectra; (**b**) Normalized using the Favre averaged $\eta$ and $\varepsilon$ . . . . . 126

5.33 1D dissipation spectra on the plane corresponding to the mixture fraction equal to the stoichiometric value of 0.422 at t=20$t_j$ for case H. The inset is the zoom view of the left corner. . . . . 127
5.34 1D spectra on the plane of Favre mean stoichiometric mixture fraction at t=20$t_j$ , (**a**) for case H, the normalized form; (**b**) for case H the compensated form; (**c**) for case M the compensated form. . 130
5.35 1D compensated spectra computed from the compressible formula (Eq. 5.30) across the reacting shear layers at t=20$t_j$ for case H, (**a**) Extracted from the central plane; (**b**) Extracted from the Favre mean Stoichiometric mixture fraction plane. . . . . 131
5.36 Production/consumption rate of CO (fuel) with units $[kg/(m^3 s)]$, using different EDC-LES models (see Table5.2) compared with the exact filtered quantity for case H at t=20$t_j$. Filter width is $\overline{\Delta}/\Delta_{\mathrm{DNS}} = 8$. The correlation coefficients, (Eq. 2.26) have been calculated and shown in the inset. 138
5.37 Same as Fig.5.36 but for $H_2$ (fuel). . . . . 139
5.38 Same as Fig.5.36 but for $O_2$ (oxidizer). . . . . 140
5.39 The modeled sub-grid viscous dissipation using Eq. 3.26 with $C_\varepsilon = 1.048$ compared to the exact term extracted from case H at t=20$t_j$ using Eq. 2.134. Filter width is $\overline{\Delta}/\Delta_{\mathrm{DNS}} = 8$. The correlation coefficient (Eq. 2.26) has been calculated and shown in the inset. . . . . 141
5.40 Conditional mean of production/consumption rate of different species with units $[kg/(m^3 s)]$ conditioned on the mixture fraction, using different EDC-LES models (see Table5.2) compared with the exact filtered quantity from case H at t=20$t_j$. Filter width is $\overline{\Delta}/\Delta_{\mathrm{DNS}} = 8$. . . . . 143
5.41 Conditional mean of production/consumption rate of different species with units $[kg/(m^3 s)]$ conditioned on mixture fraction, using different EDC-LES models (see Table5.2) compared with the exact filtered quantity from case H t=20$t_j$. Filter width is $\overline{\Delta}/\Delta_{\mathrm{DNS}} = 18$. . . . . 144
5.42 Production/consumption rate of $H_2$ with units $[kg/(m^3 s)]$, (**a,c,e**) Mean; (**b,d,f**) RMS. Different filter widths are applied: (up) $\overline{\Delta}/\Delta_{\mathrm{DNS}} = 8$; (middle) $\overline{\Delta}/\Delta_{\mathrm{DNS}} = 12$; (down) $\overline{\Delta}/\Delta_{\mathrm{DNS}} = 18$. The data are extracted at t=20$t_j$. vertical dashed-blue lines: planes of maximum mean turbulent kinetic energy; vertical dot-dashed green lines: planes of mean stoichiometric mixture fraction; vertical red lines: planes of maximum mean temperature fluctuations. . . . . 147
5.43 Production/consumption rate of H with units $[kg/(m^3 s)]$, (**a,c,e**) Mean; (**b,d,f**) RMS. Different filter widths are applied: (up) $\overline{\Delta}/\Delta_{\mathrm{DNS}} = 8$; (middle) $\overline{\Delta}/\Delta_{\mathrm{DNS}} = 12$; (down) $\overline{\Delta}/\Delta_{\mathrm{DNS}} = 18$. The data are extracted at t=20$t_j$.Vertical lines are the same as in Fig. 5.42. . . . . 148
5.44 Cumulative local errors incurred using different models in prediction of different species net formation rates: (**a,c,e**) logarithm of errors for all models; (**b,d,f**) The errors are divided by the "no model" approach error. Different filter widths are applied: (up) $\overline{\Delta}/\Delta_{\mathrm{DNS}} = 8$; (middle) $\overline{\Delta}/\Delta_{\mathrm{DNS}} = 12$; (down) $\overline{\Delta}/\Delta_{\mathrm{DNS}} = 18$. The data are extracted at t=20$t_j$. Vertical lines are the same as in Fig. 5.42. . . . . 150
5.45 Heat release rates, (**a,c,e**) Mean; (**b,d,f**) RMS. Different filter widths are applied: (up) $\overline{\Delta}/\Delta_{\mathrm{DNS}} = 8$; (middle) $\overline{\Delta}/\Delta_{\mathrm{DNS}} = 12$; (down) $\overline{\Delta}/\Delta_{\mathrm{DNS}} = 18$. The data are extracted at t=20$t_j$. Vertical lines are the same as in Fig. 5.42. . . . . 151
5.46 Production/consumption rate of $H_2$ with units $[kg/(m^3 s)]$, (**a,c,e**) Mean; (**b,d,f**) RMS. Different filter widths are applied: (up) $\overline{\Delta}/\Delta_{\mathrm{DNS}} = 8$; (middle) $\overline{\Delta}/\Delta_{\mathrm{DNS}} = 12$; (down) $\overline{\Delta}/\Delta_{\mathrm{DNS}} = 18$. The data are extracted at re-ignition time, t=35$t_j$. vertical dashed-blue lines: planes of maximum mean turbulent kinetic energy; vertical dot-dashed green lines: planes of mean stoichiometric mixture fraction; vertical red lines: planes of maximum mean temperature fluctuations. . . . . 153
5.47 Production/consumption rate of H with units $[kg/(m^3 s)]$, (**a,c,e**) Mean; (**b,d,f**) RMS. Different filter widths are applied: (up) $\overline{\Delta}/\Delta_{\mathrm{DNS}} = 8$; (middle) $\overline{\Delta}/\Delta_{\mathrm{DNS}} = 12$; (down) $\overline{\Delta}/\Delta_{\mathrm{DNS}} = 18$. The data are extracted at at re-ignition time, t=35$t_j$.Vertical lines are the same as in Fig. 5.46. . . . 154
5.48 Heat release rates, (**a,c,e**) Mean; ( **b,d,f**) RMS. Different filter widths are applied: (up) $\overline{\Delta}/\Delta_{\mathrm{DNS}} = 8$; (middle) $\overline{\Delta}/\Delta_{\mathrm{DNS}} = 12$; (down) $\overline{\Delta}/\Delta_{\mathrm{DNS}} = 18$. The data are extracted at t=35$t_j$. Vertical lines are the same as in Fig. 5.46. . . . . 156
5.49 Residual $\dot{\omega}_{H_2O}$ with units $[kg/(m^3 s)]$ when DNS is filtered by using at : (**a**) Exact; (**b**) Predicted by model A. Cutted plane is the central $Oxy$ plane. . . . . 157
5.50 Case H, at t=20$t_j$ using $\overline{\Delta}/\Delta_{\mathrm{DNS}}$=12: comparison of dynamic models DA1 and DA2 performance with exact filtered $\dot{\omega}_{\mathrm{H_2O}}$ extracted from DNS database. (**a**) mean, (**b**) RMS. The vertical blue lines are the location of the planes of maximum mean turbulent kinetic energy ($TKE$). Vertical green lines represent the plane of mean stoichiometric mixture fraction, while the vertical red lines show the planes in which the maximum mean fluctuations of density occurs . . . . . 159
5.51 Case H, at t=20$t_j$ using $\overline{\Delta}/\Delta_{\mathrm{DNS}}$=12: comparison of dynamic models DA1 and DA2 performance with exact filtered $\dot{\omega}_{\mathrm{H_2O}}$ extracted from DNS database. (**a**) relative error of mean profiles and **b**) relative error of RMS profiles. . . . . 159

5.52 Case H, at t=20$t_j$ using $\overline{\Delta}/\Delta_{\mathrm{DNS}}$=12: comparison of dynamic models performance using RMSE metric in predicting locally exact filtered $\dot{\omega}_{\mathrm{H_2O}}$ extracted from DNS database. (**a**) DA1 and DA2, (**b**) DB1 and DB2 and (**c**) DC1 and DC2 dynamic scale similarity models . . . . . 160
5.53 Scatter plots of modeled versus exact filtered source terms of $\mathrm{H_2}$. Extracted from DNS databases L (left), M (middle) and H (right) at t=20$t_j$ using $\overline{\Delta}/\Delta_{\mathrm{DNS}}$=12 . . . . . 162
5.54 Comparison of dynamic and non-dynamic models performances in predicting conditional mean filtered source terms of $\mathrm{H_2}$ (left), and H (right), conditioned on the mixture fraction at t=20$t_j$ using $\overline{\Delta}/\Delta_{\mathrm{DNS}}$=12. (Top:) case L, (Middle:) case M and (Bottom:) case H . . . . . 163
5.55 Comparison of dynamic and non-dynamic models performances in predicting conditional mean filtered source terms of $\mathrm{O_2}$ conditioned on the mass fraction of $\mathrm{O_2}$ (left), and conditional mean filtered source terms of O conditioned on the temperature (right), at t=20$t_j$ using $\overline{\Delta}/\Delta_{\mathrm{DNS}}$=12 for case L (top), case M (middle), and case H (bottom) . . . . . 164
5.56 Comparison of dynamic and non-dynamic models performance in predicting conditional mean heat release rate (conditioned on mixture fraction) at t=20$t_j$ using $\overline{\Delta}/\Delta_{\mathrm{DNS}}$=12. (**a**) case L, (**b**) case M and (**c**) case H . . . . . 165

A.1 The 1D longitudinal spectra on different planes across the reacting shear layer at maximum extinction time, t=20$t_j$ extracted from M case DNS, (**a**) Non-normalized; (**b**) Normalized using Favre averaged $\eta$ and $\varepsilon$. . . . . 195
A.2 1D compensated spectra on different planes across the reacting shear layer at maximum extinction time, t=20$t_j$ extracted from M case DNS, (**a**) 1D compensated energy spectra; (**b**) 1D compensated longitudinal spectra. The horizontal lines show the constant in Kolmogorov's spectrum. . . . . 195
A.3 1D longitudinal dissipation spectra across the reacting shear layer at maximum extinction time, t=20$t_j$ extracted from M case DNS, (**a**) Non-normalized; (**b**) Normalized using Favre averaged $\eta$ and $\varepsilon$. . . . . 196
A.4 1D compensated longitudinal spectra on different planes across the reacting shear layer at maximum extinction time, t=20$t_j$ extracted from M case DNS with slopes of exponential drop-off. . . . 196
A.5 1D longitudinal velocity spectra across the reacting shear layer at maximum extinction, t=20$t_j$ and re-ignition time t=30$t_j$ extracted from M case DNS on the central plane, $P^0$ and the maximum of mean OH mass fraction plane, $P^3$ (**a**) Non-normalized; (**b**) Normalized using Favre averaged $\eta$ and $\varepsilon$. . . . . 197
A.6 1D longitudinal dissipation spectra across the reacting shear layer at maximum extinction, t=20$t_j$ and re-ignition time t=30$t_j$ extracted from M case DNS on the central plane, $P^0$ and the maximum of mean OH mass fraction plane, $P^3$ (**a**) Non-normalized; (**b**) Normalized using Favre averaged $\eta$ and $\varepsilon$. . . . . 197
A.7 The 1D longitudinal spectra on different planes across the reacting shear layer at maximum extinction time, t=20$t_j$ extracted from L case DNS, (**a**) Non-normalized; (**b**) Normalized using Favre averaged $\eta$ and $\varepsilon$. . . . . 199
A.8 1D compensated spectra on different planes across the reacting shear layer at maximum extinction time, t=20$t_j$ extracted from L case DNS, (**a**) 1D compensated energy spectra; (**b**) 1D compensated longitudinal spectra. . . . . 199
A.9 1D longitudinal dissipation spectra across the reacting shear layer at maximum extinction time, t=20$t_j$ extracted from L case DNS, (**a**) Non-normalized; (**b**) Normalized using Favre averaged $\eta$ and $\varepsilon$. . . . . 200
A.10 1D compensated longitudinal spectra on different planes across the reacting shear layer at maximum extinction time, t=20$t_j$ extracted from L case DNS with slopes of exponential drop-off. . . . . 200
A.11 1D longitudinal velocity spectra across the reacting shear layer at maximum extinction, t=20$t_j$ and re-ignition time t=30$t_j$ extracted from L case DNS on the central plane and the maximum of Favre mean OH mass fraction plane, (**a**) Non-normalized; (**a**) Non-normalized; (**b**) Normalized using Favre averaged $\eta$ and $\varepsilon$. . . . . 201
A.12 1D longitudinal dissipation spectra across the reacting shear layer at maximum extinction, t=20$t_j$ and re-ignition time t=30$t_j$ extracted from L case DNS on the central plane and the maximum of Favre mean OH mass fraction plane, (**a**) Non-normalized; (**b**) Normalized using Favre averaged $\eta$ and $\varepsilon$. . . . . 201

B.1 Case H, at t=20$t_j$ using $\Delta/\Delta_{\mathrm{DNS}} = 12$: comparison of dynamic models DB1 and DB2 performance with exact filtered $\dot{\omega}_{\mathrm{H_2O}}$ extracted from DNS database. (**a**) mean, (**b**) RMS, (**c**) relative error of mean profiles and (**d**) relative error of RMS profiles . . . . . 204
B.2 The same as in Fig. B.1 but for dynamic models DC1 and DC2 . . . . . 204

B.5 Scatter plots of the modeled versus the exact filtered source terms of $H_2O$ using different SS models. Extracted from the DNS databases L (left), M (middle) and H (right) at t=20$t_j$ using $\overline{\Delta}/\Delta_{\mathrm{DNS}} = 12$. . . . . 206
B.3 Scatter plots of modeled versus exact filtered source terms of CO. Extracted from DNS databases L (left), M (middle) and H (right) at t=20$t_j$ using $\overline{\Delta}/\Delta_{\mathrm{DNS}}$=12 . . . . . 207
B.4 Scatter plots of modeled versus exact filtered source terms of H. Extracted from DNS databases L (left), M (middle) and H (right) at t=20$t_j$ using $\overline{\Delta}/\Delta_{\mathrm{DNS}}$=12 . . . . . 208
B.6 Scatter plots of the modeled versus the exact filtered source terms of $CO_2$ using different SS models. Extracted from the DNS databases L (left), M (middle) and H (right) at t=20$t_j$ using $\overline{\Delta}/\Delta_{\mathrm{DNS}} = 12$. . . . . 209
B.7 Scatter plots of the modeled versus the exact filtered source terms of O using different SS models. Extracted from the DNS databases L (left), M (middle) and H (right) at t=20$t_j$ using $\overline{\Delta}/\Delta_{\mathrm{DNS}} = 12$. 210
B.8 Comparison of dynamic and non-dynamic SS models performances in predicting the conditional mean filtered source terms of (**left**) CO and (**right**) $O_2$ (conditioned on mixture fraction) at t=20$t_j$ using $\overline{\Delta}/\Delta_{\mathrm{DNS}} = 12$. (**top**) case L, (**middle**) case M and (**bottom**) case H . . . . . 212
B.9 Comparison of dynamic and non-dynamic SS models performances in predicting the conditional mean filtered source terms of (**left**) $H_2O$ and (**right**) $CO_2$ (conditioned on mixture fraction) at t=20$t_j$ using $\overline{\Delta}/\Delta_{\mathrm{DNS}} = 12$. (**top**) case L, (**middle**) case M and (**bottom**) case H . . . . . 213
B.10 Comparison of dynamic and non-dynamic SS models performances in predicting the conditional mean filtered source terms of (**left**) O and (**right**) OH (conditioned on mixture fraction) at t=20$t_j$ using $\overline{\Delta}/\Delta_{\mathrm{DNS}} = 12$. (**top**) case L, (**middle**) case M and (**bottom**) case H . . . . . 214
B.11 Comparison of dynamic and non-dynamic SS models performances in predicting the conditional mean filtered source terms of (**left**) $H_2$ and (**right**) CO (conditioned on the species mass fraction) at t=20$t_j$ using $\overline{\Delta}/\Delta_{\mathrm{DNS}} = 12$. (**top**) case L, (**middle**) case M and (**bottom**) case H . . . . . 216
B.12 Comparison of dynamic and non-dynamic SS models performances in predicting the conditional mean filtered source terms of (**left**) $H_2O$ and (**right**) $CO_2$ (conditioned on the species mass fraction) at t=20$t_j$ using $\overline{\Delta}/\Delta_{\mathrm{DNS}} = 12$. (**top**) case L, (**middle**) case M and (**bottom**) case H . . . . . 217
B.13 Comparison of dynamic and non-dynamic SS models performances in predicting the conditional mean filtered source terms of (**left**) H and (**right**) O (conditioned on the species mass fraction) at t=20$t_j$ using $\overline{\Delta}/\Delta_{\mathrm{DNS}} = 12$. (**top**) case L, (**middle**) case M and (**bottom**) case H . . . . . 218
B.14 Comparison of dynamic and non-dynamic SS models performances in predicting the conditional mean filtered source terms of (**left**) $H_2$ and (**right**) CO (conditioned on temperature) at t=20$t_j$ using $\overline{\Delta}/\Delta_{\mathrm{DNS}} = 12$. (**top**) case L, (**middle**) case M and (**bottom**) case H . . . . . 220
B.15 Comparison of dynamic and non-dynamic SS models performances in predicting the conditional mean filtered source terms of (**left**) $O_2$ and (**right**) $H_2O$ (conditioned on temperature) at t=20$t_j$ using $\overline{\Delta}/\Delta_{\mathrm{DNS}} = 12$. (**top**) case L, (**middle**) case M and (**bottom**) case H . . . . . 221

# List of Tables


3.1 Summary of the RANS-EDC combustion models applicable to RANS codes. In the table **R** *stands for* "RANS", **O** *stands for* "O*riginal*", **M** *stands for* "Magnussen", **E** *stands for* "Ertesvag", $\mathbf{N_G}$ *stands for* "New $\gamma^*$", $\mathbf{N_C}$ *stands for* "New C*oefficient*" . . . . . 59

3.2 Summary of the LES-EDC combustion models applicable to LES codes. In the table **L** *stands for* "LES", **O** *stands for* "O*riginal*", **F** *stands for* "Fureby", **Ly** *stands for* "Lysenco", $\mathbf{N_G}$ *stands for* "New $\gamma^*$", $\mathbf{N_C}$ *stands for* "New C*oefficient*" . . . . . 60

3.3 Summary of the LES-EDC combustion models applicable to an *a priori* DNS analysis. In the table **L** *stands for* "LES", **O** *stands for* "O*riginal*", **F** *stands for* "Fureby", **Ly** *stands for* "Lysenco", $\mathbf{N_G}$ *stands for* "New $\gamma^*$", $\mathbf{N_C}$ *stands for* "New C*oefficient*". $\zeta_{LES}$ in **EDC-L-OF** and **EDC-L-N$_{\mathrm{G}}$F** is $\zeta_{LES} = 0.566$ (see Eq. 3.31). . . . . 61

3.4 The threshold of Taylor Reynolds number for different models assessed in an *a priori* DNS analysis below which $\gamma^*$ is saturated and is equal to 0.5. In the table **L** *stands for* "LES", **O** *stands for* "O*riginal*", **F** *stands for* "Fureby", **E** *stands for* "Ertesvag", $\mathbf{N_G}$ *stands for* "New $\gamma^*$", $\mathbf{N_C}$ *stands for* "New C*oefficient*". $Re_\lambda$ is calculated based on sub-grid quantities as $Re_{\lambda,SGS} = \frac{k_{SGS}}{\overline{\nu}^{f\,1/2}\varepsilon_{\nu,SGS}{}^{1/2}}$. . . . . 62

3.5 Summary of the SGS combustion models used in the current study . . . . . 71

4.1 The 1D implementation of different filters used in the current study. $\Delta^*$ is the size of the grid on which the quantity $q$ is defined and $i$ is a grid number in $x_i$ direction. $N$ is an integer defining the width of the filter . . . . . 75

4.2 The notations used in the current study for Favre filtered composition vector (i.e., species mass fractions and temperature) and the sequential steps to compute multilevel Favre filtered quantities . 76

4.3 The steps to compute the filtered source terms used in the current study. Os++ is OpenSMOKE++ [95]. . . . . 77

4.4 The DNS databases [6] used in the current study. . . . . 81

5.1 Some turbulence parameters of case H on the selected planes and different time instants for which spectra are studied. . . . . 110

5.2 Summary of the LES-EDC combustion models applicable to *a priori* DNS analysis. In the table **L** *stands for* "LES", **O** *stands for* "O*riginal*", **F** *stands for* "Fureby", **Ly** *stands for* "Lysenco", $\mathbf{N_G}$ *stands for* "New $\gamma^*$", $\mathbf{N_C}$ *stands for* "New C*oefficient*" and **E** *stands for* "Ertesvag". $\zeta_{LES}$ in **EDC-L-OF** and **EDC-L-N$_{\mathrm{G}}$F** is $\zeta_{LES} = 0.566$ (see Eq. 3.31). . . . . 135

5.3 The threshold of sub-grid Taylor Reynolds number for different models assessed in *a priori* DNS analysis below which $\gamma^*$ is saturated and is equal to 0.5. In the table **L** *stands for* "LES", **O** *stands for* "O*riginal*", **F** *stands for* "Fureby", **Ly** *stands for* "Lysenco", $\mathbf{N_G}$ *stands for* "New $\gamma^*$", $\mathbf{N_C}$ *stands for* "New C*oefficient*" and **E** *stands for* "Ertesvag". $Re_\lambda$ is calculated based on sub-grid quantities as $Re_{\lambda,SGS} = \frac{k_{SGS}}{\overline{\nu}^{f\,1/2}\varepsilon_{\nu,SGS}{}^{1/2}}$. . . . . 136

## List of Tables

A.1 DNS parameters of the cases on selected planes of DNS case M for which spectra are studied . . . 194
A.2 DNS parameters of the cases on selected planes of DNS case L for which spectra are studied . . . . 198

CHAPTER 1

# Introduction

COMBUSTION of fossil fuels and mainly Natural Gas is the main source of energy production. However, generating energy from the combustion of conventional sources is prone to pollutant formation and emissions. NOx and soot are the most important pollutants formed in combustion. A technique which is used in non-premixed flames to reduce NOx emissions is to operate in the flameless [1, 2] mode which can be considered as a regime in which there is no visible flame and the reaction zone is distributed through the whole combustion chamber. The design of the flameless gas turbines is still under development [3] and numerical simulations along with experiments are exploited in the design phase. The distinguishing feature of flameless combustion is the very strong interactions between the fluid mixing and chemical kinetics so that models based on the separation between turbulence and chemistry are not suitable to describe the complex interactions occurring in such a regime. Therefore, models that account for finite-rate (FR) chemistry effects must be considered [4]. Moreover, towards the down-sizing of novel energy systems, the rapid mixing process is required in those operating under non-premixed combustion mode to increase the heat release rates. Many engineering applications take the advantage of such turbulent combustion, which enhances the mixing of fuel and oxidizer. However, local extinction and subsequent re-ignition processes resulting from strong Turbulence-Chemistry Interaction (TCI) may occur, especially when rates of mixing exceed combustion rates, causing harmful emissions and flame instability. The extinction and re-ignition processes are unsteady phenomena which exhibit finite-rate chemistry effects [5–7]. Since the physical mechanisms for such processes are not yet fully understood, the research is still ongoing on the subject. These two reasons among many, are showing the fact that finite-rate chemistry effects in the study of turbulent flames is of great importance.

Due to an increased computational power available today, Computational Fluid Dy-

namics (CFD) is a promising tool to study turbulent combustion processes. Each CFD approach has its own pros and cons. For example in a specific case of dealing with transient processes, Reynolds averaged solutions in the context of RANS cannot be used since the solution is the averaged one (in time) so unsteady effects cannot be captured. Among DNS and LES, the application of the former is limited up-to-now to low-to-medium Reynolds numbers and simple computational setups, because it is computationally very demanding. However, DNS results can be utilized to develop/assess LES models. The LES of reactive flows has become a popular method for CFD. LES predicts the unsteady behavior of the large scales of the flow while small scales need to be modeled. A detailed chemistry can be directly incorporated into LES of reactive flows by solving transport equations of filtered species mass fractions.

In the governing equations of both RANS and LES of reactive flows with detailed kinetics, transport equations of averaged/filtered species mass fractions are solved. Each equation contains an unclosed source term of chemistry. Since the net formation rates of species are non-linear functions of composition quantities, SGS (in the case of LES) combustion models try to include the effects of turbulence on chemistry.

FR combustion models (or FR-TCI models) in LES are those with no assumption about the flow or flame, attempting to model the low-pass filtered production/consumption rates directly [8]. Some examples of FR-TCI models for LES of non-premixed flames are the transported PDF (TPDF) models [9, 10], the Partially Stirred Reactor (PaSR) model [11, 12], the Eddy Dissipation Concept (EDC) [13–16] and the Scale Similarity (SS) models [17, 18]. The focus of the present work is on the two latter.

The first objective of this work is to systematically analyze the existing EDC and SS models as SGS combustion models and to further develop new models using the DNS databases of non-premixed jet flames.

DNS databases of reactive flows with relatively detailed chemistry can be utilized to analyze/assess or to develop combustion models in LES of reactive flows. A priori DNS analyses are adopted by comparing modeled targets (say filtered source terms) with their corresponding exact values (directly filtered ones from DNS databases). The modeled targets make use of the exact LES-like quantities directly filtered from DNS. A priori analyses have been performed in many previous works to study the performance of SGS combustion models [19–24], however, in this work, the first *a priori* DNS analysis of the EDC combustion model for LES has been carried out. The importance is that the EDC, up to some point, is a turbulence model aimed at identifying the dissipative scales in turbulent flows. Then the intermittency effects are added to the model and together with the time scale of the dissipative motions as a residence time of hypothetical reactors, it becomes a combustion model. The model makes use of turbulent quantities. Now the importance of an *a priori* DNS analysis is revealed; averaged/filtered DNS data can be regarded as exact turbulent quantities and fed to the model. So that no uncertainty regarding turbulence models exists and the pure combustion model can be assessed. In other words, we can see how the model will behave if all inputs are exact. This is also an advantage when dealing with newly developed models like the new EDC-LES or dynamic SS models developed in the current PhD. work. For the *a priori* analyses carried out in this dissertation 3 DNS databases of temporally evolving non-premixed syngas jet flames with relatively detailed chemistry, with different Reynolds numbers, performed in Sandia, have been selected [6]. The DNS databases

will be introduced in detail in Chap. 4.

Beside but also linked to the first objective, fundamental analyses were carried out using the DNS databases from the statistical point of view. The first subject is the intermittency phenomenon in general and specifically the small-scale (internal) intermittency. While the intermittency of the Turbulent Kinetic Energy (TKE) dissipation rate has been extensively studied by turbulence community in non-reactive flows (see e.g., the related works of Antonia's group [25–27] or Sreevansan's group [28–30], will be reviewed later in Sec.5.2.2), it has not drawn the same amount of attention in the combustion community. Some limited examples of the works on the topic are [31–34]. Recently, Cortion et al., [34] investigated the effect of combustion on the norm of the strain rate tensor by TPIV measurements of Sandia flame C, flame C with increased local extinction and a non-reactive jet. They saw that the strain rate magnitude is enhanced by combustion with the tail of the PDF of the magnitude of strain rate extending to the larger values (enhanced intermittency) compared to the non-reactive case. They also studied the temporal intermittency which is a very important aspect of intermittency phenomenon, however, in the current work the focus is on spatial intermittency, not the temporal one. Pouransari et al., [33] studied the skewness and flatness of velocity fluctuations, and their wall-normal gradients in DNS of plane wall-jets, both reacting and non-reacting cases. The effect of wall was revealed in the different behavior of the streamwise and wall-normal velocity gradients. It was observed that by approaching the wall, the streamwise velocity gradient flatness is decreasing while the wall-normal one is increasing. No clear difference was observed between the reacting and non-reacting results. Hamlington et al. [32] did analyze the PDF of the strain rate magnitude, enstrophy and scalar (reactant mass fraction) dissipation rate in a DNS of premixed H2-Air mixture. The simulations performed with three different initial turbulence intensities. It was observed that the PDFs of the magnitude of strain rate (pseudo dissipation) are less intermittent than the PDFs of the enstrophy with also comparatively weaker variations through the flame. Further, it was found that the PDFs of pseudo dissipation are slightly more intermittent near the products at low intensities, and the variations in the PDFs through the flame were less pronounced in elevated intensities.

Of our interest is the study of scalings of the flatness (fourth-order moment) of velocity gradients in reactive jets which is to the author's knowledge missing in the combustion community. With the Homogeneous Isotropic Turbulence (HIT) assumptions, this quantity is equal to the mean square of the instantaneous/local TKE dissipation rate divided by the square of the mean TKE dissipation rate. In particular, we are interested to study how the Favre averaged square of the instantaneous/local TKE dissipation rate divided by the square of the Favre averaged instantaneous/local TKE dissipation rate, scales with Taylor Reynolds number ($Re_\lambda$) in non-premixed jets. Although extensive studies have been done so far on this power-law scaling in different types of non-reactive turbulent flows, it seems that there is a gap in the literature on the same topic for reactive flows. One of our motivations to study this phenomenon in reactive flows is that the intermittency effect has been explicitly modeled using phenomenological arguments in the EDC model. It is of great interest, if applicable, to use recent experimental data (see the compilation of experimental data in [35]) or theoretical works (see e.g. [36]) all on non-reactive flows, in the EDC model. So the phenomenon is studied in reactive flows and is compared to the experimental data and theories for non-reactive

flows. The intermittency phenomena are studied in Sec.5.2 and the findings are applied (as an example of the application of this fundamental study) to propose modified EDC models in Sec.3.2.4 (the second modification of the EDC).

The second fundamental study carried out in the PhD. work is on velocity spectra (the TKE and its dissipation spectra) of reactive flows and in particular non-premixed jet flames. The subject is of great importance both in experiments and numerics. In experiments, one needs to know a true resolution which is required to capture scalar gradients [37]. On the other hand, many numerical models rely on scaling laws of the spectra to evaluate model constants or to justify the assumptions [38] in the models. The studies on velocity and passive scalars spectra for non-reactive flows are vast in the literature (see the old reviews of the experimentally [39] and numerically [40] produced data). DNS has been exploited to cover a wide range of $Re_\lambda$, from low-to-medium [41], to high [42]. While the low-to-medium data confirm the existence of a plateau in the compensated TKE spectra corresponding to the Kolmogorov constant [41, 43] (and also confirming Kolmogorov's $5/3$ law), the recent high Reynolds data ($Re_\lambda > 700$) show that the compensated spectrum is not actually flat, but rather tilted slightly [42]. However, this is not our current concern since $Re_\lambda$ in the DNS databases used in the current study are much lower than the mentioned critical $Re_\lambda$.

The spectral behavior of the conserved scalars like mixture fraction and temperature have been studied in reactive flows (see e.g., [37, 44, 45]), however, with the focus on the identification of the required resolution for measuring the scalars gradients. Wang et al., [37] calculated a cut-off length scale (analogous to the Batchelor scale in non-reacting flows) from the high-resolution 1D dissipation spectra of the inverted Rayleigh scattering signal in the experiments of Sandia C, D and E and also DLR-A and B flames. The cut-off length scale was calculated based on the inverse of a wavenumber at which the dissipation spectra reach $2\%$ of their peaks. It was observed that different measured spectra collapse well if they are normalized by their corresponding cut-off scales. They also observed that the dissipation spectra for the temperature and the inverse of the Rayleigh signal follow nearly a similar exponential drop-off. They suggested that the cutoff length scale determined from Rayleigh scattering measurements may be used to define the local resolution requirements to capture the scalar gradients.

Of our interest is the TKE and its dissipation spectra and their modeling in reactive flows using DNS databases. While this has been a subject of the research for many years in the turbulence community focusing on non-reactive constant-density flows, it has received a limited attention in the combustion community.

The TKE spectrum was studied by Knaus and Pantano in 2009 [46] using DNS of temporally evolving reacting shear layers. Velocity, mixture fraction and temperature spectra obtained from five DNS databases of non-reacting and reacting shear layers, using the infinitely fast chemistry approximation were studied. They saw that the scalings proposed by Kolmogorov for non-reactive constant-density flows work well in the case of variable density (due to the heat release) flows, if the spectra are scaled based on Favre averaged statistics. This means that using Favre averaged Kolmogorov's scales one is able to collapse all spectra "across" the shear layers well. Although a very interesting finding, this was not confirmed in the case of premixed jets studied in [47]. However, our non-premixed double shear layer results confirm the finding of Knaus and Pantano [46], this will be the subject of Sec.5.3. Kolla et al., [47] proposed a new

method to calculate the TKE spectrum for the variable density and in particular reactive flows using the density-weighted two-point correlations. The advantage of the new formulation compared to the conventional unweighted formula is that the integral of the energy spectrum created by this method is exactly equal to the Favre TKE. The other advantage is the capability to explicitly study the terms like pressure-dilatation which are missing in the case of using the unweighted formula. They observed that, in the inertial range, the scaling laws for the spectra involving Favre-averaged Kolmogorov scales are applicable, but in the high wavenumber range, the laminar flame thickness produces a better collapse. They suggested that a full scaling should involve the Kolmogorov scale, the laminar flame thickness, the Damkohler number, and the Karlovitz number. However, consider that the findings are for premixed flames.

The TKE dissipation spectrum was studied by Kolla et al., [48] using DNS of premixed combustion in double shear layer configurations . They observed that the dissipation spectra computed on different statistically homogeneous planes across the jets collapse when normalized by their corresponding Favre mean dissipation rate and the cutoff length scale introduced by Wang et al., [37]. However, the normalized spectra deviate noticeably from the model spectrum of Pope [38] (proposed for constant density flows). They saw that the deviation is pronounced in the high wavenumber dissipative range where a universal scaling is expected. The finding found to be different from the experimental observations in the non-premixed flames studied in [37], where a good agreement with the model spectrum was reported. This recent observation was a motivation of the study carried out in Sec.5.3 on the spectral behavior of non-premixed flames. Consider the limited works in the literature on non-premixed flames; both DNS [46] and experiments [37], reported that the TKE (in [46]) and the scalar dissipation (in [49]) spectra follow the model spectrum of Pope. At least in the case of Knaus and Pantano [46], closer inspection shows that the collapse of the model and the DNS is not so perfect. These points will be investigated comprehensively in the current study. Further, no extensive attempt has been carried out in the previous works to examine the model spectrum of Pope for reactive jets. As mentioned before, it was only shown in the recent work of Kolla et al., [48] that, in premixed jets, in high wave number ranges, the TKE dissipation spectrum does not follow the model. An analysis of the model spectrum has been carried out in the current study and an attempt is made to adapt the model spectrum to the reactive cases.

In addition to the applications of the fundamental studies on the spectral behavior of turbulent flows which are mentioned elsewhere [47, 48], another motivation to study the dissipation spectrum specifically in high wave number ranges, is its application we found in the EDC model. A theory is developed in this thesis to reduce the number of user-defined coefficients of the EDC model from two to one. A link is made through the cascade relations in wavenumber space between the two coefficients. A model dissipation spectrum is required to close the model. The adapted model spectrum was used in Sec.3.2.3 (the first modification of the EDC).

Following the above introduction, the structure of the thesis is as follows:

In Chap. 2, the turbulence theory and its modeling approaches which are used in this thesis are presented in detail. The first part is focused on the statistical point of view and presents the approaches mainly used in Chap. 5, Sections5.2 and 5.3. The second part is devoted to the modeling point of view and the governing equations and all exact

quantities which have been used in the *a priori* DNS analysis are presented.

In Chap. 3, the finite-rate combustion models (the EDC and the Scale Similarity) are presented. The first part is devoted to the EDC model. The discussion starts from the general idea of the eddy dissipation cascade as a turbulence model. The state of the art will be discussed and the new formulation of the EDC for RANS and LES obtained using newly gained physical insights (based on the studies in Sec.5.2.2 and 5.3) will be presented. The second part is devoted to the SS models. In particular the existing non-dynamic SS models and newly developed dynamic SS models will be presented.

In Chap. 4, the methodology (an *a priori* DNS analysis) used in the current dissertation is explained. DNS databases which were used will be presented in details and the tools needed for the *a priori* analysis will be briefly presented, including explicit filters, assessment metrics, and the *a priori* code developed as a part of current project.

Chapter 5 is divided in two parts. In the first part, the fundamental analyses on the intermittency and the velocity spectra (the turbulent kinetic energy and its dissipation) will be carried out using the current DNS databases of reactive temporally evolving jet flames. The DNS databases were introduced in Sec.4.5, and some related theories were already discussed in Sections 2.2.1, 2.2.4, and 2.2.7. The results of the first part of this chapter, i.e., Sections 5.2 and 5.3 were also used in Sec.3.2 to derive new EDC models. In the second part of this chapter, the performance of the existing and developed finite-rate combustion models for LES (FR-LES-TCI models), developed in Chap.3 will be *a priori* assessed using the DNS databases. This part includes Sec.5.4.1 on the EDC, Sec.5.4.2 on the non-dynamic Scale Similarity (SS) models and finally Sec.5.4.3 on the newly developed dynamic SS models.

Finally, in Chap. 6, the summary of the work, the conclusions and the proposals for future works will be presented.

In summary the highlights of the current dissertation are as follows:

- **The internal intermittency phenomenon** in reactive jets was studied using DNS databases of reactive non-premixed jets (Sec.5.2):
  - $Re_\lambda$ scaling of the normalized dissipation fluctuation was studied to find a proper definition for the internal intermittency factor in reactive non-premixed jets (Sec.5.2.2),
- **The velocity and velocity dissipation spectra** were studied using DNS databases of reactive non-premixed jets (Sec.5.3):
  - Proper scalings to collapse the spectra in different conditions were studied (Sections5.3.1 and 5.3.2),
  - A proper dissipation model spectrum were investigated (Sec.5.3.4),
- **Two separate modifications on the EDC** model were proposed (Sec.3.2):
  - The first modification is based on (i) the development of a theoretical relation between the eddy dissipation cascade in the frequency and wavenumber space and (ii) the application of the adapted dissipation model spectrum to drop one of the EDC coefficients (Sec.3.2.3),
  - The second modification is based on the application of new $Re_\lambda$ scalings of the normalized dissipation fluctuation (Sec.3.2.4),

- **New dynamic scale similarity models** for SGS combustion modeling were developed using the Germano identity (Sec.3.4),
- **The *a priori* DNS assessment** was carried out on the existing and newly developed EDC combustion models for LES (Sec.5.4.1),
- **The *a priori* DNS assessment** was carried out on the existing and newly developed SS combustion models for LES (Sections 5.4.2 and 5.4.3).

CHAPTER 2

# Turbulence

## 2.1 Introduction

In this section the theory of turbulence and its modeling approaches which have been used in this thesis are presented in detail. Wherever needed, the way they theory is applied in practical/numerical viewpoints are explained. The chapter starts with the first sub-section presenting the statistical approach of studying turbulence; the probabilities, joint probabilities and Favre statistics. The Kolmogorov theory is discussed following the presentation of all quantities used throughout the thesis. The spectral representation of the Kolmogorov theory and its generalization is explained. This is done since we dedicated a section in studying the spectra of reactive flows in Chapter 5.

In the second sub-section, the computational turbulence modeling is explained. It starts with the presentation of the Navier Stokes (NS) governing equations and their Favre averaged and Favre filtered forms. Since the current thesis is focused mainly on *a priori* DNS analysis, the exact definitions of turbulent quantities like the TKE, its dissipation, sub-grid kinetic energy and the viscous sub-grid dissipation have been explained.

## 2.2 The Theory: Statistical Approach

One of the most important characteristics of turbulence is its irregularity, or randomness. This makes a deterministic approach to turbulence impossible and instead, one should rely on statistical approaches [50]. The thing is that although Navier-Stokes equations are deterministic, the non-linearity in these equations makes them sensitive to perturbations of initial/boundary conditions or the material properties of the flow. This sensitivity becomes higher and higher by increasing the Reynolds number (Re). This causes the solution of the Navier-Stokes equations to be chaotic/random [38]. The

probability theory is used to mathematically describe the random fields or processes. Strictly speaking, there is a difference when one tries to apply the concept in practical applications like experimental measurements or numerical simulations. The link between the theory and practical applications is made through the ergodic hypothesis which comes from the Birkhoff ergodic theory [51] which will be explained below. So we start first by the mathematical viewpoints and wherever needed the approximate representation of the solid mathematics is provided. Further, we restrict the discussion on what will be used/implemented in the thesis; the aim is to define the concept and use it in the following chapters. The theory which will be explained below is mainly deduced from the books of Monin and Yaglom [52], Tennekes and Lumely [50] and Pope [38]. The interested reader should refer to the mentioned text books.

### 2.2.1 Probability Density Functions

Consider a random variable $q(\mathbf{x}, t)$ measured in a turbulent flow in a fixed position in space during a time interval $T$. In the previous expression, $\mathbf{x} = (x_1, x_2, x_3)$ *or* $(x, y, z)$ is the position vector and $t$ is time. This measurement produces a sample space, $S$, with samples $Q(t)$ which is function of time only. The probability which $q(t)$ takes the value below any value $Q$ is the the Cumulative Distribution Function (CDF), $F(Q)$, and defined as:

$$F(Q) \equiv P\{q(t) < Q\}. \tag{2.1}$$

It can be seen that $F(-\infty) = 0$ and $F(+\infty) = 1$, because there is no possibility that the value becomes below $-\infty$, and vice versa the probability of taking a value below infinity is 1. Further, the probability of $q(t)$ taking a value between $Q$ and $Q + dQ$ is:

$$P\{Q \leq q(t) < Q + dQ\} = F(Q + dQ) - F(Q) = dF(Q). \tag{2.2}$$

It can be shown that $F(Q)$ is an increasing function so its derivative is definite positive function. The derivative is called Probability Density Function (PDF):

$$PDF(Q) \equiv \frac{dF(Q)}{dQ} = \frac{F(Q + dQ) - F(Q)}{dQ}. \tag{2.3}$$

So it can be seen that the PDF is the probability that $q$ takes a value between an infinitesimal range divided by that range. The PDF (or equally the CDF) fully characterizes the random variable $q$ [38].

**Some practical notes**: In practical applications, given a time series of measured data by a probe in a fixed location within the turbulent flow, or a data set of spatial quantities in a fixed time instant sampled on a statistically homogeneous plane[1], or line, the PDF is usually calculated using histograms. The data are grouped into bins (for example $Q, Q + dQ, Q + 2dQ, ...$, so that in this case the length of the bins are all the same and equal to $dQ$ ) and the probability of a data point being in each group, viz. $P\{Q \leq q(t) < Q + dQ\} = F(Q + dQ) - F(Q) = dF(Q)$, is calculated by counting the number of data in each bin. Then it is easy to define the PDF by dividing the obtained value by the length of the bin, viz. $dQ$. The binning algorithm is of great importance. The number and the length of the bins affect significantly the resulting PDF. For example consider if the number of the bins are equal to the number of the data

[1] This is the case in the current thesis, please refer to Sec. 4.5

points in the dataset, the result is the original distribution of the data. In the thesis some times the dataset is binned into bins with equal lengths (say 100 bins) and sometimes when we expect a Gaussian distribution (will be defined later) we use Sturges' rule [53]. The PDFs computed using the method above will be used in Sec. 5.2.

#### Moments of Variables

The mean or more precisely the *probability mean*[2] of a random variable $q$, viz. $\langle q \rangle$, is defined by:

$$\langle q \rangle \equiv \int_{-\infty}^{+\infty} QPDF(Q)dQ. \tag{2.4}$$

From the mean, the fluctuation of a random quantity, viz. $q'$ can be defined:

$$q' \equiv q - \langle q \rangle. \tag{2.5}$$

From the definition of the *probability mean* it is clear that $\langle q' \rangle = 0$. A quantity with zero mean is called a *centered* quantity.

In practical applications, the *temporal mean* or the *time average*, viz. $\underline{q}_T$, is calculated by averaging the values taken out of a probe in a fixed location over a period of time $T$. The temporal mean is defined by:

$$\underline{q}_T \equiv \frac{1}{T} \int_0^T q(t)dt. \tag{2.6}$$

We can consider and infinitely large interval for integration and define $\underline{q}_{T_\infty}$ as:

$$\underline{q}_{T_\infty} \equiv \lim_{T->\infty} \frac{1}{T} \int_0^T q(t)dt. \tag{2.7}$$

The Birkhoff ergodic hypothesis states that *the time average* of a quantity is equivalent to *the probability mean* or *the ensemble average* when it is averaged over an infinitely large interval [51, 52] which means:

$$\underline{q}_{T_\infty} = \langle q \rangle. \tag{2.8}$$

Of course, we cannot integrate over an infinitely long time interval, it can be shown that [50] the error between $\underline{q}_T$ and $\langle q \rangle$ is proportional to $\mathcal{T}/T$ where $\mathcal{T}$ is the integral time scale will be defined later. So if the integration time is much larger than the integral time scale of the flow, we have:

$$\underline{q}_T \approx \underline{q}_{T_\infty} \quad if T \gg integral\, time\, scale, \tag{2.9}$$

where if we use the ergodic hypothesis in Eq. 2.8, we have:

$$\underline{q}_T \approx \langle q \rangle \quad if T \gg integral\, time\, scale. \tag{2.10}$$

Consider $q(t)$ being a velocity component, e.g., in $Ox$ direction of a 3D space characterized by $\mathbf{x} = (x, y, z) = x_i \quad i = 1, 2, 3$. Consider $q(t)$ is in a sample-space of velocity vectors, $\mathbf{U}(\mathbf{x}, t) = \{U_i(\mathbf{x}, t) \quad i = 1, 2, 3\} = (U(\mathbf{x}, t), V(\mathbf{x}, t), W(\mathbf{x}, t))$,

[2] The term is used in [52] to make a difference between the mean calculated from the PDF and the time or spatial averages.

measured in a fixed position in space during the time interval $T$. Time averages are used to define the mean in statistically stationary flows. The statistically stationary flow is a flow with $\underline{\mathbf{U}}_T$ independent of time. Likewise, we can define a statistically homogeneous flow in which the mean flow is invariant under the shift in space. If the averages are also independent of the origin in position, then the field is said to be homogeneous. Homogeneity is exactly analogous to stationary except that position is now the variable, and not time. Since the position, unlike the time, is a vector quantity, it is also possible to have only partial homogeneity. For example, a field can be homogeneous in the $Ox$ and $Oz$ directions, but not in the $Oy$ direction[3]. In fact, it appears to be impossible to have flows in reality which are homogeneous in all variables and stationary as well, but the so-called "forced" turbulence can be generated in a computer, which is both stationary and approximately homogeneous [54,55]. Consider a random variable like an $Ox$ component of the velocity vector $\mathbf{U}(\mathbf{x},t) = \{U_i(\mathbf{x},t) \quad i = 1,2,3\} = (U(\mathbf{x},t), V(\mathbf{x},t), W(\mathbf{x},t))$, in a fixed time $t$ measured in the 1D longitudinal direction $Ox$[4], $q(x,t)$. The probability which $q(x,t)$ takes a value below any value $U$ will be a function of $Ox$ and also the CDF and PDF. Then one can define the spatial average. The spatial averages are used in the so called temporal jets or in the planes parallel to the wall of the duct. In this thesis the analyses are mainly done on temporal jets in which two homogeneous directions exist. Under the same condition as explained above (i.e., the averaging interval/length must be greater than the integral length[5] scale of the flow) and considering $x$ the homogeneous direction in $\mathbf{x} = (x,y,z) = x_i \quad i = 1,2,3$ we have:

$$\underline{q}_L \approx \underline{q}_{L_\infty} \equiv \lim_{L->\infty} \frac{1}{L} \int_0^L q(x,t)dx. \tag{2.11}$$

If there exists two or three homogeneous directions, the formula above would be the dual or triple integral, respectively. As can be seen here the mean is defined based on the space not the conventional time.

**Since in the thesis we are not working with time series, hereafter we drop the $(.)_T$ and $(.)_L$ subscripts and denoting the averages by $\underline{(.)}$ only.** Then using the theorem 2.8 and approximation 2.10, from now on the thesis **we equate the *probability mean* and the *average* operators**:

$$\underline{(.)} \equiv \langle . \rangle \quad if\, averaging\, interval\, or\, length \gg integral\, length\, scale. \tag{2.12}$$

The averages are spatial averages unless otherwise mentioned. Further, in the numerical framework the integral in Eq. 2.11 is computed by using the sum so that for example one can compute the average over the whole dataset as:

$$\underline{q}(t) = \frac{\sum_{n3=1}^{n3=N_z} \sum_{n2=1}^{n2=N_y} \sum_{n1=1}^{n1=N_x} q(x_{n1}, y_{n2}, z_{n3}, t)}{N_x N_y N_z}, \tag{2.13}$$

where $x_n$, $y_n$, and $z_n$s are the points in $Ox$, $Oy$, and $Oz$ directions, respectively. $N_x$, $N_y$, $N_z$ are the total number of points in those directions.

[3] This is the case in the DNS cases we are analyzing in this thesis. Please refer to Sec. 4.5.

[4] Of course the theory can be extended in 3D space

[5] Will be defined in the following

In the specific case of DNS databases which are used in the current study, two homogeneous directions exist[6], in the $Ox$ and $Oz$ directions, so we have:

$$\underline{q}(y,t) = \frac{\sum_{n3=1}^{n3=N_z} \sum_{n1=1}^{n1=N_x} q(x_{n1}, y, z_{n3}, t)}{N_x N_z}. \tag{2.14}$$

Going back to the theory, the different moments of variables can be defined using the PDF. The first moment of a centered variable is 0[7]. The second moment of a variable, $q$, is called variance:

$$\underline{\left(q'^2\right)} = \int_{-\infty}^{+\infty} q'^2 PDF(q')dq', \tag{2.15}$$

and $\sigma$, the standard deviation or Root Mean Square (RMS), is define as:

$$\sigma \equiv \sqrt{\underline{\left(q'^2\right)}}, \tag{2.16}$$

where we already used 2.12. The standard deviation can be used to construct the standardized random variables; by dividing the centered variable by its standard deviation.

The third moment of a variable, $q$, is calculated by:

$$\underline{\left(q'^3\right)} = \int_{-\infty}^{+\infty} q'^3 PDF(q')dq'. \tag{2.17}$$

If it is divided by third power of the standard deviation, i.e., $\sigma^3$ the result is called skewness ($\mathcal{S}$):

$$\mathcal{S}_q \equiv \frac{\underline{\left(q'^3\right)}}{\left(\sqrt{\underline{\left(q'^2\right)}}\right)^3}. \tag{2.18}$$

It is obvious that unlike the variance, $\mathcal{S}$ is affected by the lack of the symmetry in PDF about the origin. The skewness is positive when large negative values of $q'^3$ are not as frequent as its large positive values [50]. The fourth moment divided by $\sigma^4$ is called flatness ($\mathcal{F}$) and is defined as[8]:

$$\mathcal{F}_q \equiv \frac{\underline{\left(q'^4\right)}}{\left(\sqrt{\underline{\left(q'^2\right)}}\right)^4}, \tag{2.19}$$

which represents the length of the tails of the PDF. High $\mathcal{F}$ means that the probability of extreme events (with values much higher than the mean) is high. It will be seen in Sec. 5.2 that the flatness of fluctuative velocity derivatives, $\partial u'/\partial x$[9], is a measure of the internal intermittency factor ($\gamma_{int}$) in turbulent regions. In Sec. 5.2 the PDF of the velocity fluctuations and their derivatives will be analyzed to study the intermittency in reactive jet flows.

[6] Please refer to Sec. 4.5.

[7] This is simply the mean of the fluctuations which is 0.

[8] In both definitions of third and fourth moments the ergodic assumption is used

[9] In general it is the RMS of fluctuative velocity gradient tensor.

#### Normal or Gaussian Distribution

A centered random variable, $q'$, is called Normal or Gaussian when its PDF set to be equal to [51]:

$$PDF(Q') \equiv \frac{1}{(2\pi\sigma^2)^{1/2}} e^{-\frac{Q'^2}{2\sigma^2}}, \tag{2.20}$$

where $Q'$ is any centered value in a sample space. It can be proved that the skewness of a centered Gaussian variable is 0 and its flatness is 3.0 [50].

#### Log-Normal distribution

If $q$ is a Gaussian random variable[10] with mean, $\langle q \rangle$, and variance, $\sigma$, then $n = e^q$ is said to be log-normally distributed [38] so that:

$$PDF(n) = \frac{1}{n\,(2\pi\sigma^2)^{1/2}} e^{-\frac{\left(\ln(n) - \langle q \rangle\right)^2}{2\sigma^2}}. \tag{2.21}$$

The assumption of the log-normal distribution in turbulence and turbulent reactive flows theory is of crucial importance which will be discussed later in Sec. 5.2.

### 2.2.2 Joint Statistics

All the statistical concepts which were defined for a random variable, can be extended to two or more random variables. These are called joint statistics which are used to define statistical behavior of two or more random variables with respect to each other. The joint Statistics will be used in the thesis to define the conditional PDFs, conditional means, Favre variables and different length scales. So it is useful to explain the concept before using it.

Consider two random variables $q_1$ and $q_2$ in a turbulent flow, these variables can be functions of space and time but for the sake of simplicity we drop this functionality in the notations below for the moment. Exactly like the PDF, here we can define the joint Probability Density Function (JPDF), which is the probability of two variables $q_1$ and $q_2$ being between two intervals in $S_1$ and $S_2$ sample spaces. Let's consider infinitesimal intervals $dQ_1$ and $dQ_2$ around $Q_1$ and $Q_2$ in sample space $S_1$ and $S_2$. In the same way as Eq. 2.2 and Eq. 2.3, the JPDF will be defined as:

$$JPDF_{q_1,q_2}(Q_1, Q_2) \equiv \frac{P\{Q_1 \leq q_1 < Q_1 + dQ_1; Q_2 \leq q_2 < Q_2 + dQ_2\}}{dQ_1 dQ_2}. \tag{2.22}$$

This clearly describes the probability that a randomly selected sample from the sample space (say a computational cell selected from a DNS result) has the two characteristics of interest (i.e., being between $Q_1, Q_1 + dQ_1$ and $Q_2, Q_2 + dQ_2$ at the same time).

The JPDF can be used to define the marginal PDFs which are actually the single variable PDFs defined in Eq. 2.3:

$$PDF_{q_1}(Q_1) \equiv \int_{-\infty}^{+\infty} JPDF_{q_1,q_2}(Q_1, Q_2) dQ_2. \tag{2.23}$$

[10] Not a centered one.

The JPDF can be used to define the conditional PDFs:

$$CPDF_{q_2|q_1}(Q_2|Q_1) \equiv \frac{JPDF_{q_1,q_2}(Q_1,Q_2)}{PDF_{q_1}(Q_1)}, \tag{2.24}$$

which can be considered as the conditional probability of having characteristic $Q_2 \leq q_2 < Q_2 + dQ_2$ given the characteristic $Q_1 \leq q_1 < Q_1 + dQ_1$. Vice versa we can define $CPDF_{q_1|q_2}(Q_1|Q_2)$. The conditional PDFs can be used to define the conditional means:

$$\langle q_2|q_1 = Q_1\rangle \equiv \int_{-\infty}^{+\infty} Q_2 CPDF_{q_2|q_1}(Q_2|Q_1)dQ_2. \tag{2.25}$$

The JPDF can be used to define the correlation coefficient ($\rho_{q_1q_2}$):

$$\rho_{q_1q_2} \equiv \langle q_1' q_2'\rangle / \sqrt{\langle {q_1'}^2\rangle \langle {q_2'}^2\rangle}. \tag{2.26}$$

The $\rho_{q_1q_2}$ is defined as the covariance of the two random variables divided by the multiplication of the individual variances. It is bounded by $\pm 1$, with $+1$ representing a perfect correlation while $-1$ shows a perfect anti-correlation. When the $\rho_{q_1q_2}$ is zero this means that the two variables are uncorrelated. Uncorrelated variables, however, are not necessarily independent of each other [50]. In Sec. 5.4 we will use these concepts to search for a correlation between modeled terms and the exact ones from DNS databases.

To extend the theory to turbulent fields, we now turn into the random fields which are functions of space and time. Consider the velocity as a random variable in space and time in a turbulent flow:

$$\mathbf{U} = \mathbf{U}(\mathbf{x}, t). \tag{2.27}$$

Let's focus on the special case of temporally evolving flows, which is the case we are dealing with in this thesis, and focus on an instant of time. We already defined the statistically homogeneous flow in Sec. 2.2.1. We can define a correlation between any two random quantities measured along the statistically homogeneous lines or on the homogeneous planes. We set these quantities any two components of the velocity vector, i.e., $\mathbf{U}(\mathbf{x}, t) = (u_1, u_2, u_3)$, we denote the components of the velocity in the first point as $u_i$ $i = 1, 2, 3$ and the second point as $u_j$ $j = 1, 2, 3$). These quantities are measured in two points with separation distance of $\mathbf{r} = r_i = (r_1, r_2, r_3)$. Since these quantities are functions of time and space, so the correlation between them is also a function of time and space. The two point correlation function ($R_{ij}$) or correlation tensor is defined as[11]:

$$R_{ij}(\mathbf{r}, \mathbf{x}, t) \equiv \langle u_i'(\mathbf{x}, t) u_j'(\mathbf{x} + \mathbf{r}, t)\rangle, \tag{2.28}$$

which as can be seen, is actually the covariance between the two components of the velocity vector field in two different points separated by $\mathbf{r}$. If the turbulence is homogeneous, the correlation tensor is a function of the separation distance $\mathbf{r}$ and the time only [50]:

$$R_{ij}(\mathbf{r}, t) \equiv \langle u_i'(\mathbf{x}, t) u_j'(\mathbf{x} + \mathbf{r}, t)\rangle. \tag{2.29}$$

The quantity is of great importance and can be used in the spectral representation of turbulent flows which will be discussed later in Sec. 2.2.7.

[11] $u_i'$ can be defined by Eq. 2.5

**Some practical notes**: In the practical applications, the JPDFs are calculated using the joint or 2D histograms. The sample spaces of the two variables can be defined from all values within the computational domain in the DNS (say on a specified plane). Then the two sample spaces are binned using the method described in Sec.2.2.1. The joint histograms then can be defined by counting the number of variables satisfying the conditions in the joint bins. The conditional means can then be easily calculated using:

$$\underline{q_2|q_1} = \sum_{Q_2} Q_2 CPDF(Q_2|Q_1), \tag{2.30}$$

which will be used in the results sections.

### 2.2.3 Favre Variables and Statistics

Up to this point, we introduced the moments of random variables and their PDF. The equations presented are suitable for constant density flows. When the mean operator Eq. 2.4 applied on the equations of motions of variable density flows like reactive flows, many unclosed correlations between any quantity $q$ and the density fluctuations,$\rho'$ will be introduced [56]. It is convenient to define another mean operator which is called the Favre mean operator. In the Favre averaging, quantities are weighted by their instantaneous density before averaging. The Favre PDF is defined as [57]:

$$FPDF(Q) \equiv \frac{1}{\langle\rho\rangle} \int_0^\infty \rho JPDF(\rho, Q) d\rho, \tag{2.31}$$

where $JPDF(\rho, Q)$ is the joint PDF of $\rho$ and $Q$. Then the Favre mean is defined as:

$$\langle q\rangle_f \equiv \frac{\langle\rho q\rangle}{\langle\rho\rangle} = \int_Q Q\ FPDF(Q) dQ. \tag{2.32}$$

From the Favre mean one can define the Favre fluctuation[12]:

$$q'' \equiv q - \langle q\rangle_f. \tag{2.33}$$

The $n^{th}$ Favre central moments, $n \geq 2$, can be defined as:

$$\langle q''^n\rangle_f \equiv \frac{\langle\rho q''^n\rangle}{\langle\rho\rangle} = \int_Q (Q - \langle q\rangle_f)^n\ FPDF(Q) dQ. \tag{2.34}$$

**Some practical notes**: In the practical applications, and throughout the current thesis, the probability mean, i.e. Eq. 2.32, is not used and is replaced with the average operator. In particular, in our temporally evolving jets where two statistically homogeneous directions exists [13], we define the Favre average of a quantity $q(x, y, z, t)$ by:

$$\underline{q}_f(y,t) \equiv \frac{1}{\underline{\rho}(y,t)} \frac{\sum_{n3=1}^{n3=N_z} \sum_{n1=1}^{n1=N_x} \rho(x_{n1}, y, z_{n3}, t) q(x_{n1}, y, z_{n3}, t)}{N_x N_z}, \tag{2.35}$$

where $\underline{\rho}(y,t)$ can be calculated by using Eq. 2.14. From Eq. 2.35 and Eq. 2.33 in the temporally evolving jet considered in this thesis can be numerically computed by:

$$q''(y,t) \equiv q(x,y,z,t) - \underline{q}_f(y,t). \tag{2.36}$$

[12] Note that in this way $\langle q''\rangle \neq 0$ but $\langle q''\rangle_f = 0$.

[13] Please see Sec. 4.5.

The central Favre moments of order $n$ of quantity $q(x, y, z, t)$ can also be computed by:

$$\underline{q''^n}_f(y,t) \equiv \underline{\Big(q(x,y,z) - \underline{q}_f(y,t)\Big)^n}_f, \tag{2.37}$$

where spatial averaging is carried out in two statistically homogeneous directions $Ox$ and $Oz$. The Favre RMS can then be defined as:

$$q_{FRMS}(y,t) \equiv \sqrt{\underline{\Big(q(x,y,z,t) - \underline{q}_f(y,t)\Big)^2}_f}. \tag{2.38}$$

### 2.2.4 Structure Functions

Before the presentation of the Kolmogorov theory, a statistical tool used by Kolmogorov must be explained. In its general form, the second order structure function tensor is defined by [38]:

$$D_{ij}(\mathbf{r}, \mathbf{x}, t) \equiv \langle (U_i(\mathbf{x}+\mathbf{r}, t) - U_i(\mathbf{x}, t))\,(U_j(\mathbf{x}+\mathbf{r}, t) - U_j(\mathbf{x}, t))\rangle. \tag{2.39}$$

It is the covariance of the difference in velocities between two points in a turbulent flow separated by a distance $\mathbf{r}$.

It can be proved that in statistically homogeneous (which is previously defined) and locally isotropic (i.e., statistics are invariant under rotations and reflections of the coordinate system), this tensor first only depends on the difference $\mathbf{r}$ but not $\mathbf{x}$, and second is determined by the single longitudinal structure function which is a scalar function of $r = |\mathbf{r}|$. The longitudinal structure function is:

$$D_{LL}(r,t) \equiv D_{11}(r,t) = \langle (U_1(\mathbf{x} + \boldsymbol{e_1} r, t) - U_1(\mathbf{x}, t)))^2 \rangle. \tag{2.40}$$

It is assumed that the coordinate system is chosen so that $\mathbf{r}$ is in the $Ox$ direction (i.e. $\mathbf{r} = \boldsymbol{e_1} r$) [38]. In some text books like [51] a more general definition of the longitudinal and transversal structure functions are provided, which does not require the specific choice of the coordinate system, so that we can define the longitudinal structure functions of order $p$ as:

$$D_{LL_p}(r,t) \equiv \langle \big(\mathbf{U}(\mathbf{x}+\mathbf{r}, t) - \mathbf{U}(\mathbf{x}, t).\boldsymbol{e}_{\parallel}\big)^p \rangle, \tag{2.41}$$

and also the transversal structure functions of order $p$ as:

$$D_{NN_p}(r,t) \equiv \langle (\mathbf{U}(\mathbf{x}+\mathbf{r}, t) - \mathbf{U}(\mathbf{x}, t).\boldsymbol{e}_{\perp})^p \rangle. \tag{2.42}$$

The structure functions, especially the longitudinal structure function is of great importance in the turbulence theory. Consider a component of the velocity vector, for example $U_1$ in Eq. 2.40, using the Taylor expansion when $r$ is not too large [29]:

$$U_1(\mathbf{x} + \boldsymbol{e_1} r, t) - U_1(\mathbf{x}, t) \simeq \frac{\partial U_1}{\partial x} r, \tag{2.43}$$

which can be interpreted as a fluctuation representing the small-scales of the flow behavior. So Eq. 2.40 can be seen as the energy of fluctuations. Having in mind that wavenumbers in Fourier space, i.e. $\kappa$, are related to the distances in physical space by $\kappa \sim 1/r$, we see that if a formula for the second order structure function in terms

of $r$ can be found, we can predict the distribution of the energy as a function of the wavenumber [58]. We will see in the next section that Kolmogorov actually did propose a formula for the structure functions of order 2 and 3 and further Obukhov[14] derived the famous $\kappa^{-5/3}$ law from them [51].

### 2.2.5 The Kolmogorov 1941 Theory

With the all statistical definitions introduced above, now it is the time to apply the above theories on random processes or random fields to get some physical understanding of turbulent flows.

Here we present Frisch's treatment of the Kolmogorov theory [51] . The first Kolmogorov universality assumption also called Kolmogorov's first similarity hypothesis is:

**Kolmogorov's first universality assumption.** *At very high, but not infinite, Reynolds number, all of the small-scale statistical properties are uniquely and universally determined by the length scale $r$, the mean dissipation rate (per unit mass) $\underline{\varepsilon}$[15] and the viscosity $\nu$*[16].

His second universality assumption is:

**Kolmogorov's second universality assumption.** *In the limit of infinite Reynolds number, all small-scale statistical properties are uniquely and universally determined by the length scale $r$ and the mean dissipation rate $\underline{\varepsilon}$.*

Both the above assumptions are about thw statistics of "small-scales" quantities. According to Pope [38] and Frisch [51] in the first assumption we mean scales so smaller than the large scales of flow and in the second assumption we have the additional restriction which is for scales so larger than the small, dissipative scales of the flow. We call the scales in this range the "inertial range" scales.

There are three main results of the K41 theory, namely, the finite dissipation rate, the $2/3$ law and the $4/5$ law. Here we just discuss the two latter, interested readers should refer to chapters 5 and 6 of Frisch [51] for the discussion on the finite dissipation rate.

The result of the second universality assumption is:

**Kolmogorov's 2/3 Law.** *In a turbulent flow at very high Reynolds number, the mean-square velocity increment between two points separated by a distance $r$ behaves approximately as the two-thirds power of the distance. That is:*

$$D_{LL2}(r,t) \propto r = C_2 \left(\underline{\varepsilon} r\right)^{2/3}, \tag{2.44}$$

with $C_2$ a universal constant, and

**Kolmogorov's 4/5 Law.** *In the limit of infinite Reynolds number, the third-order longitudinal structure function of homogeneous isotropic turbulence, evaluated for increments $r$ small compared with the integral scale, is given in terms of the mean energy dissipation rate per unit mass as:*

[14] The original papers are [59] and [60] but here we used Frisch's explanation [51].

[15] The correct form is actually the probability mean i.e., $\langle \varepsilon \rangle$, however, we already showed that in some specific conditions the probability mean and temporal/spatial averages can be assumed to be equal.

[16] There is no need to define the average or the mean of the viscosity since the original theory is presented for constant density flows. In variable density flows like reactive flows, the Favre average of $\nu$ i.e., $\underline{\nu}_f$ must be used.

$$D_{LL3}(r,t) = -\frac{4}{5}\underline{\varepsilon}r. \tag{2.45}$$

This is an exact equation. It can be derived directly from the Navier-Stokes equations. The derivation can be found in [51, 52].

According to Kolmogorov's second assumption, for small separations $r$, $D_{LLp}(r,t)$ depends only on $\underline{\varepsilon}$ and $r$, and hence the dimensional analysis yields [38]:

$$D_{LLp}(r,t) = C_p\left(\underline{\varepsilon}r\right)^{p/3}. \tag{2.46}$$

The coefficient for the third order structure function is exact and equal to $C_3 = -4/5$. For the second order structure function the experimental value of $C_2 = 2 \pm 0.4$ is obtained [39]. However, for higher orders $p \geq 4$ there is a large deviation from $p/3$ power law factor. This is believed to be related to the internal intermittency of small-scales (will be discussed more in Sec. 5.2), effects of which had not been included in the K41 theory (but attempts at this were made in the K62 theory) [38, 51].

Here it should be mentioned that usually we prefer (as it is also the case in the current thesis) to work with the spectral equivalent of Eq. 2.44 because the statistical convergence is better. This will be further discussed in Sec. 2.2.7.

### 2.2.6 Turbulent Scales

Now using the Kolmogorov theory and the statistical approach explained in the previous sections, we try to connect the theory and physics. In FIG. 2.1 a jet of water with Reynolds number of approximately 2300 is shown [61]. As can be seen, a turbulent flow consists of a broad range of scales.

The scales exist in a turbulent motion can be divided in four groups [58]:

- the large scales, based on the problem domain geometry,
- the integral scales, which is an O(1) fraction (often taken to be 0.2) of the large scales,
- the inertial range scales or Taylor micro scales which are intermediate scales, basically corresponding to (actually,within) the Kolmogorov inertial sub-range,
- the Kolmogorov (or dissipative) scales which can be considered as the smallest of turbulence scales[17].

#### Large Scales

The largest scales of a turbulent flow depend on the geometry or the boundaries of the flow. The characteristic length scale is $L$ which is usually the size of the physical domain for example the radius of pipes in internal flows or the radius of jets inlet in external flows, or in the specific cases of temporally evolving jets considered in this thesis[18] the initial width of the jet. We further have the velocity of the large scales, $\underline{U}_f$, which is the Favre mean velocity for example in the center-line of a jet. From these

[17] In fact, this is the mean view, locally or instantaneously there can be length scales orders of magnitude smaller than the Kolmogorov scales [32, 62, 63]. This is caused by the intermittency of turbulent kinetic energy dissipation rate.

[18] Please refer to Sec. 4.5.

**Figure 2.1:** *Turbulent water jet, adapted from [61].*

two scale the largest "convective" time scale of the flow can be defined as $t_c = L/\underline{U}_f$. Further, another time scale is the time scale of the molecular diffusion which is $t_d = L^2/\underline{\nu}_f$ where $\underline{\nu}_f$ is the Favre average kinematic viscosity of the flow. It can be calculate either using:

$$\underline{\nu}_f = \underline{\mu}/\underline{\rho}, \tag{2.47}$$

or

$$\underline{\nu}_f = \underline{\left(\frac{\mu}{\rho}\right)}, \tag{2.48}$$

with $\mu$, the viscosity. The above equations produce indistinguishable results [46]. From the two large time scales one can defined a ratio which is actually the large scale Reynolds number, $Re_L$:

$$\frac{t_d}{t_c} = \frac{L^2/\underline{\nu}_f}{L/\underline{U}_f} = Re_L = Re. \tag{2.49}$$

Hereafter we drop the subscript $(.)_L$ and refer to $Re$ as the large scale Reynolds number unless otherwise mentioned.

#### Integral Scales

The next level of the turbulent scales are the integral scales of the flow. These do not cover a wide range and are associated with a single wavenumber corresponding to the maximum in turbulence energy [58].

The integral velocity scale ($u_{int}$) sometimes taken as the RMS of the velocity fluctuations [58], but it is more common to use the isotropic definition, i.e., $\sqrt{1/3}u_{RMS}$ [38, 64, 65]. In the case of variable density flows we take $\sqrt{1/3}u_{FRMS}$ as the integral velocity scale [46, 47]. Using the general second moment of the form Eq. 2.34 or more specifically for the current thesis the spatial form of Eq. 2.38, one can define the spatial Favre RMS of the velocity as:

$$u_{FRMS} \equiv \sqrt{\underline{u_i'' u_i''}_f}, \tag{2.50}$$

and so the $u_{int}$ is defined as:

$$u_{int} \equiv \sqrt{\frac{1}{3}} u_{FRMS} = \sqrt{\frac{1}{3}\underline{u_i'' u_i''}_f} = \sqrt{\frac{2}{3}\underline{k}_f}, \tag{2.51}$$

where a new term, i.e., Favre averaged TKE is introduced:

$$\underline{k}_f \equiv \frac{1}{2}\underline{u_i'' u_i''}_f, \tag{2.52}$$

The integral length scale ($l_{int}$) is defined by using Eq. 2.29:

$$l_{iiint}(\mathbf{x}, t) \equiv \frac{\int_0^\infty R_{ii}(e_i r, \mathbf{x}, t) dr}{R_{ii}(0, \mathbf{x}, t)}, \tag{2.53}$$

where different longitudinal ($l_{11int}$) or transverse ($l_{22int}$) or span-wise ($l_{33int}$) length scales can be defined. We are usually interested to define these scale in homogeneous directions.

There also other definitions exist [50]:

$$l_{int} \equiv \underline{k}_f^{3/2} / \underline{\varepsilon}_f, \tag{2.54}$$

and [47]

$$l_{int} \equiv u_{int}^3 / \underline{\varepsilon}_f. \tag{2.55}$$

In the current thesis the definition Eq. 2.55 will be used.

The integral time scale ($t_{int}$) is defined in statistically stationary flows[19] by the using one-point two-times correlation:

$$t_{int} \equiv \frac{\int_0^\infty R(s)ds}{R(0)} = \int_0^\infty \rho(s)ds. \tag{2.56}$$

The integral Reynolds number ($Re_{int}$) is defined by using

$$Re_{int} \equiv \frac{u_{int} l_{int}}{\underline{\nu}_f}. \tag{2.57}$$

#### Taylor Scales

The Taylor length scale ($\lambda$) is dealing with scales between the integral and the Kolmogorov dissipative scales. In constant density homogeneous isotropic turbulence one can prove that[20] [66]:

$$\varepsilon^s = 15\nu \underline{\left(\frac{\partial u_1'}{\partial x_1}\right)^2}, \tag{2.58}$$

where pseudo dissipation ($\varepsilon^s$) is defined. Consider that $\nu$ is constant. Then Taylor defined a new length scale, namely the $\lambda$, using the longitudinal velocity gradient as:

$$\lambda^2 \equiv \frac{u_1'^2}{\underline{\left(\frac{\partial u_1'}{\partial x_1}\right)^2}}, \tag{2.59}$$

and we can define the $Re_\lambda$ as:

$$Re_\lambda \equiv \frac{u_1' \lambda}{\nu}. \tag{2.60}$$

For variable density flows, we still keep using the assumption Eq. 2.58, with some modifications [46, 47, 67] we have:

$$Re_\lambda = u_{int} \lambda / \underline{\nu}_f, \tag{2.61}$$

in which the Favre average of viscosity was used to account for variable density flows. With $u_{int}$ from Eq. 2.51, the compressible form of $\lambda$ can be defined as:

$$\lambda^2 = \left(15 \underline{\nu}_f u_{int}^2\right) / \underline{\varepsilon}_f, \tag{2.62}$$

where $\underline{\varepsilon}_f$ is the Favre average turbulent kinetic energy dissipation rate ($\varepsilon$). It should be mentioned that Eq. 2.61 and Eq. 2.62 are the ones used in the thesis.

[19] In the thesis, since we are dealing with statistically homogeneous not stationary flows we can evaluate the integral scale by using the integral length scale and velocity scale, i.e. $t_{int} = l_{int}/u_{int}$.

[20] We will see in Sec. 2.3.1 that the TKE dissipation rate is related to the mean fluctuating rate of strain consists of several terms like $\underline{\left(\frac{\partial u_i}{\partial x_j}\right)^2}$. If one consider isotropy Eq. 2.58 can be derived.

**The Kolmogorov Scales**

One of the results of the Kolmogorov first similarity hypothesis is that since the small scale motions only depend on the rate of the energy transfer to them, $\underline{\varepsilon}_f$, and viscosity, $\underline{\nu}_f$[21], there are unique length, velocity, and time scales that can be formed [38, 50]. These are called the Kolmogorov or dissipative scales[22]:

$$\underline{\eta}_f \equiv \left(\frac{\underline{\nu}_f^{\,3}}{\underline{\varepsilon}_f}\right)^{1/4}, \tag{2.63a}$$

$$\underline{u_\eta}_f \equiv \left(\underline{\nu}_f \underline{\varepsilon}_f\right)^{1/4}, \tag{2.63b}$$

$$\underline{t_\eta}_f \equiv \left(\frac{\underline{\nu}_f}{\underline{\varepsilon}_f}\right)^{1/2}, \tag{2.63c}$$

where $\underline{\eta}_f$, $\underline{u_\eta}_f$, $\underline{t_\eta}_f$ are the Favre average of instantaneous or local Kolmogorov's length scale ($\eta$), instantaneous or local Kolmogorov's velocity scale ($u_\eta$) and local Kolmogorov's time scale ($t_\eta$), respectively. The exact expression for $\underline{\varepsilon}_f$ will be derived later in Sec. 2.3.1.

The above turbulent scales, mainly the Taylor and Kolmogorv's scales will be widely used in Sections 2.2.7 and 5.3 for the scaling of spectra.

### 2.2.7 Turbulent Kinetic Energy and its Dissipation Spectra

Now Consider the two-point correlation of fluctuative velocity[23] in homogeneous turbulent flow in an instant of time, i.e. Eq. 2.29. The velocity spectrum tensor ($\Phi_{ij}$) is the Fourier transform of it which reads:

$$\Phi_{ij}(\boldsymbol{\kappa}, t) \equiv \frac{1}{(2\pi)^3} \iiint_{-\infty}^{\infty} e^{-i\boldsymbol{\kappa}.\mathbf{r}} R_{ij}(\mathbf{r}, t) d\mathbf{r}, \tag{2.64}$$

which wavenumber vector ($\boldsymbol{\kappa}$) is used where $\boldsymbol{\kappa} \in \mathbb{R}^3 \equiv (\kappa_x, \kappa_y, \kappa_z)$. $\boldsymbol{\kappa}$ will be defined later.

The sum of the diagonal components of $\Phi_{ij}$ viz. $\Phi_{ii} = \Phi_{11} + \Phi_{22} + \Phi_{33}$, represents the kinetic energy of the fluctuations of a given wavenumber vector. This is because:

$$R_{ii}(0, t) = \langle u_i' u_i' \rangle = \iiint_{-\infty}^{\infty} \Phi_{ii}(\boldsymbol{\kappa}) d\boldsymbol{\kappa}. \tag{2.65}$$

Because of the directional information it has, the quantity in Eq. 2.65 contains more information than we can handle [50]. In order to remove the directional information in Eq. 2.65, the energy spectrum is usually integrated over the spherical shells around the origin of the wavenumber space which gives us a spectrum that is a function of the scalar wavenumber magnitude ($\kappa$), $\kappa = |\boldsymbol{\kappa}| = \sqrt{\kappa_i \kappa_i}$. The resulting function is called the 3D turbulent kinetic energy spectrum function ($E^{3D}(\kappa)$) [50].[24] We will drop the

[21] Here we present the Favre variants of the Kolmogorov scales.

[22] Of course in the compressible form.

[23] The Favre fluctuative velocity will be considered later.

[24] The reason that it is called the 3D spectrum although it is a scalar function of scalar wavenumber magnitude is that it is deduced from the 3D Fourier transform. In other words it contains informations of 3 directions in the wavenumber space, although it is then averaged to be a function of the magnitude of the wavenumber vector. On the other hand, the 1D spectrum is the result of the 1D Fourier transform and is a function of only one component of the wavenumber vector (not the magnitude of it).

$3D$ notation from now on and call it the turbulent kinetic energy spectrum function ($E(\kappa)$):

$$E(\kappa,t) \equiv \frac{1}{2}\iiint_{-\infty}^{\infty} \Phi_{ii}(\boldsymbol{\kappa})\delta(|\boldsymbol{\kappa}|-\kappa)d\boldsymbol{\kappa}. \tag{2.66}$$

one can see that:

$$\int_0^\infty E(\kappa,t)d\kappa = \frac{1}{2}R_{ii}(0,t) = \frac{1}{2}\langle u_i' u_i'\rangle = \frac{1}{2}\underline{u_i' u_i'} = \underline{k}, \tag{2.67}$$

where the term mean or averaged TKE ($\underline{k}$) is introduced.

#### The Kolmogorov Spectrum Function

The Kolmogorov spectrum function or breifly the Kolmogorov spectrum can be derived for example by dimensional analysis using the Kolmogorov's assumptions. The proof can be found in [51]. The Kolmogorov model for the 3D energy spectrum function for homogeneous isotropic incompressible flows in the inertial range reads:

$$E(\kappa) = C_K(\underline{\varepsilon})^{2/3}\kappa^{-5/3}, \tag{2.68}$$

where the Kolmogorov's constant ($\mathrm{C_K}$) is introduced, $C_K \approx 1.5$. It is also useful here to introduce the 1D form of Eq. 2.68. If $Ox$ direction is considered as a longitudinal direction, the 1D velocity spectrum in longitudinal direction ($E_{11}^{1D}(\kappa)$) [25] reads [39,52]:

$$E_{11}^{1D}(\kappa_x) = \frac{18}{55}C_K(\underline{\varepsilon})^{2/3}\kappa_x^{-5/3}, \tag{2.69}$$

where $\kappa_x$ is the longitudinal component of the wavenumber vector. The 1D velocity spectrum in transversal direction ($E_{22}^{1D}(\kappa)$) can also be calculated by:

$$E_{22}^{1D}(\kappa_x) = \frac{24}{55}C_K(\underline{\varepsilon})^{2/3}\kappa_x^{-5/3}, \tag{2.70}$$

where the factors $18/55$ and $24/55$ are exact, derived by using incompressible homogeneous isotropic turbulence assumptions [52].

The 3D normalized turbulent kinetic energy spectrum function ($E_{Normal}$) as a function of the wavenumber magnitude, $\kappa$, and the averaged Kolmogorov's length scale, $\eta$, for constant density flows is defined as[26]:

$$E(\kappa) \equiv \left(\underline{\varepsilon}\nu^5\right)^{1/4} E_{Normal}(\kappa\underline{\eta}) \tag{2.71a}$$

$$= \underline{\eta}\underline{u_\eta}^2 \quad E_{Normal}(\kappa\underline{\eta}) \tag{2.71b}$$

$$= \underline{\varepsilon}^{2/3}\underline{\eta}^{5/3}E_{Normal}(\kappa\underline{\eta}). \tag{2.71c}$$

According to the first universality assumption, the velocity statistics for the inertial range have a universal form [38]; $E_{Normal}(\kappa\underline{\eta})$ is the universal form in the wavenumber space derived by Obukhov, although it is called the Kolmogorov spectrum function. For

[25] Note that this is not an energy spectrum since it does not contain all 3 diagonal components.

[26] It can be extended to variable density flows by using the Favre averaged Kolmogorov's length scale, $\underline{\eta}_f$, the Favre averaged Kolmogorov's velocity scale, $\underline{u_\eta}_f$, the Favre averaged TKE dissipation rate, $\underline{\varepsilon}_f$, and the Favre averaged viscosity, $\underline{\nu}_f$.

example re-arranging the last equation in 2.71 one can see the proposed universal form of the spectrum in inertial range:

$$E_{Normal}(\kappa\underline{\eta}) = \left(\kappa\underline{\eta}\right)^{-5/3} C_K. \tag{2.72}$$

The 3D compensated turbulent kinetic energy spectrum function ($E_{Compensated}$) as a function of the wavenumber magnitude, $\kappa$, and the averaged Kolmogorov's length scale, $\eta$, for constant density flows is defined as[27]:

$$E_{Normal}(\kappa\underline{\eta}) \equiv \left(\kappa\underline{\eta}\right)^{-5/3} E_{Compensated}(\kappa\underline{\eta}), \tag{2.73}$$

which we expect to be equal to $C_K$ in the inertial range. However, the universal form of $E_{Compensated}(\kappa\underline{\eta})$ in the dissipation range is unknown [28] i.e., cannot be theoretically evaluated. In Sec. 5.3 this will be further discussed. The existence of the compensated form of the spectrum has been validated using many previous experiments[28] or numerics [40, 69, 70].

In the near (e.g. $0.5 \leq \kappa\underline{\eta} \leq 1.5$) and far ($\kappa\underline{\eta} \gg 1$) dissipation ranges, there is no direct derivation of the TKE spectrum. Many authors tried to fit different forms of function $E_{Normal}(\kappa\underline{\eta})$ in Eq. 2.71 [68, 70–74]. A famous form is [70]:

$$E_{Normal}(\kappa\underline{\eta}) = C_{DR}(\kappa\underline{\eta})^{\alpha} exp[-\beta(\kappa\underline{\eta})], \tag{2.74}$$

where $\alpha, \beta$ and $C_{DR}$ are constants independent of $\kappa$ [63, 72, 73].

The model spectrum of Pope [38] for the 3D energy spectrum is another example which reads:

$$E_{Normal}(\kappa\underline{\eta}) = C_K \left(\kappa\underline{\eta}\right)^{-5/3} exp[-\beta_P \left(\left(\kappa\underline{\eta}\right)^4 + c_\eta^4\right)^{1/4} - c_\eta] f_L(\kappa L), \tag{2.75}$$

where the the integral range multiplier for Pope's model spectrum function ($f_L$) is added to cover the low wavenumber ranges and it reads:

$$f_L(\kappa L) \equiv \left(\frac{\kappa L}{\left((\kappa L)^2 + c_L\right)^{1/2}}\right)^{5/3+P_0}, \tag{2.76}$$

with experimentally obtained constants of $\beta_P$ equals to 5.2, $c_\eta$= 0.4, $P_0$= 2, $c_L$= 6.78, and $L$ the integral length scale. It is easy to see that if $c_\eta = 0$ the function is very similar to Eq. 2.74 but with different powers and constants. It is discussed in [38] that the simple exponential form of Eq. 2.74 departs from unity too rapidly for small $\kappa\underline{\eta}$.

It is interesting to see that Eq. 2.75 is a unique function of $Re_\lambda$, since from isotropic relations:

$$(\kappa L)/(\kappa\underline{\eta}) = Re_L^{3/4} = (3/20)^{3/4} Re_\lambda^{3/2}, \tag{2.77}$$

so that:

$$\kappa L = (\kappa\underline{\eta})(3/20)^{3/4} Re_\lambda^{3/2}. \tag{2.78}$$

By replacing Eq. 2.78 in Eq. 2.76, Pope's model spectrum Eq. 2.75 will be a unique function of $Re_\lambda$.

[27] It can be extended to variable density flows by using the compressible form of the normalized spectrum and the Favre averaged Kolmogorov's length scale, $\underline{\eta}_f$.

[28] The review can be found in [68] and [39].

The 3D turbulent kinetic energy dissipation spectrum ($D(\kappa)$) has an exact expression like [38, 75]:

$$D(\kappa) \equiv 2\nu\kappa^2 E(\kappa), \tag{2.79}$$

and like Eq. 2.67, the TKE dissipation rate ,$\underline{\varepsilon}$, can be evaluated as:

$$\int_0^\infty D(\kappa, t)d\kappa = \underline{\varepsilon}. \tag{2.80}$$

$D(\kappa)$ can be computed from DNS data by computing the 3D $E(\kappa)$. Like the model proposed for the 3D energy spectrum, a model for the normalized 3D turbulent kinetic energy dissipation spectrum ($D_{Normal}$) can be obtained from Eq. 2.79 and Eq. 2.75:

$$\begin{aligned} &D_{Normal}(\kappa\underline{\eta}) = \\ &2C_K \left(\kappa\underline{\eta}\right)^{1/3} exp[-\beta_P \left(\left(\kappa\underline{\eta}\right)^4 + c_\eta^4\right)^{1/4} - c_\eta] f_L(\kappa L), \end{aligned} \tag{2.81}$$

which is again a unique function of $Re_\lambda$. In Eq. 2.81 $D_{Normal}(\kappa\underline{\eta})$ is by definition[29]:

$$D_{Normal}(\kappa\underline{\eta}) \equiv \frac{D(\kappa)}{\underline{u_\eta}^3} = \frac{D(\kappa)}{\underline{\eta\varepsilon}}. \tag{2.82}$$

The universal form of Eq. 2.71 is of great importance. Many efforts have been done so far to experimentally or numerically prove the universality of Eq. 2.71 [39, 40, 52, 68] with success. In another word we can say that we are searching for the collapse of all velocity spectra if scaled properly. For incompressible flows, it was found that the Kolmogorov idea to scale the spectra as proposed in the sets of Eq. 2.71 is acceptable. Of course, we are not just talking about the form Eq. 2.71, because it is the re-expression of Eq. 2.44 in the wavenumber space. So the research is on finding an evidence for Kolmogorov's assumptions and laws, either in the physical space form of laws or in their wavenumber forms of Obukhov. Further, the universal form have been used explicitly or implicitly in the evaluation of constants in turbulence models (e.g., the Smagorinsky model constant obtained by Lilly [76]). In Sec. 5.3 we will review the findings on the spectra of reactive flows and will analyze both the TKE and its dissipation spectra using the DNS databases of reactive flows with the focus on the effect of extinction on the spectra. The existence of the universal scaling of the form Eq. 2.71 or its 1D counterpart will be also analyzed. This is of great importance in both turbulence modeling and finite-rate turbulence-chemistry interactions models which will be discussed in the next sections.

**Some practical notes**: In the practical applications, the wavenumber vector components, $\kappa_x$, $\kappa_y$, $\kappa_z$, are defined as:

$$\kappa_x \equiv \frac{2\pi}{L_x}(1...\frac{N_x}{2}), \tag{2.83a}$$

$$\kappa_y \equiv \frac{2\pi}{L_y}(1...\frac{N_y}{2}), \tag{2.83b}$$

$$\kappa_z \equiv \frac{2\pi}{L_z}(1...\frac{N_z}{2}), \tag{2.83c}$$

[29] Again the compressible form can be defined using the Favre averaged quantities for normalization.

where $L_x$, $L_y$, $L_z$ and $N_x$, $N_y$, $N_z$ are the length of the computational domain and the number of computational cells in $Ox$, $Oy$, $Oz$ directions, respectively. The $\frac{N_x}{2}$ is used to limit the maximum wavenumber in space by the Nyquist limit which is $\kappa_{i,max} = \frac{\pi}{\Delta_i}$ with $\Delta_i$ the grid spacing in $i^{th}$ direction. In practical applications, we use the 1D Discrete Fourier Transform (DFT) to construct the 1D spectrum. The DFT of a vector $\boldsymbol{V} \in \mathbb{R}^N$ reads:

$$DFT_{\boldsymbol{V}}(n) = \sum_{j=1}^{N} \boldsymbol{V}(j) e^{\frac{-2\pi i(j-1)(n-1)}{N}} \qquad n \in \mathbb{Z} : 1 \leq n \leq N, \tag{2.84}$$

where $N$ is the size of vector $\boldsymbol{V}$ (we can consider $\boldsymbol{V}$ the $Ox$ component of velocity fluctuations in each cell in direction $Ox$ so that $N = N_x$, the number of cells in $Ox$ direction). The first output corresponds to the zeroth frequency component. The components in the interval of $2 \leq n \leq N/2$ corresponds to the wavenumbers range of $0 < \kappa_i < \kappa_{i,max}$ and the components in the interval of $N/2 + 2 \leq n \leq N$ corresponds to the wavenumbers range of $-\kappa_{max} < \kappa < 0$. The $n = N/2 + 1$ corresponds to both $-\kappa_{i,max}$ and $\kappa_{i,max}$. The DFT output is symmetric so usually we just consider half of it, further we don't usually consider the zeroth frequency component, i.e., the components in the interval of $2 \leq n \leq N/2 + 1$ are only considered. Note that in this way the last component shows the maximum wavenumber which is calculated from Eq. 2.83.

In a discrete representation of the flow field, such as in the DNS databases which is used in the thesis, $E(\kappa)$ can be constructed as the average (in wavenumber space over spherical shells) of the product of all the Fourier coefficients of $u_i''$ with a wavenumber magnitude of $\kappa$[30]. However, this required the 3D Fourier transform. The 3D Fourier transform requires 3 homogeneous direction in the physical space. This is usually the case in the DNS of HIT configurations which is not always the case in experiments or the DNS of jets. In particular, in the temporally evolving jet flame configuration studied in this thesis, considering two homogeneous directions in $Ox$ and $Oz$, one has two options. First, to construct a 2D spectrum from the 2D Fourier transform and then averaging in the different rings of equal wavenumbers ($\kappa_{2D} = \sqrt{\kappa_x^2 + \kappa_z^2}$). Second, to construct a 1D spectrum using the 1D Fourier transforms in one direction (e.g. $\kappa_x$) and averaging using all ensembles of equal $\kappa_x$ on another direction. The result is the 1D spectrum as a function of the scalar $\kappa_x$. In this thesis the latter is adopted. Since the lengths of the domain in two existing homogeneous directions are not the same, this causes a problem in the 2D Fourier transforms. Further, the theory is developed either for the 3D or the 1D spectra and the theoretical formulation exists to relate these two.

Consider the velocity vector $\mathbf{U}(\mathbf{x}, t) = (u_1, u_2, u_3) = u_i \; i = 1, 2, 3$, first we transform any component to the centered one using the Favre averaging operator i.e. Eq. 2.36. Then the 1D velocity spectrum in $i^th$ direction as a function of the longitudinal wavenumber($E_{ii}^{1D}(\kappa_x)$) is evaluated as:

$$E_{ii}^{1D}(\kappa_x) = \langle DFT_{u_i''} DFT_{u_i''}^* \rangle \tag{2.85}$$

[30] As mentioned earlier to remove the directional information from Eq. 2.65

where $DFT^*$ is the complex conjugate of $DFT$. The $\langle . \rangle$ operator here is the averaging operator in the second homogeneous direction i.e.

$$E_{ii}^{1D}(\kappa_x) = \sum_{z=1}^{N_z} DFT(u_i'')DFT^*(u_i''), \tag{2.86}$$

where the DFT is calculated using all $u_i''$ values in one homogeneous direction (i.e., $Ox$) and averaging over the second direction (i.e. $Oz$ with $N_z$ the number of cells in $Oz$ direction).

## 2.3 The Modelling: Navier-Stokes Equations

In this section, first, the reactive NS equations are introduced and the terms including the reactive source terms are described. Then the two approaches of manipulating turbulent flows namely the Reynolds averaging and filtering approaches are introduced. In each subsection, the related kinetic energy equation is introduced. This is done since we will extract the exact terms from the DNS databases in Chapter 5 and use in the *a priori* DNS analysis, instead of modeling them.

In the absence of external body forces and heat sources, the reactive NS equations reads:

$$\frac{\partial \rho}{\partial t} + \frac{\partial}{\partial x_i}\left(\rho u_i\right) = 0, \tag{2.87a}$$

$$\frac{\partial}{\partial t}\left(\rho u_i\right) + \frac{\partial}{\partial x_j}\left(\rho u_i u_j\right) = -\frac{\partial p}{\partial x_i} + \frac{\partial}{\partial x_j}\left(\tau_{ij}\right), \tag{2.87b}$$

$$\frac{\partial}{\partial t}\left(\rho Y_k\right) + \frac{\partial}{\partial x_i}\left(\rho u_i Y_k\right) = -\frac{\partial}{\partial x_i}\left(\rho V_{i,k} Y_k\right) + \dot{\omega}_k \quad k = 1, ...N_s, \tag{2.87c}$$

$$\frac{\partial}{\partial t}\left(\rho E\right) + \frac{\partial}{\partial x_i}\left(\rho u_i E\right) = -\frac{\partial}{\partial x_i}\left(p u_i\right) + \frac{\partial}{\partial x_i}\left(\tau_{ij} u_j\right) - \frac{\partial}{\partial x_i}\left(q_i\right) + \dot{Q}, \tag{2.87d}$$

where $\rho$ is the density of the fluid, $u_i$ are the velocity components, $p$ the static pressure, $E$ the total energy (including kinetic, chemical and internal energy), $N_s$ the number of species in the kinetic mechanism. $Y_k$ and $\dot{\omega}_k$ are the mass fraction and the net formation rate of species $k$, respectively. $\tau_{ij}$ is the viscous stress tensor which is defined as:

$$\tau_{ij} \equiv 2\mu\left(S_{ij} - \Delta_v \delta_{ij}/3\right), \tag{2.88}$$

where $\mu$ is the molecular viscosity of the mixture and $S_{ij}$ is the strain-rate tensor[31]:

$$S_{ij} \equiv \frac{1}{2}\left(\frac{\partial u_i}{\partial x_j} + \frac{\partial u_j}{\partial x_i}\right). \tag{2.89}$$

In Eq. 2.88, $\Delta_v$ is $\Delta_v = S_{ii}$; the flow dilatation and $\delta_{ij}$ the Kronecker delta ($\delta_{ij}$ = 1 if $i = j$ and $\delta_{ij}$=0 otherwise)). In the energy equation of Eqs. 2.87, $q_i$ is the heat flux which is defined as:

$$q_i \equiv -\lambda\frac{\partial T}{\partial x_i} + \sum_{k=1}^{N_s} \rho h_k Y_k V_{i,k}, \tag{2.90}$$

[31] The symmetric part of the velocity gradient tensor, $\frac{\partial u_i}{\partial x_j}$

with $\lambda$ the thermal conductivity and $h_k$ the sensible enthalpy of species $k$. In the species equation of Eqs. 2.87, $V_{i,k}$ are the diffusion velocities of species $k$ in direction $i$. It is evaluated by Fick's law:

$$V_{i,k} \equiv -\Gamma_{k,mix} \frac{\partial Y_k}{\partial x_i} / Y_k, \tag{2.91}$$

where $\Gamma_{k,mix}$ is the mass diffusion coefficient of species $k$ into the mixture. Consider a chemical kinetics mechanism with $N_s$ species and $N_r$ reactions. In the short format it is written like:

$$\sum_{k=1}^{N_s} \nu'_{k,j} \Phi_k \rightleftharpoons \sum_{k=1}^{N_s} \nu''_{k,j} \Phi_k \quad j = 1, ..., N_r, \tag{2.92}$$

where $\nu'_{k,j}$ and $\nu''_{k,j}$ are the molar stoichiometric coefficients of species $k$ in forward and backward reactions, receptively and $\Phi_k$ the species $k$ symbol. The stoichiometric coefficients should satisfy Eq. 2.93 relations to enforce the mass conservation:

$$\sum_{k=1}^{N_s} \nu_{k,j} W_k = 0 \quad j = 1, ..., N_r, \tag{2.93}$$

with $W_k$ the molecular weight of species $k$ and:

$$\nu_{k,j} = \nu''_{k,j} - \nu'_{k,j} \quad j = 1, ..., N_r. \tag{2.94}$$

The law of mass action states that the reaction rate is proportional to the product of concentration of reactants. For reversible reactions like what is introduced in Eq. 2.92, the net reaction rate of reactions $j$ ($\dot{r}_j$) can be computed as:

$$\dot{r}_j \equiv k_{f,j} \prod_{k=1}^{N_s} \left( \frac{\rho Y_k}{W_k} \right)^{\nu'_{k,j}} - k_{b,j} \prod_{k=1}^{N_s} \left( \frac{\rho Y_k}{W_k} \right)^{\nu''_{k,j}}, \tag{2.95}$$

where $k_{f,j}$ and $k_{r,j}$ are forward and backward rates of reactions $j$, respectively. These rates depend on the temperature and are computed from the Arrhenius law and using equilibrium constants:

$$k_{f,j} \equiv A_{f,j} T^{\beta_j} \exp\left( -\frac{E_{f,j}}{RT} \right), \tag{2.96a}$$

$$k_{b,j} \equiv \frac{k_{r,j}}{\left( \frac{p_a}{RT} \right)^{\sum_{k=1}^{N_s} \nu_{k,j}} \exp\left( \frac{\Delta \hat{S}^0_j}{R} - \frac{\Delta \hat{H}^0_j}{RT} \right)}, \tag{2.96b}$$

where $E_{f,j}$ is the forward activation energies of reactions $j$, $p_a = 1$ bar and $\Delta \hat{S}^0_j$ and $\Delta \hat{H}^0_j$ refer to the enthalpy and the entropy changes occurring when passing from reactants to products.

Finally, the net rate of the production of species, $\dot{\omega}_k$, is computed from:

$$\dot{\omega}_k \equiv \sum_{j=1}^{N_r} (\nu_{k,j} \dot{r}_j) \quad j = 1, ..., N_s \tag{2.97}$$

In Eq. 2.87, $\dot{Q}$ is the heat release rate due to combustion:

$$\dot{Q} \equiv -\sum_{k=1}^{N_s} \Delta H^0_{f,k} \dot{\omega}_k, \tag{2.98}$$

where $\Delta H^0_{f,k}$ is the enthalpy of the formation of species $k$. The set of equations 2.87 together with the equation of state ($p = \rho RT$), with universal gas constant (R), create a closed system of partial differential equations for Newtonian fluids.

The set of Eqs. 2.87 can be solved directly in DNS, however the mesh and time steps needs to resolve both the Kolmogorov scales for the fluid and the flame thickness/velocity scale for chemistry which makes the computational cost prohibitive. In many applications we are interested in the mean values of the variables, and therefore the conservation equations for the mass of species, momentum and energy can be averaged in time/space. When this averaging is performed, the equations describing the mean flow-field contain the averages of product of fluctuating velocities. In general this will result in more unknowns than the number of equations available. Such difficulty can be resolved by the turbulence models with additional equations being provided to match the number of unknowns.

The averaging process can be either time averaging or spatial (volume) averaging. If the governing equations are time averaged and then solved, this is called RANS. In theory, the averaging must be performed by the statistical mean operator Eq. 2.4 however, in practical applications we use Eq. 2.10 and we already showed that under certain conditions they are approximately the same. In theory, it is possible for the averaging time interval in Eq. 2.10 not be much larger than the integral time scale. If this is the case, the result of the simulation is called URANS. Actually we are calculating directly only certain low frequency modes in time. The URANS equations are the usual RANS equations, but with the transient (unsteady) term retained. Even if the results from URANS are unsteady, one is often interested only in the time-averaged flow. If the averaging process is performed in small volumes (the spatial averaging) and we calculate only the low-frequency modes in space, the solution is called LES.

In the spectral point of view (see Fig. 2.2), if all range of the wavenumbers (in space or frequencies in time) in the spectrum (e.g., the TKE spectrum introduced before) are resolved, this is called DNS. If the spectrum is cut in a specific wavenumber, this means that the simulation is just resolving the wavenumbers lower than the cutoff wavenumber; all the remaining must be modeled. In LES usually the cutoff wavenumber is placed in the inertial range. In RANS only mean variables are resolved, this means that no wavenumber (or frequency) is resolved by the simulation and all the spectrum must be modeled.

### 2.3.1 Favre Averged Navier-Stokes

If a Favre averaging operator (the time average not the spatial average) introduced in Sec. 2.2 is applied on the set of Eqs. 2.87 while keeping the time dependency of the

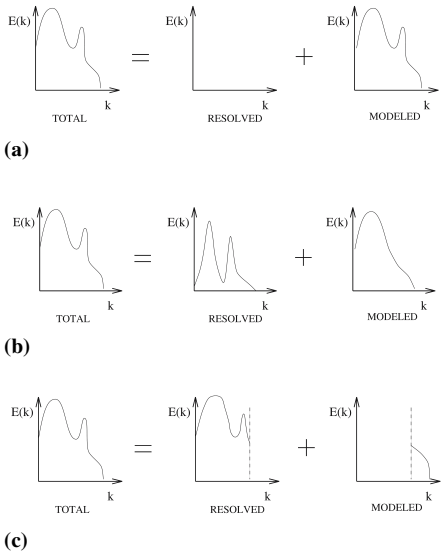


**Figure 2.2:** *From [77]; Decomposition of the energy spectrum by different solution methods. (**a**) RANS; (**b**) URANS; (**c**) LES.*

dependent variables, the results is the set of Favre averaged NS equations in URANS:

$$\frac{\partial \overline{\rho}}{\partial t} + \frac{\partial}{\partial x_i}\left(\underline{\rho u_i}_f\right) = 0, \tag{2.99a}$$

$$\begin{aligned}\frac{\partial}{\partial t}\left(\underline{\rho u_i}_f\right) + \frac{\partial}{\partial x_j}\left(\underline{\rho u_i}_f \underline{u_j}_f\right) &= -\frac{\partial \underline{p}}{\partial x_i} + \frac{\partial}{\partial x_j}\left(\underline{\tau_{ij}}\right) \\ &- \frac{\partial}{\partial x_j}\left(\underline{\rho u_i'' u_j''}_f\right),\end{aligned} \tag{2.99b}$$

$$\begin{aligned}\frac{\partial}{\partial t}\left(\underline{\rho Y_k}_f\right) + \frac{\partial}{\partial x_i}\left(\underline{\rho u_i}_f \underline{Y_k}_f\right) &= -\frac{\partial}{\partial x_i}\left(\underline{\rho \Gamma_{k,mix} \frac{\partial Y_k}{\partial x_i}}\right) + \underline{\dot{\omega}_k} \\ &- \frac{\partial}{\partial x_i}\left(\underline{\rho}\ \underline{u_i'' Y_k''}_f\right) \quad k = 1, ...N_s,\end{aligned} \tag{2.99c}$$

$$\begin{aligned}\frac{\partial}{\partial t}\left(\underline{\rho E}_f\right) + \frac{\partial}{\partial x_i}\left(\underline{\rho u_i}_f \underline{E}_f\right) &= -\frac{\partial}{\partial x_i}\left(\underline{p u_i}\right) + \frac{\partial}{\partial x_i}\left(\underline{\tau_{ij} u_j}\right) \\ &- \frac{\partial}{\partial x_i}\left(\underline{q_i}\right) + \underline{\dot{Q}} - \frac{\partial}{\partial x_i}\left(\underline{\rho}\ \underline{u_i'' E''}_f\right),\end{aligned} \tag{2.99d}$$

which introduces many unclosed terms. In CFD applications, the flux terms are modeled as:

$$\underline{\rho}\ \underline{u_i'' Y_k''}_f \approx \frac{\underline{\rho}\,\nu_t}{Sc_{kt}} \frac{\partial}{\partial x_i}\left(\underline{Y_k}_f\right), \tag{2.100a}$$

$$\underline{\rho}\ \underline{u_i'' E''}_f \approx \frac{\underline{\rho}\,\nu_t}{Pr_t} \frac{\partial}{\partial x_i}\left(\underline{E}_f\right), \tag{2.100b}$$

$$\underline{\rho\Gamma_{k,mix}\frac{\partial Y_k}{\partial x_i}} \approx \underline{\rho}\,\underline{\Gamma_{k,mix}} \frac{\partial}{\partial x_i}\left(\underline{Y_k}_f\right), \tag{2.100c}$$

$$\underline{q_i} = \underline{\lambda\frac{\partial T}{\partial x_i}} \approx \underline{\lambda} \frac{\partial}{\partial x_i}\left(\underline{T}_f\right), \tag{2.100d}$$

$$\frac{\partial}{\partial x_i}\left(\underline{\tau_{ij} u_j}\right) \approx 0, \tag{2.100e}$$

$$\underline{p u_i} = \underline{p}\ \underline{u_i}_f + \frac{1}{C_p/C_v Ma^2}\underline{\rho u_i'' T''}_f \approx \underline{p}\ \underline{u_i}_f, \tag{2.100f}$$

where turbulent viscosity ($\nu_t$) is introduced and will be defined in the following. Since Mach number (Ma) is low the approximation in Eq. 2.100f can be used. The turbulent Schmidt number ($Sc_{kt}$) and tutbulent Prandtl number ( $Sc_{kt}$) are kept constant.

The unclosed reaction source and its heat release (i.e., $\underline{\dot{\omega}_k}$ and $\underline{\dot{Q}}$) which introduces the turbulence-chemistry interactions issue will be discussed in the next Chapter.

The most important unclosed term regarding the turbulence is the Reynolds stress tensor $\underline{\rho u_i'' u_j''}_f$. The Boussinesq assumption leads to relate turbulent stresses to the mean flow strain rate:

$$-\underline{\rho u_i'' u_j''}_f \sim \underline{\rho S_{ij}}_f = 2\underline{\rho}\nu_t \underline{S_{ij}}_f. \tag{2.101}$$

For Eq. 2.101 being valid upon the contraction, we reformulate it so that:

$$\underline{\rho u_i'' u_j''}_f \sim -\underline{\rho S_{ij}}_f = -2\underline{\rho}\nu_t\left(\underline{S_{ij}}_f - 1/3\delta_{ij}\underline{S_{kk}}_f\right) + \frac{2}{3}\delta_{ij}\underline{\rho k}_f, \tag{2.102}$$

where $\underline{k}_f$ already introduced in Eq. 2.52.

Now the closure problem is to evaluate $\nu_t$. These types of models called the eddy viscosity type models. The wide range of approaches exist, for example the zero-equation models like Prandtl's mixing length model [50, 66], two equation models like $k-\varepsilon$ models [78], three equation models like $k-\varepsilon-\gamma$ [79], and 6 equation models or the so called Reynolds Stress equation Model (RSM) [80]. The two equation model, $k-\varepsilon$ models [78], are the most famous ones which relate the $\nu_t$ to TKE and its dissipation. The dimension of $\nu_t$ is $[m^2/s]$, a turbulent velocity scale multiplied with a turbulent length scale has the same dimension:

$$\nu_t \propto \mathcal{U}\ell, \tag{2.103}$$

with $\mathcal{U}$ as a velocity scale:

$$\mathcal{U} = \underline{k}_f^{1/2}, \tag{2.104}$$

and $\ell$ as a length scale:

$$\ell = \frac{\underline{k}_f^{3/2}}{\underline{\varepsilon}_f}. \tag{2.105}$$

one can get the $\nu_t$ as:

$$\nu_t \propto \mathcal{U}\ell \propto \underline{k}_f^{1/2}\frac{\underline{k}_f^{3/2}}{\underline{\varepsilon}_f} = C_\mu \frac{\underline{k}_f^2}{\underline{\varepsilon}_f}, \tag{2.106}$$

with $C_\mu$ a constant of proportionality. The details of the $k-\varepsilon$ model can be found in [78].

#### Exact Favre Mean Turbulent Kinetic Energy (TKE) Budgets

The Favre averaged turbulent kinetic energy (TKE), $\underline{k}_f$, was introduced before in Eq. 2.52. The exact transport equation for the TKE can be directly derived. We start from the exact transport equation for the Reynolds stress tensor in the compressible[32] form [82]:

$$\frac{\partial}{\partial t}\left(\underline{\rho u_i'' u_j''}\right) + \frac{\partial}{\partial x_k}\left(\underline{u_k}_f \underline{\rho u_i'' u_j''}\right) = \underline{\rho}\left(P_{ij} - \varepsilon_{ij}\right) + T_{ij} + \Pi_{ij} + \Sigma_{ij}, \tag{2.107}$$

where the terms are mean production of Reynolds stresses ($P_{ij}$):

$$P_{ij} = -\underline{\rho u_j'' u_k''}_f \frac{\partial}{\partial x_k}\left(\underline{u_i}_f\right) - \underline{\rho u_i'' u_k''}_f \frac{\partial}{\partial x_k}\left(\underline{u_j}_f\right), \tag{2.108}$$

the mean dissipation of Reynolds stresses ($\varepsilon_{ij}$):

$$\varepsilon_{ij} = \frac{1}{\underline{\rho}}\left(\underline{\tau_{ki}'\frac{\partial}{\partial x_k}\left(u_j''\right)} + \underline{\tau_{kj}'\frac{\partial}{\partial x_k}\left(u_i''\right)}\right), \tag{2.109}$$

the mean turbulent kinetic energy transport ($T_{ij}$):

$$T_{ij} = \frac{\partial}{\partial x_k}\left(\underline{\rho u_i'' u_j'' u_k''} + \underline{u_j'' \sigma_{ki}'} + \underline{u_i'' \sigma_{kj}'}\right), \tag{2.110}$$

mean pressure-strain ($\Pi_{ij}$):

$$\Pi_{ij} = \underline{p'\left(\frac{\partial}{\partial x_j}\left(u_i''\right) + \frac{\partial}{\partial x_i}\left(u_j''\right)\right)}, \tag{2.111}$$

mass flux coupling[33]

$$\Sigma_{ij} = \underline{u_j''}\frac{\partial}{\partial x_k}\left(\underline{\sigma}_{ki}\right) + \underline{u_i''}\frac{\partial}{\partial x_k}\left(\underline{\sigma}_{kj}\right). \tag{2.112}$$

In Eq. 2.109, $\tau_{ki}'$ is $\tau_{ki} - \underline{\tau_{ki}}$.

The exact transport equation of the TKE is derived by contraction of free indexes and dividing by two in Eq. 2.107:

$$\frac{\partial}{\partial t}\left(\underline{\rho}\underline{k}_f\right) + \frac{\partial}{\partial x_j}\left(\underline{\rho}\,\underline{u_j}_f \underline{k}_f\right) = \underline{\rho}\left(P - \underline{\varepsilon}_f\right) + T + \Pi + \Sigma, \tag{2.113}$$

[32] The incompressible form can be found in [81]

[33] It should be noted that in Eq. 2.107 the term $\underline{u_i''}$ is not zero since this is the Reynolds average of the Favre fluctuation. The relation between two averages of a quantity, $q$ is: $\underline{q''} = \underline{q} - \underline{q}_f$

with mean production of turbulent kinetic energy ($P$):

$$P = -\underline{u_i'' u_j''}_f \frac{\partial}{\partial x_j}\left(\underline{u_i}_f\right), \tag{2.114}$$

and mean dissipation of turbulent kinetic energy ($\varepsilon$) or better to say $\underline{\varepsilon}_f$:

$$\underline{\varepsilon}_f = \underline{\frac{1}{\rho}\tau_{ij}' \frac{\partial}{\partial x_j}(u_i'')}, \tag{2.115}$$

Diffusion:

$$T = \frac{\partial}{\partial x_k}\left(1/2\underline{\rho u_i'' u_i'' u_j''} + \underline{u_i'' \sigma_{ij}'}\right), \tag{2.116}$$

mass flux coupling

$$\Sigma = \underline{u_i''} \frac{\partial}{\partial x_j}\left(\underline{\sigma_{ij}}\right), \tag{2.117}$$

pressure-strain:

$$\Pi = \underline{p' \frac{\partial}{\partial x_j}\left(u_j''\right)}. \tag{2.118}$$

The exact terms in Eq. 2.118 are directly calculated from the DNS databases to be used in the *a priori* DNS analysis. Of great importance is the mean production and mean dissipation terms.

### 2.3.2 Favre Filtered Navier-Stokes

In LES, the large energy-containing turbulent structures are directly represented, these are called the resolved structures. The effects of smaller eddies, i.e., the residual fields, are modeled [83]. In LES, a low-pass filtering operation, using a filter kernel, is applied to the governing equations to derive the equations for large structures. A filtered quantity $\overline{q}$ is computed as:

$$\overline{q} = \iiint q\left(\boldsymbol{X'}\right) F\left(\boldsymbol{X} - \boldsymbol{X'}\right) d^3\boldsymbol{X'}. \tag{2.119}$$

Equivalently a Favre filtered quantity is given by:

$$\overline{q}^f = \frac{1}{\overline{\rho}}\left(\iiint \rho q\left(\boldsymbol{X'}\right) F\left(\boldsymbol{X} - \boldsymbol{X'}\right) d^3\boldsymbol{X'}\right), \tag{2.120}$$

where $F\left(\boldsymbol{X}\right)$ represents the 3D filter kernel. Theoretically, it can be a simple top-hat, Gaussian or the sharp spectral filter [38, 77]. In Sec. 4.3, the explicit top-hat filter used in the current study is introduced. However, in LES, it is implicitly introduced by the grid. Although mathematically the filter type in LES is not known but we can assume that it is most likely to be a top-hat filter corresponding to the mesh size. As pointed out by daSilva [84]: a box filter corresponds to the filter implicitly associated with the discretization in a centered second-order finite difference or finite volume code, which is often used in LES. Filtering a quantity $q$ using any filter kernel, one can divide the fluctuating quantity $q$ as, $q = \overline{q} + q_{residual} = \overline{q} + q_{SGS}$, where $q_{residual}$ or $q_{SGS}$ is the residual field after applying the filtering operator on the original field. $q_{SGS}$ is different

from $q'$, the residual field after application of Reynolds operator, with the properties of, $\overline{q}_{residual} \neq 0$ and $\overline{\overline{q}} \neq \overline{q}$. Applying Eq. 2.120 to Eq. 2.87 results in the following set of Favre filtered Navier-Stokes equations:

$$\frac{\partial \overline{\rho}}{\partial t} + \frac{\partial}{\partial x_i}\left(\overline{\rho}\,\overline{u_i}^f\right) = 0, \tag{2.121a}$$

$$\begin{aligned}\frac{\partial}{\partial t}\left(\overline{\rho u_i}^f\right) + \frac{\partial}{\partial x_j}\left(\overline{\rho u_i}^f \overline{u_j}^f\right) &= -\frac{\partial}{\partial x_j}\left(\overline{p}\right) \\ &+ \frac{\partial}{\partial x_j}\left(\overline{\tau_{ij}}\right) - \frac{\partial}{\partial x_j}\left(\overline{\tau_{ij}}^R\right),\end{aligned} \tag{2.121b}$$

$$\begin{aligned}\frac{\partial}{\partial t}\left(\overline{\rho}\overline{Y_k}^f\right) + \frac{\partial}{\partial x_i}\left(\overline{\rho u_i}^f \overline{Y_k}^f\right) &= \frac{\partial}{\partial x_i}\left(\overline{\rho \Gamma_{k,mix} \frac{\partial Y_k}{\partial x_i}}\right) \\ &+ \overline{\dot{\omega}}_k - \frac{\partial}{\partial x_i}\left(\overline{\rho}\overline{J_i}^R\right) \quad k = 1, ...N_s,\end{aligned} \tag{2.121c}$$

$$\begin{aligned}\frac{\partial}{\partial t}\left(\overline{\rho}\overline{E}^f\right) + \frac{\partial}{\partial x_i}\left(\overline{\rho u_i}^f \overline{E}^f\right) &= -\overline{p\frac{\partial u_i}{\partial x_i}} + \frac{\partial}{\partial x_i}\left(\overline{\tau_{ij} u_j}\right) + \overline{\dot{Q}} \\ &+ \frac{\partial}{\partial x_i}\left(\overline{\lambda \frac{\partial T}{\partial x_i}}\right) - \frac{\partial}{\partial x_i}\left(\overline{\rho \pi_i}^R\right),\end{aligned} \tag{2.121d}$$

which introduces many unclosed terms. In CFD applications, the flux terms are modeled as:

$$\overline{\tau_{ij}} \approx 2\overline{\mu}\left(\overline{S_{ij}}^f - \overline{\Delta_v}^f \delta_{ij}/3\right), \tag{2.122a}$$

$$\overline{\rho \Gamma_{k,mix} \frac{\partial Y_k}{\partial x_i}} \approx \overline{\rho}\,\overline{\Gamma_{k,mix}}^f \frac{\partial \overline{Y_k}^f}{\partial x_i}, \tag{2.122b}$$

$$\overline{J_i}^R = \overline{u_i Y_k}^f - \overline{u_i}^f \overline{Y_k}^f \approx \frac{\overline{\rho}\,\nu_{SGS}}{Sc_{kt}} \frac{\partial \overline{Y_k}^f}{\partial x_i}, \tag{2.122c}$$

$$\overline{\pi_i}^R = \overline{u_i E}^f - \overline{u_i}^f \overline{E}^f \approx \frac{\overline{\rho}\,\nu_{SGS}}{Pr_t} \frac{\partial \overline{E}^f}{\partial x_i}, \tag{2.122d}$$

$$\overline{q_i} = \overline{\lambda \frac{\partial T}{\partial x_i}} \approx \overline{\lambda} \frac{\partial \overline{T}^f}{\partial x_i}, \tag{2.122e}$$

$$\overline{p\frac{\partial u_i}{\partial x_i}} \approx \overline{p} \frac{\partial \overline{u_i}^f}{\partial x_i}, \tag{2.122f}$$

$$\frac{\partial}{\partial x_i}\left(\overline{\tau_{ij} u_j}\right) \approx 0. \tag{2.122g}$$

$$\tag{2.122h}$$

Apart from the filtered reaction rate and heat release rate source terms (i.e., $\overline{\dot{\omega}}_k$ and $\overline{\dot{Q}}$) which will be discussed in the next Chapter, the Residual Stress Tensor ($\tau_{ij}^R$) as an unclosed term is introduced:

$$\tau_{ij}^R = \overline{\rho}\left(\overline{u_i u_j}^f - \overline{u_i}^f \overline{u_j}^f\right). \tag{2.123}$$

Like the closure for the Reynolds stresses in Eq. 2.101, the Boussinesq type hypothesis leads to relating the deviatoric part of the $\tau_{ij}^R$ to the resolved strain rate:

$$\begin{aligned}\tau_{ij}^R &= \overline{\rho}\left(\overline{u_i u_j}^f - \overline{u_i}^f \overline{u_j}^f\right) \sim -\overline{\rho}\overline{S_{ij}}^f \\ &= -2\overline{\rho}\nu_{SGS}\left(\overline{S_{ij}}^f - 1/3\delta_{ij}\overline{S_{kk}}^f\right) + \frac{2}{3}\delta_{ij}\overline{\rho}k_{SGS},\end{aligned} \tag{2.124}$$

where the subgrid viscosity ($\nu_{SGS}$) is introduced. Further, sub-grid kinetic energy ($k_{SGS}$) is:

$$\overline{\rho}k_{SGS} = \frac{1}{2}\tau_{kk}^R = \frac{1}{2}\overline{\rho}\left(\overline{u_i u_i}^f - \overline{u_i}^f \overline{u_i}^f\right). \tag{2.125}$$

Now the closure problem is to evaluate $\nu_{SGS}$. These types of models called the sub grid viscosity models. The wide range of approaches exist [77], e.g., the most famous one, i.e., the Smagorinsky model [85] or the one equation $k$ model [86]. and the dynamic approaches of the mentioned models, using the Germano identity [87] to evaluate the models coefficients[34].

#### Exact Resolved Kinetic Energy Equation

The exact transport equation for large scale (resolved) kinetic energy ($k_r$), $k_r = \left(\overline{u_i}^f \overline{u_i}^f\right)/2$, can be derived by multiplying Eq. 2.121b by $\overline{u_i}^f$ and using Eq. 2.121a. The equation reads:

$$\frac{\partial}{\partial t}\left(\overline{\rho}k_r\right) + \frac{\partial}{\partial x_i}\left(\overline{\rho}\,\overline{u_i}^f k_r\right) = \alpha + \Pi - \overline{\rho}\varepsilon_\nu - \overline{\rho}P_{SGS}, \tag{2.126}$$

where the exact terms are,the redistribution ($\alpha$):

$$\alpha = \frac{\partial}{\partial x_i}\left(-\overline{p}\,\overline{u_i}^f + \overline{\tau_{ij}u_j}^f - \tau_{ij}^R\overline{u_j}^f\right), \tag{2.127}$$

and the pressure dilatation ($\Pi$):

$$\Pi = \overline{p}\overline{\Delta_v}^f, \tag{2.128}$$

where $\Delta_v$ is introduced in Eq. 2.88. The next terms are the viscous dissipation ($\varepsilon_\nu$):

$$\varepsilon_\nu = \frac{1}{\overline{\rho}}\overline{\tau_{ij}}\overline{S_{ij}}^f, \tag{2.129}$$

and the Grid-scale to sub-grid scale energy transfer ($P_{SGS}$) or the production of sub-grid kinetic energy:

$$P_{SGS} = -\frac{1}{\overline{\rho}}\tau_{ij}^R\overline{S_{ij}}^f. \tag{2.130}$$

The above terms are exact and can be extracted directly from the DNS databases. In particular the grid-scale-subgrid-scale transfer rate is of great importance. It represents the energy transferred through the cutoff wavenumber to smaller scales. In Chapter 5 we use the exact value obtained by Eq. 2.130 in the sub-grid EDC cascade model.

[34] Will be explained in the next Chapter.

#### Exact Sub-Grid Kinetic Energy Equation

The exact transport equation for $k_{SGS}$, $k_{SGS} \equiv \left(\overline{u_i u_i}^f - \overline{u_i}^f \overline{u_i}^f\right)/2$, can be obtained by subtracting Eq. 2.126 from the filtered kinetic energy equation, $\overline{K}^f = \overline{u_i u_i}^f/2$:

$$\begin{aligned} \frac{\partial}{\partial t}\left(\overline{\rho} k_{SGS}\right) + \frac{\partial}{\partial x_i}\left(\overline{\rho}\,\overline{u_i}^f k_{SGS}\right) = \\ \alpha_{SGS} + \Pi_{SGS} - \overline{\rho}\varepsilon_{\nu,SGS} + \overline{\rho} P_{SGS}, \end{aligned} \tag{2.131}$$

where the sub-grid redistribution ($\alpha_{SGS}$) term is:

$$\begin{aligned} \alpha_{SGS} = \frac{\partial}{\partial x_i}\left(\overline{p}\,\overline{u_i}^f - \overline{p u_i} + \overline{\tau_{ij} u_j} - \overline{\tau_{ij}}\,\overline{u_j}^f\right) \\ + \frac{\partial}{\partial x_i}\left(\overline{\rho}\,\overline{u_i}^f \overline{K}^f - \overline{\rho}\,\overline{u_i K}^f\right), \end{aligned} \tag{2.132}$$

the sub-grid pressure dilatation ($\Pi_{SGS}$) term is:

$$\Pi_{SGS} = \overline{p\Delta_v} - \overline{p}\overline{\Delta_v}^f, \tag{2.133}$$

and the sub-grid viscous dissipation ($\varepsilon_{\nu,SGS}$) term is:

$$\varepsilon_{\nu,SGS} = \frac{1}{\overline{\rho}}\left(\overline{\tau_{ij} S_{ij}} - \overline{\tau_{ij}}\,\overline{S_{ij}}^f\right). \tag{2.134}$$

The above exact terms are directly extracted from the DNS databases and will be used in the *a priori* DNS analyses presented in Chapter 5. Further, models for the above terms can be used to derive the model equation for $k_{SGS}$ solved in *a posteriori* analyses or real LES. The one equation k model [77] can be used in LES. The obtained $k_{SGS}$ value can be used to close the set of Eq. 2.121.

CHAPTER 3

# Turbulence-Chemistry Interactions: Finite-Rate Combustion Models

## 3.1 Introduction

In the governing equations of LES of reactive flows with detailed kinetics, the transport equations of the filtered species mass fractions are solved. The filtered transport equation for species $k$ has a filtered production/consumption rate $\overline{\dot{\omega}}_k(\boldsymbol{\varphi})$ which needs to be modeled. In $\overline{\dot{\omega}}_k(\boldsymbol{\varphi})$, $\boldsymbol{\varphi}$ is the composition vector together with the temperature (T) and pressure (p), and $\overline{(.)}$ the filter operator in LES. Since the net formation rates of species are non-linear functions of $\boldsymbol{\varphi}$, the equality $\overline{\dot{\omega}}_k(\boldsymbol{\varphi}) = \dot{\omega}(\overline{\boldsymbol{\varphi}}^f)$, which is called the "no model" or "quasi laminar" approach, in many conditions does not hold. In the previous statement, $\overline{(.)}^f$ is the Favre filtered operator defined as $\overline{\rho(.)}/\overline{\rho}$ with $\rho$ the density. The SGS combustion models try to include the effects of turbulence on chemistry (Turbulence-Chemistry Interaction or TCI) in such a way that $\overline{\dot{\omega}}_k(\boldsymbol{\varphi})$ can be computed by using $\overline{\boldsymbol{\varphi}}^f$. The same holds when solving RANS with detailed chemistry, i.e., the averaged production/consumption rate needs to be modeled.

In fact, LES combustion models can be divided in two main categories [8, 88]: the flamelet-based (FL) and the finite-rate (FR) combustion models. The assumption of mixed is burnt (in non-premixed flames) leads to the widely used flamelet based combustion models, treating turbulent flames as an ensemble of thin laminar flames called flamelets. The consideration of turbulent conditions is achieved by using a probability density function (PDF) of parametrized progress variables, e.g., conserved scalar like mixture fraction. A presumed form is usually applied. A transport equation for the PDF can also be solved but remains computationally expensive. The main issue in flamelet based models is in building the table and turbulence-chemistry interaction steps for which an *a priori* knowledge of the flow and the flame behavior is needed. Fur-

thermore, for concurrent non-premixed and premixed combustion regimes, the flamelet approach needs suitable but complex modifications, as reported in [89–91].

In contrast to the flamelet-based models, the finite-rate combustion models in LES try to evaluate $\overline{\dot{\omega}}_k(\boldsymbol{\varphi})$ as a function of filtered quantities which are available after the solution. In finite-rate combustion models, which are the focus of the present study, there is no assumption about the flow or flame, but instead they attempt to model the low-pass filtered net formation rates [8]. Models in this class are the Thickened Flame Model (TFM) [92–94], transported PDF (TPDF) models [9, 10], the Eddy Dissipation Concept (EDC) model [13–15], the Partially Stirred Reactor (PaSR) model [11, 12], and the Scale Similarity (SS) models [17, 18]. The TFM was developed primarily for turbulent premixed flames. TPDF models can deal with both premixed, non-premixed and multi-regime combustion, but they are reported to be computationally very expensive. EDC and PaSR, which have been developed for Reynolds Average Naiver Stokes (RANS) simulations, are now being extended to LES. However, no systematic and comprehensive analysis is carried out on EDC-LES models. In this chapter, the theory behind the EDC and the Scale Similarity models will be discussed. Sec.3.2 devoted to the EDC, starts with the general concept of the cascade model in RANS view point and will be further extended to the sub-grid cascade. New EDC-LES models will be derived based on the new findings in Sections5.3 and 5.2. Sec.3.3 is devoted to the SS models. It starts with the non-dynamic SS concept for finite-rate (FR), sub-grid scale (SGS) combustion modeling and ends in the explanation of the mathematical derivations of the new dynamic SS models, based on the Germano type dynamic methods.

## 3.2 Eddy Dissipation Concept (EDC)

The EDC FR-TCI model is based on the idea that the chemical reactions take place when the fuel and oxidizer in non-premixed flames or the cold reactive mixture and the hot products in premixed flames are perfectly mixed on the molecular level. The mixing indicator is the $\varepsilon$ or the scalar dissipation rate ($\chi$). In the EDC, the former is considered as the rate of mixing. Since the $\varepsilon$ is an intermittent process as will be discussed in Sec. 5.2, the model tries to include this effect in the evaluation of unclosed chemistry source term. Consider a fully turbulent region in the physical domain. In this region, due to the intermittency of $\varepsilon$ there are some sub-regions where $\varepsilon'$ is much higher than the mean of it. If one considers those regions as the regions where the final mixing takes place, then we expect that the reaction also takes place near those regions. These highly dissipative regions are called fine structures. Within the fine structures everything is well mixed, the covariances are zero so that for example in the Reynolds averaged form, $\underline{\dot{\omega}}_k(\boldsymbol{\varphi}) \propto \dot{\omega}(\underline{\boldsymbol{\varphi}}_f)$. In the other sub-region (outside the fine structures), since there is no intense mixing, there is no reaction, viz. $\dot{\omega}_k^0\left(\underline{\boldsymbol{\varphi}}_f\right) = 0$. Now if one can find the volume that each sub-region occupies, it will be possible to define the mean or the filtered form of a quantity using the weighted average.

In RANS-EDC we will have:

$$\begin{aligned}\underline{\dot{\omega}}_k(\boldsymbol{\varphi}) &= \mathcal{I}_{RANS}\left(\dot{\omega}^*(\underline{\boldsymbol{\varphi}}_f)\right) + (1-\mathcal{I}_{RANS})\left(\dot{\omega}_k^0\left(\underline{\boldsymbol{\varphi}}_f\right)\right)\\ &= \mathcal{I}_{RANS}\left(\dot{\omega}^*(\underline{\boldsymbol{\varphi}}_f)\right),\end{aligned} \tag{3.1}$$

where $\dot{\omega}^*$ is the chemical source term in dissipative regions (shown by $^*$) which can be calculated by solving the governing ODE equations (batch reactors) [95] over a residence time evaluated by the EDC. $\mathcal{I}_{RANS}$ is a prefactor related to the internal intermittency factor ($\gamma_{int}$). The intermittency phenomenon is discussed in detail in Sec. 5.2.2. Likewise, in LES we have:

$$\begin{aligned}\overline{\dot{\omega}}_k(\boldsymbol{\varphi}) &= \mathcal{I}_{LES}\left(\dot{\omega}^*(\overline{\boldsymbol{\varphi}}^f)\right) + (1-\mathcal{I}_{LES})\left(\dot{\omega}_k^0\left(\overline{\boldsymbol{\varphi}}^f\right)\right) \\ &= \mathcal{I}_{LES}\left(\dot{\omega}^*(\overline{\boldsymbol{\varphi}}^f)\right),\end{aligned} \tag{3.2}$$

The EDC can be used to find $\mathcal{I}$ (either in LES , $\mathcal{I}_{LES}$, or RANS, $\mathcal{I}_{RANS}$) using the estimated scales of dissipative eddies. Further, the time scale of these eddies modeled by EDC will be used as a residence time of reactive mixture in a hypothetical reactor inside a numerical cell. The residence time is needed to find the $^*$ values.

In this thesis, the EDC is considered as a kind of cascade model not a combustion model. In this new viewpoint, it can be regarded as a pure turbulence model. The goal of the concept is to find the turbulent dissipative scales. Then, finding the volume fraction occupied by these scales. Up to this point, it is purely related to the turbulence modeling. The link through the turbulence and combustion modeling is made by an important hypothesis. The hypothesis is that in high Reynolds numbers the combustion and dissipation fluctuations are correlated.

In the following, first, an explanation of the general idea of the eddy dissipation cascade in Sec. 3.2.1 will be presented. It is explained in RANS viewpoint. The LES viewpoint is discussed in Sec. 3.2.2. The existing approaches are discussed in these two sections. The EDC has two (in the case of Fureby model only one) coefficients resulting from the proportionality relations. The existing and the newly proposed methods to evaluate the coefficients are discussed in Sec. 3.2.3. A method to find the volume fraction of the dissipative fine structures are discussed in Sec. 3.2.4. Up to this point the EDC is viewed as a pure turbulence model, the final section (Sec. 3.2.5) describes the link of the model with turbulent combustion through introducing the time scale of the fine structures and the way it is introduced to batch reactors.

### 3.2.1 EDC for RANS

From the Kolmogorov theory we know that the characteristic size of the dissipative motions scale with $\underline{\eta}_f$[1]. The EDC is a model which tries to find the scales of the dissipative eddies using the quantities available during the numerical simulation. The EDC has a cascade model inside, like Richardson's cascade [51] with some modifications.

We start with the cascade model. The idea is shown in Fig. 3.1. As can be seen, the energy of the mean flow is transferred to lowered levels through the cascade to the scales where all energy is dissipated.

An important assumption in RANS-EDC approach is that the whole cascade is in each computational cell. Each level $n$, is characterized by its velocity scale, $u_n$, length scale $L_n$, and its vorticity, $w_n$. The velocity scale is defined as:

$$u_n \equiv \sqrt{\frac{2}{3}\underline{k_n}}, \tag{3.3}$$

[1]The Kolmogorov hypotheses imply that the characteristic size of the dissipative motions scale with (not equal to) $\underline{\eta}_f$ [38].

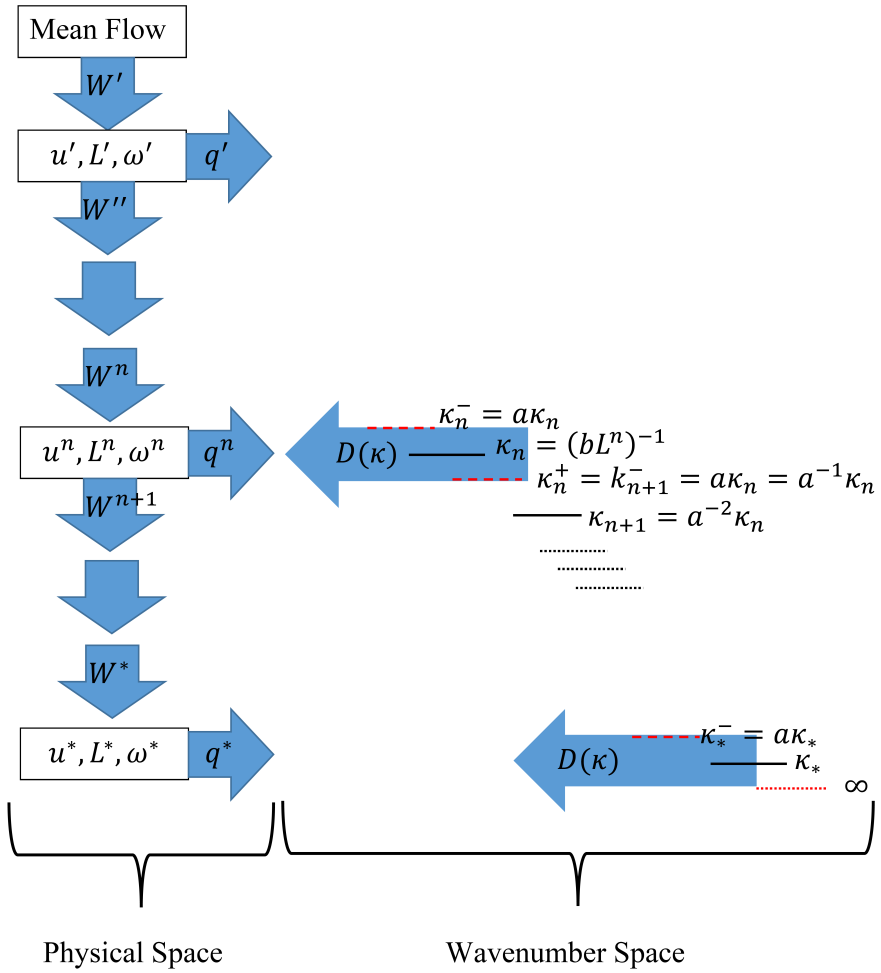


**Figure 3.1:** *The EDC cascade. Left side shows the cascade in physical space, the right side is in wavenumber space.*

where $\underline{k_n}$ is the average of kinetic energy in the scales of length $n$ ($k_n$). In the wavenumber space, it is the kinetic energy of scales with wavenumbers greater than the one corresponding to the level $n$ in the cascade, $\kappa_n$. This will be discussed more below. It should be noted that in this section the Reynolds averaging operator, $\underline{(.)}$ mainly used without the loss of generality as the Favre averaging operator $\underline{(.)}_f$ can also be used. The length scale is defined as:

$$L_n \equiv \frac{\underline{k_n}^{3/2}}{\underline{\varepsilon}}, \tag{3.4}$$

and the vorticity is defined by:

$$w_n \equiv \frac{u_n}{L_n}. \tag{3.5}$$

It is assumed that the vorticity at each level is twice the previous level. This is consistent with Richardson's cascade [51]. So the relation between steps is governed by the vorticity ratio:

$$w_{n+1} = 2w_n. \tag{3.6}$$

At each level, a part of the mechanical energy, viz. $q_n$, is dissipated. We need two definitions for the rate of the mechanical energy transferred to the $n^{th}$ level and also the rate of dissipation of energy to heat from the $n^{th}$ level, i.e., definitions for $W^n$ and $q_n$ at each level. Magnussen [13] assumes that production, which feeds mechanical energy to the first level, viz. $W'$, is a product of the turbulent stress and the mean flow strain rate. This is similar to the definition of the production term in the transport equation of turbulent kinetic energy, Eq. 2.114. The feed to the second level, viz. $W''$, can be modeled according to the same pattern so that at each level $n$, $W^n$ can be modeled as:

$$W^n \propto \underline{k_n} w_n = CD_1 \frac{3}{2} {u_n}^2 w_n, \tag{3.7}$$

where $CD_1$ is the first proportionality coefficient. At each level the rate of transfer of mechanical energy to thermal energy, $q_n$, is proportional to:

$$q_n \propto \underline{\nu} {w_n}^2 = CD_2 \underline{\nu} {w_n}^2, \tag{3.8}$$

where $CD_2$ is the second proportionality coefficient. Again the above definition is analogous to the dissipation term in the transport equation of TKE, Eq. 2.115. From the equations 3.7 and 3.8 one can derive the equations for the length and velocity scales at * level which can be further used to evaluate $\mathcal{I}$ and the mass transfer rate (the time scale of the dissipative eddies) between the fine structures and the surrounding fluid. From Fig. 3.1 we can see that:

$$\underline{\varepsilon} = q' + q'' + ... + q^*. \tag{3.9}$$

By using the assumption of Eq. 3.6 in Eq. 3.8 one can find:

$$q_n = 4 q_{n-1}. \tag{3.10}$$

By using Eq. 3.10 in Eq. 3.9 and using the series theory we can reduce Eq. 3.9 to Eq. 3.11:

$$3\underline{\varepsilon} = 4q^* - q'. \tag{3.11}$$

Here we use another important assumption in which in high Reynolds numbers the dissipation from the first level can be considered negligible so that ,$q' = 0$. This is analogous to statement of being in the inertial range in Kolmogorov's language. By using this in Eq. 3.11 we have the first relation for the dissipation rate:

$$3\underline{\varepsilon} = 4q^*. \tag{3.12}$$

From Fig. 3.1 it can be also found that in the last level of the cascade we have, $W^* = q^*$. By using this in Eq. 3.12 we can derive the second equation for the dissipation rate:

$$3\underline{\varepsilon} = 4W^*. \tag{3.13}$$

By replacing $W^*$ and $q^*$ from their relations, i.e., Eq. 3.7 and Eq. 3.8 in Eq. 3.12 and Eq. 3.13, respectively, we have:

$$3\underline{\varepsilon} = 4\left(\frac{3}{2} CD_1 {u^*}^2 w^*\right), \tag{3.14a}$$

$$3\underline{\varepsilon} = 4\left(CD_2 \underline{\nu} {w^*}^2\right). \tag{3.14b}$$

By replacing Eq. 3.5 into Eq. 3.14 we have:

$$3\underline{\varepsilon} = 4\left(\frac{3}{2}CD_1\frac{u^{*3}}{L^*}\right), \tag{3.15a}$$

$$3\underline{\varepsilon} = 4\left(CD_2\underline{\nu}\frac{u^{*2}}{L^{*2}}\right). \tag{3.15b}$$

From these two equations one can finally find the velocity and length scale of the fine structures:

$$L^* = \frac{2}{3}\left(\frac{3CD_2{}^3}{CD_1{}^2}\right)^{1/4}\left(\frac{\underline{\nu}^3}{\underline{\varepsilon}}\right)^{1/4} = \frac{2}{3}\left(\frac{3CD_2{}^3}{CD_1{}^2}\right)^{1/4}\underline{\eta}, \tag{3.16a}$$

$$u^* = \left(\frac{CD_2}{3CD_1{}^2}\right)^{1/4}(\underline{\nu}\,\underline{\varepsilon})^{1/4} = \left(\frac{CD_2}{3CD_1{}^2}\right)^{1/4}\underline{u_\eta}. \tag{3.16b}$$

This derivation of the cascade was proposed by Ertesvag and presented in [15]. However, the older model proposed by Magnussen [13, 14] has some differences. Although the Ertesvag derivation seems to be more rational, here the original Magnussen version is also presented since it is the base of the LES-EDC derivation in Fureby's group [96] which is further used in the subsequent works in his group (see e.g., [8, 91, 97–100]). In the Magnussen original derivation, instead of using two separate coefficients of proportionality in Eq. 3.7 and Eq. 3.8, only one coefficient ($\zeta$) has been used, viz.:

$$W_n \propto \underline{k_n}w_n = \zeta^2 6{u_n}^2 w_n, \tag{3.17}$$

$$q_n \propto \underline{\nu}{w_n}^2 = \zeta^2 15\underline{\nu}{w_n}^2. \tag{3.18}$$

The point is that instead of separately relating energy transfer rate, $W_n$, and dissipation to heat rate, $q_n$, to turbulence quantities, Magnussen modeled the total dissipation at each level:

$$\varepsilon_n \propto \left(6{u_n}^2 w_n + 15\underline{\nu}{w_n}^2\right) = \zeta^2\left(6{u_n}^2 w_n + 15\underline{\nu}{w_n}^2\right), \tag{3.19}$$

where the term $15\underline{\nu}{w_n}^2 = 15\underline{\nu}{u_n}^2/{L_n}^2$ coming from the dissipation definition with HIT assumptions (see Eq. 2.58).

Now using the same procedure as before, i.e., using Eq. 3.12 and Eq. 3.13, one can find:

$$L^* = \left(125\zeta^2\right)^{1/4}\left(\frac{\underline{\nu}^3}{\underline{\varepsilon}}\right)^{1/4} = \left(125\zeta^2\right)^{1/4}\underline{\eta}, \tag{3.20a}$$

$$u^* = \left(\frac{5}{16\zeta^2}\right)^{1/4}(\underline{\nu}\,\underline{\varepsilon})^{1/4} = \left(\frac{5}{16\zeta^2}\right)^{1/4}\underline{u_\eta}. \tag{3.20b}$$

Eq. 3.20 has been used in Fureby's group to derive the LES version of the EDC. However, we keep using Eq. 3.16 unless otherwise mentioned. It will be shown theoretically in Sec.3.2.3 that the two coefficients in Eq. 3.16 can be reduced to one, using the dissipation spectrum, however, the relation will be found to be much stronger than $\frac{CD_2}{CD_1} = \frac{15}{4}$ which is inferred from Eq. 3.20[2].

[2]It needs some math exercise to relate Eq. 3.20 to Eq. 3.16 and extract the ratio of $\frac{CD_2}{CD_1} = \frac{15}{4}$.

### 3.2.2 EDC for LES

To extend the model to LES, the idea is to assume that the cascade process or part of it occurs in a LES grid (see Fig. 3.2). In each LES computational cell the energy from the "filtered level" is transferred to the smaller eddies down to the dissipative scales. The cascade process should result in the sub-grid dissipative structure scales. Here it is assumed that the whole cascade occurs in a LES cell. A blending function [101] can be added in applications to take into account the ratio of the grid size in LES and Kolmogorov's scale. However, for the moment we keep using the assumption that the LES grid size is much bigger than $\underline{\eta}_f$ when the filter cutoff placed in the inertial range. So it is reasonable to assume that the whole cascade occurs inside each grid cell. On the other hand, the theoretical derivations in this section are based on the general assumptions usually used in turbulence modeling, i.e, the Reynolds number is so high that there is no overlap in the range of scales. This is a fundamental assumption in many theoretical derivations.

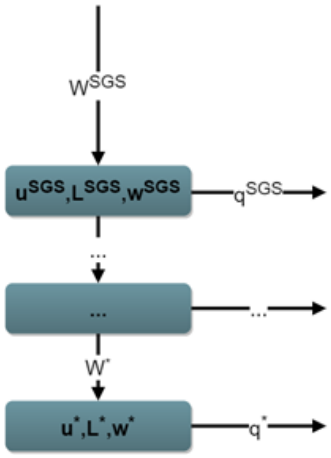


**Figure 3.2:** *The EDC cascade in sub-grid scales.*

#### Ertesvag Group Approach

Lysenko et al., [16, 101, 102] consider the SGS level in Fig. 3.2 as the prime level in Fig. 3.1. With this, starting from Eq. 3.9 we have:

$$\varepsilon_{\nu,SGS} = q^{SGS} + ... + q^*. \tag{3.21}$$

Same as RANS-EDC, by replacing Eq. 3.10 in Eq. 3.21 and using series theory we can reduce Eq. 3.21 to Eq. 3.22:

$$3\varepsilon_{\nu,SGS} = 4q^* - q^{SGS}. \tag{3.22}$$

Here we assume that the transfer to heat at the first level in sub-grid scale is zero so that:

$$3\varepsilon_{\nu,SGS} = 4q^*. \tag{3.23}$$

Again in the last level, $W^* = q^*$ so:

$$3\varepsilon_{\nu,SGS} = 4W^*. \tag{3.24}$$

With the same procedure used in Eq. 3.14 to Eq. 3.16 we can finally have the EDC equations for $u^*$ and $L^*$ in LES:

$$L^* = \frac{2}{3}\left(\frac{3{CD_2}^3}{{CD_1}^2}\right)^{1/4}\left(\frac{\overline{\nu}^3}{\varepsilon_{\nu,SGS}}\right)^{1/4} \tag{3.25a}$$

$$u^* = \left(\frac{CD_2}{3{CD_1}^2}\right)^{1/4}\left(\overline{\nu}\varepsilon_{\nu,SGS}\right)^{1/4}, \tag{3.25b}$$

where $\overline{\nu}$ is the filtered viscosity and $\varepsilon_{\nu,SGS}$ is the viscous dissipation in sub-grid, i.e. Eq. 2.134. In the *a priori* DNS analysis, the scales can be directly evaluated from the above equations. In LES, a model is required for $\varepsilon_{\nu,SGS}$. The common approach is to use [77]:

$$\varepsilon_{\nu,SGS} = C_\varepsilon \frac{\left(k_{SGS}\right)^{3/2}}{\Delta}, \tag{3.26}$$

where $k_{SGS}$ is the sub-grid kinetic energy (already defined in Eq. 2.125). Again, to model $k_{SGS}$, the transport equation of sub-grid kinetic energy can be solved (e.g., one equation eddy model [86]). $C_\varepsilon$ can be set constant equal to 1.048 or can be evaluated dynamically [77].

#### Fureby Group Approach

The Swedish group developed the LES-EDC based on the original Magnussen model, i.e. Eq. 3.20. The assumptions and derivations are the same as what described before in Sec.3.2.2. The difference between the models in the two groups is using either one or two numerical coefficients in the cascade model. The Fureby group approach leads to :

$$L^* = \left(125\zeta^2\right)^{1/4}\left(\frac{\overline{\nu}^3}{\varepsilon_{\nu,SGS}}\right)^{1/4} \tag{3.27a}$$

$$u^* = \left(\frac{5}{16\zeta^2}\right)^{1/4}\left(\overline{\nu}\varepsilon_{\nu,SGS}\right)^{1/4}, \tag{3.27b}$$

### 3.2.3 Evaluation of EDC Model Coefficients

Like every model, the dissipation cascade model has some coefficients to be set by the user. The coefficients are $CD_1$ and $CD_2$ in Eq. 3.16 or $\zeta$ in Eq. 3.20. These coefficients can be fine tuned by the user to give the best prediction of a specific target. However, since the equations are based on the physical arguments, the coefficients can be evaluated in some ideal conditions. Like what Lilly did to evaluate the coefficient in the Smagorinsky model [76]. In the original EDC model both coefficients are free coefficients. Since in the model, ideal assumption have been used (as any other model does, like the Smagorinsky constant for the Smagorinsky LES model or etc.), free coefficients give the degree of freedom and the best fit to the reality should be searched for by changing the model coefficients. If extra relations can be found, it can be possible to reduce the degree of freedom. If an identity can be found in the physics or numerics (like Germano's identity), it may result in a self adaptive model where the coefficients

can be set dynamically. An optimum model, is a self adaptive one where the coefficients can be set dynamically by the model itself. However, if an optimum model does not work for a specific reality, this is not necessarily the fault of the optimum model, it can be due to the departure (in reality) from the assumptions used in the model. For example if at the end the dynamic Smagorinsky model in LES does not work for a case, this is not the intrinsic issue of the model or Germano's identity, it is simply because the case under consideration departs from some assumptions in the model, for example the alignment of the deviatoric part of the SGS (residual) stress tensor and the resolved strain rate in this case. The best example is the Kolmogorov's 1941 (K41) theory (discussed in Sec.2.2.5). The theory assumes that in high Reynolds numbers, the velocity structure function of order $n$, viz. $D_{LLp}(r)$, scales as $r^{p/3}$. When $r \to 0$, this implies that the skewness of the longitudinal gradient of the streamwise velocity, $S_{\frac{\partial u}{\partial x}}$, in HIT is constant. Soon after K41 theory, the departures from the theory were reported in experiments which led to the refined theory of K62. However, recently, it is shown that K41 prediction for the skewness being constant is true and the departures observed in the experiments and DNS databases are due to Finite Reynolds Number (FRN) effect [35]. This means simply the assumption of being in high Reynolds numbers regime is not satisfied so one cannot argue that the model is wrong. Following this short discussion, here it is tried to reduce the degree of freedom in the EDC by finding a relation between the two coefficients. For that, no extra assumption is added. The assumptions are the ones in Kolmogorov's theory which were already used in the EDC model. Looking at Eq. 3.7, $CD_1$ is a coefficient to relate the production to velocity and vorticity scales. Likewise, in Eq. 3.8, $CD_2$ is introduced to relate the dissipation to the vorticity scales. It is first tried to relate $CD_2$ to $CD_1$. So the model will only include $CD_1$. Next the evaluation of $CD_1$ will be discussed. Since $CD_1$ is related to the large scale production of TKE, it can be differently evaluated in RANS or LES applications.

#### Evaluation of $\zeta$ for RANS

For RANS, Magnussen [13, 14] used:

$$\zeta_{RANS} = 0.18, \tag{3.28}$$

in Eq. 3.20. The author could not find any reference of how the value is concluded but it seems that it is evaluated based on some experimental observations.

#### Evaluation of $\zeta$ for LES

The Swedish group is the only group used the model Eq. 3.20 in LES. This was discussed in Sec. 3.2.2. To evaluate $\zeta$ in LES, they equate "the SGS dissipation" and the energy transfer at the first level in the model. It must be mentioned that the "the SGS dissipation" here means the sub-grid viscous dissipation, i.e. Eq. 2.134. This means: [91, 96]:

$$\varepsilon_{\nu,SGS} = 6\zeta^2 \frac{U^{SGS^3}}{\Delta} = 6\zeta^2 \frac{\left(\frac{2}{3}k_{SGS}\right)^{3/2}}{\Delta}, \tag{3.29}$$

where $k_{SGS}$ is defined in Eq. 2.125.

The above equation can be directly used in *a priori* DNS analyses since the exact $\varepsilon_{\nu,SGS}$ can be calculated from the DNS databases (by Eq. 2.134) to compute $\zeta$ locally and there is no need for modeling. In LES, the model already introduced in Eq. 3.26, can be used for $\varepsilon_{\nu,SGS}$. Finally, $\zeta$ is:

$$\zeta_{LES}^2 = \frac{C_\varepsilon}{6\left(\frac{2}{3}\right)^{3/2}}. \tag{3.30}$$

If the constant value of $C_\varepsilon = 1.048$ is used in Eq. 3.30, it leads to the coefficient equal to the constant of:

$$\zeta_{LES} \approx 0.566. \tag{3.31}$$

Consider that in the final equations of LES-EDC, derived to be used in LES codes (see Table 3.2), $\zeta$ and $C_\varepsilon$ will be canceled out so that the final equations do not have any coefficient.

#### A New Method for Evaluation of $CD_2$ in RANS and LES

Although in many previous applications of the EDC, the value proposed for RANS, viz. $CD_2 = 0.5$, [15] has been used (even for LES e.g., [16, 101, 102]), here, a new theoretical basis is proposed to relate $CD_2$ to $CD_1$ so that there is no need to set a value. The relation can be used both in RANS and LES. The idea of relating theEDC cascade in the physical space to the wavenumber space is inferred from [15]. Here, using the dissipation model spectrum obtained in Sec. 5.3.4, it will be newly used to extract a theoretical relation between the two coefficients.

In Fig. 3.1, the representation of the EDC cascade in the wavenumber space is shown. If one wants to relate the stepwise cascades to the continuous wavenumber space, it is needed to define the wavenumber ranges representative of each step in the cascade. The range of wavenumbers representative of level $n$ of the stepwise cascade is defined as $\kappa \in (\kappa_n^-, \kappa_n^+)$ with, $\kappa_n$, the center of the range. The next level is $\kappa_{n+1}$ in the range $\kappa \in (\kappa_{n+1}^-, \kappa_{n+1}^+)$. Tennekes and Lumley [103] chose unity steps on a logarithmic scale which means, $\kappa_n^- = e^{-1/2}\kappa_n$, $\kappa_n^+ = e^{1/2}\kappa_n$ and $\kappa_{n+1} = e\kappa_n$. From these, a factor $a = e^{-1/2} \approx 0.6$ can be defined where $\kappa_n^- = a\kappa_n$. The relations are shown in Fig. 3.1. On the other hand, it can be proven that [15] using assumptions in the EDC (almost no dissipation in the first level of the cascade, i.e. being in the inertial range), $\kappa_{n+1} \approx 2\sqrt{2}\kappa_n$ so that centering $\kappa_n$ in the range of $(\kappa_n^-, \kappa_n^+)$ will result in $a = 1/\sqrt{2\sqrt{2}} \approx 0.59$ which is close to Tennekes and Lumley stepwise representation of the cascade in the wavenumber space.

The relation between the EDC cascade in the physical space and the stepwise cascade in the wavenumber space can be drawn using the relation between the physical length scales and the corresponding wavenumbers. We know that in general $L$ in the physical space is proportional to $1/\kappa$ in the wavenumber space with $\kappa$ the wavenumber magnitude. Consider the proportionality constant as $b$ which means at each level $n$ we have:

$$\kappa_n \propto \frac{1}{L_n} = \frac{1}{bL_n}. \tag{3.32}$$

Using Eq. 2.67, one can find a relation for $b$. It starts from:

$$\frac{3}{2}(u_n)^2 = k_n = \int_{\kappa_n^-}^{\infty} E(\kappa, t)d\kappa, \tag{3.33}$$

writing the same equation for level $n+1$ and subtracting the two we have:

$$\frac{3}{2}\left((u_n)^2 - (u_{n+1})^2\right) = \int_{\kappa_n^-}^{\kappa_n^+} E(\kappa, t)d\kappa. \tag{3.34}$$

If the energy transfer from level $n$ is assumed to be equal to the one from $n+1$, with level $n$ and $n+1$ being in the inertial range[3], i.e., no direct dissipation from these levels ($W_n = W_{n+1}$ in the cascade model), from Eq. 3.7 and Eq. 3.34, we have:

$$\frac{3}{2}\left((u_n)^2 - (u_{n+1})^2\right) = \frac{3}{4}(u_n)^2 = \int_{\kappa_n^-}^{\kappa_n^+} E(\kappa, t)d\kappa. \tag{3.35}$$

Using Kolmogorov's spectrum function in the inertial range, Eq. 2.68:

$$\frac{3}{4}(u_n)^2 = \int_{\kappa_n^-}^{\kappa_n^+} C_K(\underline{\varepsilon})^{2/3}\kappa^{-5/3}. \tag{3.36}$$

By using $\kappa_n^- = a\kappa_n$ and $\kappa_n^+ = a^{-2}\kappa_n$, integrating the spectrum and re-arranging we have:

$$\frac{(u_n)^2}{\underline{\varepsilon}^{2/3}} = C_K a^{-2/3}\kappa_n^{-2/3}. \tag{3.37}$$

Another relation for $(u_n)^2/\underline{\varepsilon}^{2/3}$ can be drawn by using Eq. 3.7, and Eq. 3.32 so that:

$$\frac{(u_n)^2}{\underline{\varepsilon}^{2/3}} = L_n^{2/3}(\frac{2}{3})^{2/3}CD_1^{-2/3}. \tag{3.38}$$

Finally, using the two relations Eq. 3.37 and Eq. 3.38, $b$ can be found as:

$$b^{-2/3} = C_K a^{-2/3} C D_1^{2/3}(2/3)^{-2/3}, \tag{3.39}$$

where $C_K$ is the Kolmogorov's constant. The relation will be used in the next part to find $CD_2$. Note that $a$ can be replaced by $a = 0.59$ as discussed before. The value $C_K \approx 2.3$ (instead of common value 1.5 in non-reactive constant density flows) found for Kolmogorov's constant for the 3D spectrum function using the current reactive DNS databases in Sec. 5.3. In this way $b$ is a function of only $CD_1$.

To find $CD_2$, Eq. 2.80 will be used. Considering the assumptions in the EDC, it is shown that the dissipation from the last level of the cascade is $3/4$ of the total dissipation (see Eq. 3.12), so that using Eq. 2.80 we have:

$$\frac{3}{4}\underline{\varepsilon} = \int_{\kappa_*^-}^{\infty} D(\kappa)d\kappa, \tag{3.40}$$

[3] In other words it is assumed that $\kappa_n$ and $\kappa_{n+a}$ are in the inertial range. This is consistent with using Kolmogorov's inertial range spectrum function as $E(\kappa)$ in Eq. 3.33 and Eq. 3.34.

or using Eq. 2.82, Eq. 3.40 can be written in the normalized form:

$$\frac{3}{4} = \int_{\kappa_*^- \underline{\eta}}^{\infty} D_{Normal}(\kappa\underline{\eta}) d(\kappa\underline{\eta}). \tag{3.41}$$

Note to the change of the variables in the definite integrals above.

Equation 3.41 leads us to the below conclusion:

*If a normalized model spectrum can be found for the dissipation range of reactive flows, the normalized wavenumber, viz. $\kappa_*^- \underline{\eta}$, corresponding to the last level in the EDC cascade, is the wavenumber at which the integral in Eq. 3.41 is* $3/4$.

Using $\kappa_*^- = a\kappa_*$ and Eq. 3.32 to relate $\kappa_*$ to $L^*$ one leads to:

$$\kappa_*^- \underline{\eta} = a\kappa_* \underline{\eta} = \frac{a\underline{\eta}}{bL^*}. \tag{3.42}$$

Then using Eq. 3.16 for $L^*$ in Eq. 3.42, leads to:

$$\kappa_*^- \underline{\eta} = \frac{3}{2}\frac{a}{b}\left(\frac{CD_1^2}{3CD_2^3}\right)^{1/4}, \tag{3.43}$$

where if $b$ is replaced from Eq. 3.39:

$$\kappa_*^- \underline{\eta} = \left(\frac{3}{2}\right)^2 \left(\frac{1}{3}\right)^{1/4} \frac{CD_1^{3/2}}{CD_2^{3/4}} C_K^{3/2}, \tag{3.44}$$

re-arranging for $CD_2$:

$$CD_2 = \left(\frac{3}{2}\right)^{8/3} \left(\frac{1}{3}\right)^{1/3} \frac{CD_1^2}{\left(\kappa_*^- \underline{\eta}\right)^{4/3}} C_K^2, \tag{3.45}$$

where, $CD_2$ is uniquely determined by $CD_1$ if a universal form of $D_{Normal}(\kappa\underline{\eta})$ is used to find the value of $\kappa_*^- \underline{\eta}$.

In Sec. 5.3.4, Using 3 DNS databases of the non-premixed temporally evolving jet flames in different bulk jet Reynolds numbers and 3 time instants in each case representing different flame dynamics (extinction/re-ignition), a model with a functional form similar to the form of Pope's spectrum Eq. 2.81 was found to represent the dissipation spectra in reactive flows. The model spectrum of Pope (blue dashed line) is shown along with the modified spectrum (solid red line) in Fig. 3.3. The integrals of the curves are approximately equal however the peak locations and the rates of exponential drop-off are not the same. A normalized wavenumber where the area below the red curve reaches $\frac{1}{4}$ of the total area is the wavenumber ($\kappa_*^- \underline{\eta}$) corresponding to the EDC last level, $L^*$. Numerical integration shows $\kappa_*^- \underline{\eta} \approx 0.15$. Using this value and the value for Kolmogorov's constant ($C_K = 2.3$) obtained in Sec. 5.3.4 in Eq. 3.45, $CD2$ will reduce to:

$$CD_2 = \frac{3^{7/3} 2.3^2}{2^{8/3} 0.15^{4/3}} CD_1^2 \approx 135.7 CD_1^2. \tag{3.46}$$

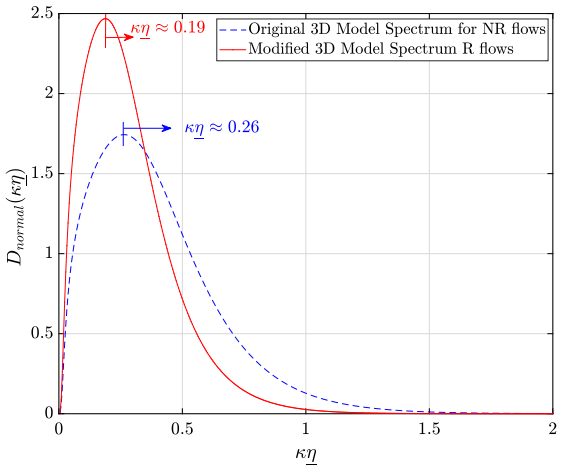


**Figure 3.3:** *The 3D model dissipation spectrum of Pope for non-reacting (NR) flows and the proposed 3D model dissipation spectrum for rective (R) flows.*

#### Evaluation of $CD_1$ for RANS

$CD_1$ is a coefficient resulting from the assumption that the transfer rate of the turbulent kinetic energy from each level is proportional to the TKE multiplied by the strain rate. Since the same coefficient is used at each level, using the relation at the first level, in RANS mode and again assuming the direct dissipation from the first level is negligible, viz. $q' \approxeq 0$, one can write:

$$\underline{\varepsilon} = W' = W'' = CD_1 \frac{3}{2} u'^3 / L'. \tag{3.47}$$

On the other hand, for RANS, the turbulent viscosity is defined as (Eq. 2.106 where the Favre average operator is changed to the Reynolds average):

$$\nu_t = u' L' = C_\mu \frac{\underline{k}^2}{\underline{\varepsilon}}, \tag{3.48}$$

where using Eq. 3.4 for $L'$ and Eq. 3.3 for $u'$, one can write:

$$\nu_t = \frac{2}{3} CD_1 \frac{\underline{k}^2}{\underline{\varepsilon}} = C_\mu \frac{\underline{k}^2}{\underline{\varepsilon}}, \tag{3.49}$$

so that

$$\frac{2}{3} CD_1 = C_\mu, \tag{3.50}$$

By using the standard value of $C_\mu = 0.09$ which is used in RANS $k-\varepsilon$ model, one can find a good estimate for $CD_1$.

The above idea proposed in [15], however, originally the coefficient was set using the experimental results in the log-law region of boundary layer. In the log-law region, the production is equal to dissipation, so that the assumption used in the model is satisfied. Both methods lead to the same coefficient since $C_\mu$ is also found from the same assumptions using experimental observations.

**Evaluation of $CD_1$ for LES**

For the application of EDC in LES (see e.g., [16, 101, 102]), the same value obtained for RANS, $CD_1 = \frac{3}{2}C_\mu = 0.135$, has been used so far.

Of course there are other interesting options without adding extra assumptions. Note that the derivations below are theoretical derivations so they are general and supposed to be valid if the assumptions are satisfied (e.g., in high Reynolds number flows when the filter is placed in the inertial range).

The approach is simply similar to what has used in the Swedish group to evaluate $\zeta$ in LES, viz. $\zeta_{LES}$, which was explained before in Sec. 3.2.3. The theoretical derivation below holds in high Reynolds number flows and it is assumed that the filter is in the inertial range which is a common requirement for all turbulence models.

Equating "the viscous SGS dissipation" and the energy transfer at the first level in the model leads to:

$$\begin{aligned} \varepsilon_{\nu,SGS} &= CD_1 \frac{3}{2} \frac{U^{SGS^3}}{L^{SGS}} \\ &= CD_1 \frac{3}{2} \frac{U^{SGS^3}}{\Delta} \\ &= CD_1 \frac{3}{2} \frac{\left(\frac{2}{3} k_{SGS}\right)^{3/2}}{\Delta}. \end{aligned} \tag{3.51}$$

The above equation can be used in *a priori* DNS analyses since the exact $\varepsilon_{\nu,SGS}$ can be directly extracted from the DNS databases using Eq. 2.134 to calculate $CD_1$ locally. In LES, using the model for $\varepsilon_{\nu,SGS}$ in Eq. 3.26 one can find $CD_1$ as:

$$CD_{1LES} = \frac{C_\varepsilon}{\left(\frac{2}{3}\right)^{1/2}}. \tag{3.52}$$

If the constant value of $C_\varepsilon = 1.048$ is used in Eq. 3.52, this leads to the coefficient equal to the constant:

$$CD_{1LES} \approx 1.28. \tag{3.53}$$

Consider that in LES codes, $C_\varepsilon$ in Eq. 3.53 can be computed dynamically making this LES-EDC version a dynamic method for LES codes (see Table 3.2). This can be done e.g., using the Vreman method [104] or the more complicated method of Ghosal et al., [105] or even the standard dynamic method using Germano's identity[4]. Note that the statement Eq. 3.26 coming from the idea that at the first level in the SGS cascade, the dissipation to heat is zero so that $W^{SGS} = P_{SGS} = \varepsilon_{\nu,SGS}$. In other words, " Local Equilibrium Hypothesis " [77] is used in local/instantaneous manner (not the average manner) which is a common assumption in LES, although may not be fully satisfied [106]. Consider Lilly's approach [76] to find a theoretical value for the Smagorinsky constant. Although the Lilly theory relies on "average" equations, but practically, the value obtained from it, has been used locally in LES codes.

[4] Although Ghosal et al., [105] argue that Grmano's identity for this term will be zero in high Reynolds number flows because turbulent dissipation is a small-scale phenomenon and no dissipation is left at resolved scales for high Reynolds number flows.

### 3.2.4 Volume Fraction of Fine Structures: Internal Intermittency Factor

The eddy dissipation cascade is a model to find the dissipative length, velocity and time scales. However, it does not provide the fraction of the volume that the structures with these scales occupy. The problem is that soon after the K41 theory, it was revealed that the dissipation is an intermittent phenomenon [107]. This means that the dissipative structures (if exists) are not homogeneously distributed in space/time. This is the so-called small-scale, internal or intrinsic intermittency. It is usually associated with the tendency to spatial and temporal localization of the fine or small-scale structures of turbulent flows. The small-scale intermittency of turbulence is associated with its spotty (spatio-temporal) structure [108]. The whole story is discussed in detail in Sec. 5.2.2. The reader is suggested to first go through Sec. 5.2 before reading the current section. Here only a very brief discussion was presented to create a rational and reasonable context to present the equations.

As stated before, the result of the dissipation cascade is $u^*$, $L^*$ and $\tau^*$. The eddy dissipation cascade is not like the fractal [51, 109] or multi-fractal [110] theories which directly model the scaling of the structure functions and so the flatness factor. So Magnussen used an explicit expression to define the volume fraction occupied by the fine structures. For the moment to be consistent with the notation of the Norwegian group, i.e., Magnussen in 1981 [13] (hereafter M81) and Ertesvag in 2000 [15] (hereafter E2000), we use $\gamma^*$ to denote the "ratio of the fine-structure mass to the total mass" or "mass fraction occupied by fine-structures". In the early versions of the EDC, M81 and E2000 defined $\gamma^*$ as:

$$\gamma^* \equiv \left(\frac{u^*}{u'}\right)^3 \propto \frac{L^*}{L'} \propto Re_\lambda^{-3/2} \tag{3.54}$$

The proportionality relations can be derived easily in RANS. Note that depending on the model used in RANS or LES or Magnussen/Fureby or Ertesvag versions, $L^*$ and $u^*$ can be replaced by Eq. 3.16, Eq. 3.20, Eq. 3.25, or Eq. 3.27, respectively. This results in ${\gamma^*}_{RANS}$ or ${\gamma^*}_{LES}$ and can be tested in *a priori* DNS analyses.

Corrsin in 1962 [111], assumed that the dissipative structures are vortex sheets with the thickness of $\underline{\eta}$ embedded in bigger structures of the integral length scale i.e. $l_{int}$. Then he showed that:

$$\gamma_{int} \equiv \frac{\varepsilon^2}{\underline{\left(\varepsilon^s_{inst}{}^2\right)}} \propto \frac{\underline{\eta}}{l_{int}} \propto Re_\lambda^{-3/2}. \tag{3.55}$$

In incompressible flows using HIT assumptions it can be shown that (see Sec.5.2.2) $\frac{\varepsilon^{s2}}{\underline{\left(\varepsilon^s_{inst}{}^2\right)}} \propto \frac{1}{\mathcal{F}_{\frac{\partial u'}{\partial x}}}$, where $\varepsilon^s$ is the average pseudo-dissipation already defined in Eq. 2.58, $\varepsilon^s_{inst}$ the instantaneous (without averaging) one-dimensional surrogate for the dissipation can be defined in Eq. 5.5 and $\mathcal{F}_{\frac{\partial u'}{\partial x}}$ is the flatness of longitudinal gradient of stream wise velocity fluctuations. The flatness was already introduced in Eq. 2.19.

Tennekes in 1968 considered the dissipative structures as vortex tubes with the diameter of $\underline{\eta}$ inside bigger structures of $\lambda$. He clearly stated that the volume fraction

occupied by these vortical structures is $\frac{\eta^2}{\lambda^2}$ and found a relation for $\mathcal{F}_{\frac{\partial u'}{\partial x}}$ as:

$$\gamma_{int} \equiv \frac{\varepsilon^{s\,2}}{\underline{\left(\varepsilon^{s}_{inst}{}^{2}\right)}} \propto \frac{1}{\mathcal{F}_{\frac{\partial u'}{\partial x}}} \propto \frac{\eta^2}{\lambda^2} \propto Re_\lambda^{-1}. \tag{3.56}$$

The recent version of the EDC developed by the Norwegian group, Magnussen in 2005 [14] (hereafter M2005) and Lysenko et al., in 2014 [101, 102] (hereafter L2014) uses:

$$\gamma^* \equiv \left(\frac{u^*}{u'}\right)^2 \propto Re_\lambda^{-1} \tag{3.57}$$

It seems natural to assume that the Norwegian group intentionally defined $\gamma^*$ to represent the phenomenological models. This was also clearly mentioned by Ertesvag [15] and Lysenko et al., [101].

In Ertesvag [15] it is written that :

"This (i.e. $\gamma^*$) is the intermittency factor of the fine structures. If the Taylor microscale ... This is similar to the model by Corrsin (1962)".

and from the same group in Lysenko et al., [16], it is written that:

"The previous model (i.e. Eq. 3.54 ) corresponds to a sheet-like turbulence fine structure (Corrsins model), whereas Eq. 16 (i.e. Eq. 3.57) corresponds to a tube-like structure (Tennekes model)".

So it can be concluded that $\gamma^*$ in the EDC model is actually the internal intermittency factor, i.e. $\gamma_{int}$. However, note that M81 did not mention clearly this fact.

Now the problem is that in 1971, Kuo and Corrsin [112] did measure the flatness of the longitudinal gradient of the streamwise velocity in grid-generated turbulence experiments and on the axis of a round jet and saw $\mathcal{F}_{\frac{\partial u'}{\partial x}}$ scales as $Re_\lambda^{0.2}$ in $Re_\lambda < 200$ range, following a transition zone up to $Re_\lambda \approx 500$, increases more rapidly as $Re_\lambda^{0.6}$. The power law is much weaker than the predicted ones by phenomenological models!

It seems that M81 was aware of this work (see figure 5 in [13] where he compared the flatness factor resulting from the EDC with the data of Kuo and Corrsin [112]). However, it was not clear explained why he chose $\gamma^{*1/3} = \frac{u^*}{u'}$ as the inverse of the flatness factor to compare with Kuo and Corrsin data. In above, we showed that in the context of the EDC model, $\gamma^*$ is proportional to the inverse of flatness of velocity gradient not $\gamma^{*1/3}$.

Since the work of Kuo and Corrsin in 1971 there has been many works on the topic (see the literature review in Sec. 5.2.2). The recent conclusions of Antonia's group [35, 113, 114] is that the flatness factor approaches a constant after a critical Reynolds number ($Re_\lambda \geq 300 - 500$). This is consistent with the original K41 theory! But let's forget about this range of high Reynolds number and focus on the regime with $Re_\lambda$ below this critical values.

In Sec. 5.2.2, for the low $Re_\lambda$ ($Re_\lambda < 300$), we found that $\frac{\left(\underline{\varepsilon}_f\right)^2}{\underline{\left(\varepsilon^2_{inst}\right)}_f}$, i.e., the Favre version of $\frac{\varepsilon^{s2}}{\underline{\left(\varepsilon^{s}_{inst}{}^2\right)}}$ scales as $Re_\lambda^{-0.28}$ (see Fig.5.13) using the DNS data on the central plane of the reacting jets away from the mean shear. Further, using a turbulent Reynolds number defined as $Re = u_{rms}L/\nu$ with $u_{rms} = \sqrt{2\,TKE}$ and $L$ the initial width of the fuel jet in the current DNS databases (consistent with the definition of Reynolds number in [32]), we found that $\frac{\left(\underline{\varepsilon}_f\right)^2}{\underline{\left(\varepsilon^2_{inst}\right)}_f}$ agrees well with the theoretical prediction of Yakhot [36] (see Fig.5.14). The new scaling is $Re^{0.152}$. Note that this scaling shows that $\frac{\left(\underline{\varepsilon}_f\right)^2}{\underline{\left(\varepsilon^2_{inst}\right)}_f} \propto u_{rms}$. More importantly, we could not find a noticeable trend across the jet, i.e., crossing the turbulent region to the laminar co flow stream, versus the Reynolds number (see Fig.5.18). It seems that the effect of the external intermittency is so high that it affects the statistics even when they are calculated based on only turbulent zones. For more discussion the reader is referred to Sec.5.2.2. It seems that much more study is needed on this topic. Although there is a very little hope that one can find a scaling across the shear, it is interesting to start the study on variable density flows following the previous studies on constant density homogeneous shear flows. This will be more discussed in the conclusion section. So let's keep on using the ideal assumption of HIT (away from the maximum mean gradient) where the reactive data already shown to follow the non-reactive HIT data and the theoretical formula. Also, let's forget about the perfect power law behavior of $\frac{\left(\underline{\varepsilon}_f\right)^2}{\underline{\left(\varepsilon^2_{inst}\right)}_f}$ with respect to the large scale Reynolds number $Re$ and stick to the $Re_\lambda$ scaling. Also, consider that the scalings found in Sec. 5.2.2 are for the fluctuations of the dissipation with respect to the mean. For LES, an extension of the current work is required to study the intermittency scalings in the sub-grid scales. In the sub-grid, $\left(\varepsilon_{\nu,SGS}\right)^2$ can be considered as $\left(\underline{\varepsilon}_f\right)^2$ and the local sub-grid dissipation should be calculated using high-passed filtered velocity gradients. This requires a DNS database with high resolution $\kappa_{max}\underline{\eta} \gg 1$. This will be further discussed in the conclusions and future works chapter.

From the above discussion, the simplest model which can be proposed is the correction of M2005 or L2014, i.e., Eq. 3.57. The new model reads:

$$\begin{aligned}\gamma^* = \gamma_{int} &= \left(\frac{u^*}{u'}\right)^{2\times\frac{0.28}{1}} \\ &\propto Re_\lambda^{-1\times\frac{0.28}{1}} \\ &\propto \left(\frac{L^*}{L'}\right)^{\frac{2}{3}\frac{0.28}{1}} = \left(\frac{L^*}{L'}\right)^{3-2.81}\end{aligned} \tag{3.58}$$

In the above model $\gamma^*_{RANS}$ or $\gamma^*_{LES}$ can be calculated. For RANS, $u' = \sqrt{\frac{2}{3}\overline{k}_f}$ and for LES, $u' = U^{SGS} = \sqrt{\frac{2}{3}k_{SGS}}$. For RANS, $u^*$ can be either Eq. 3.16 or Eq. 3.20 and for LES Eq. 3.27 or Eq. 3.25. The coefficient can be calculated in different ways as discussed in Sec.3.2.3. Interestingly, the last term in the above formula gives a fractal dimension ($D_3 = 2.81$) which is very similar to the previously used ones [115, 116], although we reached this value from a different way.

### 3.2.5 Residence Time in Fine Structures

The link of the cascade model with combustion modeling is through the hypothesis that combustion mainly takes place in the intermittent and highly dissipative regions or the fine structures [13]. The velocity and the length scales of these structures were already evaluated by the EDC model. From these scales, one can define the mass transfer rate between the dissipative structures (fine structures) and the surrounding per unit of mass of the fine structures:

$$\dot{m}^* \equiv 2\frac{u^*}{L^*}, \tag{3.59}$$

and the time scale of the fine structures is defined as:

$$\tau^* \equiv \frac{1}{\dot{m}^*}. \tag{3.60}$$

On the other hand, the mass transfer between the dissipative structures (fine structures) and the surrounding per unit of total mass will be:

$$\dot{m} \equiv \dot{m}^*\gamma^*, \tag{3.61}$$

where depending on the model used in RANS or LES or Magnussen/Fureby or Ertesvag versions, $L^*$ and $u^*$ can be replaced by Eq. 3.16, Eq. 3.20, Eq. 3.25, or Eq. 3.27, respectively. Further, $\gamma^*_{RANS}$ or $\gamma^*_{LES}$ can be calculated from the discussions in Sec. 3.2.4 which finally results in $\dot{m}^*_{RANS}$ or $\dot{m}^*_{LES}$. The coefficients in each model can be evaluated by either the experimental values (in non-reactive flows) of RANS model or the newly theoretical derivations discussed before. The factor of 2 in Eq. 3.59 stems from the original Magnussen theory which has been used in all the subsequent works, e.g., [15, 100, 101]. Magnussen stated that this definition is "on the basis of simple geometrical considerations". Although it may need to be re-examined in future works, we keep using the current definition in Eq. 3.59 with the same factor of 2.

If the fine structure regions are regarded as 0D reactors (say PSRs or batch reactors), the time scale introduced in Eq. 3.60 can be seen as the residence time of scalars inside these reactors. The ODE system governing the reactors is considered to be the batch reactor one [95]:

$$\frac{dY_i}{dt} = \frac{W_k}{\rho_{mix}}\dot{\omega}_k \tag{3.62a}$$

$$\frac{dT}{dt} = \frac{1}{\rho_{mix}cp_{mix}}\dot{Q} \tag{3.62b}$$

$$\frac{dp}{dt} = 0 \tag{3.62c}$$

with $Y_i$ the mass fraction of species, $\rho_{mix}$ and $cp_{mix}$ the density and heat capacity of the mixture of species, respectively. $\dot{\omega}_k$ and $\dot{Q}$ were defined in Eq. 2.97 and Eq. 2.98, respectively. As can be seen, the ODE system represents the adiabatic batch reactor with a constant volume. Depending on the RANS or LES versions of the model, the initial value of the ODE system and the density and heat capacity of the mixture can be the averaged or the filtered quantities. OpenSMOKE++ [95] will be used to solve the stiff ODE system in the *a priori* DNS analysis adopted in the next chapters over a residence time defined by Eq. 3.60. This mimics the conditions applied in LES. The evolution of chemical species by set of Eq. 3.62 results in the final averaged or filtered net formation rate of species inside each computational cell:

$$\underline{\dot{\omega}_k} = \mathcal{I}_{RANS}\left(\dot{\omega}^*(\underline{\boldsymbol{\varphi}}_f)\right) = \frac{1}{(1-\gamma^*_{RANS})}\frac{\underline{\rho}_{mix}\gamma^*_{RANS}\left(Y_i^F - Y_i^0\right)}{\tau^*_{RANS}} \tag{3.63a}$$

$$\overline{\dot{\omega}_k} = \mathcal{I}_{LES}\left(\dot{\omega}^*(\overline{\boldsymbol{\varphi}}^f)\right) = \frac{1}{(1-\gamma^*_{LES})}\frac{\overline{\rho}_{mix}\gamma^*_{LES}\left(Y_i^F - Y_i^0\right)}{\tau^*_{LES}}, \tag{3.63b}$$

where $Y_i^0$ and $Y_i^F$ are input and outputs of Eq. 3.62. For RANS $Y_i^0 = \underline{Y_i}_f$ and for LES $Y_i^0 = \overline{Y_i}^f$. These were the final links which made the EDC a combustion model.

The way the theory is implemented (i.e. using PFR or batch reactors as in Eq. 3.63 ), means that the mean/filtered chemical state evolves via a linear relaxation process, typical for mixing, towards a reacted state which would be reached by a nonlinear reaction process after a time scale $\tau^*$ [117]. $\tau^*$ is defined in Eq. 3.60. This imposes a constraint on the value of $\gamma^*$ as [117]:

$$\frac{\frac{\tau^*}{1-\gamma^*}}{\dot{m}} = \frac{\gamma^*}{1-\gamma^*} < 1, \tag{3.64}$$

which results in a constraint of:

$$\gamma^* < \gamma^*_{threshold} = 0.5. \tag{3.65}$$

### 3.2.6 Summary

In this section, i.e, Sec. 3.2, the EDC model is discussed. EDC is a model to account for un-closed species source term in FR turbulent combustion modelling. As can be seen in the EDC formula set 3.63, the time scale of final dissipative fine structures, $\tau^*$, and also the internal intermittency factor, $\gamma^*$ is required in the model. The first quantity can be derived from the step-wise turbulence cascade while $\gamma^*$ is a physical quantity corresponds to the normalized fluctuation of TKE dissipation rate. Due to using proportionality relations in the model developments, two proportionality coefficients, namely $CD_1$, and $CD_2$ remains in the final EDC model. In the original EDC models, the conventional $CD_1 = 0.135$, and $CD_2 = 0.5$ are used. In this section a relation, viz. $CD_2 \approx 135.7CD_1^2$ was derived which reduced the degree of freedoms from two to one. Moreover, a new Taylor Reynolds number scaling is used for $\gamma^*$. The new scaling is a direct observation of the scaling of flatness of fluctuative velocity gradients in reactive jets which has been discussed in Sec. 5.2.2.

The two above modifications along with a new proposal to calculate $CD_1$ result in different new EDC models.

In Table3.1 a summary of the proposed and existing EDC combustion models which can be used in RANS codes are presented.

In Table3.2 a summary of the proposed and existing EDC combustion models which can be used in LES codes are presented.

Note that both **EDC-L-OF** and **EDC-L-N** does not have any coefficient in the model since $\zeta$ and $C_\varepsilon$ will be canceled out in the model derivations.

Note that **EDC-L-LyN**$_{\mathrm{C}}$ or **EDC-L-N**$_{\mathrm{G}}$**LyN**$_{\mathrm{C}}$ models in Table3.2 can be used both in dynamic or non-dynamic modes. The non-dynamic mode makes use of constant $C_\varepsilon = 1.048$. In the dynamic version, $C_\varepsilon$ can be calculated dynamically as was discussed in the last paragraph of Sec.3.2.3.

The proposed models for RANS and LES applications must be verified in RANS and LES of real burners or *a posteriori* analysis of current DNS databases. However, this will be the topic of the future works and for the current thesis no RANS or LES has been carried out.

In Table3.3 a summary of the proposed and existing EDC combustion models which were used in the *a priori* DNS analysis in Sec.5.4.1 are presented.

The difference between the models in Table3.3 and Table3.2 is that in the former $\varepsilon_{\nu,SGS}$ has not been replaced by Eq. 3.26. $\varepsilon_{\nu,SGS}$ will be directly computed from DNS databases by its exact definition in Eq. 2.134 for the *a priori* DNS analysis of SGS combustion models.

Note that the constraint in Eq. 3.65, imposes a minimum required Taylor Reynolds number based on sub-grid quantities, viz. $Re_{\lambda,SGS} = \dfrac{k_{SGS}}{\overline{\nu}^{f\,1/2}{\varepsilon_{\nu,SGS}}^{1/2}}$, for each model. If the $Re_{\lambda,SGS}$ of a computational cell is below the threshold, $\gamma^*$ will be saturated and posses the value of 0.5. Then the difference between the results of each model is only because of the difference in the modeled residence time, $\tau^*$, (or mass flow rate, i.e. $\dot{m}^*$).

For the *a priori* analysis using the values of the coefficients of each model in Table 3.3, the thresholds for Taylor Reynolds number are obtained which reported in Table 3.4.

**Table 3.1:** *Summary of the RANS-EDC combustion models applicable to RANS codes. In the table* **R** *stands for* "RANS", **O** *stands for* "O*riginal*", **M** *stands for* "Magnussen", **E** *stands for* "Ertesvag", $\mathbf{N_G}$ *stands for* "New $\gamma^*$", $\mathbf{N_C}$ *stands for* "New C*oefficient*"

| **Model** | $\gamma^*$ | $\dot{\mathbf{m}}^*$ | $\mathbf{CD_1}$ | $\mathbf{CD_2}$ | $\zeta$ |
|---|---|---|---|---|---|
| **EDC-R-OM** | | | | | |
| (Magnussen [13]) | $\left(\frac{45}{64\zeta^2}\right)^{3/4}\left(\frac{\underline{\nu}_f\underline{\varepsilon}_f}{\underline{k}_f{}^2}\right)^{3/4}$ | $\frac{1}{2.23\zeta}\left(\frac{\underline{\varepsilon}_f}{\underline{\nu}_f}\right)^{1/2}$ | – | – | 0.18 |
| **EDC-R-N$_\mathrm{G}$M** | | | | | |
| (Present work) | $\left(\frac{45}{64\zeta^2}\right)^{0.14}\left(\frac{\underline{\nu}_f\underline{\varepsilon}_f}{\underline{k}_f{}^2}\right)^{0.14}$ | $\frac{1}{2.23\zeta}\left(\frac{\underline{\varepsilon}_f}{\underline{\nu}_f}\right)^{1/2}$ | – | – | 0.18 |
| **EDC-R-OE** | | | | | |
| (Ertesvag [15]) | $\left(\frac{3CD_2}{4CD_1^2}\right)^{3/4}\left(\frac{\underline{\nu}_f\underline{\varepsilon}_f}{\underline{k}_f{}^2}\right)^{3/4}$ | $\left(\frac{3}{CD_2}\right)^{1/2}\left(\frac{\underline{\varepsilon}_f}{\underline{\nu}_f}\right)^{1/2}$ | 0.135 | 0.5 | – |
| **EDC-R-N$_\mathrm{G}$E** | | | | | |
| (Present work) | $\left(\frac{3CD_2}{4CD_1^2}\right)^{0.14}\left(\frac{\underline{\nu}_f\underline{\varepsilon}_f}{\underline{k}_f{}^2}\right)^{0.14}$ | $\left(\frac{3}{CD_2}\right)^{1/2}\left(\frac{\underline{\varepsilon}_f}{\underline{\nu}_f}\right)^{1/2}$ | 0.135 | 0.5 | – |
| **EDC-R-EN$_\mathrm{C}$** | | | | | |
| (Present work) | $32.04\left(\frac{\underline{\nu}_f\underline{\varepsilon}_f}{\underline{k}_f{}^2}\right)^{3/4}$ | $\left(\frac{3}{135.7CD_1^2}\right)^{1/2}\left(\frac{\underline{\varepsilon}_f}{\underline{\nu}_f}\right)^{1/2}$ | 0.135 | – | – |
| **EDC-R-N$_\mathrm{G}$EN$_\mathrm{C}$** | | | | | |
| (Present work) | $1.91\left(\frac{\underline{\nu}_f\underline{\varepsilon}_f}{\underline{k}_f{}^2}\right)^{0.14}$ | $\left(\frac{3}{135.7CD_1^2}\right)^{1/2}\left(\frac{\underline{\varepsilon}_f}{\underline{\nu}_f}\right)^{1/2}$ | 0.135 | – | – |

**Table 3.2:** *Summary of the LES-EDC combustion models applicable to LES codes. In the table* **L** *stands for* "LES", **O** *stands for* "O*riginal*", **F** *stands for* "Fureby", **Ly** *stands for* "Lysenco", $\mathbf{N_G}$ *stands for* "New $\gamma^*$", $\mathbf{N_C}$ *stands for* "New C*oefficient*"

| **Model** | $\gamma^*$ | $\dot{\mathbf{m}}^*$ | $\mathbf{CD_1}$ | $\mathbf{CD_2}$ | $\mathbf{C}_\varepsilon$ |
|---|---|---|---|---|---|
| **EDC-L-OF** | | | | | |
| (Fureby [91,96]) | $1.865\left(\frac{\overline{\nu}^f}{\Delta {k_{SGS}}^{0.5}}\right)^{3/4}$ | $0.809\left(\frac{{k_{SGS}}^{3/2}}{\Delta\overline{\nu}^f}\right)^{1/2}$ | – | – | – |
| **EDC-L-N$_G$F** | | | | | |
| (Present work) | $1.06\left(\frac{\overline{\nu}^f}{\Delta {k_{SGS}}^{0.5}}\right)^{0.14}$ | $0.809\left(\frac{{k_{SGS}}^{3/2}}{\Delta\overline{\nu}^f}\right)^{1/2}$ | – | – | – |
| **EDC-L-OLy** | | | | | |
| (Lysenco [102]) | $\left(\frac{3CD_2C_\varepsilon}{4CD_1^2}\right)^{1/2}\left(\frac{\overline{\nu}^f}{\Delta {k_{SGS}}^{0.5}}\right)^{1/2}$ | $\left(\frac{3C_\varepsilon}{CD_2}\right)^{1/2}\left(\frac{{k_{SGS}}^{3/2}}{\Delta\overline{\nu}^f}\right)^{1/2}$ | 0.135 | 0.5 | 1.048 |
| **EDC-L-N$_G$Ly** | | | | | |
| (Present work) | $\left(\frac{3CD_2C_\varepsilon}{4CD_1^2}\right)^{0.14}\left(\frac{\overline{\nu}^f}{\Delta {k_{SGS}}^{0.5}}\right)^{0.14}$ | $\left(\frac{3C_\varepsilon}{CD_2}\right)^{1/2}\left(\frac{{k_{SGS}}^{3/2}}{\Delta\overline{\nu}^f}\right)^{1/2}$ | 0.135 | 0.5 | 1.048 |
| **EDC-L-LyN$_C$** | | | | | |
| (Present work) | $\left(\frac{407.1C_\varepsilon}{4}\right)^{1/2}\left(\frac{\overline{\nu}^f}{\Delta {k_{SGS}}^{0.5}}\right)^{1/2}$ | $\left(\frac{2}{135.7C_\varepsilon}\right)^{1/2}\left(\frac{{k_{SGS}}^{3/2}}{\Delta\overline{\nu}^f}\right)^{1/2}$ | – | – | 1.048 or Dyn. |
| **EDC-L-N$_G$LyN$_C$** | | | | | |
| (Present work) | $\left(\frac{407.1C_\varepsilon}{4}\right)^{0.14}\left(\frac{\overline{\nu}^f}{\Delta {k_{SGS}}^{0.5}}\right)^{0.14}$ | $\left(\frac{2}{135.7C_\varepsilon}\right)^{1/2}\left(\frac{{k_{SGS}}^{3/2}}{\Delta\overline{\nu}^f}\right)^{1/2}$ | – | – | 1.048 or Dyn. |

**Table 3.3:** *Summary of the LES-EDC combustion models applicable to an a priori DNS analysis. In the table* **L** *stands for* "LES", **O** *stands for* "O*riginal*", **F** *stands for* "Fureby", **Ly** *stands for* "Lysenco", $\mathbf{N_G}$ *stands for* "New $\gamma^*$", $\mathbf{N_C}$ *stands for* "New C*oefficient*". $\zeta_{LES}$ in **EDC-L-OF** and **EDC-L-N$_G$F** is $\zeta_{LES} = 0.566$ (see Eq. 3.31).

| **Model** | $\gamma^*$ | $\dot{\mathbf{m}}^*$ | $\mathbf{CD_1}$ | $\mathbf{CD_2}$ |
|---|---|---|---|---|
| **EDC-L-OF** (Fureby [91, 96]) | $\left(\frac{45}{64\zeta^2}\right)^{3/4}\left(\frac{\overline{\nu}^f\varepsilon_{\nu,SGS}}{{k_{SGS}}^2}\right)^{3/4}$ | $\left(\frac{1}{25\zeta^4}\right)^{1/4}\left(\frac{\varepsilon_{\nu,SGS}}{\overline{\nu}^f}\right)^{1/2}$ | – | – |
| **EDC-L-N$_G$F** (Present work) | $\left(\frac{45}{64\zeta^2}\right)^{0.14}\left(\frac{\overline{\nu}^f\varepsilon_{\nu,SGS}}{{k_{SGS}}^2}\right)^{0.14}$ | $\left(\frac{1}{25\zeta^4}\right)^{1/4}\left(\frac{\varepsilon_{\nu,SGS}}{\overline{\nu}^f}\right)^{1/2}$ | – | – |
| **EDC-L-OLy** (Lysenco [102]) | $\left(\frac{3CD_2}{4CD_1^2}\right)^{1/2}\left(\frac{\overline{\nu}^f\varepsilon_{\nu,SGS}}{{k_{SGS}}^2}\right)^{1/2}$ | $\left(\frac{3}{CD_2}\right)^{1/2}\left(\frac{\varepsilon_{\nu,SGS}}{\overline{\nu}^f}\right)^{1/2}$ | 0.135 | 0.5 |
| **EDC-L-N$_G$Ly** (Present work) | $\left(\frac{3CD_2}{4CD_1^2}\right)^{0.14}\left(\frac{\overline{\nu}^f\varepsilon_{\nu,SGS}}{{k_{SGS}}^2}\right)^{0.14}$ | $\left(\frac{3}{CD_2}\right)^{1/2}\left(\frac{\varepsilon_{\nu,SGS}}{\overline{\nu}^f}\right)^{1/2}$ | 0.135 | 0.5 |
| **EDC-L-LyN$_C$**(Present work) | $10.09\left(\frac{\overline{\nu}^f\varepsilon_{\nu,SGS}}{{k_{SGS}}^2}\right)^{1/2}$ | $\left(\frac{3}{135.7CD_1^2}\right)^{1/2}\left(\frac{\varepsilon_{\nu,SGS}}{\overline{\nu}^f}\right)^{1/2}$ | 0.135 or 1.28 | – |
| **EDC-L-N$_G$LyN$_C$** (Present work) | $1.91\left(\frac{\overline{\nu}^f\varepsilon_{\nu,SGS}}{{k_{SGS}}^2}\right)^{0.14}$ | $\left(\frac{3}{135.7CD_1^2}\right)^{1/2}\left(\frac{\varepsilon_{\nu,SGS}}{\overline{\nu}^f}\right)^{1/2}$ | 0.135 or 1.28 | – |

**Table 3.4:** *The threshold of Taylor Reynolds number for different models assessed in an a priori DNS analysis below which $\gamma^*$ is saturated and is equal to 0.5. In the table* **L** *stands for* "LES", **O** *stands for* "O*riginal*", **F** *stands for* "Fureby", **E** *stands for* "Ertesvag", $\mathbf{N_G}$ *stands for* "New $\gamma^*$", $\mathbf{N_C}$ *stands for* "New C*oefficient*". $Re_\lambda$ is calculated based on sub-grid quantities as $Re_{\lambda,SGS} = \frac{k_{SGS}}{\overline{\nu}^{f\,1/2}\varepsilon_{\nu,SGS}{}^{1/2}}$.

| Model | Threshold |
|---|---|
| **EDC-L-OF** (Fureby [91, 96]) | $Re_{\lambda,SGS} \geq 2.3$ |
| **EDC-L-N$_{\mathrm{G}}$F** (Present work) | $Re_{\lambda,SGS} \geq 17.6$ |
| **EDC-L-OLy** (Lysenco [102]) | $Re_{\lambda,SGS} \geq 9$ |
| **EDC-L-N$_{\mathrm{G}}$Ly** (Present work) | $Re_{\lambda,SGS} \geq 54$ |
| **EDC-L-LyN$_{\mathrm{C}}$** (Present work) | $Re_{\lambda,SGS} \geq 16$ |
| **EDC-L-N$_{\mathrm{G}}$LyN$_{\mathrm{C}}$** (Present work) | $Re_{\lambda,SGS} \geq 120$ |

## 3.3 Non-Dynamic Scale Similarity Combustion Models for LES

In their general form, SS models are type of soft deconvolution methods [118], which use the first order approximation to reconstruct the exact field based on filtered fields. More advanced deconvolution methods are still under development for reactive flow applications [49, 119]. First, Bardina et al. [120] proposed a SS model for SGS stress tensor. Thereby, the exact velocity field in the SGS tensor is replaced by its "grid filtered" counterpart resulting in "double grid filtered" quantities which are exploited to model SGS stress tensor. In other words, the SGS stress tensor is replaced by the modified Leonard stress in Germano's decomposition [121]. Liu et al. [122], based on decomposition of the velocity field in logarithmic bands, proposed to use "test grid filtered" instead of "double grid filtered" quantities in the definition of SGS stress. The ability of SS models in capturing the locations where the contribution of SGS stress field is high was proven in many studies using both *a priori* analysis based on DNS data (e.g. [120]), as well as experimental data (e.g. [122]). However, the drawback of the original models was their slight dissipative character. This can be explained by considering that SS models are actually low order soft deconvolution models. The issue comes from the fact that in LES the information lost by inherent grid filter is unrecoverable [77]. So each soft deconvolution model needs a complementary model to handle the lost data. This is the idea behind "mixed models" which take the advantages of both SS models and eddy viscosity type models. In the context of LES of reactive flows, DesJardin and Frankel [17] proposed to use SS idea to close the filtered production/consumption rates, $\overline{\dot{\omega}}_k(\boldsymbol{\varphi})$. The first non-dynamic scale similarity model for $\overline{\dot{\omega}}_k(\boldsymbol{\varphi})$, originally called SSRRRM (hereafter denoted as model A), was proposed by Desjardin and Frankel [17]. According to that model:

$$\overline{\dot{\omega}}^A(\boldsymbol{\varphi}) = \dot{\omega}(\overline{\boldsymbol{\varphi}}^f) + C_A^{\overline{\Delta}}\mathcal{L}_{\dot{\omega}^A}, \tag{3.66}$$

$$\mathcal{L}_{\dot{\omega}^A} = \overline{\dot{\omega}}(\overline{\boldsymbol{\varphi}}^f) - \dot{\omega}(\overline{\overline{\boldsymbol{\varphi}}}^f), \tag{3.67}$$

where $C_A^{\overline{\Delta}}$ is a coefficient to be evaluated dynamically according to the approach described in Sec. 3.4 and set equal to 1 in the case of the non-dynamic approach. $\mathcal{L}_{\dot{\omega}^A}$ is the residual field representing the SGS effects. If one filters Eq. 3.66 and uses the same decomposition for the residual field as in Eq. 3.66, it ends in Eq. 3.67 for the residual field in the first filtering level. As it can be seen, the "double grid Favre filtered" field $\overline{\overline{\boldsymbol{\varphi}}}^f$ is introduced. The way to compute this type of fields using explicit filters and OpenSMOKE++ open source library [95] has been explained in [123] and also in detail in Appendix A. Note that $\overline{(.)}$ and $\overline{(.)}$ are virtually the same filters with the same filter widths, however, since the numerical implementations are different, different notations have been used (see Appendix A for more details).

The second model, originally called SSFRRM [17] and hereafter denoted as model B, uses the filtered formation rate of filtered fields instead of resolved ones in the first decomposition step, which results in equation Eq. 3.68:

$$\overline{\dot{\omega}}^B(\boldsymbol{\varphi}) = \overline{\dot{\omega}}(\overline{\boldsymbol{\varphi}}^f) + C_B^{\overline{\Delta}}\mathcal{L}_{\dot{\omega}^B}, \tag{3.68}$$

where $C_B^{\overline{\Delta}}$ is the coefficient of similarity which is set to 1 for model B, to be evaluated dynamically in model DB which will be introduced in Sect. 3.4. The same procedure

previously described is carried out to find an expression for the residual field $\mathcal{L}_{\dot{\omega}^B}$, which ends in Eq. 3.69:

$$\mathcal{L}_{\dot{\omega}^B} = \overline{\overline{\dot{\omega}}}(\overline{\boldsymbol{\varphi}}^f) - \overline{\overline{\dot{\omega}}}(\overline{\overline{\boldsymbol{\varphi}}}^f), \tag{3.69}$$

where the "double grid Favre filtered" field is introduced for both original fields and the formation rates.

Liu et al. [122] proposed to use a filter (say $\widehat{\Delta}$) larger than the grid filter ($\overline{\Delta}$) in the similarity model formulation of the SGS stress field. By the extension of this idea to the formation rates of species, a non-dynamic model C is introduced:

$$\overline{\dot{\omega}}^C(\boldsymbol{\varphi}) = \dot{\omega}(\overline{\boldsymbol{\varphi}}^f) + C_C^{\overline{\Delta}} \mathcal{L}_{\dot{\omega}^C}, \tag{3.70}$$

$$\mathcal{L}_{\dot{\omega}^C} = \widehat{\dot{\omega}}(\overline{\boldsymbol{\varphi}}^f) - \dot{\omega}(\widehat{\overline{\boldsymbol{\varphi}}}^f), \tag{3.71}$$

where $\widehat{\Delta} = 2\overline{\Delta}$ in this study. The non-dynamic similarity coefficient ($C_C^{\overline{\Delta}}$) is set equal to 1 and will be evaluated dynamically for model DC in Sect. 3.4.

The non-dynamic models will be assessed in an a priori DNS analysis in Sec. 5.4.2.

## 3.4 New Dynamic Scale Similarity Models for LES

### 3.4.1 DA: Dynamic formulation of SSRRRM (model A)

To derive the dynamic versions of the previous models, the generalized Germano's identity [87] can be used. A non-linear operator $\mathcal{N}(\boldsymbol{\varphi})$ is defined, where in general $\mathcal{N}(\boldsymbol{\varphi}) \neq \mathcal{N}(\overline{\boldsymbol{\varphi}})$. The difference between these two is the contribution of the sub-grid scales [124]. One may try to write the difference in additive form, viz. $\overline{\mathcal{N}}(\boldsymbol{\varphi}) = \mathcal{N}(\overline{\boldsymbol{\varphi}}) + \mathcal{M}_F$, where the "model" $\mathcal{M}_F$ can be of any type and the subscript $F$ is used to remark that the model is defined at the $F$ filter level, $\overline{(.)}$, with cutoff $\overline{\Delta}$. A second filter called "test filter", at $G$ level, with cutoff larger than $F$ level, viz. $\widehat{\Delta} > \overline{\Delta}$, is introduced, which is denoted by $\widehat{(.)}$. The Favre filtered version of a quantity again is marked by $f$ and defined as $\widehat{\boldsymbol{\varphi}}^f = \widehat{\rho\boldsymbol{\varphi}}/\widehat{\rho}$. If one filters the non-linear operator using the test filter, the operator at the $FG$ level is derived, viz. $\widehat{\overline{\mathcal{N}}}(\boldsymbol{\varphi}) = \widehat{\mathcal{N}}(\overline{\boldsymbol{\varphi}}) + \widehat{\mathcal{M}_F}$. On the other hand, the non-linear operator can be directly defined at the $FG$ level, viz. $\widehat{\overline{\mathcal{N}}}(\boldsymbol{\varphi}) = \mathcal{N}(\widehat{\overline{\boldsymbol{\varphi}}}) + \mathcal{M}_{FG}$. The generalized Germano's identity is defined by equating the two expressions of $\mathcal{N}(\boldsymbol{\varphi})$ at the $FG$ level, viz. $\widehat{\mathcal{N}}(\overline{\boldsymbol{\varphi}}) + \widehat{\mathcal{M}_F} = \mathcal{N}(\widehat{\overline{\boldsymbol{\varphi}}}) + \mathcal{M}_{FG}$ [124]. The identity can be used to evaluate the coefficients in the "model" part of the filtered operator. Here it should be noted that $\mathcal{M}_{FG}$ is by definition the scale similarity model defined at the $FG$ level [125]. Some authors proposed to use the information at the $F$ level instead of $FG$ level to reduce model complexity [18, 126]. In the context of scale similarity models in reactive flows, $\mathcal{N}(\boldsymbol{\varphi}) = \dot{\omega}(\boldsymbol{\varphi})$ and $\mathcal{M}_F = C\mathcal{L}_{\dot{\omega}}$ defined above. Replacing the definitions in the generalized Germano's identity, dynamic models will be derived.

The dynamic version of model A will be named DA and categorized with respect to the filtering level to be used. So, DA1 will refer to the use of $FG$ level while DA2 to the $F$ level. To derive $\dot{\omega}^{DA1}$, we start from writing the Germano's identity explained above:

$$\begin{aligned} &\widehat{\dot{\omega}}(\overline{\boldsymbol{\varphi}}^f) + C^{\overline{\Delta}}_{DA1}\left(\widehat{\overline{\dot{\omega}}}(\overline{\boldsymbol{\varphi}}^f) - \widehat{\dot{\omega}}(\overline{\overline{\boldsymbol{\varphi}}}^f)\right) \\ &= \dot{\omega}(\widehat{\overline{\boldsymbol{\varphi}}}^f) + C^{\widehat{\Delta}}_{DA1}\left(\widehat{\overline{\dot{\omega}}}(\widehat{\overline{\boldsymbol{\varphi}}}^f) - \dot{\omega}(\widehat{\overline{\overline{\boldsymbol{\varphi}}}}^f)\right). \end{aligned} \tag{3.72}$$

In Eq. 3.72, the second term on the left hand side is the residual field filtered using the test filter ($\widehat{\mathcal{L}}_{\dot{\omega}^A}$) and the second term on the right hand side is the scale similarity model A defined at the $FG$ level ($\Lambda_{\mathrm{A1}}$). The coefficient in each level is also marked by the corresponding filter width. It should be mentioned that $C^{\overline{\Delta}}_{DA1}$ is actually $\widehat{C}^{\overline{\Delta}}_{DA1}$ so in Eq. 3.72 and also all the following applications of Germano's identity it is implicitly assumed that $C^{\overline{\Delta}} = \widehat{C}^{\overline{\Delta}}$. The effect of this simplification might be quite strong and it can be a topic of the future studies. Rearranging equation Eq. 3.72 leads to:

$$\begin{aligned} &\widehat{\dot{\omega}}(\overline{\boldsymbol{\varphi}}^f) - \dot{\omega}(\widehat{\overline{\boldsymbol{\varphi}}}^f) \\ &= C^{\overline{\Delta}}_{DA1}\left(\frac{C^{\widehat{\Delta}}_{DA1}}{C^{\overline{\Delta}}_{DA1}}\left(\widehat{\overline{\dot{\omega}}}(\widehat{\overline{\boldsymbol{\varphi}}}^f) - \dot{\omega}(\widehat{\overline{\overline{\boldsymbol{\varphi}}}}^f)\right) - \left(\widehat{\overline{\dot{\omega}}}(\overline{\boldsymbol{\varphi}}^f) - \widehat{\dot{\omega}}(\overline{\overline{\boldsymbol{\varphi}}}^f)\right)\right), \end{aligned} \tag{3.73}$$

which can be written in a compact form as:

$$\Upsilon_{\mathrm{A}}{=}C^{\overline{\Delta}}_{DA1}(\mathcal{X}_{A1}), \tag{3.74}$$

where $\Upsilon_{\mathrm{A}}$ is the resolved covariance:

$$\Upsilon_{\mathrm{A}} = \widehat{\dot{\omega}}(\overline{\boldsymbol{\varphi}}^f) - \dot{\omega}(\widehat{\overline{\boldsymbol{\varphi}}}^f), \tag{3.75}$$

and $\mathcal{X}_{A1}$ is

$$\begin{aligned}\mathcal{X}_{A1} &= \frac{C^{\widehat{\Delta}}_{DA1}}{C^{\overline{\Delta}}_{DA1}}\left(\widehat{\overline{\dot{\omega}}}(\widehat{\overline{\boldsymbol{\varphi}}}^f) - \dot{\omega}(\widehat{\overline{\overline{\boldsymbol{\varphi}}}}^f)\right) - \left(\widehat{\overline{\dot{\omega}}}(\overline{\boldsymbol{\varphi}}^f) - \widehat{\dot{\omega}}(\overline{\overline{\boldsymbol{\varphi}}}^f)\right)\\ &= \frac{C^{\widehat{\Delta}}_{DA1}}{C^{\overline{\Delta}}_{DA1}}\Lambda_{\mathrm{A1}} - \widehat{\mathcal{L}}_{\dot{\omega}^A}.\end{aligned} \tag{3.76}$$

Thus:

$$\overline{\dot{\omega}}^{DA1} = \dot{\omega}(\overline{\boldsymbol{\varphi}}^f) + C^{\overline{\Delta}}_{DA1}\,\mathcal{L}_{\dot{\omega}^A}. \tag{3.77}$$

It should be mentioned that in Eq. 3.76, $\Lambda_{\mathrm{A1}}$ is a similarity closure for $FG$ level based on the fields defined at $FG$ level. This is the mathematically consistent formulation suggested by Vreman [125] in computations of SGS stress fields using SS models. In this paper, it is applied to non-linear chemical formation rates to see its effects.

To derive $\dot{\omega}^{DA2}$, one needs to define the similarity model in Eq. 3.73 at the $FG$ level using the fields at $F$ level. It is inspired by the work of Zang et. al. [126] for SGS stress field. It reads:

$$\Upsilon_{\mathrm{A}} = C^{\overline{\Delta}}_{DA2}\left(\frac{C^{\widehat{\Delta}}_{DA2}}{C^{\overline{\Delta}}_{DA2}}\left(\widehat{\overline{\dot{\omega}}}(\overline{\boldsymbol{\varphi}}^f) - \dot{\omega}(\widehat{\overline{\overline{\boldsymbol{\varphi}}}}^f)\right) - \left(\widehat{\overline{\dot{\omega}}}(\overline{\boldsymbol{\varphi}}^f) - \widehat{\dot{\omega}}(\overline{\overline{\boldsymbol{\varphi}}}^f)\right)\right), \tag{3.78}$$

which again in a compact form reads:

$$\Upsilon_{\mathrm{A}}{=}C^{\overline{\Delta}}_{DA2}(\mathcal{X}_{A2}), \tag{3.79}$$

where

$$\begin{aligned}\mathcal{X}_{A2} &= \frac{C^{\widehat{\Delta}}_{DA2}}{C^{\overline{\Delta}}_{DA2}}\left(\widehat{\overline{\dot{\omega}}}(\overline{\boldsymbol{\varphi}}^f) - \dot{\omega}(\widehat{\overline{\overline{\boldsymbol{\varphi}}}}^f)\right) - \left(\widehat{\overline{\dot{\omega}}}(\overline{\boldsymbol{\varphi}}^f) - \widehat{\dot{\omega}}(\overline{\overline{\boldsymbol{\varphi}}}^f)\right)\\ &= \frac{C^{\widehat{\Delta}}_{DA2}}{C^{\overline{\Delta}}_{DA2}}\Lambda_{\mathrm{A2}} - \widehat{\mathcal{L}}_{\dot{\omega}^A}.\end{aligned} \tag{3.80}$$

Thus:

$$\overline{\dot{\omega}}^{DA2} = \dot{\omega}(\overline{\boldsymbol{\varphi}}^f) + C^{\overline{\Delta}}_{DA2}\,\mathcal{L}_{\dot{\omega}^A}. \tag{3.81}$$

As it can be seen, the difference between $\overline{\dot{\omega}}^{DA1}$ and $\overline{\dot{\omega}}^{DA2}$ models is only in the definition of $\Lambda_{\mathrm{A}}$ in $\mathcal{X}_A$. Using scale invariance assumption between F level and FG level, i.e. $C^{\widehat{\Delta}} = C^{\overline{\Delta}}$, $\mathcal{X}_{A1}$ is simplified to:

$$\begin{aligned}\mathcal{X}_{A1} &= \left(\widehat{\overline{\dot{\omega}}}(\widehat{\overline{\boldsymbol{\varphi}}}^f) - \dot{\omega}(\widehat{\overline{\overline{\boldsymbol{\varphi}}}}^f)\right) - \left(\widehat{\overline{\dot{\omega}}}(\overline{\boldsymbol{\varphi}}^f) - \widehat{\dot{\omega}}(\overline{\overline{\boldsymbol{\varphi}}}^f)\right)\\ &= \Lambda_{\mathrm{A1}} - \widehat{\mathcal{L}}_{\dot{\omega}^A},\end{aligned} \tag{3.82}$$

and $\mathcal{X}_{A2}$ is simplified to:

$$\begin{aligned}\mathcal{X}_{A2} &= \left(\widehat{\overline{\dot{\omega}}}(\overline{\boldsymbol{\varphi}}^f) - \dot{\omega}(\widehat{\overline{\overline{\boldsymbol{\varphi}}}}^f)\right) - \left(\widehat{\overline{\dot{\omega}}}(\overline{\boldsymbol{\varphi}}^f) - \widehat{\dot{\omega}}(\overline{\overline{\boldsymbol{\varphi}}}^f)\right) \\ &= \widehat{\dot{\omega}}(\overline{\overline{\boldsymbol{\varphi}}}^f) - \dot{\omega}(\widehat{\overline{\overline{\boldsymbol{\varphi}}}}^f) \\ &= \Lambda_{\mathrm{A2}} - \widehat{\mathcal{L}}_{\dot{\omega}^A},\end{aligned} \tag{3.83}$$

which is the model derived by Jaberi and James [18]. Some issues exist in numerical implementation of $\mathcal{X}_{A1}$ in a consistent manner proposed in [122]. Indeed, $\overline{\boldsymbol{\varphi}}^f$ is computed based on DNS field, i.e., $\boldsymbol{\varphi}$ is defined on a fine DNS grid and should be sampled on a coarse grid of mesh size $\overline{\Delta} = N\Delta_{DNS}$, where $N$ is an integer defining the filter width. Further, $\widehat{\overline{\boldsymbol{\varphi}}}^f$ should be computed based solely on the $\overline{\boldsymbol{\varphi}}^f$ field and then sampled on a coarser grid of mesh size $\widehat{\Delta} = 2N\Delta_{DNS}$. Now the problem is in the evaluation of terms $\widehat{\overline{\dot{\omega}}}(\widehat{\overline{\boldsymbol{\varphi}}}^f)$ or $\widehat{\overline{\overline{\boldsymbol{\varphi}}}}^f$ which again (after two consecutive filtering at $F$ and $G$ level) needs filtering on $F$ level, which is not possible for the data defined on grid points of mesh $\widehat{\Delta} = 2N\Delta_{DNS}$. To remedy this, one has two options: i) to write the similarity model ($\Lambda_{\mathrm{A}}$) using the fields at the $F$ level instead of $FG$ level (by doing this, $\mathcal{X}_{A2}$ will be recovered); ii) to skip the sampling step after evaluation of $\widehat{\overline{\overline{\boldsymbol{\varphi}}}}^f$, which means that both $\widehat{\overline{\overline{\boldsymbol{\varphi}}}}^f$ and $\overline{\boldsymbol{\varphi}}^f$ will be defined on a grid with mesh size $\overline{\Delta} = N\Delta_{DNS}$.

### 3.4.2 DB: Dynamic formulation of SSFRRM (model B)

Following similar notations as in Sec. 3.4.1, models of type DB1 and DB2 will be obtained. Relying on Eq. 3.73 one can obtain:

$$\begin{aligned}&\widehat{\overline{\dot{\omega}}}(\overline{\boldsymbol{\varphi}}^f) - \widehat{\overline{\dot{\omega}}}(\widehat{\overline{\boldsymbol{\varphi}}}^f) = \\ &\qquad C^{\overline{\Delta}}_{DB1}\left(\frac{C^{\widehat{\Delta}}_{DB1}}{C^{\overline{\Delta}}_{DB1}}\left(\widehat{\overline{\overline{\dot{\omega}}}}(\widehat{\overline{\boldsymbol{\varphi}}}^f) - \widehat{\overline{\overline{\dot{\omega}}}}(\widehat{\overline{\overline{\boldsymbol{\varphi}}}}^f)\right) - \left(\widehat{\overline{\overline{\dot{\omega}}}}(\overline{\boldsymbol{\varphi}}^f) - \widehat{\overline{\overline{\dot{\omega}}}}(\overline{\overline{\boldsymbol{\varphi}}}^f)\right)\right),\end{aligned} \tag{3.84}$$

which can be written in a compact form as:

$$\Upsilon_{\mathrm{B}} = C^{\overline{\Delta}}_{DB1}(\mathcal{X}_{B1}), \tag{3.85}$$

where $\Upsilon_{\mathrm{B}}$ is

$$\Upsilon_{\mathrm{B}} = \widehat{\overline{\dot{\omega}}}(\overline{\boldsymbol{\varphi}}^f) - \widehat{\overline{\dot{\omega}}}(\widehat{\overline{\boldsymbol{\varphi}}}^f), \tag{3.86}$$

and $\mathcal{X}_{B1}$ is

$$\begin{aligned}\mathcal{X}_{B1} &= \frac{C^{\widehat{\Delta}}_{DB1}}{C^{\overline{\Delta}}_{DB1}}\left(\widehat{\overline{\overline{\dot{\omega}}}}(\widehat{\overline{\boldsymbol{\varphi}}}^f) - \widehat{\overline{\overline{\dot{\omega}}}}(\widehat{\overline{\overline{\boldsymbol{\varphi}}}}^f)\right) - \left(\widehat{\overline{\overline{\dot{\omega}}}}(\overline{\boldsymbol{\varphi}}^f) - \widehat{\overline{\overline{\dot{\omega}}}}(\overline{\overline{\boldsymbol{\varphi}}}^f)\right) \\ &= \frac{C^{\widehat{\Delta}}_{DB1}}{C^{\overline{\Delta}}_{DB1}}\Lambda_{\mathrm{B1}} - \widehat{\mathcal{L}}_{\dot{\omega}^B}.\end{aligned} \tag{3.87}$$

Thus:

$$\overline{\dot{\omega}}^{DB1} = \overline{\dot{\omega}}(\overline{\boldsymbol{\varphi}}^f) + C^{\overline{\Delta}}_{DB1}\,\mathcal{L}_{\dot{\omega}^B}. \tag{3.88}$$

Again, if one evaluates the similarity model at the FG level (the first term on the right hand side of Eq. 3.84) using fields at $F$ level, it results in the fourth dynamic similarity model which reads:

$$\Upsilon_{\mathrm{B}} = C^{\overline{\Delta}}_{DB2}\left(\frac{C^{\widehat{\Delta}}_{DB2}}{C^{\overline{\Delta}}_{DB2}}\left(\widehat{\overline{\dot{\omega}}}(\overline{\boldsymbol{\varphi}}^f) - \widehat{\overline{\dot{\omega}}}(\widehat{\overline{\boldsymbol{\varphi}}}^f)\right) - \left(\widehat{\overline{\dot{\omega}}}(\overline{\boldsymbol{\varphi}}^f) - \widehat{\overline{\dot{\omega}}}(\overline{\overline{\boldsymbol{\varphi}}}^f)\right)\right), \tag{3.89}$$

which again in a compact form reads:

$$\Upsilon_{\mathrm{B}}{=}C^{\overline{\Delta}}_{DB2}(\mathcal{X}_{B2}), \tag{3.90}$$

where:

$$\begin{aligned}\mathcal{X}_{B2} &= \frac{C^{\widehat{\Delta}}_{DB2}}{C^{\overline{\Delta}}_{DB2}}\left(\widehat{\overline{\dot{\omega}}}(\overline{\boldsymbol{\varphi}}^f) - \widehat{\overline{\dot{\omega}}}(\widehat{\overline{\boldsymbol{\varphi}}}^f)\right) - \left(\widehat{\overline{\dot{\omega}}}(\overline{\boldsymbol{\varphi}}^f) - \widehat{\overline{\dot{\omega}}}(\overline{\overline{\boldsymbol{\varphi}}}^f)\right)\\ &= \frac{C^{\widehat{\Delta}}_{DB2}}{C^{\overline{\Delta}}_{DB2}}\Lambda_{\mathrm{B2}} - \widehat{\mathcal{L}}_{\dot{\omega}^B}.\end{aligned} \tag{3.91}$$

Thus:

$$\overline{\dot{\omega}}^{DB2} = \overline{\dot{\omega}}(\overline{\boldsymbol{\varphi}}^f) + C^{\overline{\Delta}}_{DB2}\,\mathcal{L}_{\dot{\omega}^B}. \tag{3.92}$$

Using scale invariance assumption between F level and FG level i.e., $C^{\widehat{\Delta}} = C^{\overline{\Delta}}$, $\mathcal{X}_{B1}$ is simplified to:

$$\begin{aligned}\mathcal{X}_{B1} &= \left(\widehat{\overline{\dot{\omega}}}(\widehat{\overline{\boldsymbol{\varphi}}}^f) - \widehat{\overline{\dot{\omega}}}(\widehat{\overline{\boldsymbol{\varphi}}}^f)\right) - \left(\widehat{\overline{\dot{\omega}}}(\overline{\boldsymbol{\varphi}}^f) - \widehat{\overline{\dot{\omega}}}(\overline{\overline{\boldsymbol{\varphi}}}^f)\right)\\ &= \Lambda_{\mathrm{B1}} - \widehat{\mathcal{L}}_{\dot{\omega}^B},\end{aligned} \tag{3.93}$$

and $\mathcal{X}_{B2}$ is simplified to:

$$\begin{aligned}\mathcal{X}_{B2} &= \left(\widehat{\overline{\dot{\omega}}}(\overline{\boldsymbol{\varphi}}^f) - \widehat{\overline{\dot{\omega}}}(\widehat{\overline{\boldsymbol{\varphi}}}^f)\right) - \left(\widehat{\overline{\dot{\omega}}}(\overline{\boldsymbol{\varphi}}^f) - \widehat{\overline{\dot{\omega}}}(\overline{\overline{\boldsymbol{\varphi}}}^f)\right)\\ &= \Lambda_{\mathrm{B2}} - \widehat{\mathcal{L}}_{\dot{\omega}^B}.\end{aligned} \tag{3.94}$$

### 3.4.3 DC: Dynamic formulation of model C

The same procedure can be used to evaluate the similarity coefficient of model C dynamically. Following [127] and writing the Germano's identity for the two filter levels for model C, one finds:

$$\begin{aligned}&\widehat{\dot{\omega}}(\overline{\boldsymbol{\varphi}}^f) - \dot{\omega}(\widehat{\overline{\boldsymbol{\varphi}}}^f) =\\ &\qquad C^{\overline{\Delta}}_{DC1}\left(\frac{C^{\widehat{\Delta}}_{DC1}}{C^{\overline{\Delta}}_{DC1}}\left(\overbrace{\dot{\omega}}(\widehat{\overline{\boldsymbol{\varphi}}}^f) - \dot{\omega}(\overbrace{\widehat{\overline{\boldsymbol{\varphi}}}}^f)\right) - \left(\widehat{\dot{\omega}}(\overline{\boldsymbol{\varphi}}^f) - \widehat{\dot{\omega}}(\widehat{\overline{\boldsymbol{\varphi}}}^f)\right)\right),\end{aligned} \tag{3.95}$$

where $\overbrace{(.)}$ represents a spatial filter at scale $4\overline{\Delta}$. In a compact form:

$$\Upsilon_{\mathrm{C}}{=}C^{\overline{\Delta}}_{DC1}\mathcal{X}_{C1}, \tag{3.96}$$

where $\Upsilon_{\mathrm{C}}$ and $\mathcal{X}_{C1}$ are:

$$\Upsilon_C = \widehat{\dot{\omega}}(\overline{\boldsymbol{\varphi}}^f) - \dot{\omega}(\widehat{\overline{\boldsymbol{\varphi}}}^f), \tag{3.97}$$

$$\begin{aligned}\mathcal{X}_{C1} &= \frac{C^{\widehat{\Delta}}_{DC1}}{C^{\overline{\Delta}}_{DC1}}\left(\widehat{\dot{\omega}}(\widehat{\overline{\boldsymbol{\varphi}}}^f) - \dot{\omega}(\widehat{\overline{\boldsymbol{\varphi}}}^f)\right) - \left(\widehat{\widehat{\dot{\omega}}}(\overline{\boldsymbol{\varphi}}^f) - \widehat{\dot{\omega}}(\widehat{\overline{\boldsymbol{\varphi}}}^f)\right) \\ &= \frac{C^{\widehat{\Delta}}_{DC1}}{C^{\overline{\Delta}}_{DC1}}\Lambda_{C1} - \widehat{\mathcal{L}}_{\dot{\omega}^C}.\end{aligned} \tag{3.98}$$

It should be emphasized that $\Upsilon_C = \Upsilon_A$ for two models A and C. This is because both models decompose the non-linear term $\overline{\mathcal{N}}(\boldsymbol{\varphi})$ in a similar way, i.e., $\overline{\mathcal{N}}(\boldsymbol{\varphi}) = \mathcal{N}(\overline{\boldsymbol{\varphi}}) + \mathcal{M}_F$. The difference between the models comes from the way they treat the residual field i.e. $\mathcal{M}_F$.

Using the scale invariance assumption between F level and FG level, i.e., $C^{\widehat{\Delta}} = C^{\overline{\Delta}}$, $\mathcal{X}_{C1}$ is:

$$\begin{aligned}\mathcal{X}_{C1} &= \left(\widehat{\dot{\omega}}(\widehat{\overline{\boldsymbol{\varphi}}}^f) - \dot{\omega}(\widehat{\overline{\boldsymbol{\varphi}}}^f)\right) - \left(\widehat{\widehat{\dot{\omega}}}(\overline{\boldsymbol{\varphi}}^f) - \widehat{\dot{\omega}}(\widehat{\overline{\boldsymbol{\varphi}}}^f)\right) \\ &= \Lambda_{C1} - \widehat{\mathcal{L}}_{\dot{\omega}^C}.\end{aligned} \tag{3.99}$$

Again, if the fields at the F level are used to evaluate $\Lambda_{C1}$, the second dynamic version of model C is derived as below:

$$\begin{aligned}\mathcal{X}_{C2} &= \left(\widehat{\dot{\omega}}(\overline{\boldsymbol{\varphi}}^f) - \dot{\omega}(\widehat{\overline{\boldsymbol{\varphi}}}^f)\right) - \left(\widehat{\widehat{\dot{\omega}}}\left(\overline{\boldsymbol{\varphi}}^f\right) - \widehat{\dot{\omega}}(\widehat{\overline{\boldsymbol{\varphi}}}^f)\right) \\ &= \Lambda_{C2} - \widehat{\mathcal{L}}_{\dot{\omega}^C}.\end{aligned} \tag{3.100}$$

Thus:

$$\Upsilon_{\mathrm{C}} = C^{\overline{\Delta}}_{DC2}(\mathcal{X}_{C2}). \tag{3.101}$$

In all models above $C^{\overline{\Delta}}_{DA1}$ , $C^{\overline{\Delta}}_{DA2}$, $C^{\overline{\Delta}}_{DB1}$, $C^{\overline{\Delta}}_{DB2}$, $C^{\overline{\Delta}}_{DC1}$, and $C^{\overline{\Delta}}_{DC2}$ (in compact form $C^{\overline{\Delta}}_{Dij}$, where $i$ is A, B or C and $j$ is 1 or 2) are evaluated using the least square method to minimize the error of scale similarity assumption at the $FG$ level as below (no summation over repeated indexes):

$$C^{\overline{\Delta}}_{Dij} = \underline{\Upsilon_{\mathrm{i}}\mathcal{X}_{ij}}/\underline{\mathcal{X}_{ij}\mathcal{X}_{ij}}, \tag{3.102}$$

where, as mentioned before, $\underline{(.)}$ is the averaging operator which can be over $Oxz$ planes with $Ox$ and $Oz$ the homogeneous directions in the case considered. This will give only one value of the coefficient on each statistically homogeneous plane. Since Eqs. 3.75, 3.79, 3.85, 3.90, 3.96, and 3.101 are scalar equations, alternatively one can directly solve for the dynamic similarity coefficients, i.e. $C^{\overline{\Delta}}_{Dij} = \Upsilon_{\mathrm{i}}/\mathcal{X}_{ij}$ locally at each grid point or to evaluate the coefficients in an average form $C^{\overline{\Delta}}_{Dij} = \underline{\Upsilon_i}/\underline{\mathcal{X}_{ij}}$ in statistically homogeneous directions (e.g. time or space coordinates). However, the results obtained by these two alternatives (not reported here) show that they produce large oscillations, which deteriorates the final results even in average. The best results are obtained by least square error minimization (Eqs. 3.102) and only this method has been exploited in the results shown in the next section.

### 3.4.4 Summary

In this section, i.e., Sec. 3.4, the finite-rate dynamic Scale Similarity (SS) SGS combustion models for LES were developed by applying Germano's identity directly for the species source terms in the original SS combustion model (Sec. 3.3).

Two variants of dynamic versions for each existing non-dynamic model, A, B, and C (see Sec. 3.3) were derived. Two versions of dynamic models (DA1, DA2, DB1, DB2 and DC1, DC2) resulted from using different filtering levels in the mathematical formulations.

The summary of the developed models are presented in Table 3.5. The models will be assessed by an *a priori* analysis in Sec. 5.4.3.

**Table 3.5:** *Summary of the SGS combustion models used in the current study*

| model | Definition | Residualfield ($\mathcal{L}_{\dot{\omega}}$) | Similarity constant | $\Upsilon$ | $\mathcal{X}$ |
|---|---|---|---|---|---|
| **Non-dynamic A** (DesJardin and Frankel [17]) | $\overline{\dot{\omega}}^{A}(\boldsymbol{\varphi}) = \dot{\omega}(\overline{\boldsymbol{\varphi}}^{f}) + C_{A}^{\overline{\Delta}}\,\mathcal{L}_{\dot{\omega}^{A}}$ | Eq. 3.67 | $C_{A}^{\overline{\Delta}} = 1$ | – | – |
| **Dynamic A1** (Present work) | $\overline{\dot{\omega}}^{DA1}(\boldsymbol{\varphi}) = \dot{\omega}(\overline{\boldsymbol{\varphi}}^{f}) + C_{DA1}^{\overline{\Delta}}\,\mathcal{L}_{\dot{\omega}^{A}}$ | Eq. 3.67 | $C_{DA1}^{\overline{\Delta}} = \underline{\Upsilon_{\mathrm{A}}\mathcal{X}_{A1}}/\underline{\mathcal{X}_{A1}\mathcal{X}_{A1}}$ | Eq. 3.75 | Eq. 3.82 |
| **Dynamic A2** (Jaberi and James [18]) | $\overline{\dot{\omega}}^{DA2}(\boldsymbol{\varphi}) = \dot{\omega}(\overline{\boldsymbol{\varphi}}^{f}) + C_{DA2}^{\overline{\Delta}}\,\mathcal{L}_{\dot{\omega}^{A}}$ | Eq. 3.67 | $C_{DA2}^{\overline{\Delta}} = \underline{\Upsilon_{\mathrm{A}}\mathcal{X}_{A2}}/\underline{\mathcal{X}_{A2}\mathcal{X}_{A2}}$ | Eq. 3.75 | Eq. 3.83 |
| **Non-dynamic B** (DesJardin and Frankel [17]) | $\overline{\dot{\omega}}^{B}(\boldsymbol{\varphi}) = \overline{\dot{\omega}}(\overline{\boldsymbol{\varphi}}^{f}) + C_{B}^{\overline{\Delta}}\,\mathcal{L}_{\dot{\omega}^{B}}$ | Eq. 3.69 | $C_{B}^{\overline{\Delta}} = 1$ | – | – |
| **Dynamic B1** (Present work) | $\overline{\dot{\omega}}^{DB1}(\boldsymbol{\varphi}) = \overline{\dot{\omega}}(\overline{\boldsymbol{\varphi}}^{f}) + C_{DB1}^{\overline{\Delta}}\,\mathcal{L}_{\dot{\omega}^{B}}$ | Eq. 3.69 | $C_{DB1}^{\overline{\Delta}} = \underline{\Upsilon_{\mathrm{B}}\mathcal{X}_{B1}}/\underline{\mathcal{X}_{B1}\mathcal{X}_{B1}}$ | Eq. 3.86 | Eq. 3.93 |
| **Dynamic B2** (Present work) | $\overline{\dot{\omega}}^{DB2}(\boldsymbol{\varphi}) = \overline{\dot{\omega}}(\overline{\boldsymbol{\varphi}}^{f}) + C_{DB2}^{\overline{\Delta}}\,\mathcal{L}_{\dot{\omega}^{B}}$ | Eq. 3.69 | $C_{DB2}^{\overline{\Delta}} = \underline{\Upsilon_{\mathrm{B}}\mathcal{X}_{B2}}/\underline{\mathcal{X}_{B2}\mathcal{X}_{B2}}$ | Eq. 3.86 | Eq. 3.94 |
| **Non-dynamic C** (Inspired from [128]) | $\overline{\dot{\omega}}^{C}(\boldsymbol{\varphi}) = \dot{\omega}(\overline{\boldsymbol{\varphi}}^{f}) + C_{C}^{\overline{\Delta}}\,\mathcal{L}_{\dot{\omega}^{C}}$ | Eq. 3.67 | $C_{C}^{\overline{\Delta}} = 1$ | – | – |
| **Dynamic C1** (Present work) | $\overline{\dot{\omega}}^{DC1}(\boldsymbol{\varphi}) = \dot{\omega}(\overline{\boldsymbol{\varphi}}^{f}) + C_{DC1}^{\overline{\Delta}}\,\mathcal{L}_{\dot{\omega}^{C}}$ | Eq. 3.67 | $C_{DC1}^{\overline{\Delta}} = \underline{\Upsilon_{\mathrm{C}}\mathcal{X}_{C1}}/\underline{\mathcal{X}_{C1}\mathcal{X}_{C1}}$ | Eq. 3.97 | Eq. 3.99 |
| **Dynamic C2** (Present work) | $\overline{\dot{\omega}}^{DC2}(\boldsymbol{\varphi}) = \dot{\omega}(\overline{\boldsymbol{\varphi}}^{f}) + C_{DC2}^{\overline{\Delta}}\,\mathcal{L}_{\dot{\omega}^{C}}$ | Eq. 3.67 | $C_{DC2}^{\overline{\Delta}} = \underline{\Upsilon_{\mathrm{C}}\mathcal{X}_{C2}}/\underline{\mathcal{X}_{C2}\mathcal{X}_{C2}}$ | Eq. 3.97 | Eq. 3.100 |

CHAPTER 4

# Methodology

## 4.1 Introduction

In this section the methodology used in the current thesis to analyze the jet flames and their modeling aspects using DNS databases is explained. The section starts with the explanation of two main methods to use DNS data in model assessments/developments. Next, the DNS databases used in the current study will be presented in details. The tools needed for the methodology adopted here will be briefly presented, including explicit filters, assessment metrics, and an *a priori* code developed as a part of current project.

## 4.2 Model Assessments Using DNS Data: *A Priori* and *A Posteriori* Analysis

The DNS databases of reactive flows with relatively detailed chemistry, which are now available thanks to massively large parallel computational resources, can be utilized to assess the combustion models in the LES of reactive flows. The two main ways of DNS data utilization are *a priori* and *a posteriori* tests [129].

An *a priori* analysis is adopted by comparing the "modeled" targets with the "exact" filtered ones from DNS databases. The modeled targets make use of the directly filtered quantities from DNS. With this approach, the uncertainties caused by any other model (e.g. for SGS the stress field) are skipped and one can focus directly on the performance of a combustion model itself. The main drawback in *a priori* analyses is their inability to predict the time properties of sub-grid closures [130]. It is not guaranteed that if a model performs well in an *a priori* analysis it will also perform well in a real LES simulation. The reverse is also possible, this means that some models may fail in *a priori* DNS analyses while in LES giving acceptable results. The advantage of *a priori* analyses is that the target models can be assessed in an isolated system, to a good extent,

free from the errors or uncertainties caused by other models. In the special case of the SGS combustion modeling, using the *a priori* DNS analysis, the uncertainties regarding the using of turbulence models for the SGS stress field are skipped and one can focus directly on the performance of a combustion model itself. If a model is considered as a system with inputs and outputs, it is of interest to study the outputs while the inputs are free from errors. Considering the relatively small computational time required for the *a priori* analysis, it is a very good choice for comparing the models' performance. *A priori* analyses have been performed in many previous works to study the performance of SGS combustion models [19–24].

In an *a posteriori* analysis, real LES/RANS will be carried out. The DNS case is simulated using LES/RANS codes and the results are compared with the filtered DNS data. All the simulation parameters kept similar to the DNS except the mesh size and the initial condition which usually set to be the filtered initial condition of the DNS. This is a more realistic approach to test LES/RANS sub-models since they are tested in real simulations, however, the main issue is that if error exists, the source of error is unknown, it can be from any of the sub-models used in the LES code. On the other hand, if the results are perfect, it can be due to the error compensation and the direct conclusion on the model behavior cannot be drawn. This is the reason why the perfect assessment is said to be the combination of both *a priori* and *a posteriori* analyses.

## 4.3 Explicit Filters

A "simple filtered" quantity $\overline{q}$ in 3D is computed as:

$$\overline{q} = \iiint q\left(\mathbf{X}'\right) F\left(\mathbf{X} - \mathbf{X}'\right) d^3\mathbf{X}'. \tag{4.1}$$

Equivalently a Favre filtered quantity is given by:

$$\overline{q}^f = \frac{1}{\overline{\rho}} \left( \iiint \rho q\left(\mathbf{X}'\right) F\left(\mathbf{X} - \mathbf{X}'\right) d^3\mathbf{X}' \right), \tag{4.2}$$

where $F\left(\mathbf{X}\right)$ represents the 3D filter kernel which is selected to be a top-hat filter:

$$F\left(\mathbf{X}\right) = F\left(x_1, x_2, x_3\right) = F\left(x_j\right) = \left\{ \begin{array}{cc} \dfrac{1}{\overline{\Delta}^3} & if|x_j| \leq \dfrac{\overline{\Delta}}{2} \\ 0 & otherwise \end{array} \right\}, \tag{4.3}$$

where $\overline{\Delta}$ is the filter width and is equal to $\overline{\Delta} = N\Delta^{\mathrm{DNS}}$, with $N$ an integer. Therefore, Eq. 4.1 leads to:

$$\overline{q} = \frac{1}{\overline{\Delta}^3} \left( \iiint_{-\overline{\Delta}/2}^{\overline{\Delta}/2} q\left(\mathbf{X}'\right) d^3\mathbf{X}' \right). \tag{4.4}$$

The top-hat filter corresponds to the filter implicitly associated with the discretization using centered finite difference or finite volume codes which are used more often in LES [131].

The integral in Eq. 4.4 is computed by using the trapezoidal rule. In 1D, the final equation for structured grids is given in the first row of Table 4.1. The 3D filtered data is computed by 3 consecutive applications of this formula in $Ox$, $Oy$, and $Oz$ directions,

respectively. In Table 4.1 the filters types which are used in the current study and the way they are numerically implemented have been introduced.

**Table 4.1:** *The 1D implementation of different filters used in the current study. $\Delta^*$ is the size of the grid on which the quantity $q$ is defined and $i$ is a grid number in $x_i$ direction. $N$ is an integer defining the width of the filter*

| Filter | Name | Filter width | Definition in 1D |
|---|---|---|---|
| $\overline{q}$ | simple filter | $\overline{\Delta} = N\Delta^*$ | $\overline{q}_i^{1D} = \frac{1}{2N}\left(q_{i-N/2} + 2\sum_{l=i-N/2+1}^{l=i+N/2-1} q_l + q_{i+N/2}\right)$ |
| $\bar{q}$ | grid filter | $\overline{\Delta} = \overline{\Delta}$ | $\bar{q}_i^{1D} = \frac{1}{8}\left(q_{i+1} + 6q_i + q_{i-1}\right)$ |
| $\widehat{q}$ | $1^{st}$ test filter | $\widehat{\Delta} = 2\Delta^*$ | $\widehat{q}_i^{1D} = \frac{1}{4}\left(q_{i-1} + 2q_i + q_{i+1}\right)$ |
| $\overbrace{q}$ | $2^{nd}$ test filter | $\overbrace{\Delta} = 4\Delta^*$ | $\overbrace{q_i}^{1D} = \frac{1}{8}\left(q_{i-2} + 2\left(q_{i-1} + q_i + q_{i+1}\right) + q_{i+2}\right)$ |

"Simple filter" is only applied to the original data so that the grid size is the DNS grid size, viz. $\Delta^* = \Delta_{\mathrm{DNS}}$. In the *a priori* DNS analysis, this creates LES like quantities. In the *a posteriori* DNS analysis or a real LES, there is no need to apply the "simple filter" simply because the solution is already a "simple filtered" quantity. It must be mentioned that the "simple filtered" data will be sampled on a new grid after filtering procedure. The size of the new grid will be $N$ times the original DNS grid. This will be explained in detail later. The "$1^{st}$ test filter" and "$2^{nd}$ test filter" are simple filters with a fixed filter widths of 2 and 4, respectively. The grid filter, $\overline{(.)}$, is virtually the same filter as the "simple filter" with the same filter width, however, the implementation is different. The method introduced in [126] is used in the current study which can be seen in Table 4.1.

Other filters can be applied on top of a previously filtered quantity. For example the "test grid filtered" data is computed by application of the filter in already filtered fields using a kernel with $\widehat{\Delta} = 2\overline{\Delta}$. In 3D the equation for "test grid filter" reads:

$$\left.\begin{aligned}
\overline{q}^*_{i,j,k} &= \frac{1}{4}\left(\overline{q}_{i+1,j,k} + 2\overline{q}_{i,j,k} + \overline{q}_{i-1,j,k}\right)\\
\overline{q}^{**}_{i,j,k} &= \frac{1}{4}\left(\overline{q}^*_{i,j+1,k} + 2\overline{q}^*_{i,j,k} + \overline{q}^*_{i,j-1,k}\right)\\
\widehat{\overline{q}}_{i,j,k} &= \frac{1}{4}\left(\overline{q}^{**}_{i,j,k+1} + 2\overline{q}^{**}_{i,j,k} + \overline{q}^{**}_{i,j,k-1}\right)
\end{aligned}\right\} \tag{4.5}$$

Moreover, the double grid filtered data is computed by:

$$\overline{\overline{q}}_i^{1D} = \frac{1}{8}\left(\overline{q}_{i+1} + 6\overline{q}_i + \overline{q}_{i-1}\right), \tag{4.6}$$

where $i+1$ and $i-1$ are two neighboring points. The 3D filtered data are computed by 3 consecutive applications of 1D filters in $Ox$, $Oy$, and $Oz$ directions. This reads:

$$\left.\begin{aligned}
\overline{\overline{q}}^*_{i,j,k} &= \frac{1}{8}\left(\overline{q}_{i+1,j,k} + 6\overline{q}_{i,j,k} + \overline{q}_{i-1,j,k}\right)\\
\overline{\overline{q}}^{**}_{i,j,k} &= \frac{1}{8}\left(\overline{\overline{q}}^*_{i,j+1,k} + 6\overline{\overline{q}}^*_{i,j,k} + \overline{\overline{q}}^*_{i,j-1,k}\right)\\
\overline{\overline{q}}_{i,j,k} &= \frac{1}{8}\left(\overline{\overline{q}}^{**}_{i,j,k+1} + 6\overline{\overline{q}}^{**}_{i,j,k} + \overline{\overline{q}}^{**}_{i,j,k-1}\right).
\end{aligned}\right\} \tag{4.7}$$

**Table 4.2:** *The notations used in the current study for Favre filtered composition vector (i.e., species mass fractions and temperature) and the sequential steps to compute multilevel Favre filtered quantities*

| Compact Notation | Exact Notation | Definition | Steps to Compute |
|---|---|---|---|
| $\overline{\varphi}^f$ | $\overline{\varphi}^f$ | $\frac{\overline{\rho\varphi}}{\overline{\rho}}$ | $\varphi \xrightarrow{\overline{(.)}^f} \overline{\varphi}^f$ |
| $\overline{\overline{\varphi}}^f$ | $\overline{\overline{\varphi}^f}^f$ | $\frac{\overline{\overline{\rho}\,\overline{\varphi}^f}}{\overline{\overline{\rho}}}$ | $\overline{\varphi}^f \xrightarrow{\overline{(.)}^f} \overline{\overline{\varphi}}^f$ |
| $\widehat{\overline{\varphi}}^f$ | $\widehat{\overline{\varphi}^f}^f$ | $\frac{\widehat{\overline{\rho}\,\overline{\varphi}^f}}{\widehat{\overline{\rho}}}$ | $\overline{\varphi}^f \xrightarrow{\widehat{(.)}^f} \widehat{\overline{\varphi}}^f$ |
| $\widehat{\overline{\overline{\varphi}}}^f$ | $\widehat{\overline{\overline{\varphi}^f}^f}^f$ | $\frac{\widehat{\overline{\overline{\rho}}\,\overline{\overline{\varphi}}^f}}{\widehat{\overline{\overline{\rho}}}}$ | $\overline{\varphi}^f \xrightarrow{\overline{(.)}^f} \overline{\overline{\varphi}}^f \xrightarrow{\widehat{(.)}^f} \widehat{\overline{\overline{\varphi}}}^f$ |
| $\overline{\widehat{\overline{\varphi}}}^f$ | $\overline{\widehat{\overline{\varphi}^f}^f}^f$ | $\frac{\overline{\widehat{\overline{\rho}}\,\widehat{\overline{\varphi}}^f}}{\overline{\widehat{\overline{\rho}}}}$ | $\overline{\varphi}^f \xrightarrow{\widehat{(.)}^f} \widehat{\overline{\varphi}}^f \xrightarrow{\overline{(.)}^f} \overline{\widehat{\overline{\varphi}}}^f$ |
| $\widehat{\overline{\overline{\varphi}}}^f$ | $\widehat{\overline{\overline{\varphi}^f}^f}^f$ | $\frac{\widehat{\overline{\overline{\rho}}\,\overline{\overline{\varphi}}^f}}{\widehat{\overline{\overline{\rho}}}}$ | $\overline{\varphi}^f \xrightarrow{\widehat{(.)}^f} \widehat{\overline{\varphi}}^f \xrightarrow{\overline{(.)}^f} \overline{\overline{\varphi}}^f \xrightarrow{\widehat{(.)}^f} \widehat{\overline{\overline{\varphi}}}^f$ |
| $\overbrace{\widehat{\varphi}}^f$ | $\overbrace{\widehat{\varphi}^f}^f$ | $\frac{\overbrace{\widehat{\rho}\,\widehat{\varphi}^f}}{\overbrace{\widehat{\rho}}}$ | $\overline{\varphi}^f \xrightarrow{\widehat{(.)}^f} \widehat{\varphi}^f \xrightarrow{\overbrace{(.)}^f} \overbrace{\widehat{\varphi}}^f$ |
| $\overbrace{\overline{\varphi}}^f$ | $\overbrace{\overline{\varphi}^f}^f$ | $\frac{\overbrace{\overline{\rho}\,\overline{\varphi}^f}}{\overbrace{\overline{\rho}}}$ | $\overline{\varphi}^f \xrightarrow{\overbrace{(.)}^f} \overbrace{\overline{\varphi}}^f$ |

The Favre filtered quantities and the steps to compute them which were used in Sec .3.3 are explained in Table 4.2. In Sec .3.3 a compact notation has been used for simplicity and the exact notations can be found in this table.

Care must be taken on handling the data after filtering. In this work it is tried to follow as much as possible the "consistent *a priori* DNS analysis" explained by Liu et al., [122]. In Fig. 4.1, the first step of producing LES like quantities from the DNS databases is illustrated in 1D. For simplicity, it is assumed that $\overline{\Delta} = 4\Delta_{\mathrm{DNS}}$ and it should not be mistakenly interpreted as the "$2^{nd}$ test filter". The DNS data is filtered using the "simple filter", i.e. $\overline{(.)}$, and then sampled and interpolated to a new grid. The new grid is a coarser grid with the grid size $N = 4$ times the DNS grid size. In this way, the filtered quantities, $\overline{q}$, are only available on a coarse grid. However, for the next level filter, i.e., application of $\overline{(.)}$, $\widehat{(.)}$, and $\overbrace{(.)}$ on $\overline{q}$, no more sampling will be performed. It should be mentioned that in all equations above, it is assumed that the DNS mesh is uniform i.e. $\Delta x_{DNS} = \Delta y_{DNS} = \Delta z_{DNS} = \Delta_{DNS}$, which is common in DNS setups. The filtered source terms which are used in the current study are presented in Table 4.3. The steps to compute the multi-level filtered terms are also presented. In this work, OpenSMOKE++(OS++) [95] is used to compute the Arrhenius source terms. Of course calculations can also be performed using Chemkin or Cantera. As can be seen, the input of OS++ is the Favre filtered composition vector.

In Fig. 4.2a, the location of the spectral cutoff filters with the same filter width as

**Table 4.3:** *The steps to compute the filtered source terms used in the current study. Os++ is OpenSMOKE++ [95].*

| Notation | Steps to Compute |
|---|---|
| $\bar{\dot{\omega}}(\overline{\varphi}^f)$ | $\overline{\varphi}^f \xrightarrow{\text{OS++}} \dot{\omega}(\overline{\varphi}^f) \xrightarrow{\overline{(.)}} \bar{\dot{\omega}}(\overline{\varphi}^f)$ |
| $\dot{\omega}(\bar{\overline{\varphi}}^f)$ | $\bar{\overline{\varphi}}^f \xrightarrow{\text{OS++}} \dot{\omega}(\bar{\overline{\varphi}}^f)$ |
| $\bar{\bar{\dot{\omega}}}(\overline{\varphi}^f)$ | $\overline{\varphi}^f \xrightarrow{\text{OS++}} \dot{\omega}(\overline{\varphi}^f) \xrightarrow{\overline{(.)}} \bar{\dot{\omega}}(\overline{\varphi}^f) \xrightarrow{\overline{(.)}} \bar{\bar{\dot{\omega}}}(\overline{\varphi}^f)$ |
| $\bar{\bar{\dot{\omega}}}(\bar{\overline{\varphi}}^f)$ | $\bar{\overline{\varphi}}^f \xrightarrow{\text{OS++}} \dot{\omega}(\bar{\overline{\varphi}}^f) \xrightarrow{\overline{(.)}} \bar{\dot{\omega}}(\bar{\overline{\varphi}}^f) \xrightarrow{\overline{(.)}} \bar{\bar{\dot{\omega}}}(\bar{\overline{\varphi}}^f)$ |
| $\dot{\omega}(\widehat{\varphi}^f)$ | $\widehat{\varphi}^f \xrightarrow{\text{OS++}} \dot{\omega}(\widehat{\varphi}^f)$ |
| $\bar{\dot{\omega}}(\widehat{\varphi}^f)$ | $\widehat{\varphi}^f \xrightarrow{\text{OS++}} \dot{\omega}(\widehat{\varphi}^f) \xrightarrow{\overline{(.)}} \bar{\dot{\omega}}(\widehat{\varphi}^f) \xrightarrow{\widehat{(.)}} \bar{\dot{\widehat{\omega}}}(\widehat{\varphi}^f)$ |
| $\dot{\omega}(\widehat{\bar{\varphi}}^f)$ | $\widehat{\bar{\varphi}}^f \xrightarrow{\text{OS++}} \dot{\omega}(\widehat{\bar{\varphi}}^f)$ |
| $\bar{\dot{\omega}}(\overline{\varphi}^f)$ | $\overline{\varphi}^f \xrightarrow{\text{OS++}} \dot{\omega}(\overline{\varphi}^f) \xrightarrow{\overline{(.)}} \bar{\dot{\omega}}(\overline{\varphi}^f) \xrightarrow{\widehat{(.)}} \bar{\dot{\widehat{\omega}}}(\overline{\varphi}^f)$ |
| $\dot{\omega}(\bar{\widehat{\varphi}}^f)$ | $\bar{\widehat{\varphi}}^f \xrightarrow{\text{OS++}} \dot{\omega}(\bar{\widehat{\varphi}}^f)$ |
| $\bar{\bar{\dot{\omega}}}(\widehat{\varphi}^f)$ | $\widehat{\varphi}^f \xrightarrow{\text{OS++}} \dot{\omega}(\widehat{\varphi}^f) \xrightarrow{\overline{(.)}} \bar{\dot{\omega}}(\widehat{\varphi}^f) \xrightarrow{\widehat{(.)}} \bar{\dot{\widehat{\omega}}}(\widehat{\varphi}^f) \xrightarrow{\overline{(.)}} \bar{\bar{\dot{\widehat{\omega}}}}(\widehat{\varphi}^f) \xrightarrow{\widehat{(.)}} \bar{\bar{\dot{\widehat{\omega}}}}(\widehat{\varphi}^f)$ |
| $\bar{\bar{\dot{\omega}}}(\bar{\widehat{\varphi}}^f)$ | $\bar{\widehat{\varphi}}^f \xrightarrow{\text{OS++}} \dot{\omega}(\bar{\widehat{\varphi}}^f) \xrightarrow{\overline{(.)}} \bar{\dot{\omega}}(\bar{\widehat{\varphi}}^f) \xrightarrow{\widehat{(.)}} \bar{\dot{\widehat{\omega}}}(\bar{\widehat{\varphi}}^f) \xrightarrow{\overline{(.)}} \bar{\bar{\dot{\widehat{\omega}}}}(\bar{\widehat{\varphi}}^f) \xrightarrow{\widehat{(.)}} \bar{\bar{\dot{\widehat{\omega}}}}(\bar{\widehat{\varphi}}^f)$ |
| $\bar{\bar{\dot{\omega}}}(\overline{\varphi}^f)$ | $\overline{\varphi}^f \xrightarrow{\text{OS++}} \dot{\omega}(\overline{\varphi}^f) \xrightarrow{\overline{(.)}} \bar{\dot{\omega}}(\overline{\varphi}^f) \xrightarrow{\widehat{(.)}} \bar{\dot{\widehat{\omega}}}(\overline{\varphi}^f) \xrightarrow{\overline{(.)}} \bar{\bar{\dot{\widehat{\omega}}}}(\overline{\varphi}^f) \xrightarrow{\widehat{(.)}} \bar{\bar{\dot{\widehat{\omega}}}}(\overline{\varphi}^f)$ |
| $\bar{\bar{\dot{\omega}}}(\bar{\widehat{\varphi}}^f)$ | $\bar{\widehat{\varphi}}^f \xrightarrow{\text{OS++}} \dot{\omega}(\bar{\widehat{\varphi}}^f) \xrightarrow{\overline{(.)}} \bar{\dot{\omega}}(\bar{\widehat{\varphi}}^f) \xrightarrow{\widehat{(.)}} \bar{\dot{\widehat{\omega}}}(\bar{\widehat{\varphi}}^f) \xrightarrow{\overline{(.)}} \bar{\bar{\dot{\widehat{\omega}}}}(\bar{\widehat{\varphi}}^f) \xrightarrow{\widehat{(.)}} \bar{\bar{\dot{\widehat{\omega}}}}(\bar{\widehat{\varphi}}^f)$ |
| $\bar{\bar{\dot{\omega}}}(\overline{\varphi}^f)$ | $\overline{\varphi}^f \xrightarrow{\text{OS++}} \dot{\omega}(\overline{\varphi}^f) \xrightarrow{\overline{(.)}} \bar{\dot{\omega}}(\overline{\varphi}^f) \xrightarrow{\overline{(.)}} \bar{\bar{\dot{\omega}}}(\overline{\varphi}^f) \xrightarrow{\widehat{(.)}} \bar{\bar{\dot{\omega}}}(\overline{\varphi}^f)$ |
| $\bar{\bar{\dot{\omega}}}(\bar{\overline{\varphi}}^f)$ | $\bar{\overline{\varphi}}^f \xrightarrow{\text{OS++}} \dot{\omega}(\bar{\overline{\varphi}}^f) \xrightarrow{\overline{(.)}} \bar{\dot{\omega}}(\bar{\overline{\varphi}}^f) \xrightarrow{\overline{(.)}} \bar{\bar{\dot{\omega}}}(\bar{\overline{\varphi}}^f) \xrightarrow{\widehat{(.)}} \bar{\bar{\dot{\omega}}}(\bar{\overline{\varphi}}^f)$ |
| $\dot{\widehat{\omega}}(\overline{\varphi}^f)$ | $\overline{\varphi}^f \xrightarrow{\text{OS++}} \dot{\omega}(\overline{\varphi}^f) \xrightarrow{\overline{(.)}} \bar{\dot{\omega}}(\overline{\varphi}^f) \xrightarrow{\overline{(.)}} \bar{\bar{\dot{\omega}}}(\overline{\varphi}^f) \xrightarrow{\widehat{(.)}} \dot{\widehat{\omega}}(\overline{\varphi}^f)$ |
| $\dot{\widehat{\omega}}(\bar{\overline{\varphi}}^f)$ | $\bar{\overline{\varphi}}^f \xrightarrow{\text{OS++}} \dot{\omega}(\bar{\overline{\varphi}}^f) \xrightarrow{\overline{(.)}} \bar{\dot{\omega}}(\bar{\overline{\varphi}}^f) \xrightarrow{\overline{(.)}} \bar{\bar{\dot{\omega}}}(\bar{\overline{\varphi}}^f) \xrightarrow{\widehat{(.)}} \dot{\widehat{\omega}}(\bar{\overline{\varphi}}^f)$ |
| $\widehat{\dot{\omega}}(\overline{\varphi}^f)$ | $\overline{\varphi}^f \xrightarrow{\text{OS++}} \dot{\omega}(\overline{\varphi}^f) \xrightarrow{\widehat{(.)}} \widehat{\dot{\omega}}(\overline{\varphi}^f)$ |
| $\widehat{\dot{\omega}}(\bar{\overline{\varphi}}^f)$ | $\bar{\overline{\varphi}}^f \xrightarrow{\text{OS++}} \dot{\omega}(\bar{\overline{\varphi}}^f) \xrightarrow{\widehat{(.)}} \widehat{\dot{\omega}}(\bar{\overline{\varphi}}^f)$ |
| $\widehat{\dot{\widehat{\omega}}}(\overline{\varphi}^f)$ | $\overline{\varphi}^f \xrightarrow{\text{OS++}} \dot{\omega}(\overline{\varphi}^f) \xrightarrow{\widehat{(.)}} \widehat{\dot{\omega}}(\overline{\varphi}^f) \xrightarrow{\widehat{(.)}} \widehat{\dot{\widehat{\omega}}}(\overline{\varphi}^f)$ |
| $\overbrace{\dot{\omega}}(\overline{\varphi}^f)$ | $(\overline{\varphi}^f) \xrightarrow{\text{OS++}} \dot{\omega}(\overline{\varphi}^f) \xrightarrow{\overbrace{(.)}} \overbrace{\dot{\omega}}(\overline{\varphi}^f)$ |
| $\overbrace{\dot{\omega}}(\widehat{\varphi}^f)$ | $\widehat{\varphi}^f \xrightarrow{\text{OS++}} \dot{\omega}(\widehat{\varphi}^f) \xrightarrow{\overbrace{(.)}} \overbrace{\dot{\omega}}(\widehat{\varphi}^f)$ |
| $\dot{\omega}(\overbrace{\widehat{\varphi}}^f)$ | $\overbrace{\widehat{\varphi}}^f \xrightarrow{\text{OS++}} \dot{\omega}(\overbrace{\widehat{\varphi}}^f)$ |
| $\dot{\omega}(\overbrace{\overline{\varphi}}^f)$ | $\overbrace{\overline{\varphi}}^f \xrightarrow{\text{OS++}} \dot{\omega}(\overbrace{\overline{\varphi}}^f)$ |

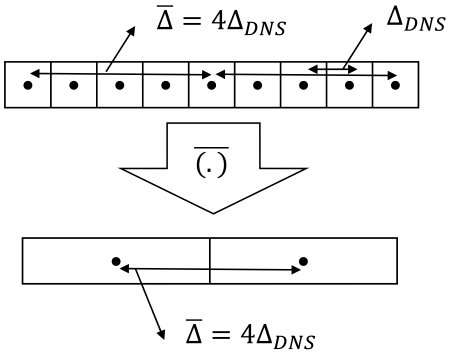


**Figure 4.1:** *1D graphical illustration of fits filtering level (simple filter) of the DNS data and the sampling on a coarse grid. It is assumed that $N$ is 4 for simplicity*

top-hat kernel is shown on a log-log diagram of the compensated energy spectrum. The spectrum is computed on the central $Oxz$ plane of the DNS case H which will be introduced in the next chapters. The location of the cut off filters lie in the inertial range, which is evident by the plateau in the compensated energy spectrum. In Fig. 4.2b, the fraction of resolved Favre mean turbulent kinetic energy (TKE) is depicted using different filter widths. It is seen that using $\Delta/\Delta_{DNS} = 8$, more than $80\%$ of the TKE is resolved. This fraction is reduced by increasing the filter width to $70\%$ for $\Delta/\Delta_{DNS} = 12$ and $60\%$ for $\Delta/\Delta_{DNS} = 18$. This allows to conclude that using the two larger filter widths is equivalent to performing very-large-eddy simulation (VLES), which is common in practical applications.

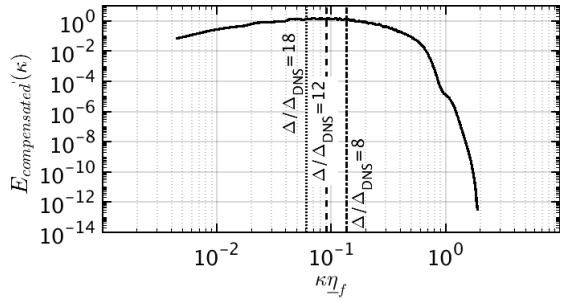


**(a)**

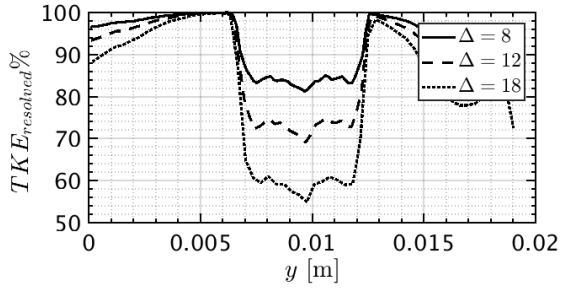


**(b)**

**Figure 4.2:** ***(a)*** *Locations of the cutoff filter with the corresponding filter widths on log-log plot of compensated energy spectrum computed on the central plane;* ***(b)*** *Fraction of the Favre averaged resolved TKE using different filter widths at $t = 20t_j$.*

## 4.4 Assessment Metrics

The first and second moments of the physical quantities will be used as first metric for comparing the modeled and exact field by DNS data. Since two homogeneous streamwise ($Ox$) and span-wise ($Oz$) directions exist, the first moment is defined as the planar average (on $Oxz$ planes) at different crosswise ($Oy$) heights. The second moment is the "RMS", which were already defined in Eq. 2.15 and Eq. 2.38, in Reynolds averaged and Favre averaged forms, respectively. Furthermore, to sum-up the local incurred errors and get one value from the whole sample space, the cumulative relative error is defined as below:

$$\epsilon \equiv \frac{\|\dot{\omega}_k^{model}(\overline{\boldsymbol{\varphi}}^f) - \overline{\dot{\omega}}_k\|_2}{\|\overline{\dot{\omega}}_k\|_2}, \tag{4.8}$$

where $\|.\|_2$ is the L2 norm with $\dot{\omega}_k^{model}(\overline{\boldsymbol{\varphi}}^f)$ the estimator and $\overline{\dot{\omega}}_k$ the exact filtered DNS data. The sample space includes the clipped data from DNS domain. The data are confined to a region where $\underline{Z}_f \geq 0.02$ with $\underline{Z}_f$ expressing the Favre mean mixture fraction. This is done to avoid nearly zero values of net formation rates in the regions outside the flame brush.

The filtered heat release in the filtered energy equation is also of great importance. It can be used to see the overall performance of the models, since it is defined as:

$$\overline{\dot{Q}} \equiv -\sum_{k=1}^{N_s} \Delta h_k^0 \overline{\dot{\omega}}_k, \tag{4.9}$$

where $\Delta h_k^0$ is the enthalpy of formation of species $k$. To compute the exact $\overline{\dot{Q}}$ of DNS, $\dot{Q}$ from DNS is directly filtered. To evaluate the modeled $\dot{Q}$, $\dot{\omega}_k^{model}(\overline{\boldsymbol{\varphi}}^f)$ formed by each model are used in Eq. 4.9 and as can be seen this includes all the net formation rates.

The final metric is the Root Mean Square Error (RMSE):

$$RMSE \equiv \sqrt{\underline{\left(\dot{\omega}_k{}^{model}\left(\overline{\boldsymbol{\varphi}}^f\right) - \overline{\dot{\omega}_k}\left(\boldsymbol{\varphi}\right)\right)^2}}. \tag{4.10}$$

This metric provides the most stringent test, since local point-wise errors can be made even if the exact field obtained by DNS and the modeled data have similar means and PDFs [132].

## 4.5 DNS Databases

The DNS databases used in the current study are the DNS of temporal evolution of syngas non-premixed jets [6]. Three flames (L, M, and H cases) with different initial Reynolds numbers are selected. The Reynolds number is defined as $\mathrm{Re} = UH/\nu_{fuel}$, with *H* the initial fuel jet width, $U$ the difference between fuel ($CO/H_2$) and oxidizer ($O_2/N_2$) streams velocities and $\nu_{fuel}$ the kinematic viscosity of fuel stream [6]. Initially, the fuel and oxidizer jet streams have equal streamwise velocities, but in the opposite directions. In Table 4.4, the three DNS databases are introduced in detail. The computational domain is a box with lengths $12H \times 14H \times 8H$ in $Ox$ (streamwise), $Oy$ (transverse or crosswise), and $Oz$ (span-wise) directions, respectively. The DNS mesh

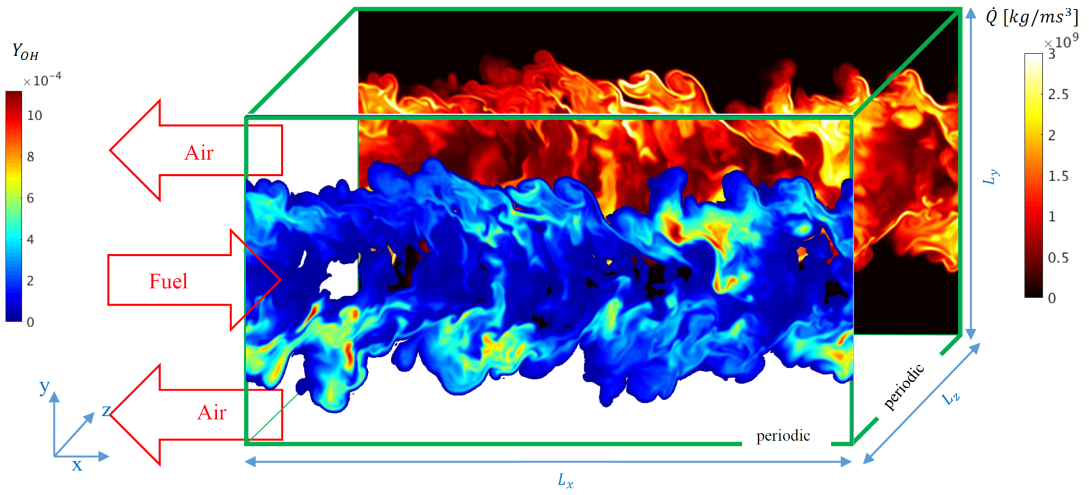


**Figure 4.3:** *Schematic of the temporal jet DNS case, including the contours of heat release rate (colored from black to white) and the mass fraction of OH radical (colored from blue to red) at the maximum extinction time ($20t_j$). Local extinction events on the shear layers are observed with low OH mass fraction and the corresponding low heat release rate*

is a uniform grid with size $\Delta_{\mathrm{DNS}}$ which is mentioned in Table 4.4. Periodic boundary conditions are used in $Ox$ and $Oz$ directions so that the flame is statistically 1D and $Oxz$ planes at each $Oy$ location can be considered as statistically homogeneous planes to extract statistical moments (the first and second moments), see Fig. 4.3. The chemical kinetic mechanism is the same used in the DNS and has 11 species and 21 elementary reactions [6].

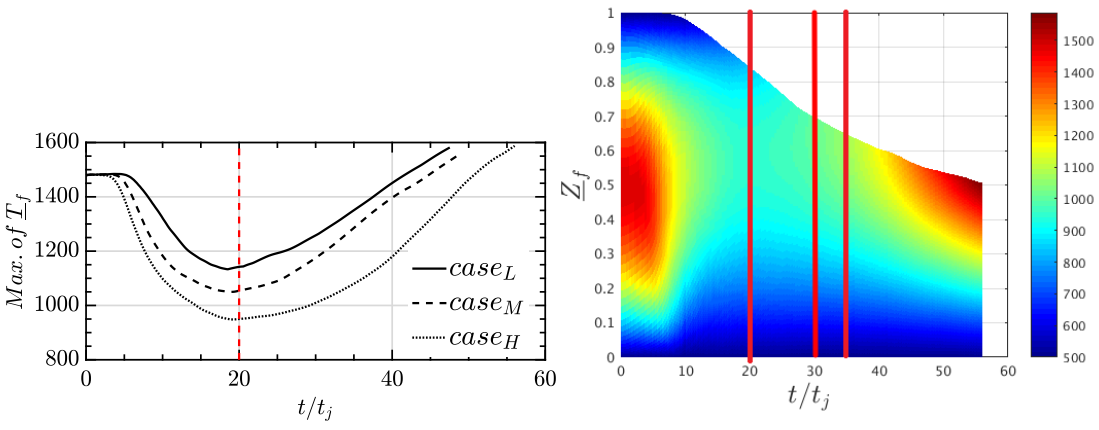


**Figure 4.4:** ***(a)*** *Maximum of Favre averaged temperature during the simulation for three DNS cases. The vertical red dashed line show the time instants with maximum local extinction;* ***(b)*** *Favre averaged mixture fraction in the whole simulation time colored by Favre averaged temperature, the vertical red lines are the time instants analyzed in the current study*

These flames experience first local extinctions up to about $20t_j$ and then re-ignition, where $t_j$ is the "transient jet time", computed as $t_j = H/U = 5\mu s$ [6] in all three cases.

**Table 4.4:** *The DNS databases [6] used in the current study.*

| | Case L | Case M | Case H |
|---|---|---|---|
| Initial jet width ($H$) [$mm$] | 0.72 | 0.96 | 1.37 |
| Initial fuel and oxidizer temperature [K] | 500 | 500 | 500 |
| Mesh ($n_x \times n_y \times n_z$) | 576×672×384 | 768×896×512 | 864×1008×576 |
| Mesh size ($\Delta_{\mathrm{DNS}}[\mu m]$) | 19 | 15 | 15 |
| Initial streamwise velocity difference ($U[ms^{-1}]$) | 145 | 194 | 276 |
| Reynolds number (Re) | 2510 | 4478 | 9079 |
| Maximum turbulent Reynolds number ($\mathrm{Re_t}$) | 92 | 172 | 318 |

In Fig. 4.4a, the maximum of Favre averaged temperature ($\underline{T}_f$) is plotted versus the normalized simulation time for the three cases considered in this study. In this work, the Reynolds averaged quantity is denoted by $\underline{(.)}$, while the Favre averaged quantity is defined as $\underline{\rho(.)}/\underline{\rho}$ and denoted by $\underline{(.)}_f$. The transient extinction/re-ignition phenomenon is clearly observed in Fig. 4.4a. The vertical dashed line is approximately the time instant with maximum local extinction in the three flames. In Fig. 4.4b the Favre averaged mixture fraction colored by Favre averaged temperature during the simulation is shown. As stated earlier and evident in this figure, the flame experiences the transient phenomena of extinction and re-ignition. Also, shown by the vertical lines, the time instants which are used in the present study ($20t_j$, $30t_j$, $35t_j$). It can be inferred that the flame reignites in partially premixed mode. Figure 4.5 shows the normalized energy spectrum (normalized by Favre averaged Kolmogorov length scale, $\underline{\eta}_f$, and Favre averaged turbulent dissipation rate $\underline{\varepsilon}_f$) obtained by velocity fluctuations on the center plane at t=20$t_j$. This figure reveals the existence of the inertial range with -5/3 law in the current case. In this figure, $\kappa$ is the wave number magnitude, $\underline{\eta}_f$, Favre averaged Kolmogorov length scale and $\underline{\varepsilon}_f$ Favre averaged turbulent dissipation rate. The examination of other time instants showed the same behavior. This implies that the inertial range exists for the current configuration although it is not distinctly separated from the dissipative scales, which is common in such a low/medium Reynolds number DNS. Note that the test cases have been used previously for assessment of LES combustion/mixing models [7, 24, 133–137].

## 4.6 *A priori* Analysis Code

The schematic of the code developed for the *a priori* DNS studies is depicted in Fig. 4.6. The DNS data, all the operators, including filtering, averaging and the dependent variables (like TKE, $\varepsilon$,...) extracting routines are all handled by MATLAB. The data are filtered and feed to the SMOKE-PP solver. The solver is a post processor consists

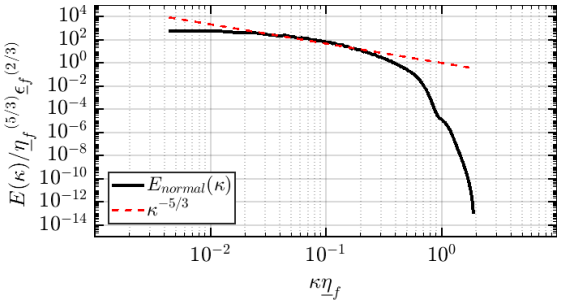


**Figure 4.5:** *Normalized energy spectrum on the center plane of the H case DNS at t=20$t_j$ (black line) and -5/3 scaling law shown by red dashed line.*

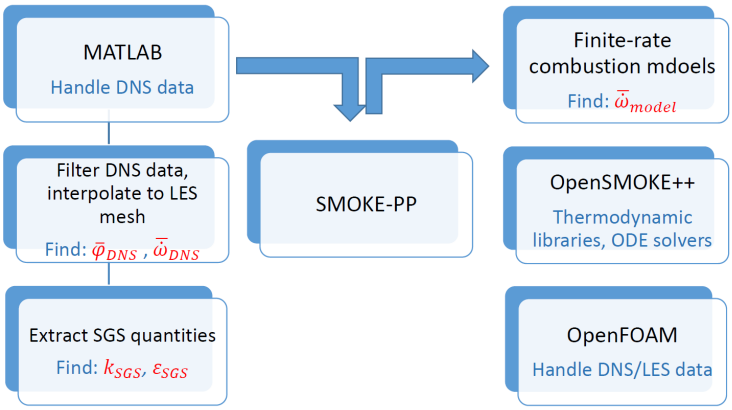


**Figure 4.6:** *Schematic of the a priori analysis codes.*

of OpenFOAM and OPENSMOKE++ [95]. Explicit combustion models are coded in OpenSMOKE++. It also handles the thermodynamic properties and ODE solvers. OpenFOAM is used to handle the LES-like quantities (explicitly filtered DNS) data.

CHAPTER 5

# Results: The *A Priori* DNS Analysis

## 5.1 Introduction

This chapter is divided in two parts. In the first part, a fundamental analysis on the intermittency phenomena and the velocity spectra (energy and its dissipation) will be carried out using the current DNS databases of reactive temporally evolving jets. The DNS databases were introduced in Sec.4.5, and some related theories were already discussed on Sections 2.2.1, 2.2.4 and 2.2.7. The results of the first part of this chapter, i.e., Sections 5.2 and 5.3 have also been used in Sec.3.2 to derive new EDC models. However, this is not the only application of these analyses as they are fundamental and have more applications.

In the second part of this chapter, the performance of the existing and developed finite-rate combustion models for LES (FR-LES-TCI models), developed in Chap.3 will be *a priori* assessed using the DNS databases. The *a priori* DNS analysis methodology including explicit filters, implemented codes and all related subjects were already discussed in detail in Chap.4. This part includes Sec.5.4.1 on the EDC, Sec.5.4.2 on thw non-dynamic Scale Similarity (SS) models and finally Sec.5.4.3 on the dynamic SS models.

## 5.2 Intermittency in Reactive Flows

Intermittency in turbulent flows, specifically turbulent jets, can be classified in two categories; the external and internal intermittency. The external intermittency is referred to a situation in which the fully developed flow co exists with nearly laminar/irrotational flow in a location during time (in spatial jets) or in an instant of time in space (in temporally evolving jets). This is mainly caused by the entrainment process; irrotational flow is drawn towards the turbulent flow. In shear flows, like jets, this is a common phenomenon. There is a debate on the physical mechanism responsible for the entrainment, if it is a large scale engulfment or a small scale nibbling process [138–140]. However, this is not the subject of the current study. Whatever a responsible mechanism is, it creates a sharp interface separates turbulent (T) and non-turbulent (NT) regions. In this work, it is intended to detect the turbulent regions and extract statistics only from those parts. This is the subject of Sec. 5.2.1.

On the next level, inside the turbulent region itself, there is another important phenomenon, called internal intermittency. The production of turbulence is not a continuous process but usually has an intermittent character and hence the turbulence appears as bursts [141]. There is no concrete definition of the internal intermittency, we can refer to the definition of Frisch, that a process is said to be intermittent when it displays activity during only fraction of the time[1], which decreases with the scale under consideration [51]. Figures 8.1 and 8.2 in Section 8 of the book [51] is quite useful to define an intermittent process. Frisch [51] and Pope [38] both agree that the internal intermittency is a dissipation-range phenomenon. The intermittent character of the energy dissipation was first discovered by Batchelor and Townsend [107] which had a profound effect on the turbulence research community. Many attempts have been made since then to characterize the phenomenon and model it, however, mainly in non-reactive flows. Modeling the intermittent behavior of turbulent kinetic energy dissipation rate (and also the scalar dissipation rate) is of great importance in both reactive and non-reactive flows. In non-reactive flows, turbulence models (specifically the $\varepsilon$ transport equation in $k-\varepsilon$ RANS models) relies on the models for intermittency. In reactive flows, the so called log-normal assumption is commonly used for the scalar dissipation rate statistics. Some combustion models, like the EDC [13] directly use the phenomenological models proposed for internal intermittency. In Sec. 5.2.2, it is tried to analyze this phenomenon in non-premixed combustion using the current DNS databases. To the author's knowledge, this is the first attempt in examining the internal intermittency in reactive jets with the focus on the scalings used in combustion models like EDC. It starts with the mathematical formulations of the phenomenon continues with the literature survey and the presentation of results on the internal intermittency.

### 5.2.1 Large Scale (External) Intermittency

In free shear flows including mixing layers and jets, there is a sharp and highly convoluted interface separating the turbulent region(T) from the quiescent non-turbulent(NT) boundaries [142] (see also [143]). The interface location is random in time/space; at a fixed location near the edge of the jet, the flow is in one time/location turbulent and the other time/location non-turbulent. This is called the large-scale or external inter-

[1] the "space" can also be used here instead of "the time" in the definition.

mittency which can be quantified by the external intermittency factor ($\gamma_{ext}$) [38]. The non-turbulent flow is entrained to the turbulent region by the so called entrainment process and mixed. This is of great importance in reactive flows, because it characterizes the mixing process essential for reactions to occur. Further, it is believed, and also shown in Fig. 5.1a, that in turbulent non-premixed jet flames, the stoichiometric mixture fraction isosurfaces usually lie within the turbulent region near the T/NT interface [144]; Combustion mainly takes place in the vicinity of the stoichiometric surface. In Fig. 5.1a the mass fraction of OH is plotted in the $Oxy$ plane at $z = 0$ in case H (see also Sec. 4.5 and Fig. 4.3) with the green lines the T/NT interface detected by the method which will be discussed in the following and the red lines the stoichiometric mixture fraction isolines.

Many works have been done in the turbulence community to characterize the external intermittency (see e.g., [140, 145]). Although not that much work has been done for the reactive flows, the current study does not aim to contribute in this field. The main goal is to use the current methods and to first detect the T/NT regions and then do the statistical analysis in only turbulent regions. Besides, some important features will be highlighted. In the numerical point of view, one can assume that a turbulence model capable of detecting the external intermittency is employed, for example a $k - \varepsilon - \gamma$ model [79] in RANS. In LES, the external intermittency effects are captured automatically without the need for an explicit sub-model.

#### Turbulent/Non-Turbulent (T/NT) Interface Detection and Conditional averages

Different methods proposed in the literature to detect the T/NT interface in shear flows (see e.g., [138, 144, 146–148]). The usual way is to define a threshold either based on vorticity or scalars to separate the T and NT regions. In [147] it was shown that the two methods result in a similar PDF of the interface location. Here, the method based on the vorticity criterion is used to detect the interfaces. It is believed that the turbulent region consists of fluctuations with vortical structures whereas the fluctuations in the non-turbulent region are approximately irrotational. The vorticity magnitude is defined as:

$$w \equiv \sqrt{w_x^2 + w_y^2 + w_z^2}, \tag{5.1}$$

where $\boldsymbol{w} = (w_x, w_y, w_z) \equiv \nabla \times \mathbf{U}$ with $\mathbf{U}$ the velocity vector. A threshold, $w_{threshold}$, is introduced based on the $10\%$ of the mean $w$ on the central plane of a jet [140, 146] where any region below this threshold is considered as non-turbulent. It should be mentioned that in our cases the value obtained by this threshold is approximately the same as the one based on the method in [149]; defined as a vorticity with which the second derivative of the volume of turbulent region is zero. In Fig. 5.2 the logarithm of the vorticity magnitude in three different planes across the jet, corresponding to the central plane ($y = 0$), Favre mean stoichiometric mixture fraction plane and the maximum of the density fluctuations (see also Fig. 5.1b), are depicted. In Fig. 5.3 the same quantities on the same planes as in Fig. 5.2 are shown, however, the non-turbulent regions are colored by dark blue. Also, shown, the stoichiometric mixture fraction isochronous with black lines. It is clearly seen that the edge of the jet is highly intermittent; the surrounding non-turbulent air is entering the jet by the so called entrainment process and mixed with the fuel. On the plane corresponding to the mean stoichiometric mixture

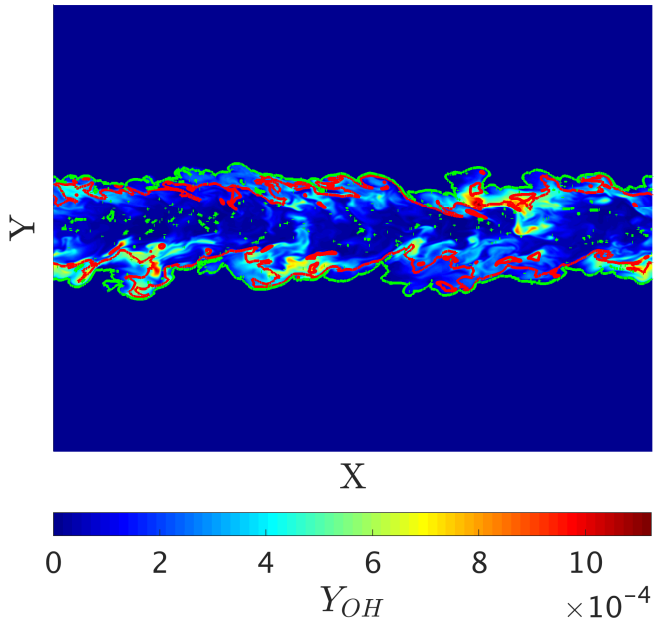


**(a)**

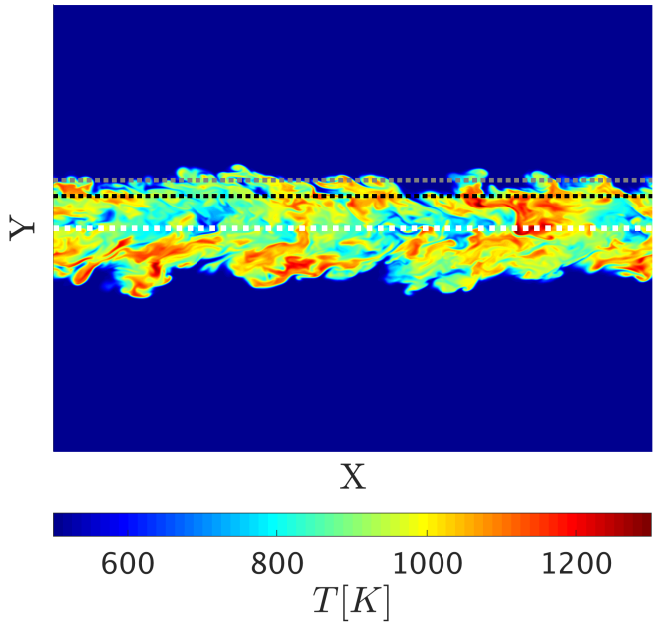


**(b)**

**Figure 5.1:** *Data extracted from case H at t=20$t_j$ on the central $Oxy$ plane: (**a**) OH mass fraction, with the green lines the T/NT interfaces and the red lines the stoichiometric mixture fraction isolines; (**b**) Temperature, with white dashed line the location of the central $Oxz$ plane, black dashed line an $Oxz$ plane corresponding to the Favre mean stoichiometric mixture fraction and the gray dashed line $Oxz$ a plane corresponding to the maximum of Favre mean density fluctuations.*

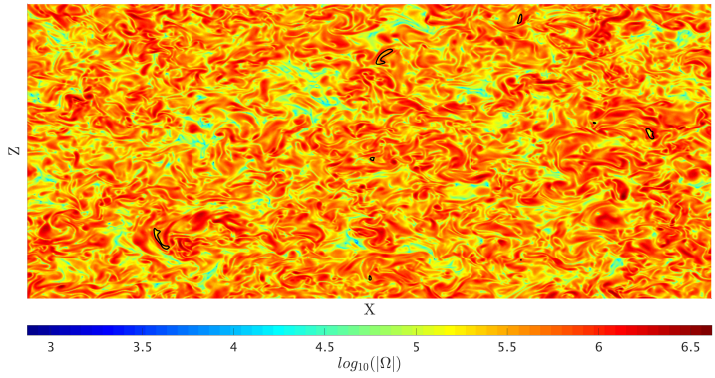


**(a)**

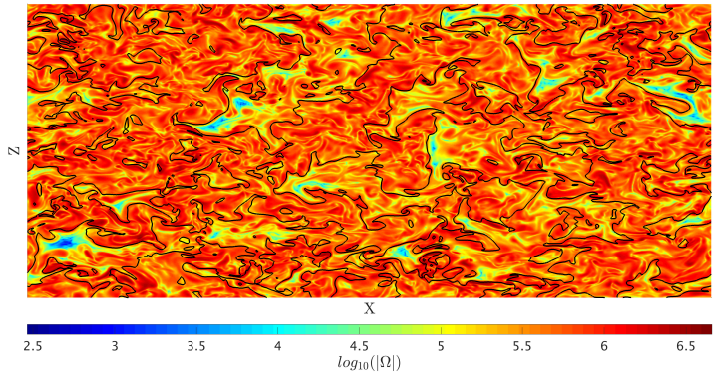


**(b)**

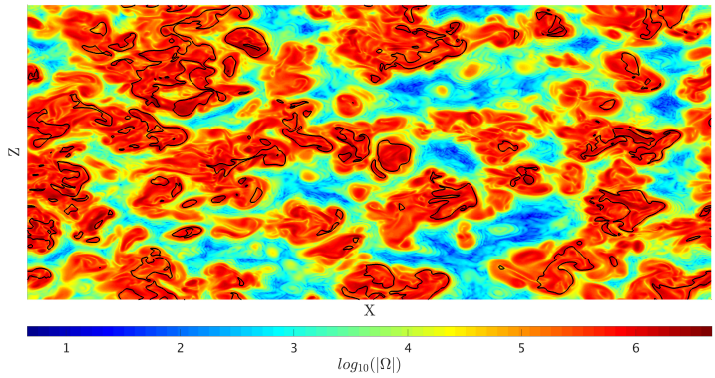


**(c)**

**Figure 5.2:** *Logarithm of the vorticity magnitude in three different planes across the jet at t=20$t_j$ for case H. (**a**) On the central plane; (**b**) On the plane corresponding to Favre mean stoichiometric mixture fraction; (**c**) On the plane corresponding to the maximum Favre mean density fluctuations. The black lines are the stoichiometric mixture fraction isolines.*

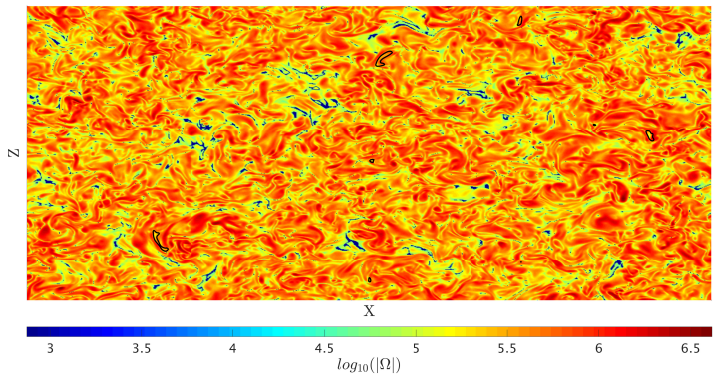


**(a)**

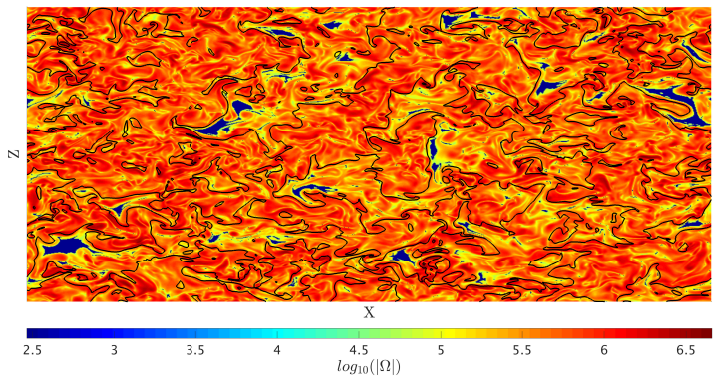


**(b)**

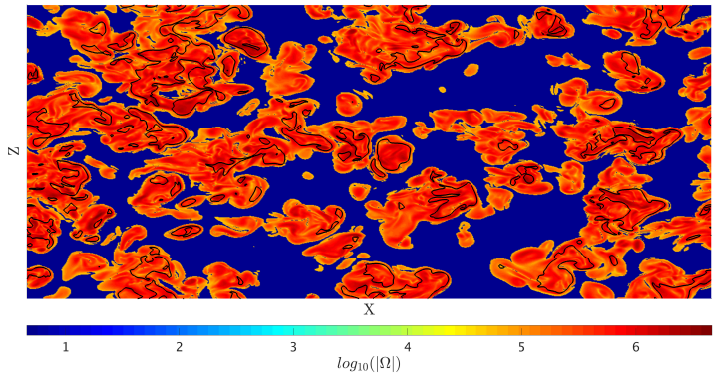


**(c)**

**Figure 5.3:** *The same as Fig. 5.2 but the dark blue color shows the non-turbulent regions detected by the threshold.*

fraction, the flow is almost everywhere turbulent. The stoichiometric surface is highly convoluted and it is clearly seen that it lies within turbulent regions.

The way to quantify the above observations is to use the external intermittency factor, $\gamma_{ext}$. The term seems to be first introduced by Townsend [150] to quantify "the mean fractional duration of turbulent flow at any given point" in the experiments of turbulent wakes. The theory then more described in [143]. In the current study, we are dealing with temporal jets and the definition is slightly different; the external intermittency factor is "the mean fractional volume (in 3D space) of turbulent flow at any given time". Further, since the cases are statistically 1D, at each time instant, the external intermittency factor can be defined in different crosswise locations. Following [38] and [151], the turbulence indicator function is defined as:

$$I(\mathbf{x},t) \equiv H(w(\mathbf{x},t) - w_{threshold}), \tag{5.2}$$

with $H$ the Heaviside function. Then, $\gamma_{ext}$ is defined as the mean of the indicator function:

$$\gamma_{ext} \equiv \langle I(\mathbf{x},t)\rangle = \underline{I(\mathbf{x},t)}, \tag{5.3}$$

where the $\underline{(.)}$ was already defined in Eq. 2.14. The external intermittency factor then can be used to define conditional means, conditioned on the turbulent/non-turbulent regions of the flow [38]. The turbulent mean of a fluctuating quantity $q$ is denoted by $\langle q\rangle_t = \underline{q}_t$ and numerically can be evaluated by a weighted average of a quantity, using the turbulence indicator function as the weight ( [152]). Then the non-turbulent average is:

$$\left(\underline{q} - \gamma_{ext}\underline{q}_t\right) / \left(1 - \gamma_{ext}\right). \tag{5.4}$$

The conditional mean, conditioned on turbulent regions, will be used in next sections. In Fig. 5.4 the external intermittency factor, $\gamma_{ext}$, computed at t=20$t_j$ using the threshold $w_{threshold} = 0.1\underline{w_{CP}}$, with $\underline{w_{CP}}$ the mean central plane vorticity magnitude [140, 146], for the DNS cases L, M and H are depicted. The vertical lines show the location $y$ of selected $Oxz$ planes used to extract the statistics (see also Fig .5.1b). As expected, in the core jet region the external intermittency factor is very close to 1 and by approaching the edges of the jet from the center ($y = 0$) the flow becomes progressively intermittent. The location of mean stoichiometric mixture fraction plane is very close to T/NT interface. Moreover, it is observed that the plane corresponding to maximum of $\underline{\rho'^2}$ is in highly intermittent flow at this time instant corresponding to the maximum local extinction events.

#### Velocity Fluctuations Statistics

In this section the objective is to analyze the PDFs of velocity fluctuations in the turbulent region and to compare them with the normal distribution. Further, the unconditioned statistics will be also presented to express the effect of external intermittency on velocity statistics. It is believed that the PDFs of velocity fluctuations in HIT are nearly Gaussian but not exactly (see [153]). In Fig. 5.5 the PDFs are plotted in three different crosswise locations (the three planes mentioned in Fig. 5.1b). Note that the data is non-dimensionalized by the use of standard deviation (Eq. 2.15). The Gaussian (normal) PDF is defined in Eq. 2.20. Since the data is normalized, the standard deviation in Eq. 2.20 is set equal to 1. The PDFs obtained by sampling in the whole region are

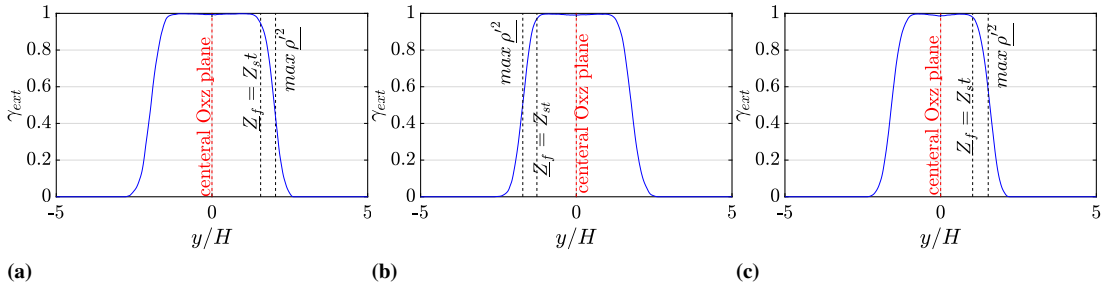


**Figure 5.4:** *The external intermittency factor, $\gamma_{ext}$, computed at t=20$t_j$ using the threshold of $w_{threshold} = 0.1 \times$ mean centerline vorticity magnitude, for case (**a**) L; (**b**) M; (**c**) H. The vertical lines show the crosswise locations, y, of selected $Oxz$ planes used to extract the statistics.*

shown by green lines, while the black lines are the conditional statistics conditioned on turbulent regions. The turbulent regions are detected by the use of the threshold explained above (i.e., $w_{threshold} = 0.1\underline{w_{CP}}$). Moreover, when sampling in turbulent regions, the mean and fluctuations are $\underline{q}_t$ and $q_t' = q - \underline{q}_t$.

First, the effect of external intermittency is clearly seen in the peaky shape (highly skewed) of PDF of unconditional data in Fig. 5.5c. The fluctuations in turbulent region (black line in Fig. 5.5c) are closer to the normal distribution. On the other hand, as can be seen in Fig. 5.5a and 5.5b, the conditional and unconditional fluctuations PDFs are similar (at least in the resolution used here to extract the PDF). This is because the large scale intermittency (simultaneous occurrence of irrotational and turbulent flows) in the central plane and the stoichiometric plane is low (see Fig. 5.3a and 5.3b). It is clear that the distribution is not normal but close to. The behavior is the same as the one in non-reacting cases; In the center of free shear flows, the PDFs are bell-shaped, but not exactly Gaussian, and the departure from Gaussian behavior becomes pronounced in the intermittent region toward the edge of the flow [38].

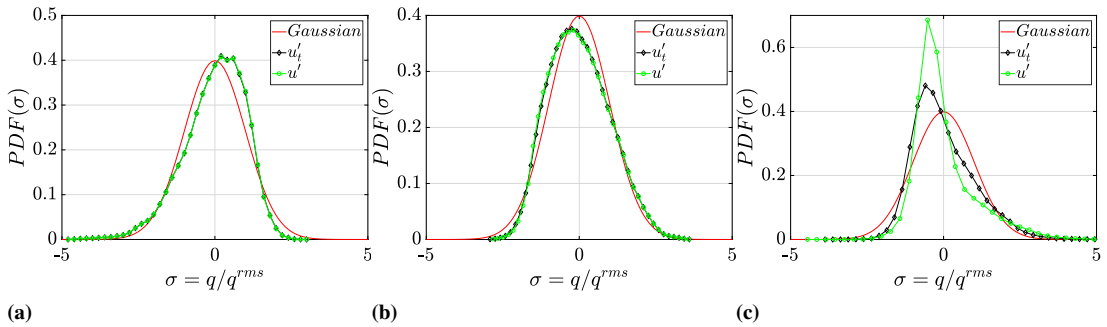


**Figure 5.5:** *Probability density functions (PDF) of the normalized velocity fluctuations in turbulent and the whole region compared with the Gaussian PDF extracted from case H at t=20$t_j$ on (**a**) the central $Oxz$ plane; (**b**) the plane corresponding to the mean stoichiometric mixture fraction; (**c**) the plane corresponding to the maximum of density fluctuations RMS.*

As explained in Sec. 2.2, higher order moments of fluctuating quantities can be used to quantify the shape of the PDFs. The skewness, i.e., Eq. 2.18 shows the degree of asymmetry of PDF. If the PDF of a function is symmetric (as is the case for a Gaus-

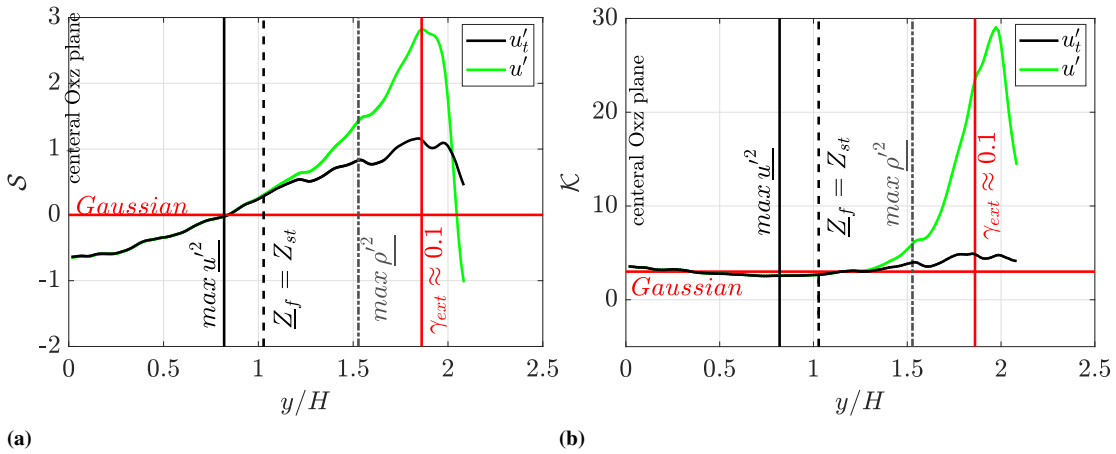


**Figure 5.6:** *The statistics of streamwise velocity fluctuation, $u'$, extracted from case H at t=20$t_j$ across the reacting shear layer, (**a**) skewness ; (**b**) flatness.*

sian), the skewness is zero. The flatness, i.e., Eq. 2.19, is the normalized fourth moment which highlights the probability of extreme events (with values much higher than the mean). The Gaussian PDF has a flatness of 3. In Figs. 5.6a and 5.6b the skewness and flatness of streamwise velocity fluctuations in different planes across the shear layer are depicted, respectively. The green and black lines are the unconditional and conditional statistics, respectively. Further, the vertical locations of different planes with respect to the central $Oxz$ plane are marked by vertical lines. Considering Fig. 5.4c the stoichiometric plane is approximately where the external intermittency effects start to increase. It is so more clear that why after this location the two skewness factors computed with and without conditioning on turbulent regions in Fig. 5.6a start to depart from each other. The flow after approximately $\gamma_{ext} \approx 0.1$ is more laminar than turbulent and the fluctuations starts to decrease; that is why the rapid decrease of skewness is observed in Fig. 5.6a. The skewness crosses zero approximately on the plane of maximum TKE which is consistent with the observation in [33] where the velocity statistics were reported in reacting turbulent wall-jets. It is believed that that turbulent bursts bringing high contributions $u' < 0$ and laminar fluid bringing small contributions $u' > 0$ [75] which creates the shape of skewness observed in Fig. 5.6a. The occurrence of zero crossing of the skewness and local minimum of flatness show that in this region the PDF is most similar to Gaussian behavior. The local minimum of flatness is more clear in Fig. 5.8b. In Fig. 5.7 the PDFs of $u'_t$ are studied in high vorticity regions. The threshold is successively increased from $0.1\underline{w_{CP}}$ to $2\underline{w_{CP}}$. In Fig. 5.7 it is clearly observed that the statistics approach to normal distribution. This means that fluctuations in high vorticity regions are very close to normal. Although the PDFs are still slightly skewed which is due to the effect of anisotropy produced by the shear. It is also more clearly shown in Fig. 5.8 where the skewness and flatness factors of $u'_t$ calculated across the jet are shown. In very high vorticity regions, the statistics tend to be closer to Gaussian. Having detected the turbulent zones, in the next section the statistics of velocity gradients will be studied in these zones.

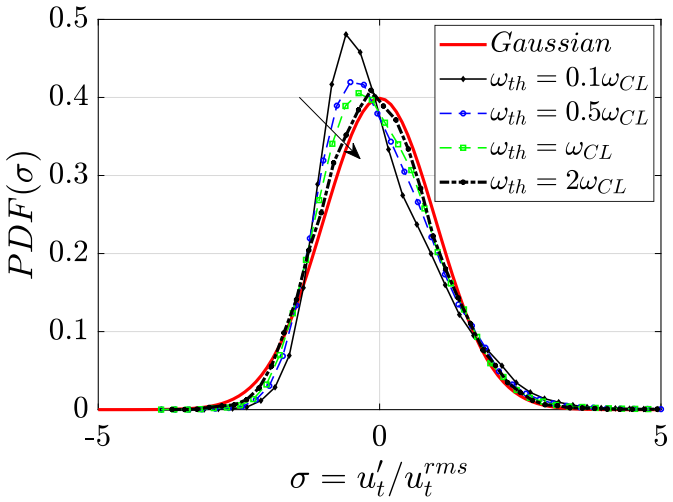


**Figure 5.7:** *Probability density function (PDF) of normalized velocity fluctuations in turbulent region detected by different magnitude of vorticity thresholds extracted from case H at t=20$t_j$ on the plane corresponding to the maximum of density fluctuations RMS. Arrows show the direction of increasing* $w_{threshold}$.

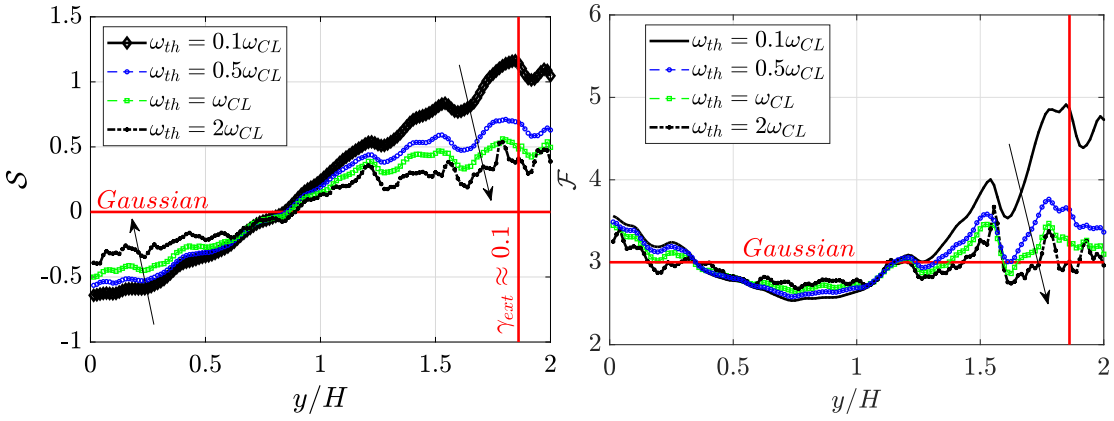


**Figure 5.8:** *The statistics of streamwise velocity fluctuation in turbulent regions,* $u_t'$*, using different magnitude of vorticity thresholds extracted from case H at t=20$t_j$ across the reacting shear layer, (**a**) skewness ; (**b**) flatness. Arrows show the direction of increasing threshold.*

### 5.2.2 Small Scale (Internal) Intermittency

The small scale (internal) intermittency is the occurrence of extreme rare events with orders of magnitude higher than the mean of the events. In the turbulent region itself, although the fluctuations of velocity and scalars are nearly Gaussian, the derivatives are not Gaussian or even close to it. The long tails of PDFs of derivatives of e.g. fluctuative velocity components are the sign of rare extreme events which can be orders of magnitude higher than the mean value. A characteristic of intermittency is that extreme amplitudes are far more probable than one may estimate from Gaussian considerations [31]. In this section we are interested to characterize such events. The intermittency in both velocity dissipation and scalar dissipation has been the subject of many previous studies. Experimentally, it is observed that the statistical behavior of scalar dissipation rate, $\chi$, is similar to that of the instantaneous turbulence dissipation, $\varepsilon$, in terms of their strong intermittency. In other words, a frequent occurrence of instantaneous values much larger than the mean is observed. However, the frequency and magnitudes of the fluctuations in scalar dissipation rate are larger than those in $\varepsilon$ [154]. The intermittency in scalar dissipation rate is much higher than the one in TKE dissipation rate. [155]. In this section the focus is on TKE dissipation intermittency. The interested reader should refer to the reviews in [28, 156] on the scalar dissipation intermittency.

Batchelor and Townsend [107] state that:

> Energy associated with large wavenumbers is very unevenly distributed in space. There appear to be isolated regions in which the large wavenumbers are 'activated', separated by regions of comparative quiescence. This spatial inhomogeneity becomes more marked with increase in the order of the velocity derivative, i.e. with increase in the wavenumber.

It is referred to large wavenumbers (small scales or fine structures) and also the order of velocity derivative. Batchelor and Townsend [107] observed that the PDF of velocity derivatives becomes increasingly non-Gaussian by increasing the order of derivative. Deviation from Gaussian behavior here means the increase of the flatness (Eq. 2.19), or in other words, rare events with values much larger than the mean. Dissipation of turbulence contains the product of velocity gradients (Eq. 2.115). Consider the simple definition of TKE dissipation in constant-density isotropic turbulence [50], Eq. 2.58. The instantaneous one-dimensional surrogate for dissipation can be defined as:

$$\varepsilon^{s}_{inst} \equiv 15\nu \left(\frac{\partial u'}{\partial x}\right)^2, \tag{5.5}$$

where $u'$ is the streamwise component of velocity fluctuation vector ($U'(\mathbf{x},t) = (u',v',w') \equiv U(\mathbf{x},t) - \underline{U(\mathbf{x},t)}$). Note the difference between Eq. 5.5 and Eq. 2.58 is that in the former no averaging operator exists. So this is the instantaneous/local dissipation. Eq. 2.58 is repeated here for convenience:

$$\varepsilon^{s} = 15\nu\underline{\left(\frac{\partial u'_1}{\partial x_1}\right)^2}. \tag{5.6}$$

Using Eq. 2.19 and computing the flatness of velocity gradient, it is readily seen

that:

$$\mathcal{F}_{\frac{\partial u'}{\partial x}} = \underline{\frac{\partial u'^4}{\partial x}} \Big/ \sqrt{\underline{\frac{\partial u'^2}{\partial x}}^4} = \underline{\frac{\partial u'^4}{\partial x}} \Big/ \left(\underline{\frac{\partial u'^2}{\partial x}}\right)^2 = \underline{\left(\varepsilon^s_{inst}{}^2\right)}/\varepsilon^{s2}, \tag{5.7}$$

where $\varepsilon^s$ is the average pseudo-dissipation already defined in Eq. 2.58. The mean square of dissipation fluctuations is related to the flatness of longitudinal gradient of streamwise velocity fluctuations, $\dfrac{\partial u'}{\partial x}$. One of the observations of Batchelor and Townsend [107] was, the increase of flatness (left hand side of Eq. 5.7) by increasing the Reynolds number in grid generated turbulence. They related this to the intermittent character of turbulent energy dissipation ($\varepsilon_{inst}$). The observation had a profound effect on the research in turbulence. Refined Kolmogorov's [157] theory in 1962 (K62) which added the internal intermittency effects in high order structure functions (see Sec. 2.2.4) and inertial range spectrum was based on this observation. Although then, it was found that the intermittency effect on the velocity spectrum is low since it can be considered as a low order ($n = 2$) structure function in physical space.

It will be interesting to check in our DNS database if the same dependency exists for the general form of instantaneous/local Favre dissipation or not. This means that the compressible form of instantaneous/local dissipation is defined as:

$$\varepsilon_{inst} \equiv \frac{1}{\rho}\tau'_{ij}\frac{\partial u''_i}{\partial x_j}, \tag{5.8}$$

and it is searched for the dependency like:

$$\mathcal{F}_{\frac{\partial u''}{\partial x}} \propto \underline{\left(\varepsilon^2_{inst}\right)}_f \Big/ \left(\underline{\varepsilon_{inst}}_f\right)^2. \tag{5.9}$$

Of course in DNS the right hand side can be computed directly, however, in experiments usually only the left hand side can be computed.

Going back to Eq. 5.7, we are interested to have a model for dissipation fluctuations or in other words $\gamma_{int}$. $\gamma_{int}$ is related to the flatness by [112]:

$$\gamma_{int} \equiv \frac{1}{\underline{\left(\varepsilon^s_{inst}{}^2\right)}/\varepsilon^{s2}} \propto \frac{1}{\mathcal{F}_{\frac{\partial u'}{\partial x}}}, \tag{5.10}$$

Note that we are not interested to calculate the exact value of internal intermittency factor from DNS as it can be an interesting topic for the future work[2]. Here it is intended to search for a power law scaling like what will be introduced in the following.

The phenomenological approaches for $\gamma_{int}$ scaling started by Townsend [158] where it was suggested that the dissipative structures are random vortex sheets and lines. Based on this argument and assuming vortex sheets of size $\underline{\eta}$ surrounded by the large eddies of integral length scale, Corrsin [111] proposed a phenomenological model:

$$\underline{\left(\varepsilon^s_{inst}{}^2\right)}/\varepsilon^{s2} \propto Re_\lambda^{3/2}. \tag{5.11}$$

The derivation can be found in [111] but the most important assumption is the sheet like dissipative structures. Note that using Eq. 5.10, the relation used in original Magnusen

[2] In [112] $\gamma_{int}$ is calculated in grid generated turbulence and round jet experiments using high-passed filters.

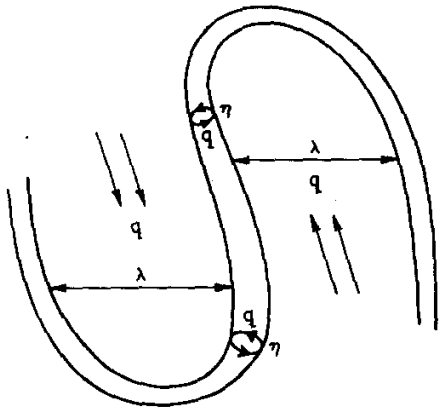


**Figure 5.9:** *From [103], the schematic of Tennekes Model for dissipative structures.*

EDC [13] and the LES version of Fureby EDC [97] to describe the volume fraction occupied by fine structures can be detected, i.e., $\gamma_{int} \propto Re_\lambda^{-3/2}$.

Tennekes [103], however, assumed that the dissipative structures are tubes (rather than sheets) with diameter $\underline{\eta}$ surrounded by the large structures of Taylor length scale (see Fig. 5.9), $\lambda$, (Eq. 2.62) which results in:

$$\underline{\left(\varepsilon_{inst}^{s\,2}\right)}/\varepsilon^{s2} \propto Re_\lambda. \tag{5.12}$$

Again using Eq. 5.10, the Tennekes model results in $\gamma_{int} \propto Re_\lambda^{-1}$ which is the intermittency factor used in other versions of EDC [14] and the LES version of EDC by the Norwegian group [16].

Finally, the (K62) theory predicts the Re dependency of $\mathcal{F}_{\frac{\partial u'}{\partial x}}$ as:

$$\underline{\left(\varepsilon_{inst}^{s\,2}\right)}/\varepsilon^{s2} \propto Re_\lambda^{3\mu/2} \propto Re_\lambda^{3/8}, \tag{5.13}$$

with an experimentally predicted and accepted value, $\mu \approx 1/4$ [38] as the so called "intermittency exponent". As can be seen the power is much lower than the one used in sheet-like or tube-like phenomenological models.

In experimental studies, Kuo and Corrsin [112] did the experiments in grid-generated turbulence and on the axis of a round jet and saw $\mathcal{F}_{\frac{\partial u'}{\partial x}}$ increases as $Re_\lambda^{0.2}$ in $Re_\lambda < 200$ range, following a transition zone up to $Re_\lambda \approx 500$, increases more rapidly as $Re_\lambda^{0.6}$. This experiment showed a dependence weaker than what proposed in Eq. 5.11 or Eq. 5.12. A kind of transition was also observed in the experimental work of [159], however, the more recent data reject it and relate it to the size and resolution of probes in previous experiments [160]. Gylfason et al., [160] found from the grid generated turbulence, the dependency like $\mathcal{F}_{\frac{\partial u'}{\partial x}} \propto Re_\lambda^{0.39}$ for the range, $100 \leq Re_\lambda \leqslant 900$ which is very close to K62 prediction (Eq. 5.13). Ishihara et al., [161] did the DNS of non-reacting HIT for $Re_\lambda > 100$: The DNS data suggest that the $Re_\lambda$ dependence of skewness and flatness of the longitudinal velocity gradients fit well with a simple power law: $\mathcal{S} \sim -0.32 Re_\lambda^{0.11}$ and $\mathcal{F} \sim 1.14 Re_\lambda^{0.34}$. As can be seen the power is close to the experiments in [160].

It should be mentioned that in most of the works, atmospheric surface layer (ASL) data in high Taylor Reynolds numbers, $Re_\lambda > 1000$ are also included when trying to

find a fit for the data. However, recently, Antonia et al., [113] argue that these data must be excluded from data compilations and fittings. They showed both theoretically and experimentally that there is an asymptotic for both the skewness and flatness of velocity derivative. Antonia showed that for sufficiently high Taylor Reynolds number, $Re_\lambda > 300$, $\mathcal{S}_{\frac{\partial u'}{\partial x}}$ is constant independent of $Re_\lambda$ and is approximately $-0.53$ in the experiments on the flow axis in the far-field of a round jet, decaying grid turbulence, the centerline of a fully developed channel flow, and the axis in the far-wake of a circular cylinder. However, the way to approach this constant depends on the flow type [26, 35, 113]. Also $\mathcal{F}$ found to be approximately constant for $Re_\lambda > 500$ on the axis of the plane jet. In fact, K41 predicts that of $\mathcal{S}_{\frac{\partial u'}{\partial x}}$ is constant. However, K62 predicts that it increases with $\mathrm{Re}_\lambda$ without bound. The same is true for $\mathcal{F}_{\frac{\partial u'}{\partial x}}$. The recent findings in Antonia's group, violates K62 and is consistent with K41. It is believed that what causes the departure from the original K41 predictions is the "finite Reynolds number" (FRN) effects not the fault in the model itself [26, 27, 35, 113, 114]. This seems to be a breakthrough in the field! The skewness of velocity fluctuations gradients is important parameter for RANS turbulence models like $k - \varepsilon$ while their flatness is important for example in EDC. So it seems that in models, the Reynolds power dependency must be dropped when the case under consideration has $\mathrm{Re}_\lambda$ larger than the critical values mentioned above. However, in the current DNS database and in many laboratory experiments, $\mathrm{Re}_\lambda$ is lower than 500. So it is expected that the dependency to Re is observed. In other words, we want to find out with which rate (power of $Re_\lambda$) the flatness in reactive jets (specifically on the centerline of plane jets) reaches the hypothesized constant discovered by Antonia.

In Fig. 5.10, $\mathcal{F}_{\frac{\partial u''}{\partial x}}$, i.e., the flatness of gradient of streamwise component of Favre fluctuations of velocity, is plotted across the upper half of the reacting shear layers for the DNS case H at t=20$t_j$. $y/H = 0$ is the central $Oxz$ plane. The green dashed and black lines show the statistics computed in the full zones (both T and NT regions) and in only the turbulent zones (T regions), respectively. The vertical lines shows the positions (cross wise location $y$) where $\gamma_{ext} = 0.99$ and 0.1. The distribution of $\gamma_{ext}$ was already shown in Fig. 5.4. From the central plane of the jet ($y = 0$) up to the first vertical dashed line in Fig. 5.10 the external intermittency factor is almost constant and the flow can be considered turbulent in the whole region. Due to entrainment of irrotational laminar flow to the core jet region, the flow becomes inhomogeneous and $\gamma_{ext}$ starts to decrease. It is obvious that the statistics are very similar until a point ($\gamma_{ext} = 0.99$) where external intermittency effects become important. In the intermittent region, the unconditional flatness (green lines) increases by decreasing the $\gamma_{ext}$. This is actually the sign of external intermittency phenomenon, i.e., increase of flatness by approaching the edge of the jet. Since in this section we were interested in internal intermittency effects, it is tried to exclude the effects of inhomogeneity caused by the shear (at least partly) by conditioning the statistics on only turbulent regions detected by the using the vorticity threshold defined in the previous section. The black lines are the conditional statistics, conditioned on turbulent regions. It is observed that the increase of flatness is much lower than the one observed in un-conditional statistics.

If one relies on the green lines in Fig. 5.10, it may be concluded that the flatness in the core jet region (the left side of vertical line showing $\gamma_{ext} = 0.99$) is almost constant. Now lets take a look at the conditional statistics itself. In Fig. 5.11 it is tried

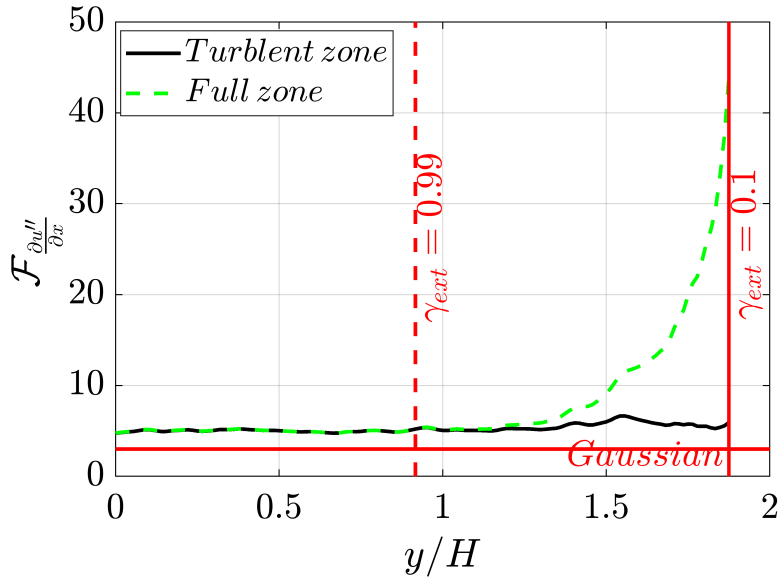


**Figure 5.10:** *Flatness of streamwise velocity fluctuation gradient computed in full zone (green dashed line) and only turbulent zones (black line), extracted at t=20$t_j$ across the reacting shear layer of case H. Upper half of the data have been used, from the center plane ($y/H = 0$) to a plane where the external intermittency factor, $\gamma_{ext} = 0.1$.*

to check the Eq. 5.9. In this figure, the flatness of $\frac{\partial u_t''}{\partial x}$ (solid black) and $\frac{\partial u_t''}{\partial y}$ (dashed black) are plotted and compared with $\underline{\varepsilon}^2_{f,t} / \left(\underline{\varepsilon}_{f,t}\right)^2$ (red line with diamond markers). It should be mentioned that hereafter $\underline{\varepsilon_{inst}}^2_{f,t} / \left(\underline{\varepsilon}_{f,t}\right)^2$ and $\underline{\varepsilon}^2_{f,t} / \left(\underline{\varepsilon}_{f,t}\right)^2$ will be used interchangeably. Like before the subscript $f$ refers to Favre averaging and the subscript $t$ refers to conditional statistics in turbulent zones only. This means that while using Eq. 2.115 to compute the TKE dissipation, the fluctuations are computed based on turbulent zones only. Further, the instantaneous/local dissipation formula is Eq. 2.115 without using Favre average operator. The Favre RMS is computed using Eq. 2.38 replacing the Favre average operators with the conditional turbulent ones.

First of all, it must be mentioned that as a first glance, it is obvious that the statistics are not well converged, there are local peaks at each $Oxz$ plane corresponding to each $y$ in the figure. To calculate the statistics, approximately $10^6$ points are used at each instant of time. At each $Oxz$ plane, about $0.5 \times 10^6$ cells exists for the case H and the data points are doubled using symmetry assumption about $y = 0$. The temporally evolving jets produce time dependent statistics and no stationary condition exists, so it is not possible to do the averaging in time. Considering the temporal evolution of flame dynamics which first experiences local extinction and then re-ignition, it will be meaningless to try to increase the data set using other time instants. The other point is the strong shear exists in the flow, so it is not also possible to increase the database using the data in the whole domain across the jet like what is done in decaying HIT DNS. The main goal of the study in this section is to study the internal intermittency in jet flames so again it will be meaningless to accumulate the data across the jet. So this is a compromise for studying complex physics. In the conclusion section of the thesis this will be more discussed.

As can be seen in Fig. 5.11, the flatness of $\frac{\partial u_t''}{\partial y}$, compared to $\frac{\partial u_t''}{\partial x}$, is more correlated with $\underline{\varepsilon}^2_{f,t}/\left(\underline{\varepsilon}_{f,t}\right)^2$ across the reactive jet. The trend (decreasing up to around $\gamma_{ext} = 0.99$ and increasing afterward ) approximately captured. The point is that the quantity we are interested in is the fluctuations of turbulent dissipation rate not the flatness factor. By assuming homogeneity and isotropy, all nine components of dissipation are related to the longitudinal gradient of streamwise velocity fluctuations, while the assumption is true in grid generated turbulence experiments, the flows like jets depart from these assumptions due to existence of a strong shear.

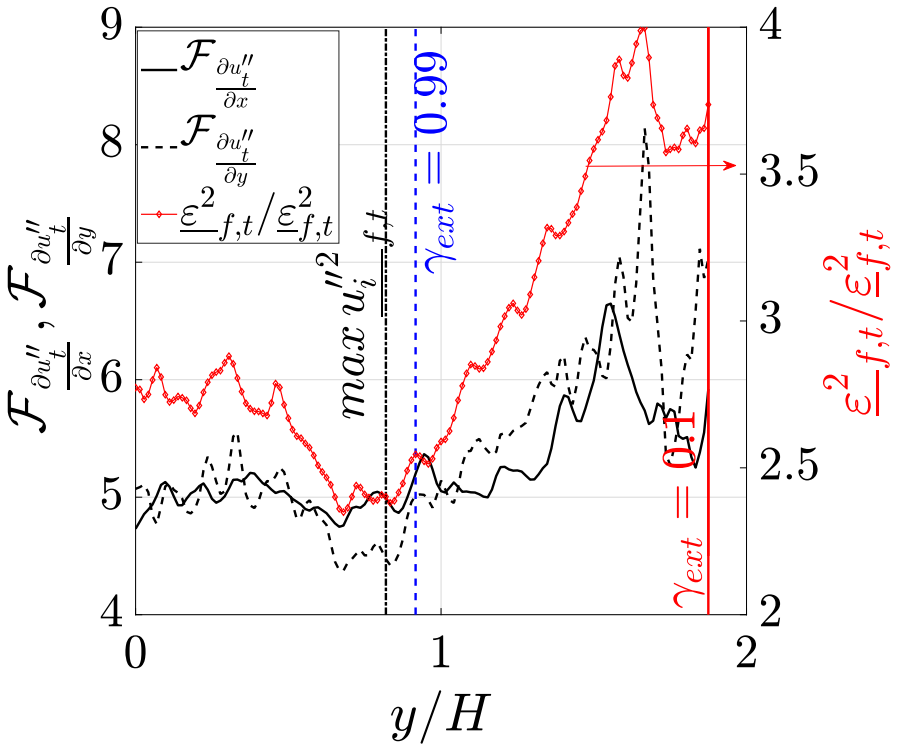


**Figure 5.11:** *Flatness of streamwise and crosswise velocity fluctuation gradients (conditioned on turbulent regions) compared with the fluctuation of dissipation rate (conditioned on turbulent regions), extracted at $t = 20t_j$ across the reacting shear layer for case H.*

Now we focus on the statistics from the central plane of the reacting jets to study the internal intermittency away from the mean shear. The data are extracted from 2 time instants of three jets (cases L, M, and H) introduced in Sec.4.5. We are interested to study the $Re_\lambda$ scaling of TKE dissipation fluctuations. In anisotropic flows, different macro scale Reynolds number can be defined using different definitions of Taylor macro scale. The three choices (i.e., in three directions in physical space) are (without summation over repeated indexes) [162][3]:

$$\lambda_{i,t}{}^2 \equiv \underline{u_i''^2}_{f,t} \Big/ \underline{\left(\frac{\partial u_i''}{\partial x_i}\right)^2}_{f,t} \qquad i = (1,2,3) = (u,v,w), \tag{5.14}$$

[3] In [162], the Reynolds version of the quantities are presented while here the Favre version conditioned on turbulent zones is presented.

which can be used to define different Taylor Reynolds numbers:

$$Re_{\lambda_i,t} \equiv \sqrt{\underline{u_i''^2}_{f,t}}\lambda_{i,t}/\underline{\nu}_{f,t} \quad i = (1,2,3) = (u,v,w), \tag{5.15}$$

Moreover, the overall Taylor Reynolds number, $\mathrm{Re}_\lambda$, was defined in Eq. 2.61 using Eq. 2.62 as the overall Taylor length scale. In Fig. 5.12 the different $\mathrm{Re}_\lambda$ are plotted for case H. It is seen that the maximum Taylor scale Reynolds number is much lower than the threshold of Antonia [113] discussed in the beginning of this section.

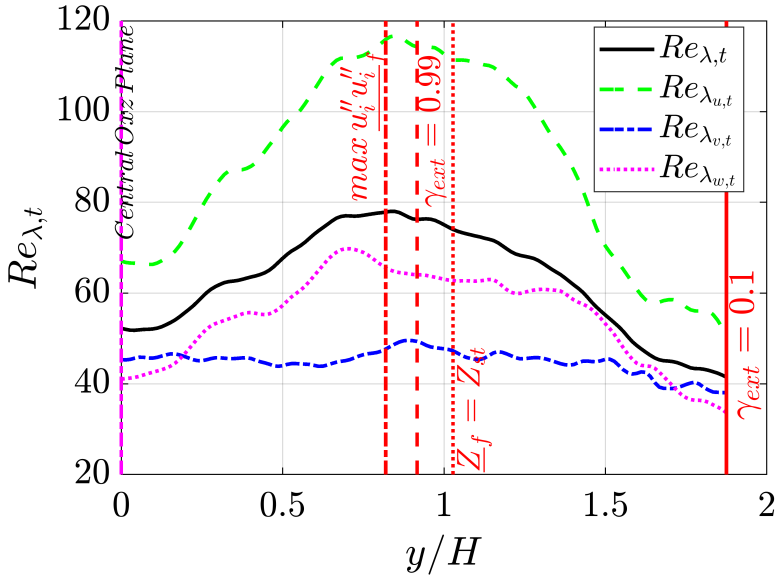


**Figure 5.12:** *Different Taylor Reynolds numbers extracted at t=20$t_j$ across the reacting shear layer for case H. Upper half of the statistics are plotted, from the center plane ($y/H = 0$) to a plane where the external intermittency factor, $\gamma_{ext} = 0.1$.*

In Fig. 5.13 $\mathcal{F}_{\frac{\partial u''}{\partial x}}$ is plotted against the $Re_{\lambda_{u,t}}$ defined in Eq. 5.15 in log-log scale. The markers colored in black are from the recent compilation of [35] in different types of non-reactive flows in low $Re_\lambda$ regime, i.e. $Re_\lambda < 300$. Of course the data from [35] are not conditional data on turbulent regions. This means to plot our reactive jet DNS data on top of the recent compilation of [35] in Fig. 5.13 we used calculated the quantities in this plot with conditional averaging (conditioned on turbulent regions) rather than conventional averaging in the whole region. Different flows are mentioned in the legend. The solid line is the fit to these reference data where the data are fitted to $\ln \mathcal{F} = \alpha + \beta \ln Re_{\lambda_u}$. Using the least square method $\alpha = 0.373$ and $\beta = 0.281$ are obtained. Then $\mathcal{F}_{\frac{\partial u''}{\partial x}}$, on the central plane of the current DNS databases are added to this compilation. It should be mentioned that here the Favre fluctuations are computed, however, the reference data is for non-reactive constant density flows. In the lower part of the diagram, the normalized second moment of the local dissipation in compressible form (i.e. the inverse of the intermittency factor in our reactive jets) computed using the same databases as before, are also added. These are unfilled color markers. The dashed line is a line with the same slope in logarithmic scale as the fitted solid line.

First of all, one should not expect that the absolute values of $\underline{\left(\varepsilon^2_{inst}\right)}_f / \left(\underline{\varepsilon}_f\right)^2$ be the same as the value of $\mathcal{F}_{\frac{\partial u''}{\partial x}}$ as we already mentioned that they are expected to be pro-

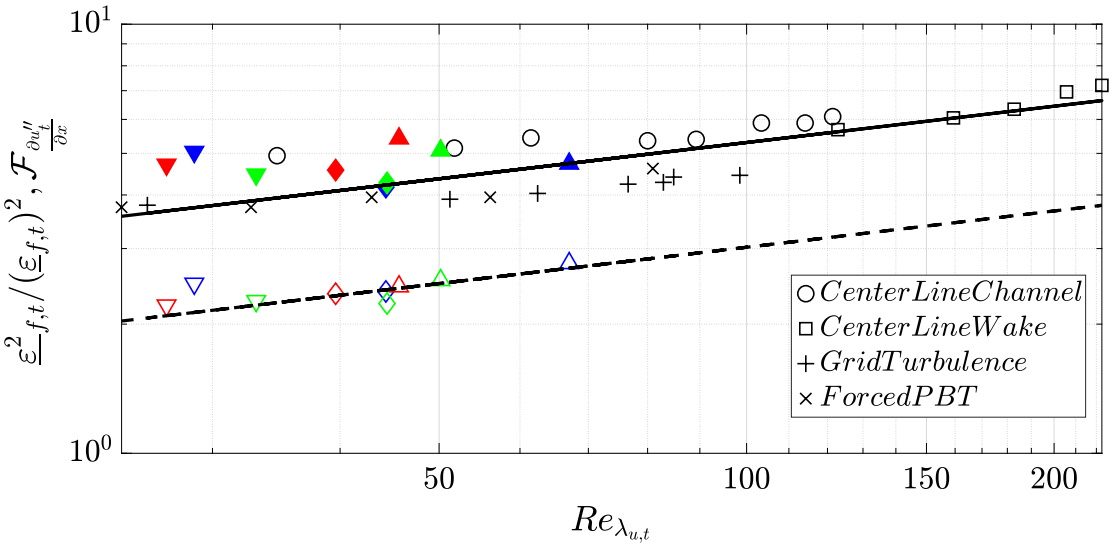


**Figure 5.13:** *The flatness factor of longitudinal gradient of streamwise velocity fluctuations versus longitudinal Taylor scale Reynolds number defined in Eq. 5.15. The inverse of intermittency factor is also shown on the lower half of the diagram. The black markers (also mentioned in the legend) are from figure 3 of [35] (the data compilation in different types of flows with low $Re_\lambda$, $Re_\lambda < 300$ ). The solid line is the fit to these reference data, $\exp(0.373)Re_{\lambda_u}^{0.281}$. The color markers are plotted on top of the diagram. These are the data extracted from the central plane of current DNS databases. Downward-pointing triangle: the low Reynolds (L) case. Diamonds: the medium Reynolds (M) case. Upward-pointing triangle: the high Reynolds (H) case. Each color refers to an instant of time. Blue: t=20$t_j$ corresponding to the maximum local extinction event in all three DNS cases. Green: t=30$t_j$. Red: t=35$t_j$. The two latter time instants are corresponding to re-ignition events where the re-ignition mainly occurs around central plane in the jet core region. Filled color markers are flatness factors. Unfilled color markers are the inverse of the intermittency factor. The dashed line is a line with the same slope in logarithmic scale as the fitted solid line.*

portional to each other using HIT assumptions not equal. Although it was observed in Fig. 5.11 that across the jet, these two seems to be not so much correlated, in Fig. 5.13 the correlation is clearly observed in the central plane of the reacting jets, away from the mean shear. This seems to be reasonable as the flow in the center of the jet is expected to be nearly homogeneous. More importantly, it is more clear that the $Re_\lambda$ scaling exists for the internal intermittency factor on the central plane of the reacting jets. The power law ($\approx 0.28$), however, is much weaker than the one predicted by the phenomenological models of Corrsin [111] ($= 1.5$) and Tennekes [103] ($= 1$) which are used for example in EDC model. One may argue that the phenomenological models and also EDC are for large Reynolds number flows. However, it is already discussed in [114] that the $Re_\lambda$ dependency becomes weaker and weaker by increasing $Re_\lambda$ and asymptotically the flatness factor of velocity gradients and so the internal intermittency factor approaches a constant value.

Now we analyze another scaling. Yakhot [36], theoretically derived a formula for the moments of the dissipation rate. Using HIT assumptions, Yakhot found a scaling like $\langle \varepsilon^n \rangle \propto Re^{0.152}$. The derivation is not presented here and the interested reader is refereed to the reference. In Yakhot derivation, $Re = u_{rms}L/\nu$ is a large scale turbulent Reynolds number, rather than the Taylor scale one. $u_{rms} = \sqrt{2TKE}$ and $L$

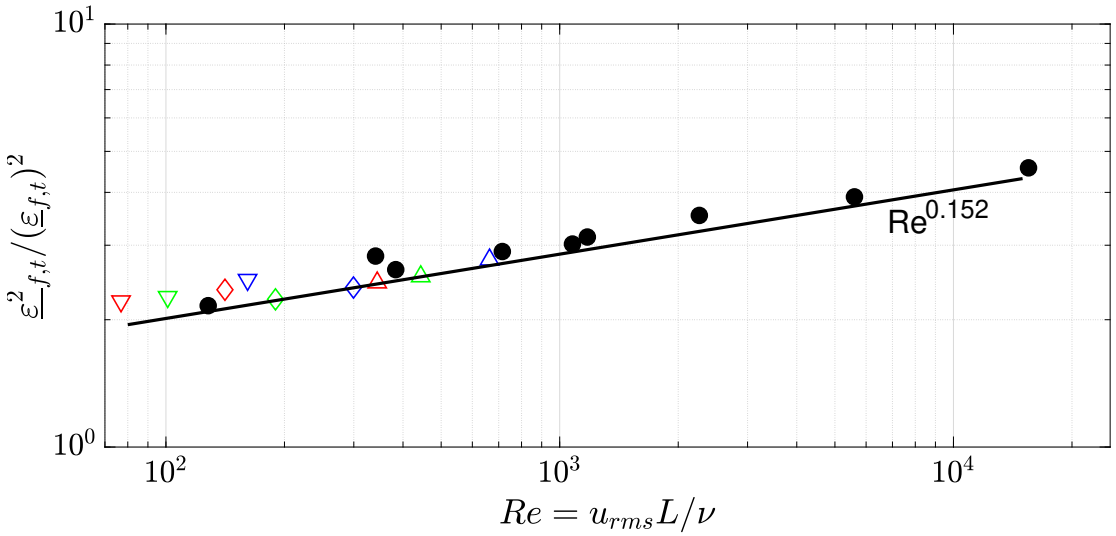


**Figure 5.14:** *Second moment of local dissipation (the inverse of internal intermittency factor) versus Reynolds number. Reynolds in defined as $Re = u_{rms}L/\nu$, with $u_{rms} = \sqrt{2TKE}$, $L$ the scale representative of large scales and $\nu$ the viscosity. The filled circles are from the HIT data compilation in [32], where $H$ was taken to be the the length of cube in DNS of HIT. The solid line is the theoretical prediction by Yakhot [36] for HIT, $Re^{0.152}$. The color markers are the data extracted from the central plane of current DNS databases. For the current reactive DNS jet data, $H$ is the initial width of the fuel jet, $Re = u_{rms,t}H/\nu_t$ is used instead of $Re$, where the subscript $t$ refers to conditional data conditioned on turbulent zones only. Downward-pointing triangle: the low Reynolds (L) case. Diamonds: the medium Reynolds (M) case. Upward-pointing triangle: the high Reynolds (H) case. Each color refers to an instant of time. Blue: t=20$t_j$ corresponding to the maximum local extinction event in all three DNS cases. Green: t=30$t_j$. Red: t=35$t_j$. The two latter time instants are corresponding to re-ignition events where the re-ignition mainly occurs around central plane in the jet core region.*

can be the integral length scale or the large scale length. For example in [32] the half of the channel width is used as $L$. In Fig. 5.14, the compilation of [32] is shown with filled circles showing the inverse of internal intermittency factor,$1/\gamma_{int} \propto \left(\varepsilon^s_{inst}{}^2\right)/\varepsilon^2$, in HIT and with solid black line the theoretical prediction of Yakhot [36]. Note that this is not the fit but the theoretical prediction. Then the data extracted from the central $Oxz$ plane of the current DNS databases are added on the plot. For simplicity we considered the initial width of the fuel jet in each DNS cases, $H$, as the length scale representing large scale. Also the TKE in the formula for $Re$ is the Favre averaged TKE defined in Eq. 2.52 conditioned on turbulent zones. Interestingly, the data fitted very well to the theoretical prediction and HIT data. Consider that the database consists of jets with different $Re$ and different regimes. It shows that the internal intermittency in these reactive jets also scales with the $Re = u_{rms}L/\nu$.

Having confirmed the increase of internal intermittency on the central plane of the reactive jets with increasing large scale Reynolds number with a power law like $\approx Re^{0.15}$, it is the time to go further and check if this is the case across the jet. The point is that, in numerical simulations, the theory proposed for non-reactive ideal cases (HIT and also on the central plane of the jet flow, away from the mean shear) are used in the whole domain. Specifically, it is observed that in jet flows, the stoichiometric surface lies adjacent to the T/NT interface, where the HIT assumptions are not in general preserved. The postulate of local isotropy implies an invariance with respect to

spatial rotations of the statistical properties of small scales of turbulence. Even though the large scales are anisotropic in all practical flows, it is thought that the small scales at high Reynolds numbers are shielded from anisotropy. However, at any finite Reynolds number, some residual effects of small-scale anisotropy may exists [163]. Further, the mean shear, exists in free shear flows like jets, is the source of large scale anisotropy.

In Fig. 5.15 the inverse of $1/\gamma_{int}$ is plotted against the Reynolds number ($Re = u_{rms}L/\nu$) defined above across the reactive jets. The left figures are data for the high Reynolds (case H) and the right ones for the medium Reynolds (case M). The top figures are the data at t=20$t_j$ corresponding to the maximum extinction event for each case. The middle and bottom figures are the data at t=30$t_j$ and t=35$t_j$, respectively, where the flame is in re-ignition mode. In these figures $y/H = 0$ is the central $Oxz$ plane of the jets and increasing $y$ is the direction toward the edge of the flame ($\gamma_{ext} \approx 0.99$) and to the highly intermittent flow($0.99 \leq \gamma_{ext} \leq 0.1$) and to the laminar dominating flow ($\gamma_{ext} > 0.1$) . From a first glance, the revealing behavior is the increase of $\overline{\left(\varepsilon^s_{inst}{}^2\right)}/\varepsilon^2$ while approaching the laminar outer flow from the edge of the flame. Consider that the term is computed solely in turbulent zones not in the whole region. As already shown in Fig. 5.10 for velocity derivative flatness and also shown here in Fig. 5.16 for second moments of energy dissipation, if one does not exclude the irrotational flow from the statistics, both flatness and dissipation moments will increase very rapidly due to external intermittency effects. Having this in mind, it is tried to exclude the effect of laminar entraining flow from the statistics. However, now, looking at Fig. 5.15, it is still observed that the moments are increasing (although with much less slope) in the intermittent zone ($0.99 \leq \gamma_{ext} \leq 0.1$). It can be postulated that, since the statistical analysis is carried out in 2D $Oxz$ planes[4], at each plane, there can be a part of stretched 3D vortexes. The dissipation structures are known to be elongated filament like structures [64, 69, 164], so that in a 2D cut away from the fully turbulent core jet region, there may be isolated highly vortical structures with elevated dissipation around them. This can be observed in Fig. 5.17 where the magnitude of vorticity and also the inverse of intermittency factor on an $Oxz$ plane are shown at $y/H = 2.625$ corresponding to the peak in Fig. 5.15f. The high vorticity region is highlighted by the yellow arrow in Fig. 5.17a and the corresponding location where high dissipation fluctuation occurs is marked in Fig. 5.17b.

The second moment of local dissipation is plotted against $Re_{\lambda,t}$ in Fig. 5.18a for the DNS cases H and M at times t=20$t_j$ and t=30$t_j$. Also the same quantities are plotted against the large scale $Re$ for cases H and M at two time instants in Figs. 5.18b and 5.18c, respectively. The black markers refers to the data in intermittent flow ($\gamma_{ext} < 0.99$). The markers are colored when entering the nearly turbulent region up to core of the jet (i.e. central $Oxz$ plane). Both axes of the figures are in logarithmic scales. It seems that the behavior is so chaotic that cannot be represented by a single scaling. On average, it may be concluded (as before) that by approaching the edge of the jet from the outer laminar coflow, the second dissipation moment is decreasing while Reynolds number (both $Re_t$ and $Re_{\lambda,t}$) are increasing. Also for example for case H a trend is similar, by continuing the path from the edge of the jet to the core jet region, we can

[4]It was already described that since 2 homogeneous direction exists in the current temporally evolving jets (i.e. $Ox$ and $Oz$ directions), all statistical averages are calculated on statistically homogeneous $Oxz$ planes across the shear layer. This is a common choice both in statistically 1D temporally evolving jets and also channel flows where the planes parallel to the walls are considered as statistically homogeneous planes.

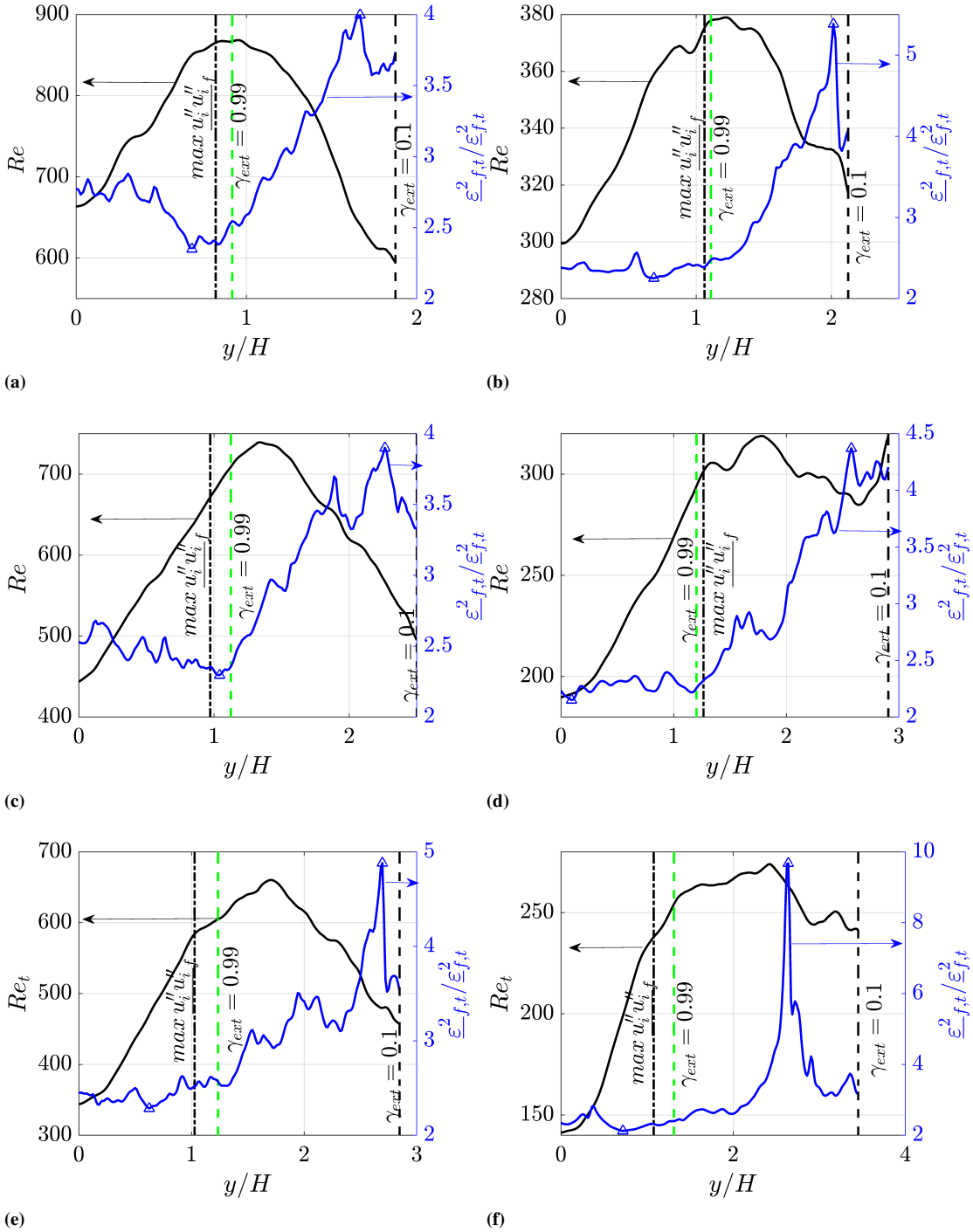


**Figure 5.15:** *The second moment of local dissipation against the Reynolds number ($Re = u_{rms}L/\nu$) across the reactive jets. (Top) t=20$t_j$; (Middle) t=30$t_j$; (Bottom ) t=35$t_j$; (Left) case H; (Right) case M.*

see the dissipation moment is increasing and Reynolds is decreasing. For case M inside the turbulent region, the dissipation moment does not show a clear behavior. One may argue that they are scattered around a constant value. Figure 3 of a very recent work in

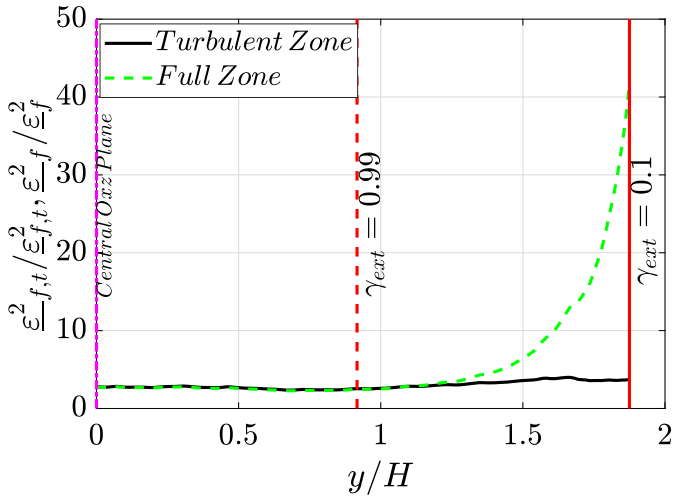


**Figure 5.16:** *The second moment of local dissipation computed in full zone (green dashed line) and only turbulent zones (black line), extracted at t=20$t_j$ across the reacting shear layer of the H case DNS. Upper half of the statistics are plotted, from the center plane ($y/H = 0$) to a plane where the external intermittency factor, $\gamma_{ext} = 0.1$.*

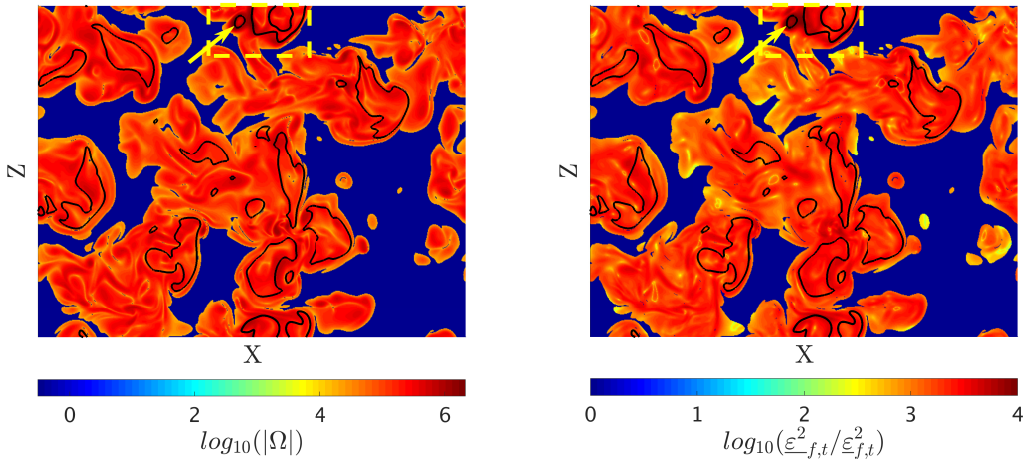


**(a)** **(b)**

**Figure 5.17:** *Data from M case DNS at t=35$t_j$ corresponding to the re-ignition mode of flame, on an $Oxz$ plane at $y/H = 2.625$ in the intermittent region of flow, corresponding to the location where a peak of normalized second moment of local dissipation occurs (see also Fig. 5.15f), (**a**) the logarithm of vorticity magnitude; (**b**) the logarithm of inverse of normalized second moment of local dissipation. Yellow arrows show the occurrence of very high vortical structure and the correspondingly, high second moment of local dissipation.*

Antonia's group [166] is reported here in Fig.5.19. $\mathcal{F}_{\frac{\partial u'}{\partial x}}$ is reported against $Re_{\lambda_u}$ for different wall bounded flows. Consider the colored markers which are the experimental data of smooth wall boundary layer. Three regions were highlighted, the near-wall region (red, $y/\delta \leq 0.04$), inertia-dominated region (yellow, $0.04 \leq y/\delta \leq 0.2$), and outer region (green, $0.2 \leq y/\delta \leq 0.6$), with $\delta$ the boundary layer thickness. Somehow the same trend but more complex is observed in this figure. Consider the green, yellow

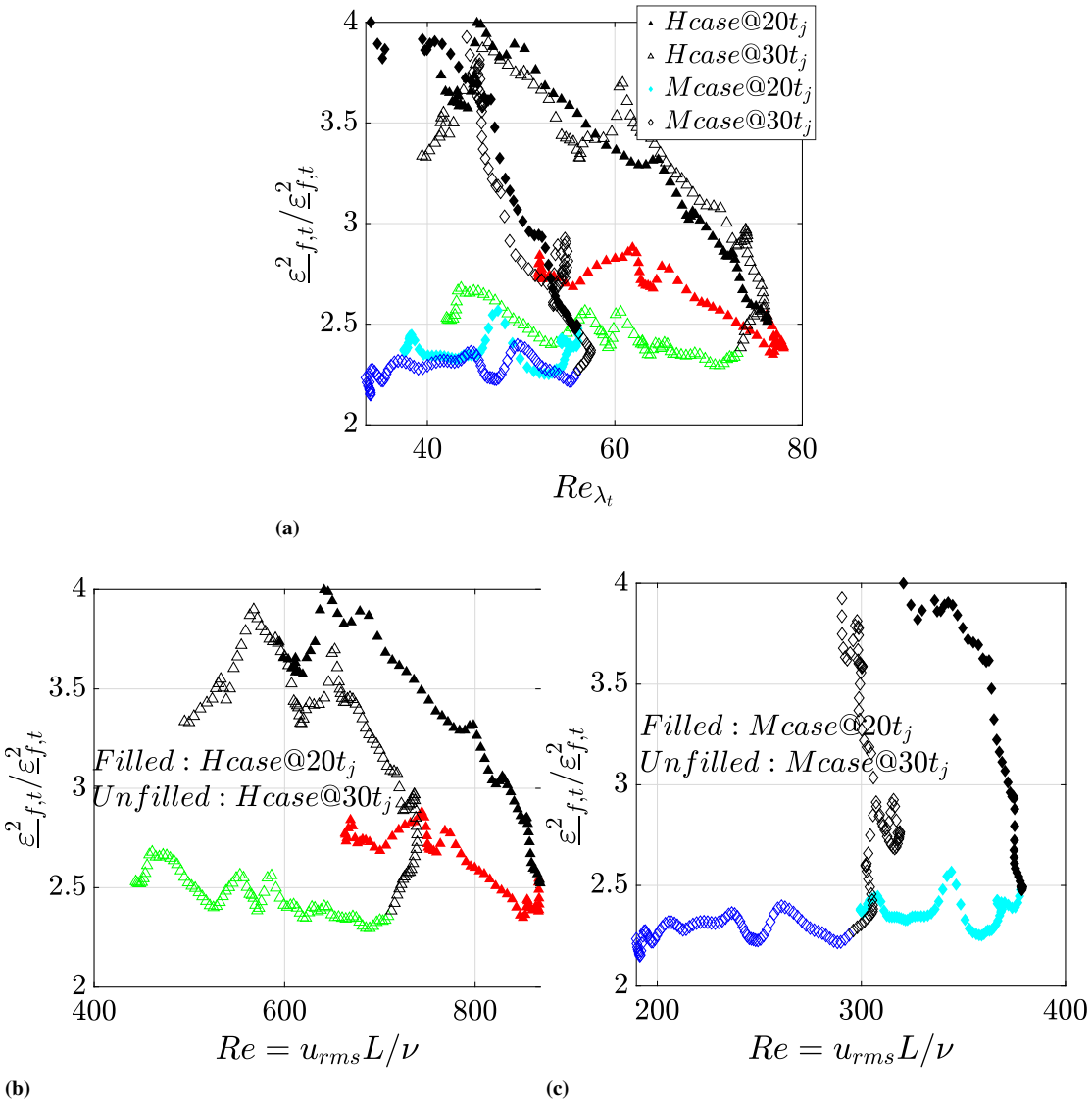


**Figure 5.18:** *Normalized second moment of local dissipation, extracted at t=20$t_j$ and t=30$t_j$ across the reacting shear layers for cases H and M, (**a**) against Taylor scale Reynolds number computed in turbulent zones only; (**b**) against large scale Reynolds number, $Re = u_{rms}L/\nu$ with $u_{rms} = \sqrt{2TKE}$ and L the initial width of the jet, showing only case H; (**c**) against large scale Reynolds number showing only case M. The data are color coded. The black markers refer to the data in intermittent flow where external intermittency factor is below 0.99. The colored data are the data in turbulent region. The upper triangles are the H case data while diamonds are the Mcase data.*

and part of red markers; by increasing the Reynolds the flatness is decreasing inside the boundary layer region. It can be concluded that the behavior observed in Fig. 5.18 cannot be only the effect of combustion.

### 5.2.3 Summary and Conclusions

In this section the intermittency phenomena (both external or large scale intermittency and internal or small scale intermittency) were studied in reactive free shear flows (temporally evolving double shear layers or jets). The three DNS databases L, M and H

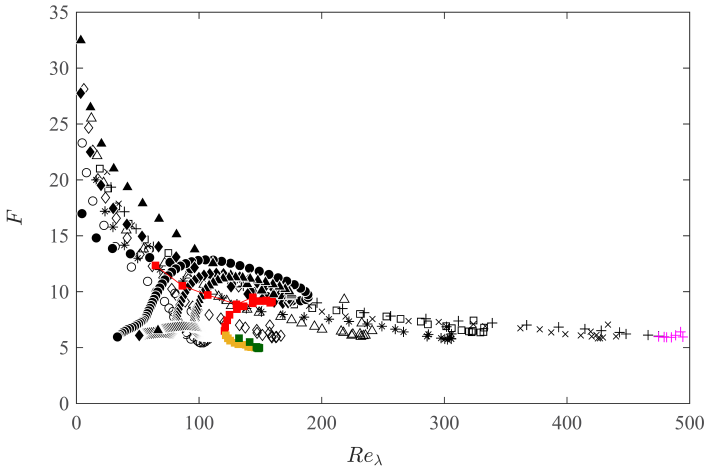


**Figure 5.19:** *From [165], $\mathcal{F}_{\frac{\partial u'}{\partial x}}$ against $Re_{\lambda_u}$ from experiments and DNS of different types of wall bounded flows. Consider the colored markers which are the data of smooth wall boundary layer and note how flatness is changing with Taylor Reynolds number. Three regions were highlighted, the near-wall region (red, $y/\delta \leq 0.04$), inertia-dominated region (yellow, $0.04 \leq y/\delta \leq 0.2$), and outer region (green, $0.2 \leq y/\delta \leq 0.6$), with $\delta$ the boundary layer thickness.*

differing in the bulk jet Reynolds number (see Sec. 4.5) were analyzed at different time instants corresponding to different flame regimes. In Sec. 5.2.2, the external intermittency effects were discussed. The jet was divided into turbulent (T) non-turbulent (NT) regions using the interface detection threshold based on vorticity magnitude. The way to extract conditional statistics conditioned on turbulent zones only using external intermittency factor, $\gamma_{ext}$, was explained in detail. The conditional statistics then used in Sec. 5.2.2 to study the statistics of velocity gradients and second moment of instantaneous/local TKE dissipation in turbulent zones of the jets. This treatment of data is required since otherwise the statistics are highly affected by the entrained laminar/irrotational coflow. The normalized second moment of local/instantaneous dissipation (i.e. $\underline{\varepsilon}^2_{f,t}/\left(\underline{\varepsilon}_{f,t}\right)^2$ ) is by definition [112] the inverse of internal intermittency factor, $\gamma_{int}$, used in combustion models like EDC [14]. It was observed that across the shear layers the behavior of $\underline{\varepsilon}^2_{f,t}/\left(\underline{\varepsilon}_{f,t}\right)^2$ is more complex than to be solely described by kind of Reynolds number scalings. This was also mentioned in [166] for the non-reacting wall bounded flows. However, interestingly, on the central plane of the reacting jets, $\underline{\varepsilon}^2_{f,t}/\left(\underline{\varepsilon}_{f,t}\right)^2$ found to scale reasonably with longitudinal Taylor scale Reynolds number, $Re_{\lambda_u}$, and very well with large scale Reynolds number (as theoretically proposed by Yakhot [36]). Large scale Reynolds number defined as $Re = u_{rms}L/\nu$, with $u_{rms}$ two times TKE and $L$ here taken to be the initial width of the fuel jet. This is very interesting since, both extinction and re-ignition time instants' statistics collapsed to the theoretical curve of Yakhot [36] for non-reactive HIT. At the extinction time there is approximately no reactivity on the central plane of the jets however, at re-ignition times, the jets are mainly re-ignited from the central planes. Consider that the power law scalings observed in this section are much weaker than the ones proposed in phenomenological models of Corrsin [111] and Tennekes [103].

## 5.3 Velocity Spectra For Reactive Flows

The analysis of the velocity and scalar spectra in reactive flows is of great importance both in experiments and numerics. In experiments, one needs to know the true resolution required to measure the scalar gradients [37]. Many numerical models also rely on the scaling laws for the spectra to evaluate model constants or to justify assumptions [38].

Many works have been done so far on the passive scalar spectra starting from the early work of Corrsin [167] and Batchelor [168] and Kraichnan [169] (see also [170] and the reviews in [156, 171] and Chapter 3 of the book [172]). In shear-less flows (where large scale anisotropy does not exist) the Schmidt number ($\mathrm{Sc}$) dependency exists. In $\mathrm{Sc} \leqq 1$ and large $Re_\lambda$, by the dimensional analysis, the scalar fluctuations spectra have an approximate universal form: $E(\kappa) = C_{OC}\underline{\chi}\underline{\varepsilon}^{-1/3}\kappa^{-5/3}$, where $C_{OC}$ is the Obukhov-Corsin contant, with $\underline{\chi}$ the mean scalar dissipation rate. If $\mathrm{Sc} \gg 1$, the $\kappa^{-1}$ power form exists [168] (also see the DNS results for the support [173]). In shear flows where large scale anisotropy exist, the form of the scalar spectrum also depends on the shear length scale [174] and $Re_\lambda$ [171]. The passive scalar spectrum is more complicated than the TKE (in general the velocity spectrum). The current work is focused on the latter.

For non-reactive constant density incompressible flows as discussed in details in Sec. 2.2.7, there is considerable evidence for the universal form of the normalized TKE spectrum function of the form Eq. 2.72 [5] (see e.g., [43] and for a review [39] or [68]), although some small deviations from the universality have been detected which will be later explained. It is expected that if the compensated form of spectra are plotted against the normalized wavenumber, one can find the Kolmogorov constant. In [39] a wide range of experiments were examined and the value for the 1D Kolmogorov constant found to be $0.53 \pm 0.055$ (which translates to the 3D constant using Eq. 2.69 as $1.62 \pm 0.17$). Approximately the same was found from DNS [40, 70]. It was mentioned in [175] that it is difficult to find $C_K$ by the compensated spectra because a perfectly horizontal region does not exist in the compensated spectrum; this is related to the inertial range intermittency. In the DNS of high $Re_\lambda$ (say $\mathrm{Re}_\lambda > 700$) [42] the compensated spectrum shows a very short nearly flat region, a tilted region and a bump near $\kappa\underline{\eta} = 0.1$. The bump was also observed in the experiments of Saddoughi and Veeravalli [43]. This is called the bottleneck effect [175]. For the first issue, the so called intermittency correction is added to the $\kappa^{-5/3}$ power law, however, it is believed that the tilted region can be seen only in high $Re_\lambda$ experiments or DNS [176]. In lower $Re_\lambda$, the intermittency correction is very low $O(10^{-2})$. Closer inspection shows also that $C_K$ is not also a real constant and has a weak $Re_\lambda$ dependency [176, 177] of about power 0.1. It can be shown that it is linked to the intermittency effects. However, since the dependency is very low, in the current study we assume that intermittency does not have a huge effect on the TKE spectrum. As we already mentioned, intermittency usually has a profound effect on the small scale scales (gradients) and high order statistics; the effect on the second order statistics (the spectrum in wavenumber space) is not high and can be considered to be negligible [39, 40, 51].

Knowing that the chemistry mostly occurs in small scales, the kinetic energy and its

[5] Strictly speaking its 1D form in experiments and both 1D and 3D forms in DNS.

dissipation spectra in the high wavenumber range are of great importance. For reactive flows the focus in the literature has been mainly on the spectra of scalars. The experiments have been carried out in Sandia focusing on the scalars spectra of non-premixed jet flames C, D, and E and DLR-A and DLR-B [37](the scalar energy and its dissipation spectra were also reported in ICE engines [178]; $CH_4/H_2/N_2$ non-premixed jet flames [44, 45] and DME/air partially premixed jet flame [179]). A cut-off length scale ($\lambda_\beta$), was introduced [37, 180] as the inverse of the wavenumber at which $2\%$ peak dissipation spectrum occurs. It was found that, when normalized by $\lambda_\beta$, the dissipation spectra of temperature and mixture fraction nearly collapsed [37]. However, due to an increased noise level in the measured data, there is no evidence of the behavior in the high wavenumber range.

Unlike non-reactive flows, the studies on the velocity and also the scalars spectra in reactive flows using DNS are limited in the literature. In [46] the effect of heat release on the velocity and scalar spectra obtained by the DNS of temporally evolving reacting shear layers was studied. Surprisingly, it was found that the effect of heat release can be well scaled out by using Favre averaged turbulence quantities in the velocity and mixture fraction spectra. Kolla et al., [47] studied the energy spectra of premixed flames using DNS of temporally evolving jets. In agreement with [46] they found out that, in the inertial range, the classical scaling laws using Favre averaged quantities are applicable. In the high wavenumber range, the laminar flame thickness ($\delta_L$) produces a better collapse while disrupts the collapse in the inertial range. Recently in [48], in the study of the dissipation spectra of premixed jets, it was observed that the scalars spectra collapse when normalized by the corresponding Favre mean dissipation rate and $\lambda_\beta$. However, in contrast to [37] and [46], they saw that the normalized dissipation spectra in all the cases deviate noticeably from those predicted by classical the scaling laws for constant-density turbulent flows.

The focus in this section is to study the TKE and its dissipation spectra in both inertial and the dissipative ranges in turbulent non-premixed jets in which unlike the work in [46] the effect of the differential diffusion is also taken into account. Further, in [46] the flame sheet approximation is utilized which assumes that the chemical reactions occur on much shorter time scales than the smallest flow scales. With this imposed one-way coupling between chemistry and turbulence they eliminated the effect of flame dynamics exists in e.g. extinction/re-ignition regimes. The DNS cases in the current study are all experiencing such transient effects. It is also of grater interest in the current work to study the scalings of the spectra. In other word, we are seeking to a normalization set by which all the spectra are collapsed on a single curve (with an acceptable deviation). The comparison with the model spectrum of Pope (Eq. 2.75) [38] will be performed and the constants will be modified using database created out of the 3 DNS cases (each studied in 3 time instants corresponding to different flame regimes).

### 5.3.1 Normalized Spectra Using Favre Averaged Kolmogorov's Scales

In [46] the 1D energy spectra using the DNS of temporally evolving reacting shear layers (Methane-air and Hydrogen-air) with 1step global reactions were studied.

The 1D energy spectrum is computed using the 1D spectra, $E_{ii}^{1D}$, and reads:

$$E^{1D}(\kappa_x) = E_{11}^{1D}(\kappa_x) + E_{22}^{1D}(\kappa_x) + E_{33}^{1D}(\kappa_x) \tag{5.16}$$

where $E_{ii}^{1D}(\kappa_x)$ can be computed by the method described in Sec. 5.3.4. It was found that the normalization proposed by Kolmogorov for non-reacting constant density flows, i.e., Eq. 2.71 can collapse all the spectra across the reacting shear layers in different cases, if it is computed by the Favre averaged quantities. In other words the universal Favre normalized 1D energy spectrum for reactive flows can be defined as:

$$E_{Normal}^{1D}(\kappa_x \underline{\eta}_f) = \frac{E^{1D}(\kappa_x)}{\underline{\varepsilon}_f{}^{2/3} \underline{\eta}_f{}^{5/3}}. \tag{5.17}$$

It is the main goal of this sub-section to check this scaling. However, it is preferred here to first work with the components of Eq. 5.16, e.g., $E_{11}^{1D}$. This is because in the literature there is no theoretical background for the 1D energy spectrum. The Kolmogorov spectrum is a 3D energy spectrum and equations were derived to relate it to the 1D spectra (i.e., components of Eq. 5.16 not the sum).

The selected databases are cases L, M and H introduced in Sec. 4.5 at 3 different time instants, $20t_j$, $30t_j$ and $35t_j$, representing the maximum local extinction event ($20t_j$) and the re-ignition ($30t_j$ and $35t_j$), however, the results of case H are only presented in this section for the purpose of brevity. Other results are reported in Appendix A. Eight different statistically homogeneous planes across the double shear layers are selected to extract the spectra. The planes are $P_0$: the $Oxz$ plane at $y = 0$, i.e., the central plane, $P_1 - P_4$, the planes corresponding to the maximum density and temperature variances, maximum Favre average $\mathrm{OH}$ mass fraction and maximum TKE, respectively and further, $P_5 - P_7$ the planes corresponding to $\underline{Z}_f$ equal to 0.7, 0.422(stoichiometric mixture fraction) and 0.02, respectively. $P_7$ is kept at a very low mean kinetic energy and approximately outside the fully turbulent flame. The Favre averaged quantities are computed using Eq. 2.35. The Favre second moments (variances) are computed by Eq. 2.37 and all are functions of the cross stream distance, $y$. In Fig. 5.20 the normalized quantities are plotted across the shear layer for case H at t=$20t_j$. In Table.5.1 the parameters of the DNS databases on the selected planes are presented.

The 1D longitudinal velocity spectra on different planes across the reacting shear layer for case H at t=$20t_j$ are presented in Fig. 5.21a. It is obvious that the non-normalized spectra are not collapsed in the low-medium range of the longitudinal wavenumbers,$\kappa_x$. The normalization proposed in [46] using the Favre averaged Kolmogorov length scale and Favre averaged TKE dissipation rate (i.e., Eq. 5.17) is tested in Fig. 5.21b. The plot shows the normalized 1D longitudinal velocity spectra versus the longitudinal wavenumber normalized by the Favre averaged Kolmogorov length scale (i.e. $\kappa_x \underline{\eta}_f$). The Favre averaged TKE dissipation rate, $\underline{\varepsilon}_f$ is exact and extracted from the DNS using Eq. 2.115 in Sec. 2.3.1. The black line in Fig. 5.21b shows the $-5/3$ slope (the inertial range). It is observed that the $\kappa^{-5/3}$ scaling exists in agreement with Kolmogorov's hypothesis (see Sec. 2.2.7) although is not extended over a large

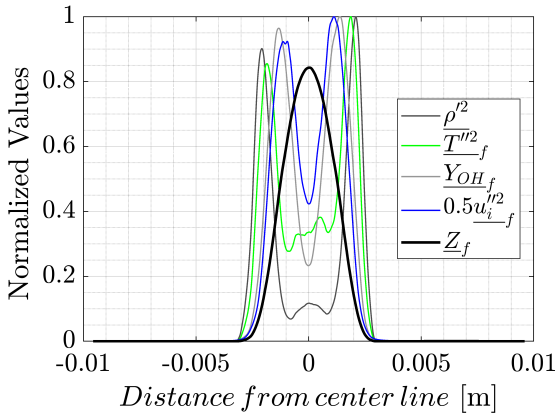


**Figure 5.20:** *Normalized quantities across the shear layer for case H at t=20$t_j$.*

**Table 5.1:** *Some turbulence parameters of case H on the selected planes and different time instants for which spectra are studied.*

| Case | Plane | $\eta_f \times 10^5[m]$(Eq.2.63) | $\lambda_f \times 10^4[m]$ (Eq.2.62) | $Re_\lambda$ (Eq.2.61) | $\lambda_\beta \times 10^5[m]$ (Eq.2.55) | $u_{int}[m/s]$ (Eq.2.51) | $Re_t$ (Eq.2.57) | $\widetilde{Z}_f$ (Eq.2.35) |
|---|---|---|---|---|---|---|---|---|
| t=20$t_j$ | $P_0$ | 1.33 | 1.92 | 53.82 | 1.952 | 26.88 | 193.1 | 0.843 |
| | $P_1$ | 1.16 | 1.67 | 53.5 | 1.952 | 19.98 | 190.94 | 0.111 |
| | $P_2$ | 1.17 | 1.9 | 68.5 | 1.967 | 28.21 | 312.96 | 0.198 |
| | $P_3$ | 1.22 | 2.12 | 78.3 | 1.882 | 39.6 | 408.33 | 0.433 |
| | $P_4$ | 1.25 | 2.2 | 80.5 | 1.952 | 41.33 | 432.64 | 0.554 |
| | $P_5$ | 1.28 | 2.14 | 72.6 | 1.952 | 37.89 | 351.55 | 0.701 |
| | $P_6$ | 1.2 | 2.11 | 77.82 | 1.882 | 39.31 | 403.72 | 0.422 |
| | $P_7$ | 1.4 | 1.59 | 33.6 | 2.012 | 9.2 | 75.13 | 0.024 |
| t=30$t_j$ | $P_0$ | 1.78 | 1.2 | 42.9 | 2.315 | 23.3 | 122.72 | 0.698 |
| | $P_1$ | 1.39 | 2.3 | 56.49 | - | 16.33 | 212.77 | 0.0981 |
| | $P_2$ | 1.38 | 2.06 | 72.39 | - | 25.43 | 349.43 | 0.2075 |
| | $P_3$ | 1.52 | 2.32 | 67.73 | 2.093 | 32.91 | 305.85 | 0.4935 |
| | $P_4$ | 1.50 | 2.47 | 70.43 | - | 33.17 | 330.72 | 0.4572 |
| | $P_5$ | 1.78 | 2.48 | 42.9 | - | 23.29 | 122.72 | 0.6987 |
| | $P_6$ | 1.63 | 2.3 | 34.03 | - | 7.8 | 77.24 | 0.0233 |
| | $P_7$ | 1.49 | 1.87 | 73.29 | - | 33.09 | 358.14 | 0.4252 |
| t=35$t_j$ | $P_0$ | 2.22 | 2.76 | 40.07 | 2.540 | 20.52 | 107.08 | 0.6391 |
| | $P_1$ | 1.52 | 2.31 | 59.46 | - | 15.62 | 235.74 | 0.0999 |
| | $P_2$ | 1.49 | 2.44 | 69.15 | - | 22.2 | 318.84 | 0.1781 |
| | $P_3$ | 1.91 | 2.95 | 61.35 | 2.378 | 28.44 | 250.9 | 0.5284 |
| | $P_4$ | 1.75 | 2.94 | 72.7 | - | 30.88 | 352.44 | 0.4287 |
| | $P_5$ | - | - | - | - | - | - | - |
| | $P_6$ | 1.73 | 2.91 | 72.58 | - | 30.83 | 351.23 | 0.4209 |
| | $P_7$ | - | - | - | - | - | - | - |

wavenumber range due to the relatively low Reynolds number of the jet. Increasing the Reynolds number will increase the range of the $\kappa^{-5/3}$ scaling (see [38]). The collapse of the spectra (i.e. the existence of a universal curve) in agreement with [46, 47] is acceptable [6] in the whole wavenumber range except the very low wavenumber in which the effect of anisotropy due to boundaries exists.

An inflection is observed in Fig. 5.21 around $\kappa\underline{\eta}_f \approxeq 1$. In [47] using the DNS of temporally evolving premixed jet flames simulated by the same S3D code as used for creating the current datasets, a inflection was observed. In that paper it was hypothesized that the inflection is due to the pressure-velocity coupling at the laminar flame scales.

In Fig. 5.22b the compensated spectra are depicted (i.e. the normalization using Eq. 2.73). This form of plotting of spectra can be used to detect the Kolmogorov constant [43]. As can be seen, the value of the constant for the longitudinal velocity spectrum ($E_{11}^{1D}$) is around $0.75$ (the same number can be observed in the other two cases; see AppendixA). The value is higher than the reported values for non-reactive jets (≈0.5). In Fig. 5.22a, the compensated energy spectra ($E^{1D}$) are also plotted for the current non-premixed jet flame and is observed that the value of the constant is around $1.1$. However, this should not be mistakenly used to suggest the constant in 3D Kolmogorov's spectrum. The correct relation (using isotropy assumption) to compute the value is Eq. 2.69 in which $E_{11}^{1D}$ (not $E^{1D}$) is related to $E$.

Now the behavior of the spectra in the dissipation and near dissipation ranges will be investigated. In these ranges of wavenumbers, Kraichnan [181] proposed that the 3D normalized energy spectrum $E_{normal}$ has an exponential drop-off of the form[7]:

$$E_{normal}(\kappa\underline{\eta}_f) = A\left(\kappa\underline{\eta}_f\right)^{\alpha}\exp\!\left(-\beta\left(\kappa\underline{\eta}_f\right)^{n}\right). \tag{5.18}$$

The value of $n = 1$ is supported by two-point closure theories [73] for $\kappa\underline{\eta}_f \gg 1$. For near dissipation range (say $0.5 \leq \kappa\underline{\eta}_f \leq 1.5$) this value is supported by experiments e.g., [43,182] and DNS e.g., [69,72,73]. It should be mentioned that we expect the same functional form of the spectrum (except the values for the constant $A$) when analyzing the 1D spectrum rather than the 3D energy spectrum.

If the compensated spectrum (i.e., $E_{normal}(\kappa\underline{\eta}_f) \times (\kappa\underline{\eta}_f)^{5/3}$) is plotted against $\kappa\underline{\eta}_f$ in a log-linear plot and if a straight line is observed, it can be concluded that $\alpha = -5/3$ and the slope of the line gives the value of $\beta$. This is shown in Fig. 5.23. In the range of $0.1 \leq \kappa_x\underline{\eta}_f \leq 0.8$ the straight line is observed. The observation of the straight line implies that $\alpha = -5/3$, consistent with Kolmogorov's spectrum. This value of $\alpha$ was also reported in the previous studies of non-reactive cases [43]. However, unlike the well documented slope of $\beta = 5.2$ for non-reactive flows [38, 43] in the near dissipation range, here the observed slope is $\beta \approx 7.2$. It should be mentioned that the same slope observed for lower Re cases M and L (see Appendix A). The inflection observed before in Fig. 5.21 is more clearly seen near $\kappa_x\underline{\eta}_f \approx 0.8$ in this figure. After that wavenumber, there is a change in the slope to approximately $\beta \approx 10$. The change of the slope was previously observed in non-reactive flows how-

[6] In the next Section another scaling using cut-off scales extracted from the dissipation spectra is shown to perform better.

[7] The theory is for non-reacting incompressible flows so the correct form is to use $\underline{\eta}$ rather than $\underline{\eta}_f$, however, since we are dealing with the reactive flow, we adopt the Favre average quantities in all formula

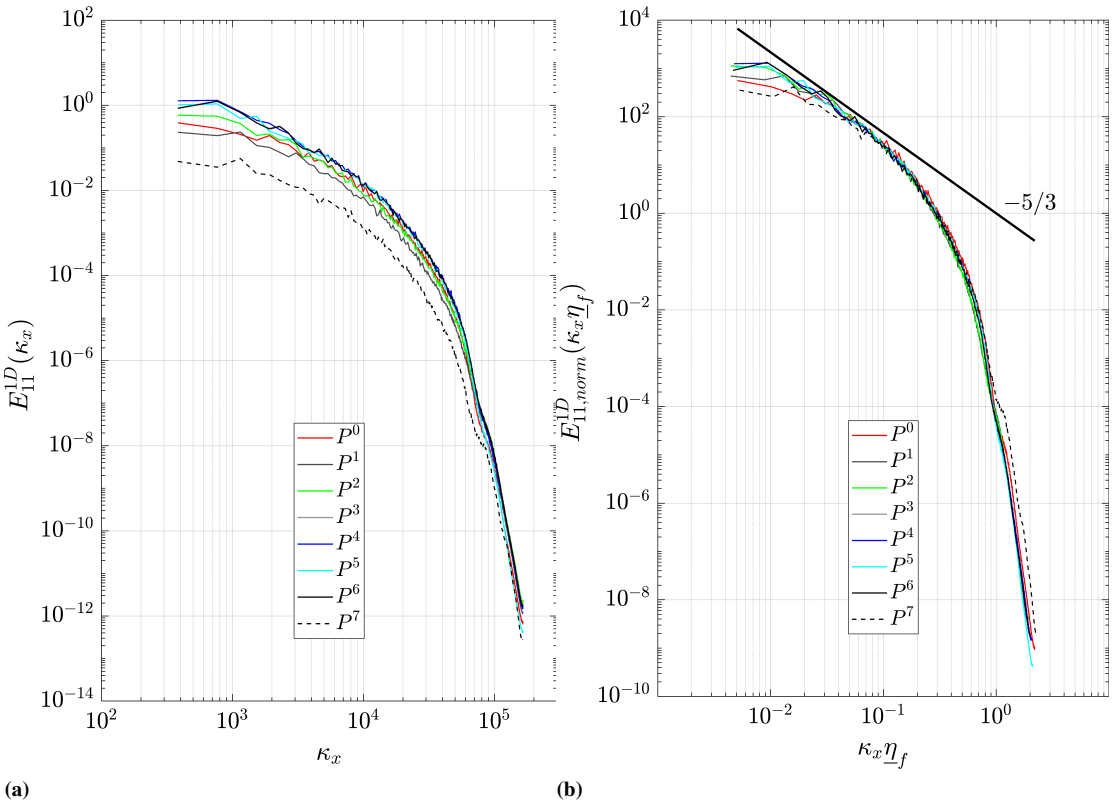


**(a)** **(b)**

**Figure 5.21:** *The 1D longitudinal spectra on different planes across the reacting shear layer at maximum extinction time, t=20$t_j$ for case H, (**a**) Non-normalized; (**b**) Normalized using Favre averaged $\eta$ and $\varepsilon$.*

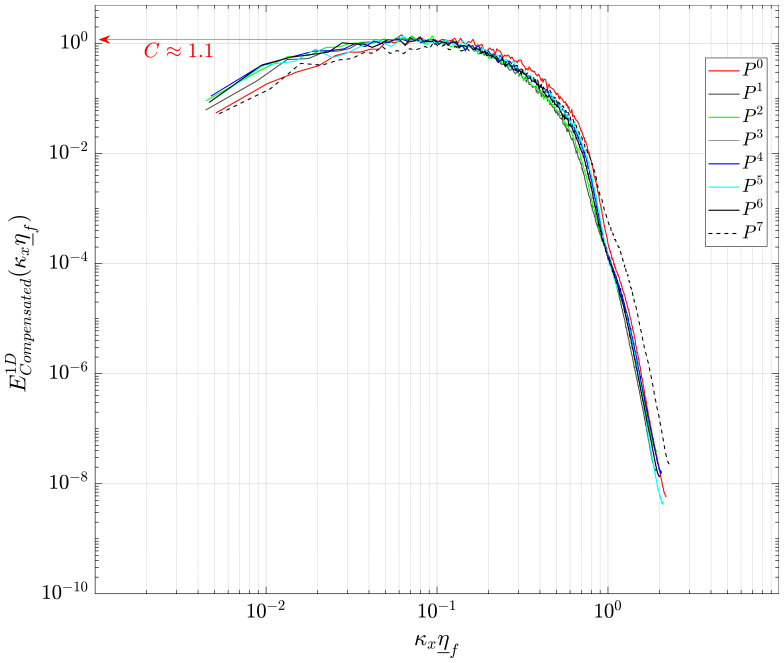


**(a)**

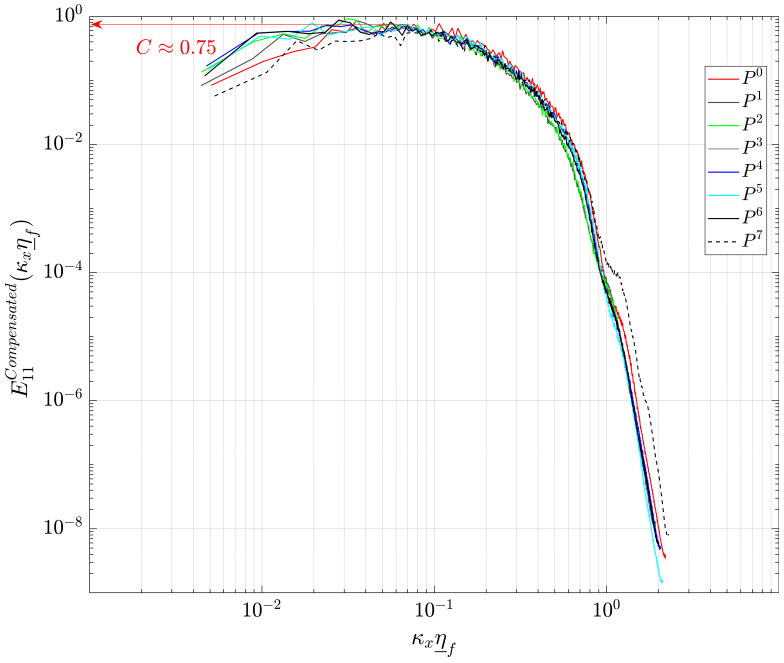


**(b)**

**Figure 5.22:** *1D compensated spectra on different planes across the reacting shear layer at maximum extinction time, t=20$t_j$ extracted from H case DNS, (**a**) 1D compensated energy spectra; (**b**) 1D compensated longitudinal spectra.*

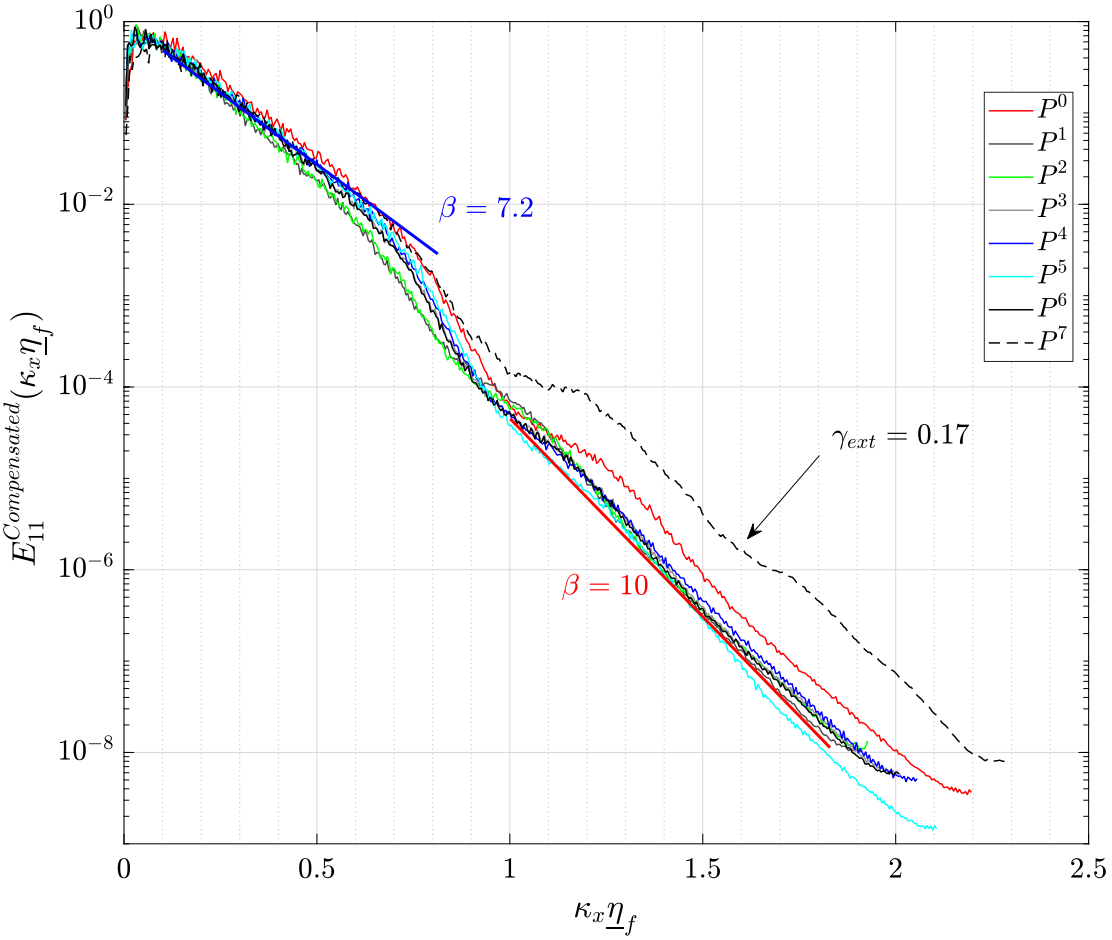


**Figure 5.23:** *1D compensated longitudinal spectra on different planes across the reacting shear layer at maximum extinction time, t=20$t_j$ for case H with the slopes of the exponential drop-off.*

ever in the very far dissipation range around $\kappa\underline{\eta} \approx 4$ in the DNS of isotropic turbulence with $Re_\lambda$ range similar to the cases considered here [72]. We can take a closer look at the different components of the 1D energy spectrum, i.e., $E_{ii}$ in Fig. 5.24. Fig. 5.24a shows the longitudinal ($E_{11}^{Compensated}(\kappa_x\underline{\eta}_f)$) and the transverse ($E_{22}^{Compensated}(\kappa_x\underline{\eta}_f)$ and $E_{33}^{Compensated}(\kappa_x\underline{\eta}_f)$) spectra extracted from the mean stoichiometric plane of case H at t=20$t_j$. Fig. 5.24b shows same quantities in a different plane which is the central plane. It is observed that the behavior of the spectra are consistent with the theory which is $E_{22} \approx E_{33} > E_{11}$. The spectra computed for cases M and L, which have higher resolution show the extended range with $\beta = 7.2$ slope and the transition occurs at higher normalized wavenumbers, $\kappa_x\underline{\eta}_f > 2$, (see Appendix A). It is ambiguous if the inflection and change of slope is an intrinsic flame behavior like what proposed in [47] for premixed flame or is the effect of tenth order filter used in the DNS code. This needs more studies, so we avoid using this part and focus on the well behaved straight line part of the spectrum in all 3 cases.

In Fig. 5.25a the dissipation spectra (Eq. 2.79 by using $E_{11}$ instead of $E$) are plotted and the corresponding normalized spectra (Eq. 2.81 using $E_{11}$ instead of $E$ and Favre averaged quantities instead of Reynolds average) are shown in Fig. 5.25b. It is obvious

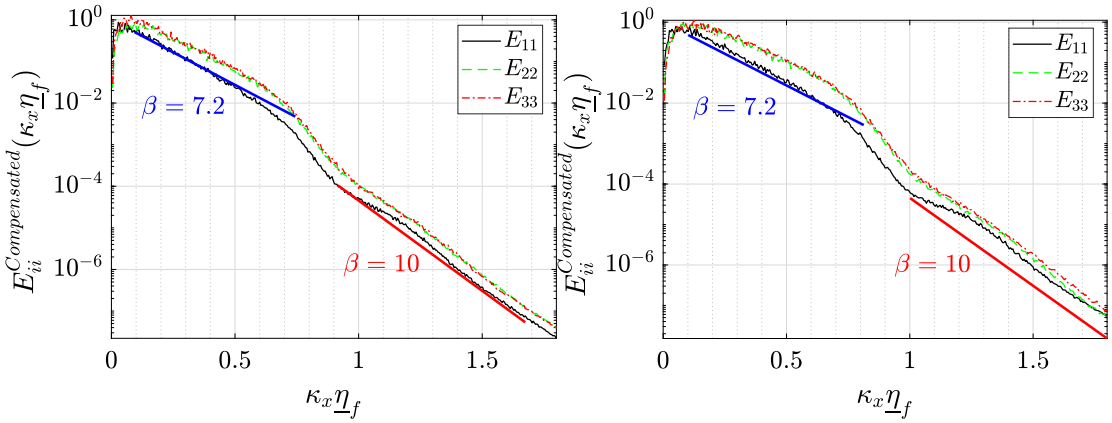


**Figure 5.24:** *1D compensated spectra across the reacting shear layer at the maximum extinction time, t=20$t_j$ for case H, (**a**) Extracted from the Favre mean Stoichiometric mixture fraction plane; (**b**) Extracted from the central plane.*

that since the plane $P^7$ is outside the fully turbulent region the dissipation is very low. By moving toward the core jet region the dissipation peak height is increasing. In the normalized dissipation spectra (Fig. 5.25b), the peak location seems to collapse and becomes approximately independent of $Re_\lambda$. The peak location is around $\kappa_x\underline{\eta} \approx 0.08$. This is of great importance. It is observed that the location of the peak of dissipation spectrum in non-premixed flames is lower than the non-reactive jet value [183] and grid generated turbulence [43] which are around 0.1. Further, the collapse of the peak location is acceptable when the dissipation spectra were normalized by $\underline{\eta}_f$ and $\underline{\varepsilon}_f$. Moreover, we do not expect that the peak height of the normalized dissipation spectra collapse perfectly. This is due to the internal intermittency effects [184].

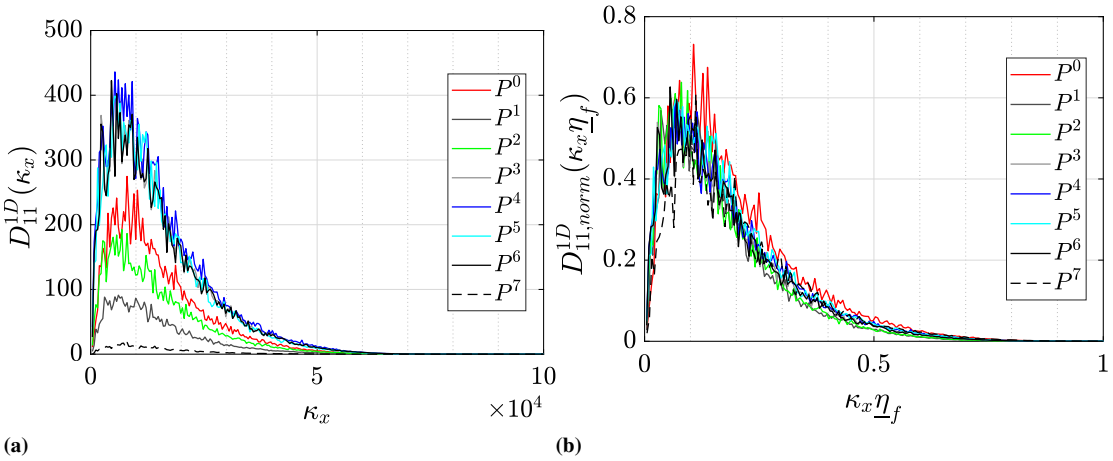


**Figure 5.25:** *1D longitudinal dissipation spectra across the reacting shear layer at t=20$t_j$ for case H, (**a**) Non-normalized spectra; (**b**) Normalized using Favre averaged $\eta$ and $\varepsilon$.*

### 5.3.2 Normalized Spectra Using Cut-off Length Scales From Velocity Dissipation Spectra

In [37], a cut-off scale ($\lambda_\beta$) was introduced as the inverse of the wavenumber at which $2\%$ peak dissipation spectrum occurs. Then, this cut-off scale was used to normalize the 1D dissipation spectra of scalars (i.e. temperature and mixture fraction) in non-premixed turbulent jets. In [37], it was found that when normalized by this cut-off scale the dissipation spectra of temperature and mixture fraction nearly collapse. However, due to the increased noise level in the measured data, there is no evidence of that in high wavenumber ranges. Further, the TKE and its dissipation spectra are not provided. Here, first the cut-off scales are extracted from the 1D velocity dissipation spectra on different planes across the shear layers and then it will be used as a length scale to normalize the spectra instead of Kolmogorov's length scale. The $\lambda_\beta$ reads:

$$\lambda_\beta \simeq \frac{1}{\kappa_{2\%}}, \tag{5.19}$$

where $\kappa_{2\%}$ is the wavenumber at which the dissipation spectrum reaches $2\%$ of its maximum [37, 44, 45]. In [154] a threshold of $7.3\%$ was used however we keep using Eq. 5.19. It should be mentioned that the threshold in Eq. 5.19 is based on the observation that in the 1D version of model spectrum of Pope, the wavenumber at $\kappa\underline{\eta}_f = 1$, corresponds to $2\%$ of the peak value of the 1D dissipation spectrum. However, the $7.3\%$ threshold is the corresponding value of the 3D spectrum i.e., Eq. 2.81. In Table.5.1 the extracted cut-off scales, $\lambda_\beta$, have been presented.

In Fig. 5.26 the two normalization methods are compared in 1D longitudinal velocity spectra. The collapse of the spectra across the shear layer layer with both methods are acceptable. Small improvement can be seen in Fig. 5.26b in the range $0.1 \leq \kappa_x\lambda_\beta \leq 1$. In Fig. 5.26 the dissipation spectra are plotted and compared. Again an improvement in the collapse of the spectra is clear near the cut-off wavenumber in Fig. 5.26b. This shows that by changing only the length scale in the normalization of the spectra one can improve the collapse at least up to $\kappa_x\lambda_\beta \approx 1$. Remember that this is the wavenumber

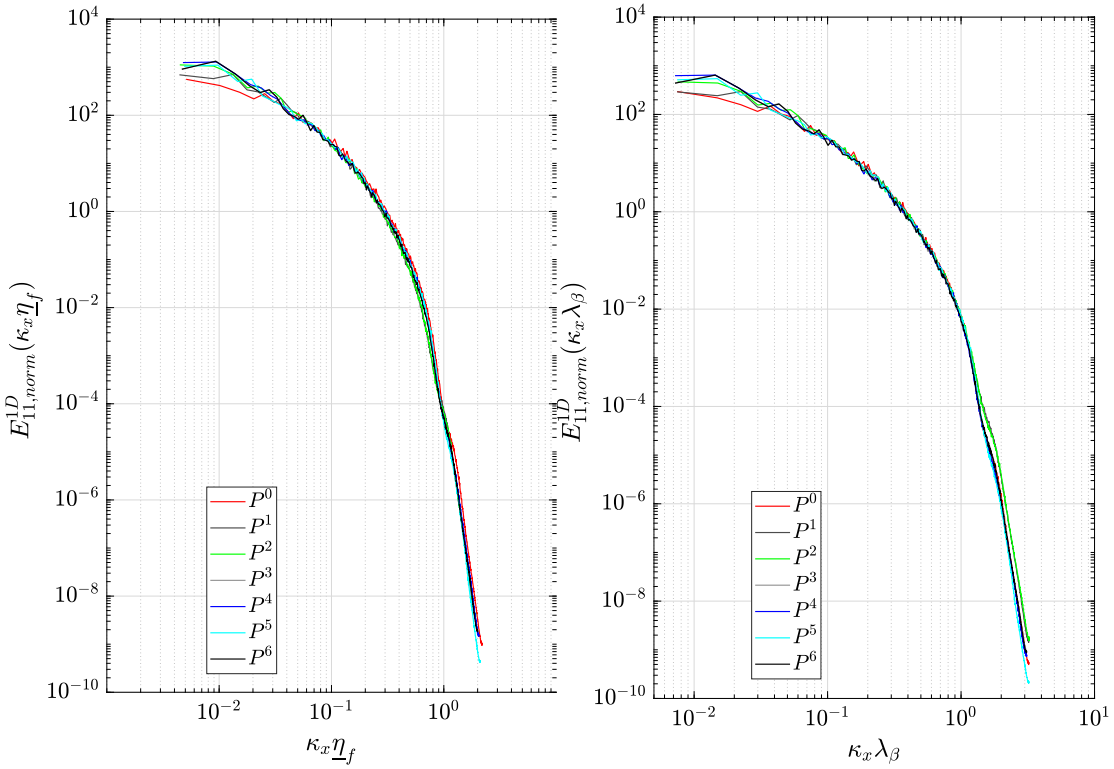


**(a)** **(b)**

**Figure 5.26:** *1D longitudinal velocity spectra across the reacting shear layer at t=20$t_j$ for case H; (**a**) Normalized using the Favre averaged $\eta$ and $\varepsilon$; (**c**) Normalized using the Batchelor length scale and Favre averaged $\varepsilon$.*

after which only small portion of dissipation occurs.

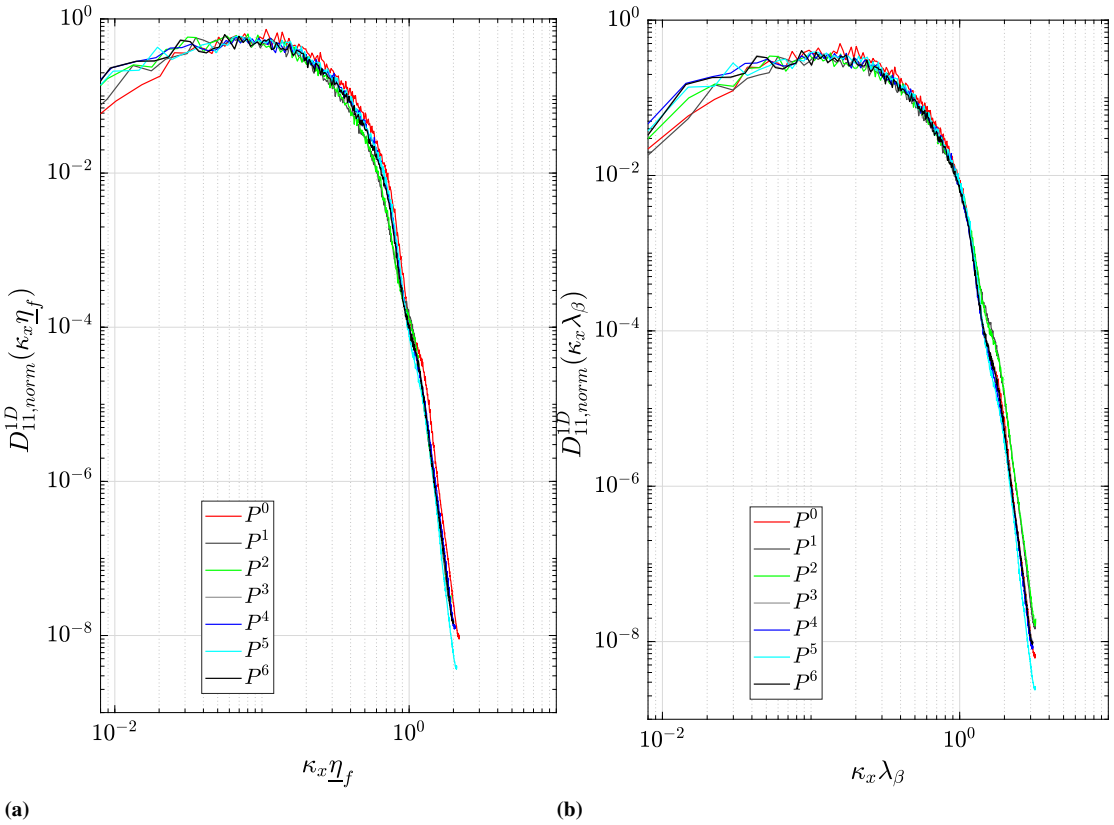


**Figure 5.27:** *1D longitudinal dissipation spectra across the reacting shear layer at maximum extinction time, t=20$t_j$ for case H; (**a**) Normalized using the Favre averaged $\eta$ and $\varepsilon$; (**c**) Normalized using the Batchelor length scale and Favre averaged $\varepsilon$.*

### 5.3.3 Normalized Spectra in Different Combustion Regimes

In this section the analysis is extended to different combustion regimes. Three time instants of the highest Reynolds number case, i.e., case H, are selected. These are t=20$t_j$ corresponding to the maximum extinction and t=30,35$t_j$ re-ignition events (see Fig. 4.4). The flame dynamic is changing during the time in this temporally evolving jet flame so that due to the decreasing scalar dissipation rate, the flame re-ignites. The objective is to see whether the scalings investigated in the previous section can be used to collapse all the velocity spectra on different planes across the jet to a single universal curve or not. In Fig. 5.28 the longitudinal velocity spectra are plotted on two different planes (the central $Oxz$ plane at $y = 0$, $P^0$ and the $Oxz$ plane corresponding to maximum Favre mean $\mathrm{OH}$ mass fraction, $P^3$). Fig. 5.28a shows the non-normalized spectra, and Fig. 5.28b the normalized spectra using $\underline{\eta}_f$, $\underline{\varepsilon}_f$. In Fig. 5.28c, the normalized spectra using $\lambda_\beta$, $\underline{\varepsilon}_f$ have been plotted. It is seen that the normalized spectra from extinction regime and re-ignition regime, although differ a lot (Fig. 5.28a), collapse well using $\underline{\eta}_f$ as a length scale (Fig. 5.28b) in the inertial range and part of near dissipation range (up to around $\kappa_x \underline{\eta}_f \leq 0.6$). It can be clearly seen that the collapse is improved mainly in near dissipation range using the cut-off scale $\lambda_\beta$ (Fig. 5.28c).

In Fig. 5.29 the same plots are shown for the longitudinal dissipation spectra. It is seen that the collapse is better using $\lambda_\beta$ compared to $\underline{\eta}_f$. However, both normalizations are acceptable.

Next we will compare the collapse of the spectra for cases with different Re (cases M and H) and in different regimes (t=20$t_j$ corresponding to the maximum extinction and t=30$t_j$, the re-ignition events). Since for each case it was already observed that the collapse is acceptable, here only the results on the plane corresponding to the maximum Favre mean $\mathrm{OH}$ mass fraction (i.e., $P^3$) is plotted in Fig. 5.30. The collapse of the spectra extracted from two different cases with two different Re and physically two different levels of extinction (see Fig. 4.4) using both normalization methods are acceptable.

In Fig. 5.31 the same plots are shown for the longitudinal dissipation spectra. It is seen again that the collapse is acceptable using both methods before the inflection wavenumber.

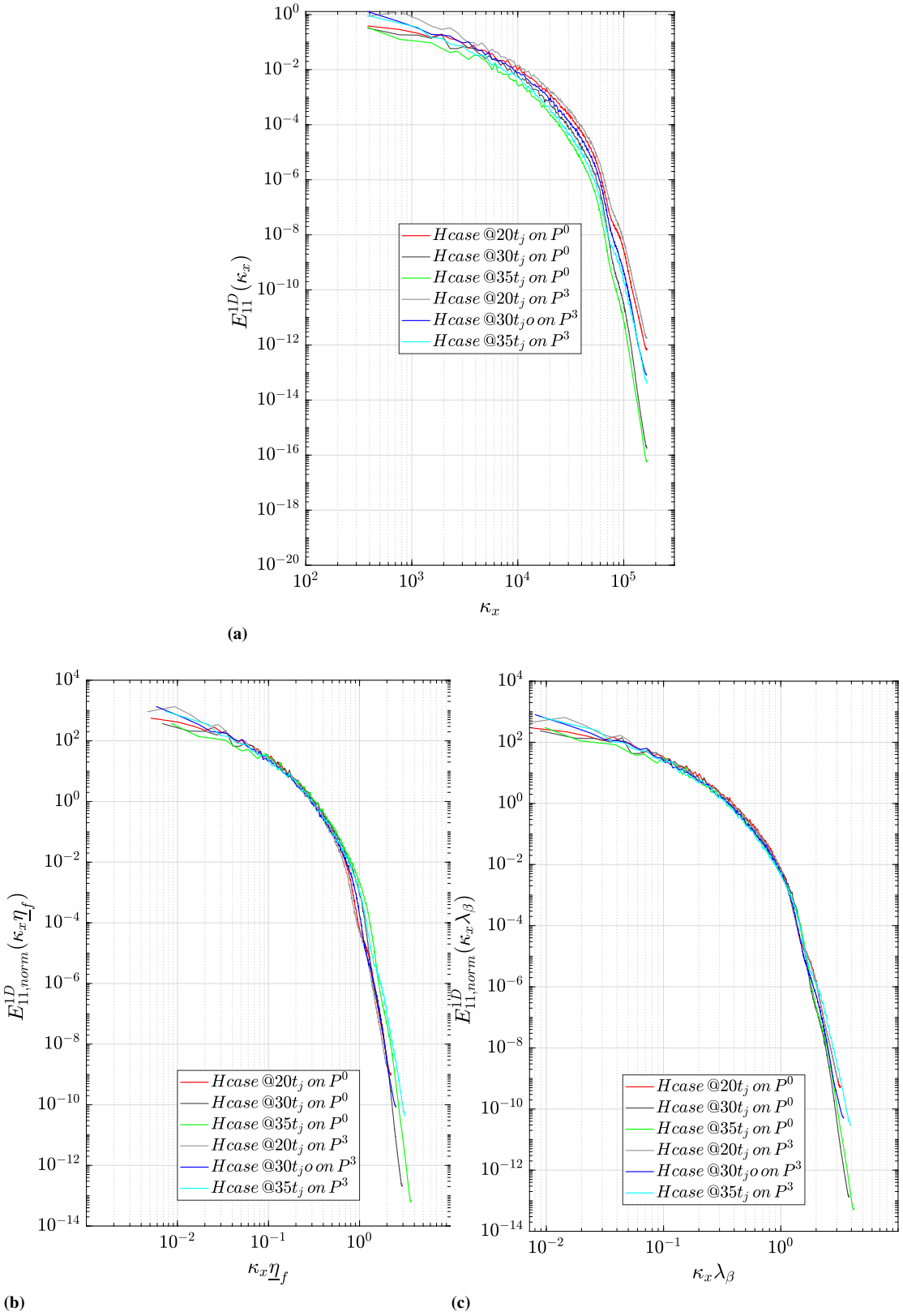


**Figure 5.28:** *1D longitudinal velocity spectra across the reacting shear layer at the maximum extinction, t=20$t_j$ and re-ignition times t=30,35$t_j$ for case H on the central plane and the mean stoichiometric plane, (**a**) Non-normalized spectra; (**b**) Normalized using the Favre averaged $\eta$ and $\varepsilon$; (**c**) Normalized using the Batchelor length scale and $\varepsilon$.*

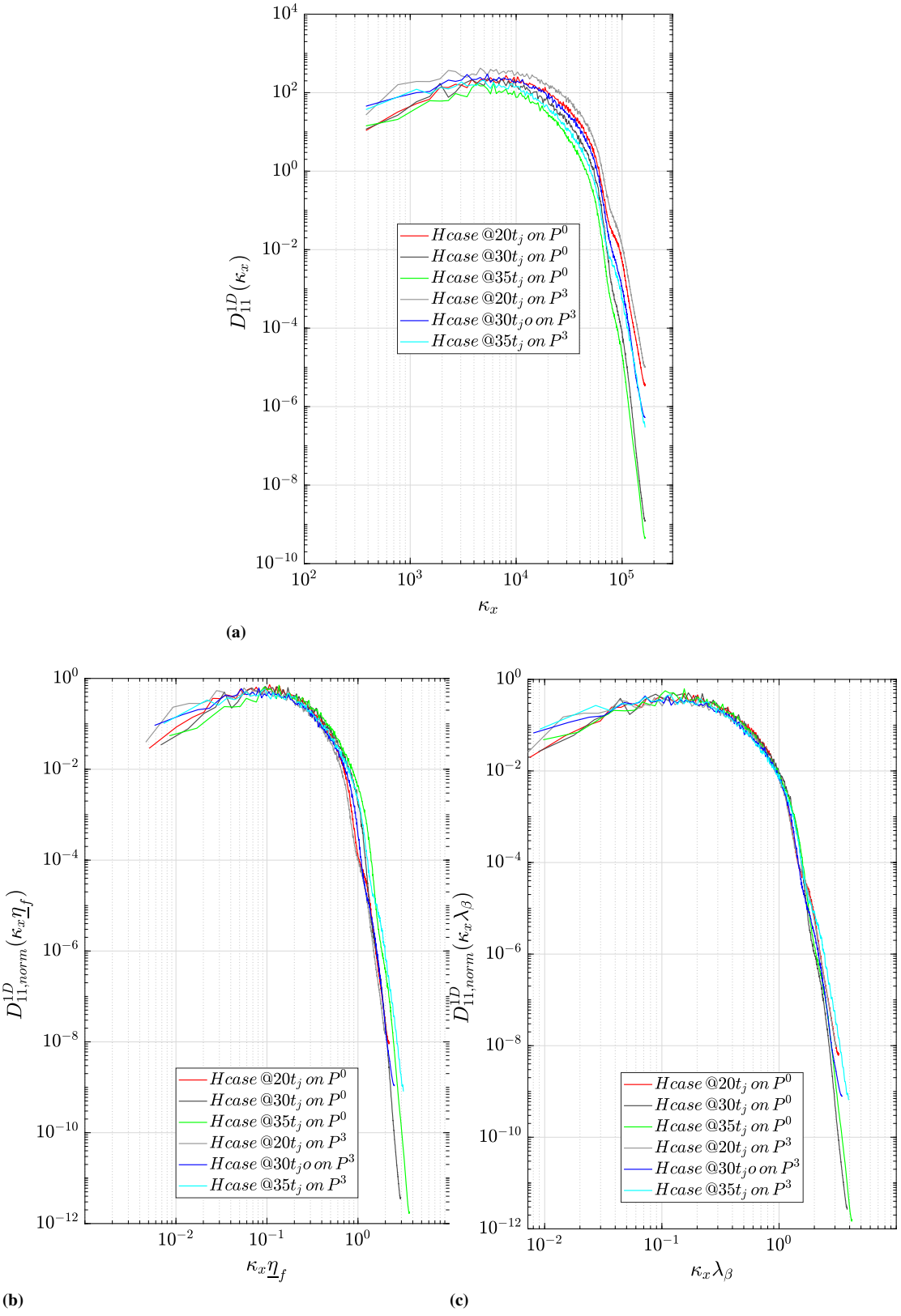


**Figure 5.29:** *1D longitudinal dissipation spectra across the reacting shear layer at the maximum extinction, t=20$t_j$ and re-ignition times t=30,35$t_j$ for case H on the central plane and the mean stoichiometric plane, (**a**) Non-normalized spectra; (**b**) Normalized using the Favre averaged $\eta$ and $\varepsilon$; (**c**) Normalized using the Batchelor length scale and $\varepsilon$.*

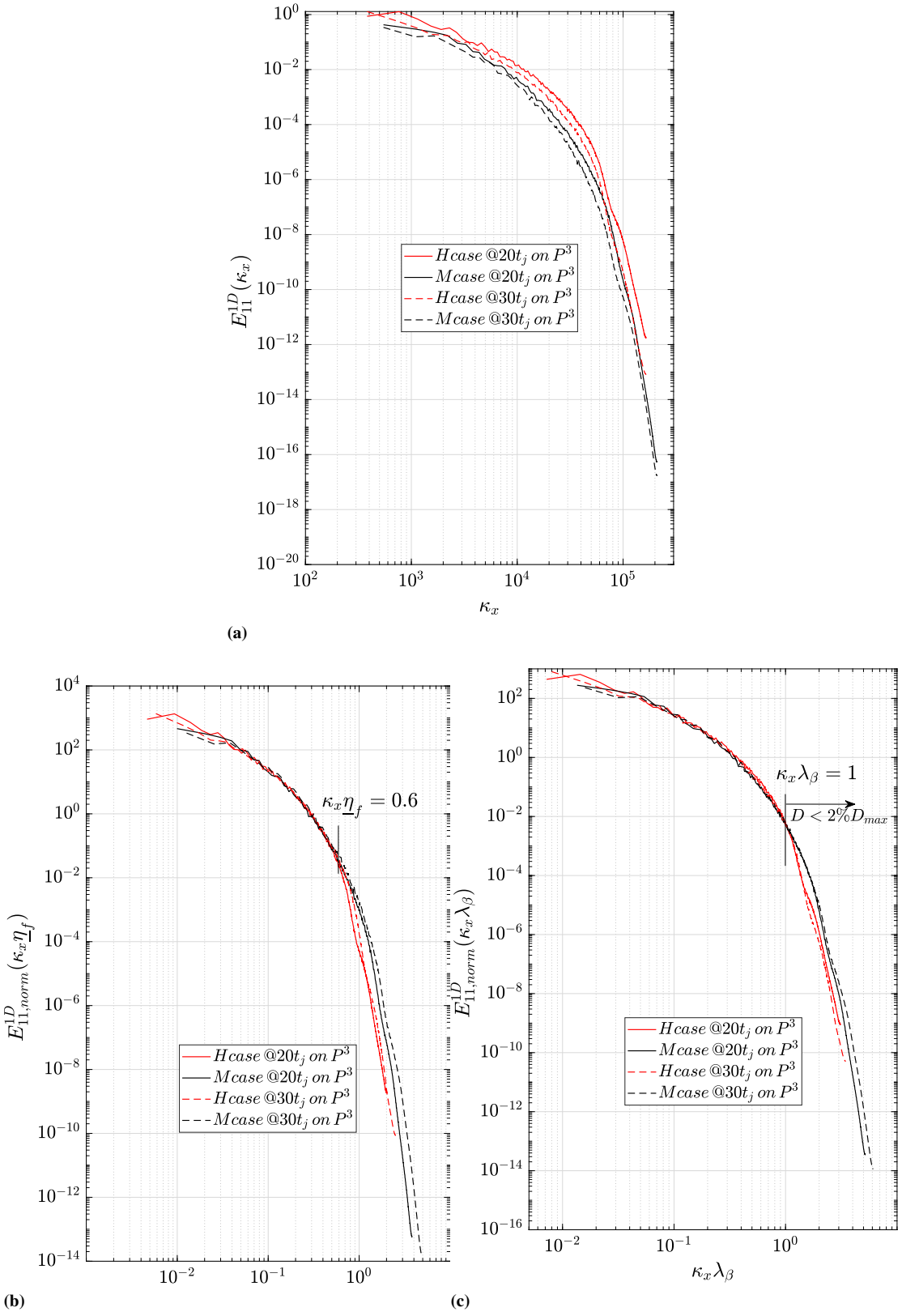


**Figure 5.30:** *1D longitudinal velocity spectra across the reacting shear layer at maximum extinction, t=20$t_j$ and re-ignition times t=30$t_j$ for cases H and M on the mean stoichiometric plane, (**a**) Non-normalized spectra; (**b**) Normalized using the Favre averaged $\eta$ and $\varepsilon$; (**c**) Normalized using the Batchelor length scale and $\varepsilon$.*

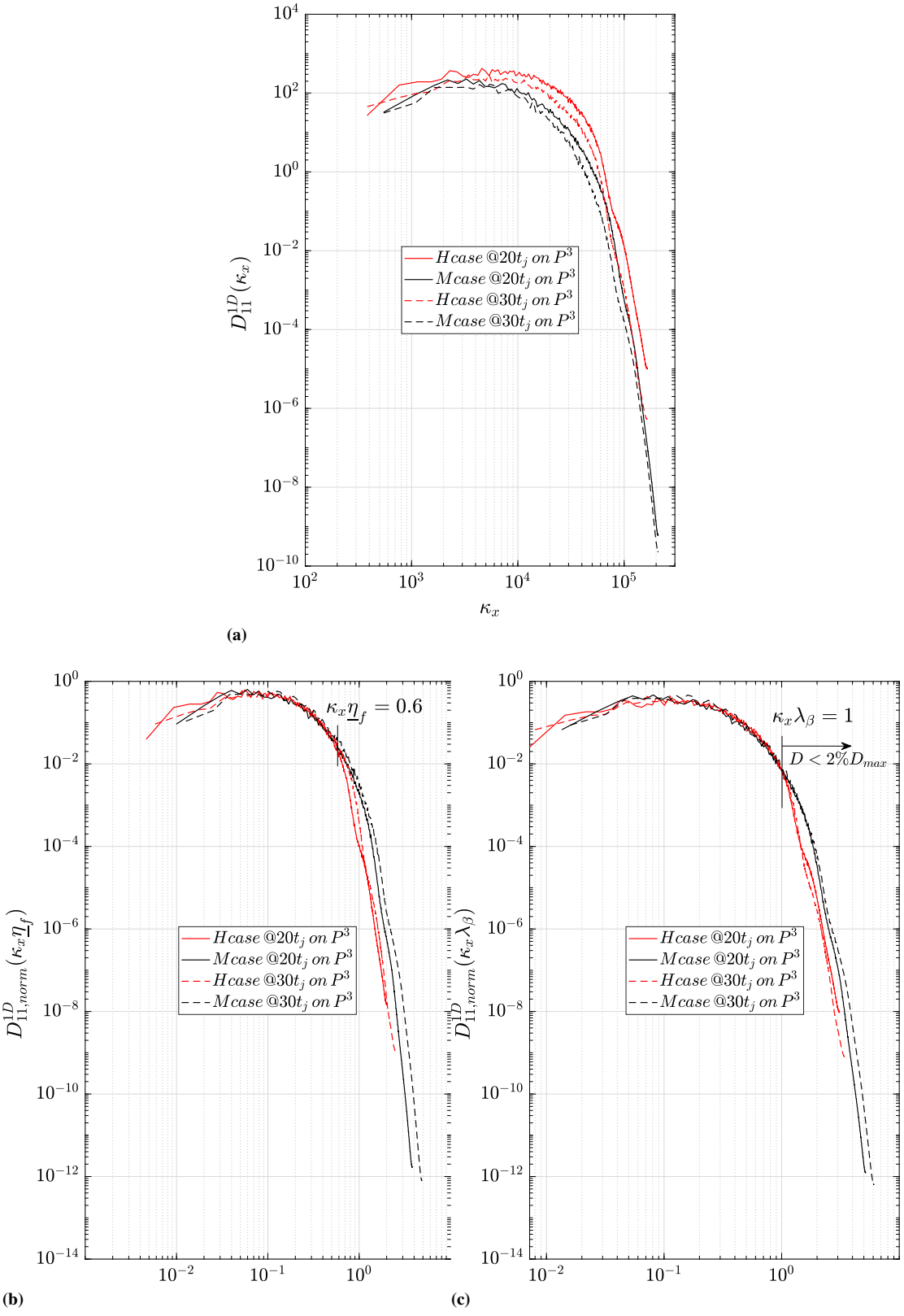


**Figure 5.31:** *1D longitudinal dissipation spectra across the reacting shear layer at maximum extinction, t=20$t_j$ and re-ignition times t=30$t_j$ for cases H and M on the mean stoichiometric plane, (**a**) Non-normalized spectra; (**b**) Normalized using the Favre averaged $\eta$ and $\varepsilon$; (**c**) Normalized using the Batchelor length scale and $\varepsilon$.*

### 5.3.4 The Model Spectrum for Reactive Flows

Pope's model for 3D energy spectrum introduced in Eq. 2.75 (also repeted here in Eq. 5.21 for convenience). The model proposed for non-reactive constant density turbulent flows and in this section it is compared with the spectra of turbulent flames. This is a model trying to cover the whole range of wavenumbers. It includes the Kolmogorov spectrum for the inertial range, $f_L(\kappa L)$ for the low wavenumber and the rest for the dissipation range. As can be seen the exponential drop-off form in the dissipation range is more complicated than the simple form of Eq. 5.18 already discussed, however, keeping the same exponential drop-off factor (if $c_\eta = 0$). This must be used with care when comparing with the extracted spectra from DNS. The 3D model energy spectrum first must be converted to the 1D spectrum (i.e., components of Eq. 5.16) and then be compared to, e.g., $E_{11}$. If isotropy is assumed, one can derive the 1D spectrum from the 3D energy spectrum [52]:

$$E_{11}^{1D}(\kappa_x) = \int_{\kappa_x}^{\infty} \left(1 - \frac{\kappa_x^2}{\kappa^2}\right) \frac{E(\kappa)}{\kappa} d\kappa \tag{5.20}$$

The equation can be used to derive an expression for the 1D model and to be compared with the 1D spectra extracted from DNS. The 3D model spectrum can be modified and then integrated to find a best fit to the 1D spectrum from DNS. It should be noted that the conversion (integration) is done numerically.

The form of Eq. 2.75 will be repeated here for the convenience.

$$E_{Model,Normal}(\kappa\underline{\eta}) = C_K \left(\kappa\underline{\eta}\right)^{-5/3} f_\eta(\kappa\underline{\eta}) f_L(\kappa L), \tag{5.21}$$

where the integral range multiplier, $f_L(\kappa L)$ is active in low wavenumber ranges:

$$f_L(\kappa L) = \left(\frac{\kappa L}{\left((\kappa L)^2 + c_L\right)^{1/2}}\right)^{5/3+P_0}, \tag{5.22}$$

Here we are not concerned with the form of $f_L(\kappa L)$ since the wavenumber ranges of interest are the inertial and the dissipation ranges. Further, it does not have a large effect on the shape of the model in these ranges. So the conventional values of constants for $f_L(\kappa L)$ i.e., $P_0 = 2$ and $c_L = 6.78$ will be used.

For the inertial range ($C_K \left(\kappa\underline{\eta}\right)^{-5/3}$), the $-5/3$ behaviour already observed for the non-premixed flames studied in this work. Further, there are many evidences e.g., [46, 47] of existence of such scaling in turbulent flames consistent with the non-reactive flows.

As mentioned earlier, in experiments, the 1D spectra are analyzed and the 1D Kolmogorov constant is evaluated. Then the using isotropic relations ($C_K \equiv C_K^{3D} = 55/18 C_K^{11}$) the 3D constant will be computed. Sreenivasan [39] collected all the data on 1D Kolmogorov's constant until 1995 and found the value $C_K^{11} = 0.53 \pm 0.055$ but at the end he suggested the value of 0.5 considering some uncertainties regarding the validity of isotropy assumption in experiments to evaluate $\underline{\varepsilon}$. Yeung and Zhou [40] did the same collection of data but from DNS results until 1997. The values were reported to be around 1.8-2. These values were higher than the one expected from experiments (which is $C_K^{3D} = 55/18 C_K^{11} = 55/18 \times 0.53 \pm 0.055 \approx 1.619$). They argued that the

deviation from isotropy can contribute to values of $C_K$ to be higher than the expected values [40]. The similar compilation of the experiments and/or DNS results in reactive flows is missing in the literature.

As shown in the previous section and also results in Appendix A, we found the value of Kolmogorov constant for the 1D longitudinal spectra being $C_K^{1D} \approx 0.75$. The corresponding constant for the 3D energy spectrum ($C_K$ in the model spectrum) is $C_K^{3D} = 55/18 C_K^{11} = 55/18 \times 0.75 \approx 2.3$. The value of $C_K^{1D} \approx 0.75$ was obtained analyzing 3 sets of DNS (cases H, M and L) in 3 time instants corresponding to different flame dynamics and 6 planes across the reactive shear layers in the mean turbulent region with low external intermittency. As can be seen, the value is higher than the experiments in non-reacting cases. However, it is not known if the higher values are due to combustion or deviations from isotropy in the current DNS of double shear layers (as pointed out in [40] for non-reactive DNS data). It can also be due to the relatively low $Re_\lambda$ in our DNS cases as mentioned in [70]. Keeping in mind this difference, we keep using the observed value, i.e. $C_K = 2.3$ in the modified model as the 3D Kolmogorov constant.

As mentioned earlier, no exact form can be derived for the spectrum in the near dissipation range (i.e., $0.5 \leq \kappa\underline{\eta} \leq 1.5$). Pope, for the constant-density flows proposed the form:

$$f_\eta(\kappa\underline{\eta}) = exp[-\beta_P \left( \left(\kappa\underline{\eta}\right)^4 + c_\eta^4 \right)^{1/4} - c_\eta], \tag{5.23}$$

and the experimentally obtained constants of $\beta_P = 5.2$ [43] and $c_\eta = 0.4$ has been used by Pope [38]. As shown in the previous sections we found a steeper exponential drop-off with $\beta \approx 7.2$ for case H in range $0.1 \leq \kappa_x \underline{\eta}_f \leq 0.8$. This range is wider in cases L and M, i.e., $0.1 \leq \kappa_x \underline{\eta}_f \leq 1.8$ and $0.1 \leq \kappa_x \underline{\eta}_f \leq 1.4$, respectively (see Appendix A). So we use this value in the modified model.

Since we already saw an acceptable collapse of the spectra across the shear layers, for the sake of clarity we just use the results extracted from $P^3$ corresponding to plane of maximum Favre mean OH mass fraction. In Fig. 5.32a the normlized spectrum is compared with the model spectrum using the modified coefficients. Further, in Fig. 5.32b the normalized velocity dissipation spectrum from DNS is compared with the normalized modified model dissipation spectrum. In both plots the agreement is acceptable before the inflection points in two plots.

It is interesting if the dissipation spectrum is investigated in lin-lin plot in Fig. 5.33. In this figure five different normalized velocity dissipation spectra are plotted. First the famous 3D dissipation model of Pope with the peak at $\kappa\underline{\eta}_f \approx 0.26$ is plotted in blue line with dot markers. The DNS spectrum is the black dashed line. It is clear that they are not collapsed. Actually it is wrong to compare these two, since the model is for the TKE ($1/2 u_i'' u_i''$) dissipation and the DNS is for the dissipation of velocity fluctuations in longitudinal direction ($1/2 u_1'' u_1''$). The DNS must be compared with the 1D form of the original Pope's model computed by Eq. 5.20. The 1D form of the original Pope's model is the green dashed-dotted line. The peak of the dissipation spectrum occurs at $\kappa\underline{\eta}_f \approx 0.11$. This value is consistent with the observations in experiments (e.g. [43]) and DNS [183] for constant-density non-reactive flows. However, it is clearly seen that the peak of the 1D dissipation spectrum from the non-premixed jet flame DNS is at lower wavenumbers ($\underline{\eta}_f \approx 0.08$). Approximately the same value was also observed in

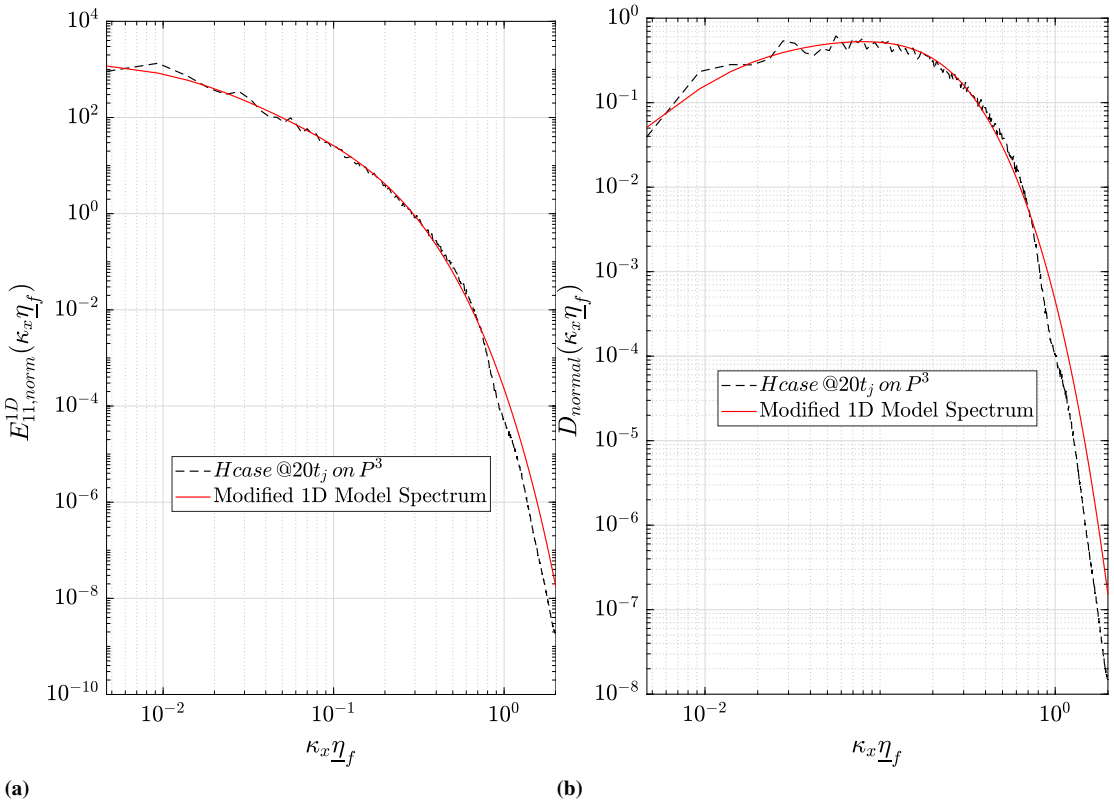


**Figure 5.32:** *1D longitudinal dissipation spectra across the reacting shear layer at the maximum extinction, t=20$t_j$ and re-ignition, t=30$t_j$, times for cases H and M on the mean stoichiometric plane compare with the modified model spectrum of Pope, (**a**) Non-normalized spectra; (**b**) Normalized using the Favre averaged $\eta$ and $\varepsilon$*

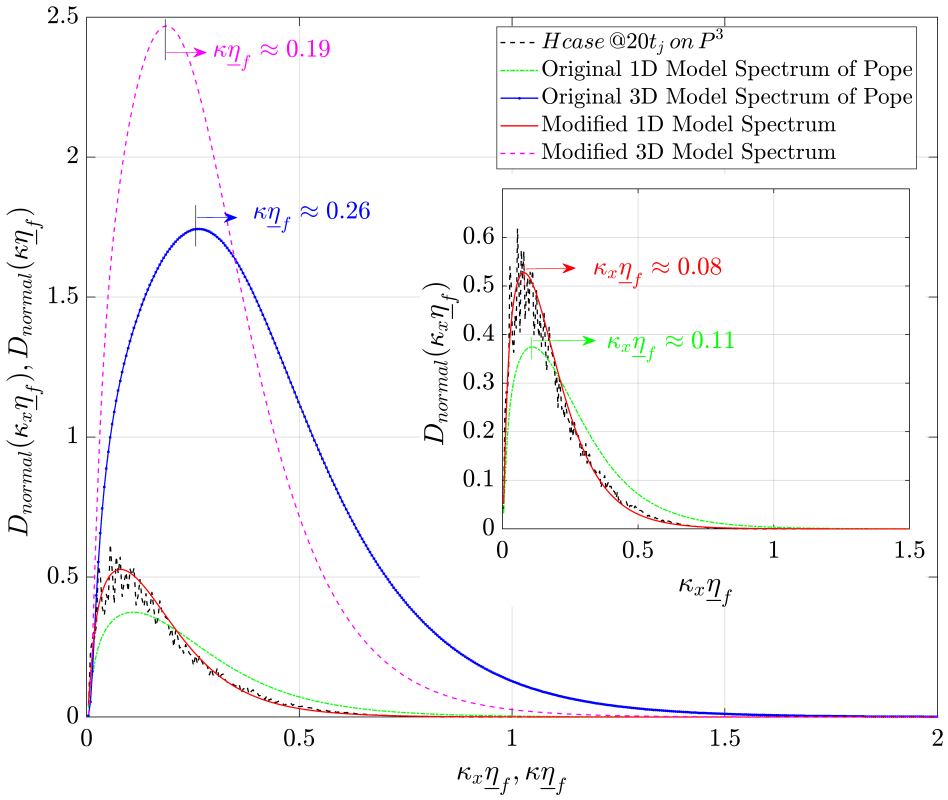


**Figure 5.33:** *1D dissipation spectra on the plane corresponding to the mixture fraction equal to the stoichiometric value of 0.422 at t=20$t_j$ for case H. The inset is the zoom view of the left corner.*

the premixed flame DNS (Fig. 9 in [48]). However, in that paper it was compared with the peak location of the 3D model ($\kappa\underline{\eta}_f \approx 0.26$) and was concluded that there is a large deviation from the results with respect to non-reactive model of Pope. It is observed that the correct value to be compared with is $\underline{\eta}_f \approx 0.11$. The red line is the newly adapted 1D model using the observed $C_K^{1D} \approx 2.3$, $\beta \approx 7.2$ and the fitted $c_\eta = 0.28$ which matches well with the DNS data (black dashed line). Finally, if the adapted 3 model is plotted, the result is the thick dashed magenta line. Now the blue and magenta lines must be compared. The blue is the 3D model spectrum for non-reactive flows and the magenta is the one obtained using the current non-premixed jets DNS databases. The peak of the modified 3D model is at $\kappa\underline{\eta}_f \approx 0.19$ instead of $\kappa\underline{\eta}_f \approx 0.26$. Further, it is less extended to the far dissipation range ($\kappa\underline{\eta}_f > 1$). Note that the area under the two curves are the same. The adapted 3D model spectrum will be used in Sec. 3.2.3 in new EDC models development.

#### Final Notes on the Compressible Form of Velocity Spectrum for Variable Density Flows

As mentioned in Eq. 2.67, if the 3D energy spectrum is integrated over all wavenumbers the result is the turbulence kinetic energy. In variable density flows we are dealing with the Favre turbulent kinetic energy (i.e. Eq. 2.52) and we have:

$$\int_0^\infty E(\kappa,t)d\kappa \neq \frac{1}{2}\langle u_i'' u_i''\rangle_f \equiv \frac{1}{2}\underline{u_i'' u_i''}_f \equiv \underline{k}_f. \tag{5.24}$$

The integral's error is at most $-6\%$ inside the turbulent flame brush and on the stoichiometric plane and $+10\%$ outside the flame on the planes of maximum fluctuations of density and temperature in our cases. Recently, in [47], the compressible form of Eq. 2.29 using density weighting is proposed as:

$$\begin{aligned} R_{ij_f}(\mathbf{r},t) \equiv & \frac{1}{2\langle\rho\rangle}\langle\rho(\mathbf{x},t)u_i''(\mathbf{x},t)u_j''(\mathbf{x}+\mathbf{r},t)\rangle \\ & + \frac{1}{2\langle\rho\rangle}\langle u_i''(\mathbf{x},t)\rho(\mathbf{x}+\mathbf{r},t)u_j''(\mathbf{x}+\mathbf{r},t)\rangle. \end{aligned} \tag{5.25}$$

This can be interpreted as the influence of momentum fluctuations at point $\mathbf{x}$ on velocity fluctuations at point $\mathbf{x}+\mathbf{r}$ and vice versa. From the definition Eq. 5.25, the density weighted or Favre velocity spectrum tensor like Eq. 2.64 can be defined:

$$\Phi_{ij_f}(\boldsymbol{\kappa},t) \equiv \frac{1}{(2\pi)^3}\iiint_{-\infty}^{\infty} e^{-i\boldsymbol{\kappa}.\mathbf{r}} R_{ij_f}(\mathbf{r},t)d\mathbf{r}, \tag{5.26}$$

where the Favre energy spectrum function can be defined from it as:

$$E_f(\kappa,t) \equiv \frac{1}{2}\iiint_{-\infty}^{\infty} \Phi_{ii_f}(\boldsymbol{\kappa})\delta(|\boldsymbol{\kappa}|-\kappa)d\boldsymbol{\kappa}, \tag{5.27}$$

and finally:

$$\int_0^{\infty} E_f(\kappa,t)d\kappa = \frac{1}{2}\langle u_i''u_i''\rangle_f = \frac{1}{2}\underline{u_i''u_i''}_f \equiv \underline{k}_f. \tag{5.28}$$

For the evaluation of the Favre spectrum suitable for variable density flows like reactive flows, consider the velocity vector $\mathbf{U}(\mathbf{x},t) = (u_1,u_2,u_3) = u_i\ i = 1,2,3$, first we make any component a centered one using the Favre average operator i.e. Eq. 2.33. Then the 1D velocity spectrum is evaluated as:

$$\begin{aligned} E_{ii}^{1D,Favre}(\kappa_x) = & \frac{1}{2\langle\rho\rangle}\langle DFT_{\rho u_i''}DFT^*_{u_i''}\rangle \\ & + \frac{1}{2\langle\rho\rangle}\langle DFT_{u_i''}DFT^*_{\rho u_i''}\rangle, \end{aligned} \tag{5.29}$$

where $DFT^*$ is the complex conjugate of $DFT$. Using the spatial Favre averaging operator Eq. 2.37 and Eq. 2.36 for the spatial Favre fluctuations we have:

$$\begin{aligned} E_{ii}^{1D,Favre}(\kappa_x) = & \frac{1}{2N_z\underline{\rho}}\sum_{z=1}^{N_z} DFT(\rho u_i'')DFT^*(u_i'') \\ & + \frac{1}{2N_z\underline{\rho}}\sum_{z=1}^{N_z} DFT(u_i'')DFT^*(\rho u_i''), \end{aligned} \tag{5.30}$$

where the DFT is calculated using all $u_i''$ values in one homogeneous direction (i.e., $Ox$) and averaging over the second direction (i.e. $Oz$ with $N_z$ the number of cells in $Oz$ direction).

The same analysis which was carried out in the previous sections has been repeated using the spectra computed by Eq. 5.30 instead of Eq. 2.86. The integral of $E^{1D,Favre} =$

$\frac{1}{2}\left(E_{11}^{1D,Favre}+E_{22}^{1D,Favre}+E_{33}^{1D,Favre}\right)$ found to be equal to the Favre TKE computed by Eq. 2.52.

In Fig. 5.34 the compressible form (Eq. 5.30) and the incompressible form (Eq. 2.86) of the spectrum function were compared. The spectra are computed for cases H and M at t=20$t_j$ on plane of stoichiometric mixture fraction, $P^6$. It is seen in Fig. 5.34a that the compressible spectrum is extended more in the dissipation range. This is consistent with the finding in [47]. The shape of the spectrum is preserved. Specifically in the compensated plot (Fig. 5.34b) the new exponential drop-off factor found before ($\beta \approx 7.2$ in the range $\kappa_x \underline{\eta}_f \leq 0.8$) is the same using both methods. The profound difference is observed after the inflection. Also a small discontinuity is observed at the very far range of Fig. 5.34b in $\kappa_x \underline{\eta}_f \approx 2$ in the compressible spectrum. This is the very few negative values of computed energy (In the log-log plot the software ignores the negative values). In Eq. 5.30, $E_{ii}^{1D,Favre}$ is not strictly positive unlike the case in the form of Eq. 2.86[8].

It seems that the inclusion of the effect of density fluctuations using the Favre correlations (see Eq. 5.25 or Eq. 5.30) mostly affects the spectrum after the inflection. This is confirmed by looking at the results of another DNS database (case M) in Fig. 5.34c. One may conclude that the inflection point has something to do with the effect of density fluctuations. However, in examining the results some un-physical behaviours in the dissipation range were detected. Examining all components of the 1D energy spectrum ($E_{11}^{1D}$,$E_{22}^{1D}$ and $E_{33}^{1D}$) computed using the compressible formula in Fig. 5.35, shows that surprisingly, after the inflection $E_{11}^{1D}$ becomes grater than the other two. This is not consistent with the expected behaviour which was already confirmed in Fig. 5.24.

No conclusion can be drawn at this point. It cannot be probable that there is a bug in the implementation of the compressible formula for computing the spectra, since as was observed in the previous figures, both forms of spectra agree in the shape up to the inflection point. If the derivation of the compressible form of the velocity spectrum in [47] is accepted, it is not clear that if the observed behaviours are physical or due to effects of noise in the databases at high wavenumber ranges, or it is the effect of the high order filter in the code. These are the reasons why in the current thesis the compressible form is not adopted and it is preferred to use the conventional incompressible form as were also previously used for reactive flows, e.g., in [45, 46, 154].

[8] In Eq. 2.86 the direct multiplication of Fourier coefficient with its complex conjugate results in a positive value, or in other words, the magnitude of the Fourier coefficients are strictly positive which is not the case in Eq. 5.30.

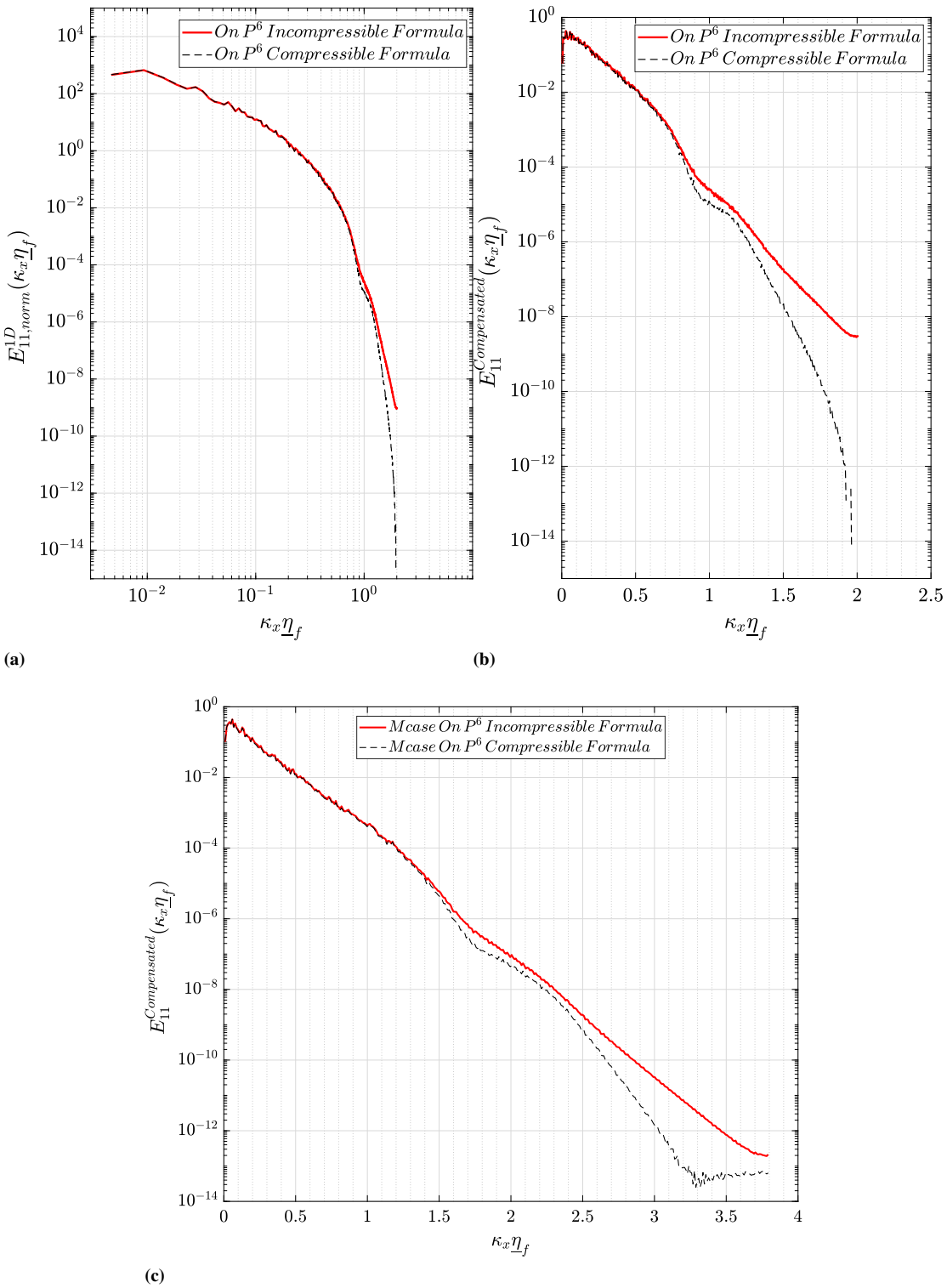


**Figure 5.34:** *1D spectra on the plane of Favre mean stoichiometric mixture fraction at t=20$t_j$ , (**a**) for case H, the normalized form; (**b**) for case H the compensated form; (**c**) for case M the compensated form.*

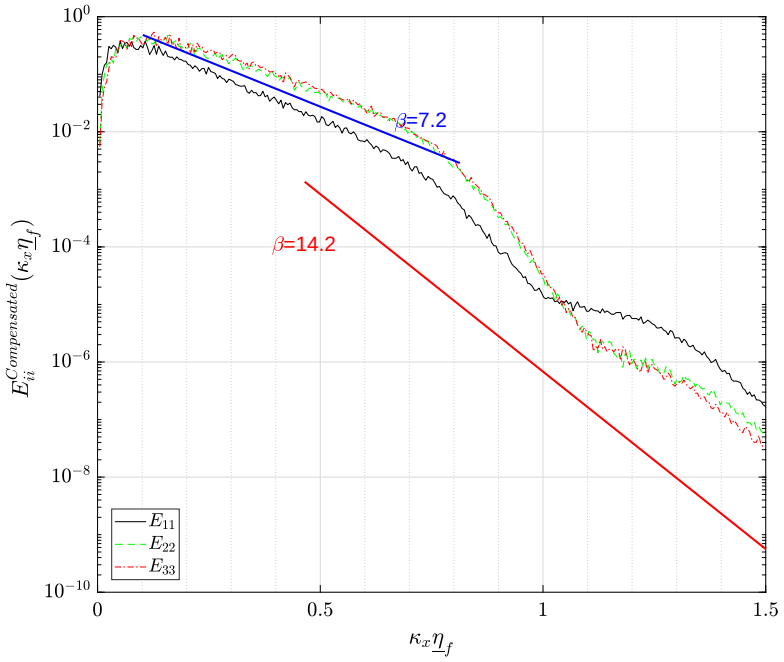


**(a)**

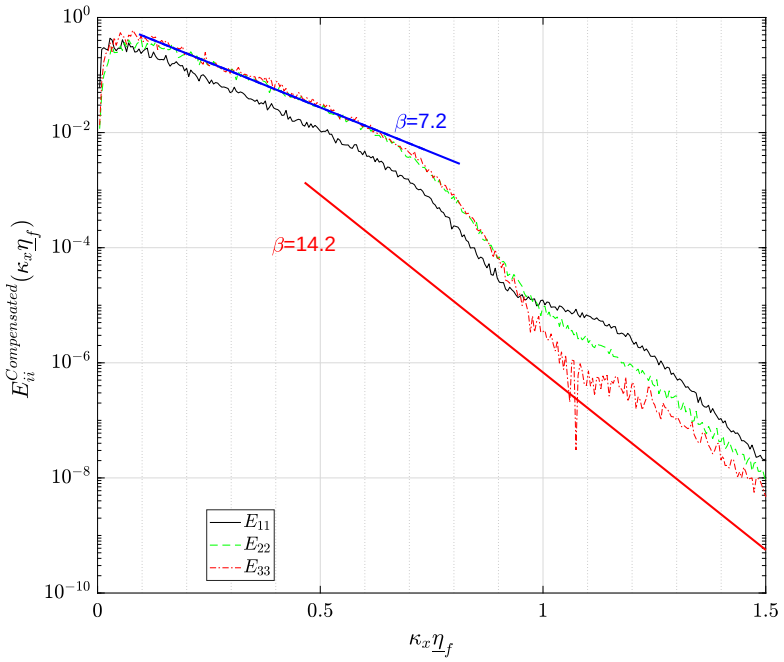


**(b)**

**Figure 5.35:** *1D compensated spectra computed from the compressible formula (Eq. 5.30) across the reacting shear layers at t=20$t_j$ for case H, (**a**) Extracted from the central plane; (**b**) Extracted from the Favre mean Stoichiometric mixture fraction plane.*

### 5.3.5 Summary and Conclusions

In this section the velocity and its dissipation spectra in non-premixed jets were analyzed using 3 different DNS databases of temporally evolving non-premixed syngas jet flames experiencing high levels of local extinction and re-ignition. In each database, 3 different time instants were selected (9 in total) corresponding to the events of maximum local extinction and re-ignition. The objective was to check Kolmogorov's scaling laws. It was observed that using $\underline{\eta}_f$ and $\underline{\varepsilon}_f$ to normalize the spectra extracted in different planes across the shear layers, at different flame dynamics instants and different Reynolds numbers, the spectra collapse on a single curve very well in the inertial range. In the dissipation range the collapse can be improved using a cut-off scale defined by the inverse of a wavenumber corresponding to $2\%$ of the dissipation spectra peaks ($\lambda_\beta$). To reach a perfect collapse of the spectra deep into the dissipation range $\kappa_x \underline{\eta}_f \gg 1$, it was hypothesized that some information of chemistry may needed, however, in non-premixed flames it is not easy to define a characteristic length scale of the flame like what is done in premixed flames.

$\kappa^{-5/3}$ power law was observed in the inertial range with the constant of proportionality, $C_K = 2.3$ instead of $1.5$. The difference between the value of $C_K = 2.3$ and the conventional $C_K = 1.5 - 1.7$ [70], is probably due to the low $Re_\lambda$ and so the very limited inertial range in the current DNS databases [42, 70].

In the dissipation range, the exponential drop-off of all velocity spectra was steeper than the corresponding non-reactive flows. It was observed that the $\exp(\beta\kappa)$ scaling exists with the value of $\beta = 7.2$ instead of non-reactive flows value of $\beta = 5.2$.

Next, the spectra were compared with the model spectrum of Pope (proposed for non-reactive flows). It is a common way to use this model spectrum to compute model constants in RANS/LES, both for velocity (e.g. [76]) or combustion sub-models (e.g. [15]). It was found that the functional form proposed by Pope [38] for non-reactive flows agrees well with the velocity and the dissipation spectra of reactive flows studied in this work, if the values of $C_K$ and $\beta$ mentioned above is used in the model. We will use this adapted version of the model spectrum in Sec. 3.2.3 to derive an analytical relation between the two coefficients in the EDC.

## 5.4 *A Priori* Analysis of FR-TCI-LES Moldels

In this section the finite-rate turbulence-chemistry interaction models for LES (FR-TCI-LES models) will be *a priori* assessed using the current DNS databases. The analyses have been done using the code mentioned in Sec.4.6. All the required exact filtered quantities are extracted from the DNS databases using the explicit filters mentioned in Sec.4.3. The assessment is done using different metrics already introduced in Sec.4.4. All the definitions of the exact quantities like sub-grid kinetic energy, sub-grid viscous dissipation and ... were already introduced and discussed in Chap.2.

### 5.4.1 Eddy Dissipation Concept (EDC) Model

In this section the EDC for SGS combustion modeling will be *a priori* assessed based on the DNS databases introduced in Sec.4.5. Details about the models were already discussed in Sec.3.2. For the convenience of the reader the variants of the EDC which will be assessed in this section is repeated in Table5.2. Also in this table, two new models (compared to Table3.3), are added. These are "**EDC-L-OE**" and "**EDC-L-EN$_{\mathrm{C}}$**".

To better understand the different variants of the models, a brief discussion is presented here. The conventional or "**O**riginal" **EDC-L**ES (mentioned by "**EDC-L-**" in Table5.2) are the ones developed by the Swedish (mentioned by "**OF"**) or Norwegian (mentioned by "**OLy**") groups. In the Swedish approach the cascade model has only one coefficient, $\zeta$, and $\gamma^*$ is modeled as $\gamma^* = \left(\frac{u^*}{U^{SGS}}\right)^3$ (assuming the dissipative structures as Corrsin's sheets [111]). On the other hand, the Norwegian group uses the cascade model with two coefficients, $CD_1$ and $CD_2$ and $\gamma^*$ is modeled as $\gamma^* = \left(\frac{u^*}{U^{SGS}}\right)^2$ (assuming the dissipative structures as Tennekes tubes [103]). Then the "**EDC-L-OE**" model will be derived by using the two coefficients cascade model and assuming the dissipative structures as Corrsin's sheets. These are the base or reference EDC-LES models

The contribution of the current thesis, using the derived model dissipation spectrum in Sec.5.3 with the application discussed in Sec.3.2.3, resulted in the relation, $CD_2 = 135.7CD_1^2$. The models which use this new relation have "$\mathbf{N_C}$" in their names. When a reference model is modified, the "**O**" will be dropped in its name and the modification name is added. For example, "**EDC-L-LyN$_{\mathrm{C}}$**" is the modified version of "**EDC-L-OLy**" by only using the new relation between two coefficients $CD_1$ and $CD_2$. Although a relation between the two coefficients was found, the models still need $CD_1$ to be set.

In Sec.3.2.3, some options to evaluate $CD_1$ were presented. The first option is to use the original value proposed by Ertesvag [15] which is the experimentally obtained value of $CD_1 = 0.135$. The other option is using the approximation $\varepsilon_{\nu,SGS} = C_\varepsilon \frac{(k_{SGS})^{3/2}}{\Delta}$, with $C_\varepsilon = 1.048$. This gives the value of $CD_1 = 1.28$. In LES one can dynamically approximate the value of $CD_1$ as was explained in Sec.3.2.3. It will be shown that the models with the approximation $\varepsilon_{\nu,SGS} = C_\varepsilon \frac{(k_{SGS})^{3/2}}{\Delta}$, and $C_\varepsilon = 1.048$ will fail in the *a priori* DNS assessment and the reason will be discussed. However, this does not

mean that these models will not work in LES while using dynamic procedures.

The other modification proposed in EDC-LES was based on the findings in Sec.5.2.2 on the internal intermittency phenomenon in reactive flows. The application in the EDC was discussed in Sec.3.2.4. It was shown that in RANS mode, i.e., studying the fluctuation of dissipation with respect to the Favre averaged dissipation, the internal intermittency factor scales as $Re_\lambda^{-0.28}$ not $Re_\lambda^{-1}$ or $Re_\lambda^{-3/2}$. Here $Re_\lambda$ is the Taylor scale Reynolds number using Favre averaged quantities. $Re_\lambda^{-1}$ or $Re_\lambda^{-3/2}$ are the results of phenomenological theories of Tennekes [103] and Corrsin [111], respectively, as discussed above. Then it is proposed to scale the $\gamma^*$ in EDC with $Re_\lambda^{-0.28}$. Although we are aware that the fluctuations with respect to the mean cannot theoretically be extended to the sub-grid fluctuations, this is a very first try to modify the EDC-LES $\gamma^*$. The future works which are needed to be done on this topic will be discussed in the last chapter.

The proposed modification based on the new internal intermittency factor was discussed in Sec.3.2.4. The models which use this new relation have "$\mathbf{N_G}$" in their names. Again, when a reference model is modified, the "**O**" will be dropped in its name and the modification name is added. For example, "**EDC-L-N$_{\mathrm{G}}$Ly**" is the modified version of "**EDC-L-OLy**" by only using the new $\gamma^*$ definition, i.e., Eq. 3.58. Further, it can be possible to apply both the "$\mathbf{N_C}$" and "$\mathbf{N_G}$" modifications. This will result in the "**EDC-L-N$_{\mathrm{G}}$LyN$_{\mathrm{C}}$**".

Note that we have not yet assessed the base or reference EDC-LES models so the modifications were applied to all existing models. That is why the number of derived models are high. In the following assessments will be carried out on all base and modified models using the DNS databases.

As stated before in Sec.3.2.5, the way the theory is implemented imposes a limit on $\gamma^*$ and so the Taylor scale Reynolds number. This limit or "threshold" is the minimum Reynolds number in a computational cell, below which, $\gamma^*$ is saturated. The threshold is calculated for different models and presented in Table5.3.

**Table 5.2:** *Summary of the LES-EDC combustion models applicable to a priori DNS analysis. In the table* **L** *stands for* "LES", **O** *stands for* "O*riginal*", **F** *stands for* "Fureby", **Ly** *stands for* "Lysenco", $\mathbf{N_G}$ *stands for* "New $\gamma^*$", $\mathbf{N_C}$ *stands for* "New C*oefficient*" and **E** *stands for* "Ertesvag". $\zeta_{LES}$ in **EDC-L-OF** and **EDC-L-N$_G$F** is $\zeta_{LES} = 0.566$ (see Eq. 3.31).

| **Model** | $\gamma^*$ | $\dot{\mathbf{m}}^*$ | $\mathbf{CD_1}$ | $\mathbf{CD_2}$ |
|---|---|---|---|---|
| **EDC-L-OF** (Fureby [91, 96, 97]) | $\left(\frac{45}{64\zeta^2}\right)^{3/4}\left(\frac{\overline{\nu}^f\varepsilon_{\nu,SGS}}{{k_{SGS}}^2}\right)^{3/4}$ | $\left(\frac{1}{25\zeta^4}\right)^{1/4}\left(\frac{\varepsilon_{\nu,SGS}}{\overline{\nu}^f}\right)^{1/2}$ | – | – |
| **EDC-L-N$_G$F** (Present work) | $\left(\frac{45}{64\zeta^2}\right)^{0.14}\left(\frac{\overline{\nu}^f\varepsilon_{\nu,SGS}}{{k_{SGS}}^2}\right)^{0.14}$ | $\left(\frac{1}{25\zeta^4}\right)^{1/4}\left(\frac{\varepsilon_{\nu,SGS}}{\overline{\nu}^f}\right)^{1/2}$ | – | – |
| **EDC-L-OLy** (Lysenco [102]) | $\left(\frac{3CD_2}{4CD_1^2}\right)^{2/4}\left(\frac{\overline{\nu}^f\varepsilon_{\nu,SGS}}{{k_{SGS}}^2}\right)^{2/4}$ | $\left(\frac{3}{CD_2}\right)^{1/2}\left(\frac{\varepsilon_{\nu,SGS}}{\overline{\nu}^f}\right)^{1/2}$ | 0.135 | 0.5 |
| **EDC-L-N$_G$Ly** (Present work) | $\left(\frac{3CD_2}{4CD_1^2}\right)^{0.14}\left(\frac{\overline{\nu}^f\varepsilon_{\nu,SGS}}{{k_{SGS}}^2}\right)^{0.14}$ | $\left(\frac{3}{CD_2}\right)^{1/2}\left(\frac{\varepsilon_{\nu,SGS}}{\overline{\nu}^f}\right)^{1/2}$ | 0.135 | 0.5 |
| **EDC-L-LyN$_C$**(Present work) | $10.09\left(\frac{\overline{\nu}^f\varepsilon_{\nu,SGS}}{{k_{SGS}}^2}\right)^{2/4}$ | $\left(\frac{3}{135.7CD_1^2}\right)^{1/2}\left(\frac{\varepsilon_{\nu,SGS}}{\overline{\nu}^f}\right)^{1/2}$ | 0.135 or 1.28 | – |
| **EDC-L-N$_G$LyN$_C$** (Present work) | $1.91\left(\frac{\overline{\nu}^f\varepsilon_{\nu,SGS}}{{k_{SGS}}^2}\right)^{0.14}$ | $\left(\frac{3}{135.7CD_1^2}\right)^{1/2}\left(\frac{\varepsilon_{\nu,SGS}}{\overline{\nu}^f}\right)^{1/2}$ | 0.135 or 1.28 | – |
| **EDC-L-OE** (Inspired by [97] and [15] ) | $\left(\frac{3CD_2}{4CD_1^2}\right)^{3/4}\left(\frac{\overline{\nu}^f\varepsilon_{\nu,SGS}}{{k_{SGS}}^2}\right)^{3/4}$ | $\left(\frac{3}{CD_2}\right)^{1/2}\left(\frac{\varepsilon_{\nu,SGS}}{\overline{\nu}^f}\right)^{1/2}$ | 0.135 | 0.5 |
| **EDC-L-EN$_C$**(Present work) | $32.04\left(\frac{\overline{\nu}^f\varepsilon_{\nu,SGS}}{{k_{SGS}}^2}\right)^{3/4}$ | $\left(\frac{3}{135.7CD_1^2}\right)^{1/2}\left(\frac{\varepsilon_{\nu,SGS}}{\overline{\nu}^f}\right)^{1/2}$ | 0.135 or 1.28 | – |

**Table 5.3:** *The threshold of sub-grid Taylor Reynolds number for different models assessed in a priori DNS analysis below which $\gamma^*$ is saturated and is equal to 0.5. In the table* **L** *stands for* "LES", **O** *stands for* "O*riginal*", **F** *stands for* "Fureby", **Ly** *stands for* "Lysenco", $\mathbf{N_G}$ *stands for* "New $\gamma^*$", $\mathbf{N_C}$ *stands for* "New C*oefficient*" and **E** *stands for* "Ertesvag". $Re_\lambda$ is calculated based on sub-grid quantities as $Re_{\lambda,SGS} = \frac{k_{SGS}}{\overline{\nu}^{f\,1/2}\varepsilon_{\nu,SGS}{}^{1/2}}$.

| Model | Threshold |
|---|---|
| **EDC-L-OF** (Fureby [91, 96]) | $Re_{\lambda,SGS} \geq 2.3$ |
| **EDC-L-N$_{\mathrm{G}}$F** (Present work) | $Re_{\lambda,SGS} \geq 17.6$ |
| **EDC-L-OLy** (Lysenco [102]) | $Re_{\lambda,SGS} \geq 9$ |
| **EDC-L-N$_{\mathrm{G}}$Ly** (Present work) | $Re_{\lambda,SGS} \geq 54$ |
| **EDC-L-LyN$_{\mathrm{C}}$** (Present work) | $Re_{\lambda,SGS} \geq 20$ |
| **EDC-L-N$_{\mathrm{G}}$EN$_{\mathrm{C}}$** (Present work) | $Re_{\lambda,SGS} \geq 120$ |
| **EDC-L-OE** (Inspired by [97] and [15] ) | $Re_{\lambda,SGS} \geq 19$ |
| **EDC-L-EN$_{\mathrm{C}}$** (Present work) | $Re_{\lambda,SGS} \geq 64$ |

**Results**

The performance of the EDC-LES models will be assessed by comparing the modeled filtered net formation rates obtained by different models with the exact filtered quantities extracted from case H (the highest Reynolds case) at the maximum local extinction time, i.e. t=20$t_j$.

In Figs. 5.36, 5.37, 5.38 the comparison is done using scatter plots for $\mathrm{CO}$, $\mathrm{H_2}$, and $\mathrm{O_2}$, respectively. The filter width is $\overline{\Delta} = 8\Delta_{\mathrm{DNS}}$.

First, the failure of the original "**EDC-L-OE**" and "**EDC-L-OF**" models is obvious using this metric (see Table5.2 for definitions).

Second, comparing the performance of models with "$\mathbf{N_C}$" modification and $CD_1 = 0.135$ with their respective original models (for example comparing Fig. 5.36b with 5.36a, and 5.36e with 5.36d) shows a high improvement. The same is true for other species.

Third, the improvement using "$\mathbf{N_G}$" modification (i.e., modified $\gamma^*$) is obvious when comparing "**EDC-L-N$_{\mathrm{G}}$F**" with the original model, "**EDC-L-OF**" (compare (**h** with **g** sub-figures in Figs.5.36,5.37, 5.38 . Also, the same is true when comparing "**EDC-L-N$_{\mathrm{G}}$Ly**" with the original model, "**EDC-L-OLy**" (compare (**i** with **d** sub-figures. Note that based on Table5.3, the threshold for "**EDC-L-N$_{\mathrm{G}}$F**" is low and $\gamma^*$ will not be saturated, so the effect of the modification in this factor can be observed.

Fourth, comparing the performance of models with "$\mathbf{N_C}$" modification and $CD_1 = 1.28$ with the same modification but using $CD_1 = 0.135$ shows failure or deterioration. As was previously discussed, the "$\mathbf{N_C}$" is using Eq. 3.46 and it needs a value for $CD_1$. The value of 1.28 obtained in Sec. 3.2.3, by using the approximation Eq. 3.26 with $C_\varepsilon = 1.048$. In Fig.5.39, the modeled sub-grid viscous dissipation is plotted against the exact field. It can be seen that although the correlation is high, it is systematically under predicted by Eq. 3.26 with $C_\varepsilon = 1.048$. The dynamic evaluation of $C_\varepsilon$ in LES, discussed in Sec.3.2.3, may be able to solve this issue. So, it cannot be concluded that this method of evaluation of $CD_1$ is wrong. As a result, it cannot be concluded that the models with "$\mathbf{N_C}$" modification and $CD_1$ evaluated dynamically instead of using $CD_1 = 0.135$ will fail in real LES. However, for the moment, since the aim is the *a priori* DNS assessment of the models, we exclude the models with $CD_1 = 1.28$ from further assessments (plots) and keep the discussion open for future *a posteriori* analyses or real LES. We will only focus on the results with $CD_1 = 0.135$.

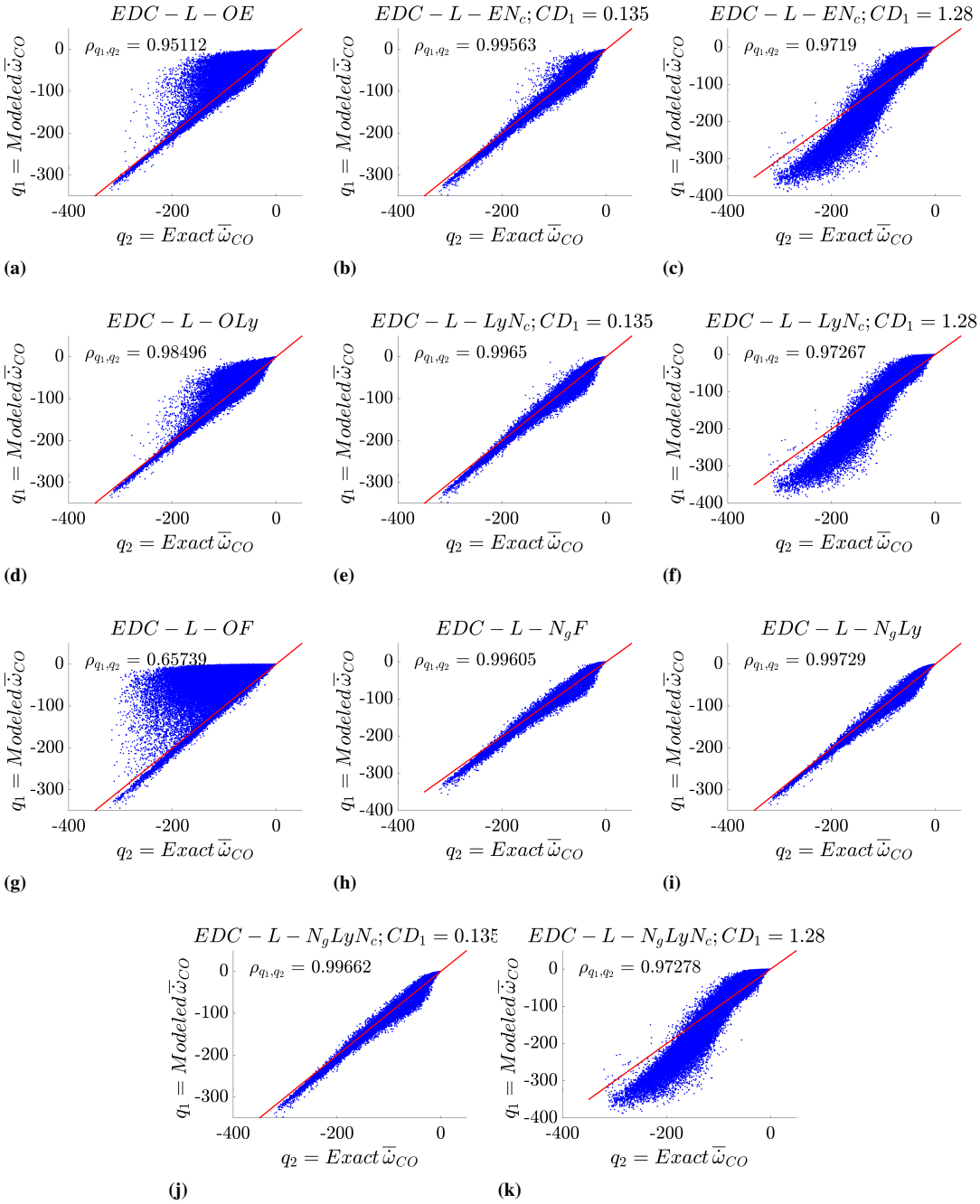


**Figure 5.36:** *Production/consumption rate of* CO *(fuel) with units* $[kg/(m^3 s)]$*, using different EDC-LES models (see Table5.2) compared with the exact filtered quantity for case H at t=20*$t_j$*. Filter width is* $\overline{\Delta}/\Delta_{\mathrm{DNS}} = 8$*. The correlation coefficients, (Eq. 2.26) have been calculated and shown in the inset.*

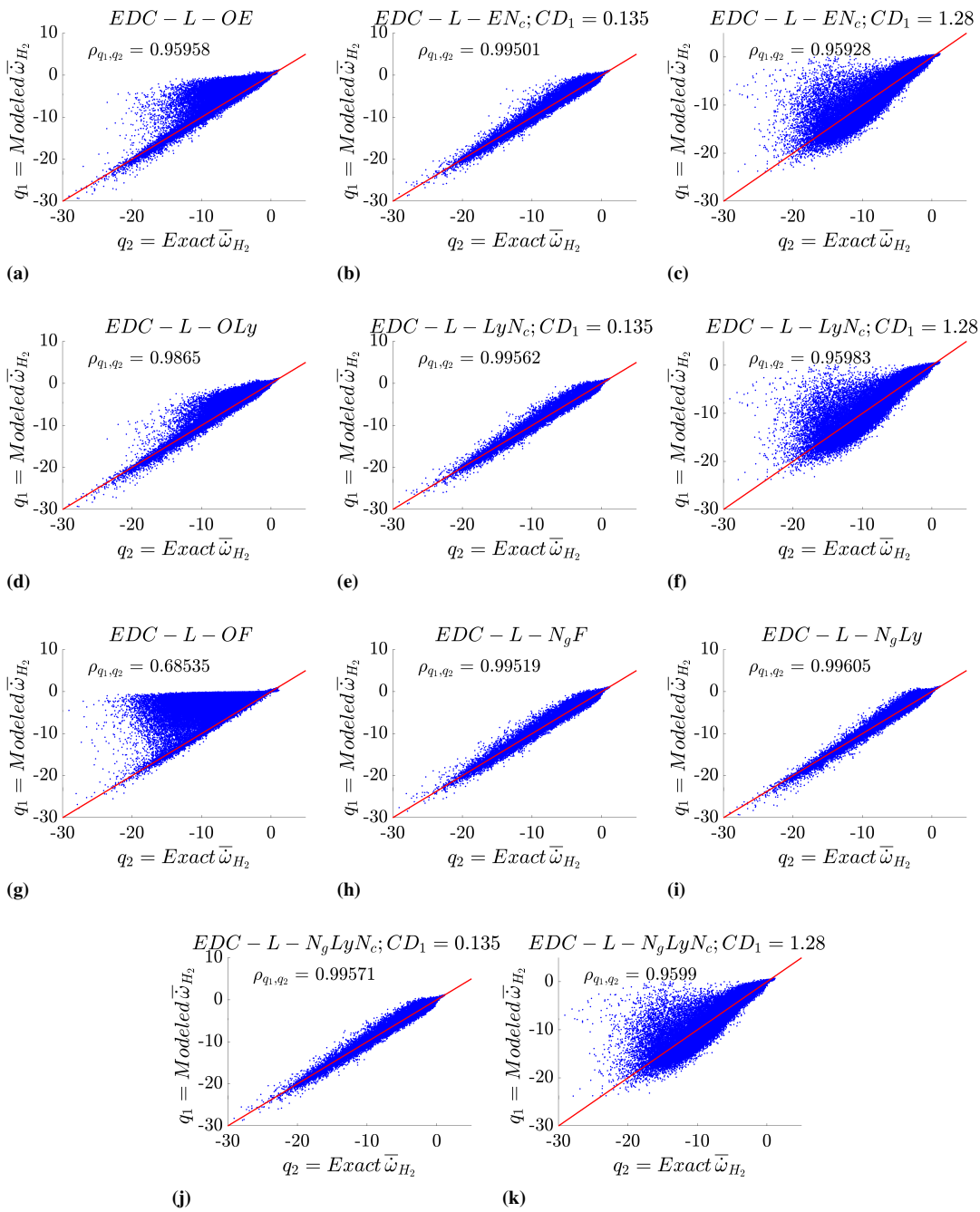


**Figure 5.37:** *Same as Fig.5.36 but for* $H_2$ *(fuel).*

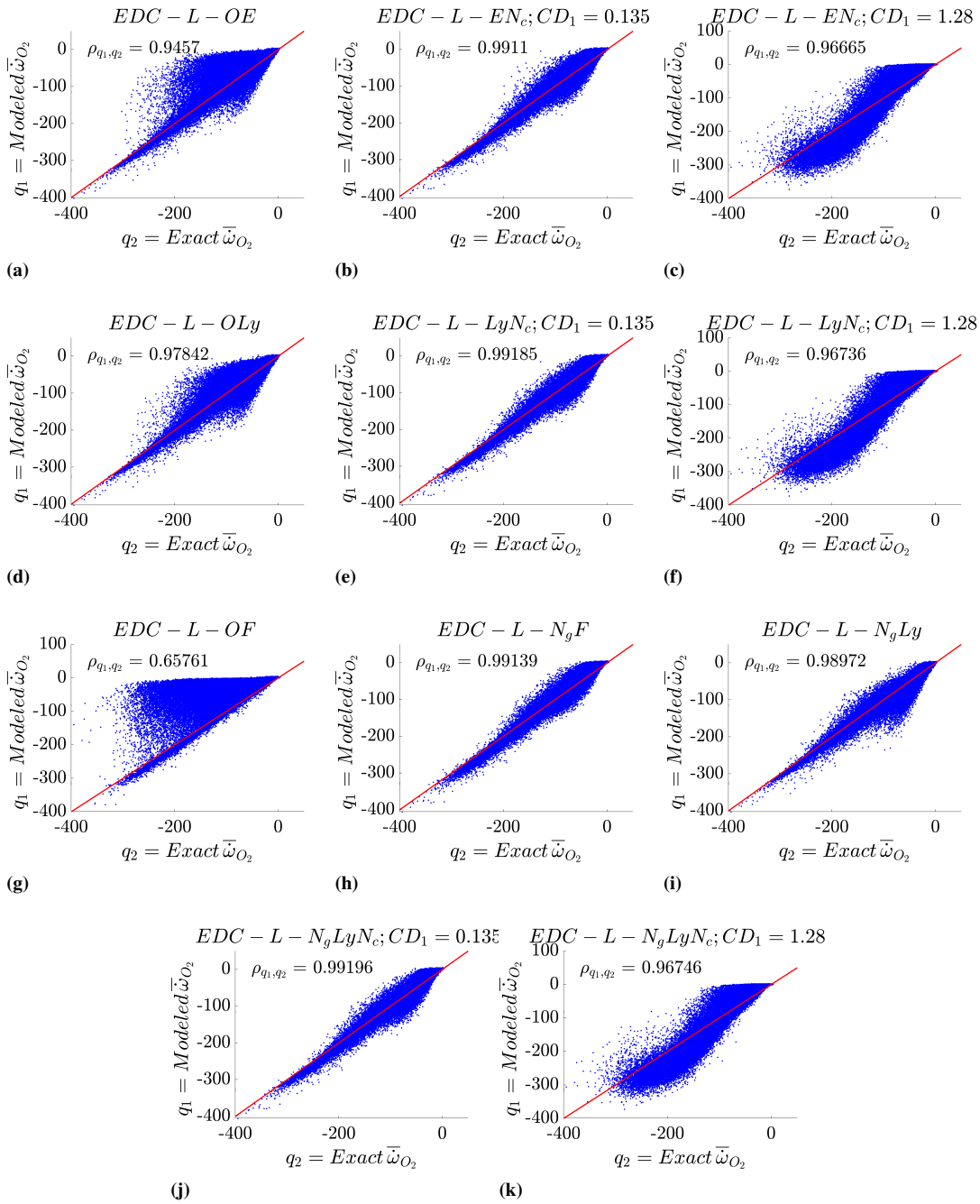


**Figure 5.38:** *Same as Fig.5.36 but for* $O_2$ *(oxidizer).*

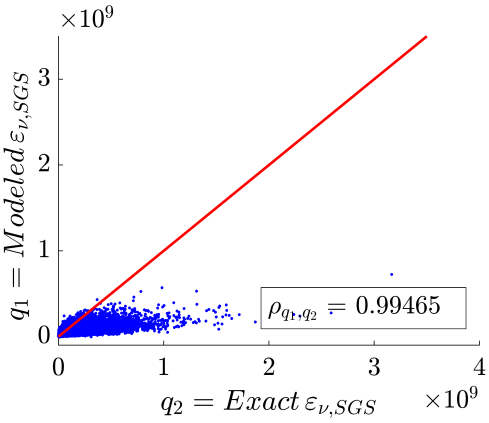


**Figure 5.39:** *The modeled sub-grid viscous dissipation using Eq. 3.26 with* $C_\varepsilon = 1.048$ *compared to the exact term extracted from case H at t=20*$t_j$ *using Eq. 2.134. Filter width is* $\overline{\Delta}/\Delta_{\mathrm{DNS}} = 8$*. The correlation coefficient (Eq. 2.26) has been calculated and shown in the inset.*

Next we look at the mean results in composition space. This can be done using conditional means. The way to compute these conditional data using joint PDFs (joint histograms) was previously discussed in Sec.2.2.2. In Fig.5.40 , the conditional means of different species net production/consumption rates using different EDC-LES models are depicted conditioned on the mixture fraction. Further, the better prediction of other models compared to "**EDC-L-OE**" is clear. Other models show seemingly similar results with "**EDC-L-OLy**" sometimes giving the best predictions. However, again the error compensation even in averages in composition space must be taken into account. The results must be assessed along with the scatter plots. As was previously shown, "**EDC-L-OLy**" results have large scatters (see e.g., Figs.5.36d and 5.37d, compared to Figs.5.36e and 5.37e).

The performance of the new models are more pronounced using larger filter widths. The conditional means in composition space for $\overline{\Delta}/\Delta_{\mathrm{DNS}} = 18$ are shown in Figs.5.41. It is clearly seen that now, the original EDC-LES models, namely "**EDC-L-OE**" and "**EDC-L-OLy**" fail to predict the correct conditional means. The scatter plots (not shown here) also show large scatters and lower correlation coefficients. In contrast, the modified versions are in better agreement with the filtered DNS data. No conclusion can be drawn at this point on which modified version is the best one. At a first glance it seems that "**EDC-L-EN**$_{\mathrm{C}}$" has the best performance in composition space. However, it should be taken into account that the differences are very low and we expect that the "$\mathrm{N_G}$" (modification in $\gamma^*$) shows its effect in high $Re_{\lambda_{SGS}}$. $Re_{\lambda_{SGS}}$ must be higher than the thresholds mentioned in Table5.3 but not that high for flatness becomes independent of Taylor scale Reynolds. With RANS fluctuations, this limit is about $Re_\lambda > 300 - 500$ [35]. For sub-grid fluctuations, this limit needs to be evaluated and is an interesting subject for the future works. In summary, it seems that the modifications proposed, especially the relation found between $CD_1$ and $CD_2$ using the model dissipation spectrum, highly improve the performances of EDC-LES models when larger filters are applied.

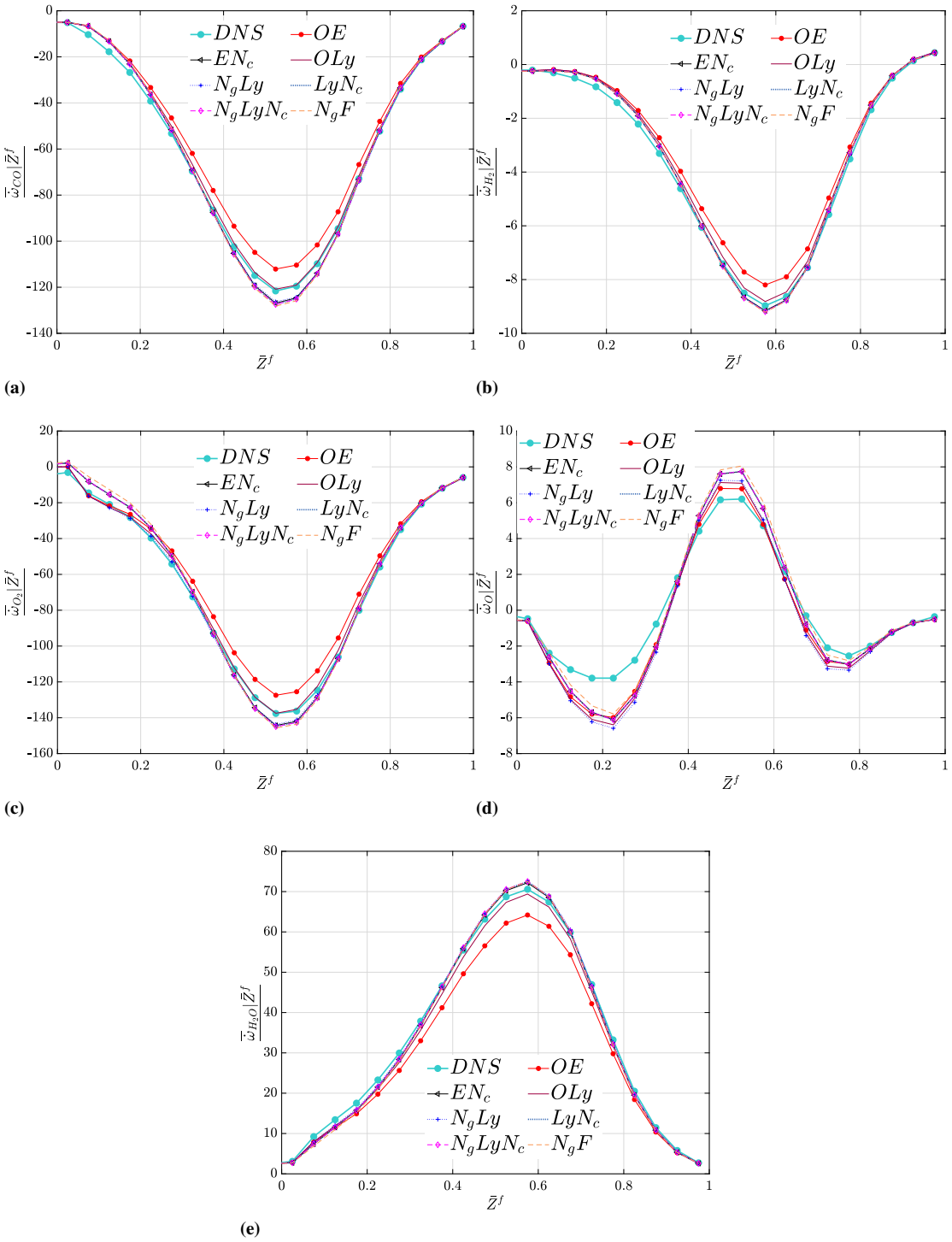


**Figure 5.40:** *Conditional mean of production/consumption rate of different species with units* $[kg/(m^3 s)]$ *conditioned on the mixture fraction, using different EDC-LES models (see Table5.2) compared with the exact filtered quantity from case H at t=20*$t_j$*. Filter width is* $\overline{\Delta}/\Delta_{\mathrm{DNS}} = 8$.

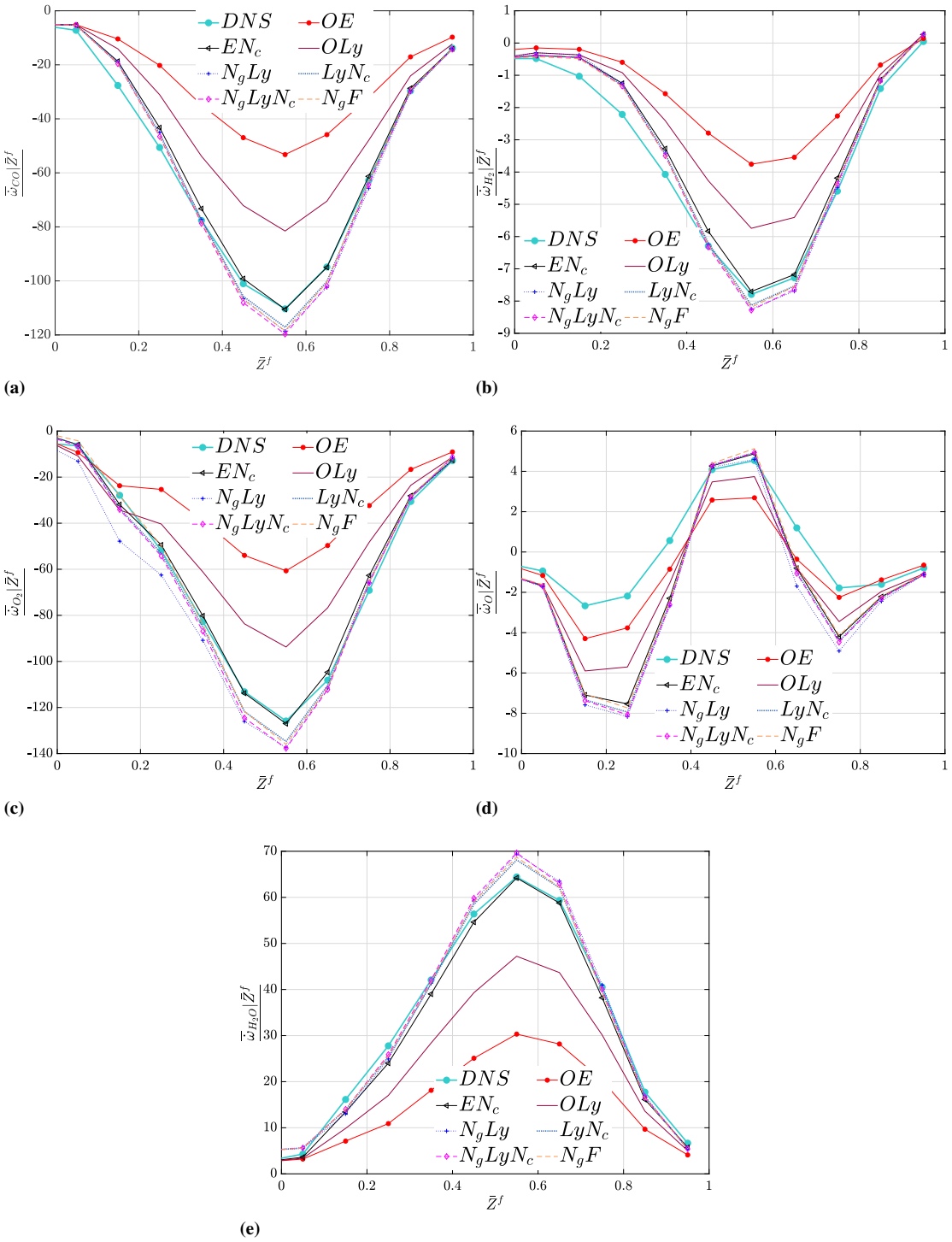


**Figure 5.41:** *Conditional mean of production/consumption rate of different species with units* $[kg/(m^3 s)]$ *conditioned on mixture fraction, using different EDC-LES models (see Table5.2) compared with the exact filtered quantity from case H t=20t$_j$. Filter width is* $\overline{\Delta}/\Delta_{\mathrm{DNS}} = 18$.

### 5.4.2 Non-Dynamic Scale Similarity Models

DesJardin and Frankel [17] used the Scale Similarity (SS) idea to model the filtered net formation rate of species $\overline{\dot{\omega}}_k(\boldsymbol{\varphi})$ in LES. They proposed two SS combustion models, namely similarity resolved reaction rate model (SSRRRM or model A), and the scale similarity filtered reaction rate model (SSFRRM or model B), which was presented in detail in Sec. 3.3. In their formulations, they were inspired from the original approach proposed by Bardina et al. [120] and used "double grid filtered" quantities. Germano et al. [128] proposed to use "test grid filtered" instead of "double grid filtered" quantities, model C, which was explained in Sec. 4.3. They reported both *a priori* and a posteriori assessments of the method using two-dimensional spatially developing non-premixed jet DNS data with one step chemistry. The results (e.g. moments of product mass fraction and reaction rates) using the proposed SS models were in a reasonable agreement with the DNS data. Potturi and Edwards [185] also tested this model in LES of DLR and UVa combustors, but they found no improvement compared to simulation without SGS combustion model for UVa combustor. SS concept has further been used to develop LES combustion models in premixed flames to postulate the filtered Flame Surface Density (FSD) in filtered progress variable balance Equation [186, 187]. It is evident that the direct application of SS idea in LES of reactive jets is limited in the literature to the early 2D DNS/LES spatial jet of Desjardin and Frankel [17] and 3D DNS/LES of isotropic decaying reactive flow of Jaberi and James [18], both tested with small filters ($\overline{\Delta}$) ($\overline{\Delta}/\Delta_{\mathrm{DNS}} = 3$ in [11] and $\overline{\Delta}/\Delta_{\mathrm{DNS}} = 4$ in [18] where $\Delta_{\mathrm{DNS}}$ is the grid size used in the DNS) and single step chemistry.

In this section we aimed at the *a priori* assessment of the performance of the non-dynamic SS models (A, B and C)[9] using 3D DNS data. The selected SS models are tested in a more challenging test case and using larger filter widths, $\overline{\Delta}/\Delta_{\mathrm{DNS}} = 8, 12, 18$, compared to the previous studies. Their capabilities in the prediction of combustion and heat release rates while the flame (case H) experiences a high level of extinction followed by re-ignition will be assessed.

#### Combustion Rates Predictions in Extinction Regime

At $t = 20t_j$ the flame is in the fully turbulent, self-similar regime [188]. In Fig. 5.42, the ability of the three SS models in predicting the filtered consumption rate of $H_2$ (fuel) is compared with the exact filtered reaction rate, $\overline{\dot{\omega}}_{H_2}(\boldsymbol{\varphi})$, obtained from the DNS database (case H). The "quasi laminar" or "no model" approach is also shown as the reference. In "no model" approach, SGS effects are neglected and $\dot{\omega}_k^{noModel}(\boldsymbol{\varphi}) = \dot{\omega}_k\left(\overline{\boldsymbol{\varphi}}^f\right)$. The analysis is done for three different filter widths. From top to bottom, the filter size increases from $\overline{\Delta}/\Delta_{\mathrm{DNS}} = 8$ to $\overline{\Delta}/\Delta_{\mathrm{DNS}} = 12$ and $\overline{\Delta}/\Delta_{\mathrm{DNS}} = 18$. The left figures compare the first moments (mean) and the right figures compare the second moments (RMS). The data are clipped to a region where $\underline{Z}_f \geq 0.02$ with $\underline{Z}_f$ expressing the Favre mean mixture fraction. In Fig. 5.42, it is shown that all the analyzed models, including the "no model" approach, can capture qualitatively the consumption rate of the fuel in terms of both mean and RMS. Looking at the mean results, in the core jet region, all models produce similar results. However, by approaching the plane of maximum Favre mean TKE (the vertical blue dashed line) deviations and differ-

[9] See Sec. 3.3

ences become higher. For $\overline{\Delta}/\Delta_{\mathrm{DNS}} = 8$ (Fig. 5.42a) the "no model" approach results in slightly higher/lower mean consumption rates. It can be observed in Figs. 5.42a, 5.42c, 5.42e that the difference compared to the exact value (blue lines) increases by increasing the filter width. For example, in Fig. 5.42e the "no model" approach results start to deviate from the exact filtered DNS values in the first plane located after the central plane ($y = 0$). However, by using a smaller filter width (see Fig. 5.42a), the "no model" approach can predict the mean in a broader spatial range. Models A and B produce almost the similar mean profiles and the error is lower than that of the other two models i.e. model C and the "no model" approach. Looking at RMS profiles, in Fig. 5.42b, 5.42d, and 5.42f, the "no model" approach reveals errors. Considering that the "no model" approach has errors both in mean and the RMS profiles, one can conclude that a model is needed to account for SGS effects. For the species analyzed here, this observation is more pronounced when using filter widths larger than $\overline{\Delta}/\Delta_{\mathrm{DNS}} = 8$.

It should be mentioned that the similar behavior is observed for other major species, where model C and the "no model" approach failed to predict the true spatial mean values while models A and B predict almost the similar mean in a good agreement with the filtered DNS data.

In Fig. 5.43, the results of the performance of SGS models in predicting filtered formation rate of $\mathrm{H}$ radical are analyzed. It should be noted that the mean formation rate of $\mathrm{H}$ is very low, since the flame is experiencing a high level of local extinction. The $\mathrm{H}$ radical is locally produced in the pockets of burning gases and also in the burning surfaces around the extinction holes [189]. Large errors are seen using the "no model" approach and model C in predicting the mean $\overline{\dot{\omega}}_H$. Considering the mean, both models A and B are in a good agreement with DNS results. In terms of RMS in Figs. 5.43b, 5.43d and 5.43f, the best performance is obtained with model B. It is interesting to observe that how SS models A and B can preserve the mean even using the larger filter width $\overline{\Delta}/\Delta_{\mathrm{DNS}} = 18$.

In Fig. 5.44, different models for different species and filter widths are assessed based on their local errors using the cumulative local error metric (defined in Eq. 4.8). First, as expected, locally the error increases with increasing the filter width for all species. Second, looking at major species, it is seen that the performance of models B and C is improved compared to the "no model" approach by increasing the filter width (see Figs. 5.44a and 5.44c). It seems that locally the two models are more effective using larger filter widths. The cumulative local error of the "no model" approach is not much higher than that of other models and for some species less than model C (see e.g. Fig. 5.44a for $\mathrm{O}_2$ and $\mathrm{H}_2\mathrm{O}$). However, one cannot conclude about the performance of models by only looking at the local errors. The results should be used together with the first and second moments statistics. For example although model B predicts higher local errors compared to the "no model" approach for $\mathrm{H}_2$ species using $\overline{\Delta}/\Delta_{\mathrm{DNS}} = 8$, the mean of filtered $\dot{\omega}_{H_2}$ i.e. $\overline{\dot{\omega}}_{H_2}$ is in a very good agreement with filtered DNS data (see Fig. 5.42a). It can be concluded that the SS model B produces data with the same mean as the exact filtered DNS, but with higher deviations. Third, looking at radicals, local errors are much higher than that for major species. The prediction for the $\mathrm{OH}$ is the worst. This is the result of the errors in both mean and RMS profiles.

It is seen that model A, independently of the filter width, results in the lowest cumulative local error for all major species except $\mathrm{O}_2$. It is reasonable to conclude that, since

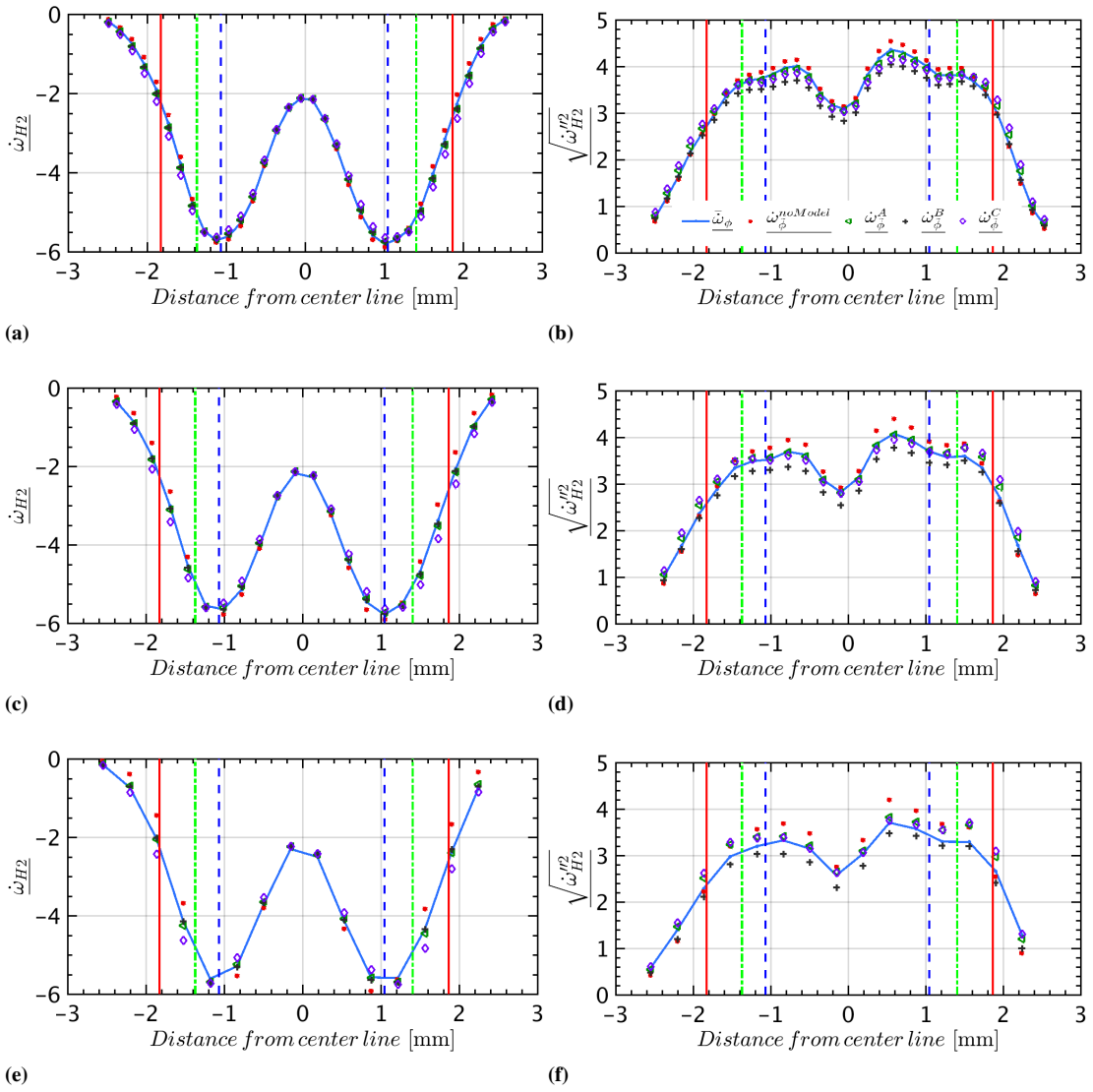


**Figure 5.42:** *Production/consumption rate of* $H_2$ *with units* $[kg/(m^3 s)]$, ***(a,c,e)*** *Mean;* ***(b,d,f)*** *RMS. Different filter widths are applied: (up)* $\overline{\Delta}/\Delta_{\mathrm{DNS}} = 8$*; (middle)* $\overline{\Delta}/\Delta_{\mathrm{DNS}} = 12$*; (down)* $\overline{\Delta}/\Delta_{\mathrm{DNS}} = 18$*. The data are extracted at t=20*$t_j$*. vertical dashed-blue lines: planes of maximum mean turbulent kinetic energy; vertical dot-dashed green lines: planes of mean stoichiometric mixture fraction; vertical red lines: planes of maximum mean temperature fluctuations.*

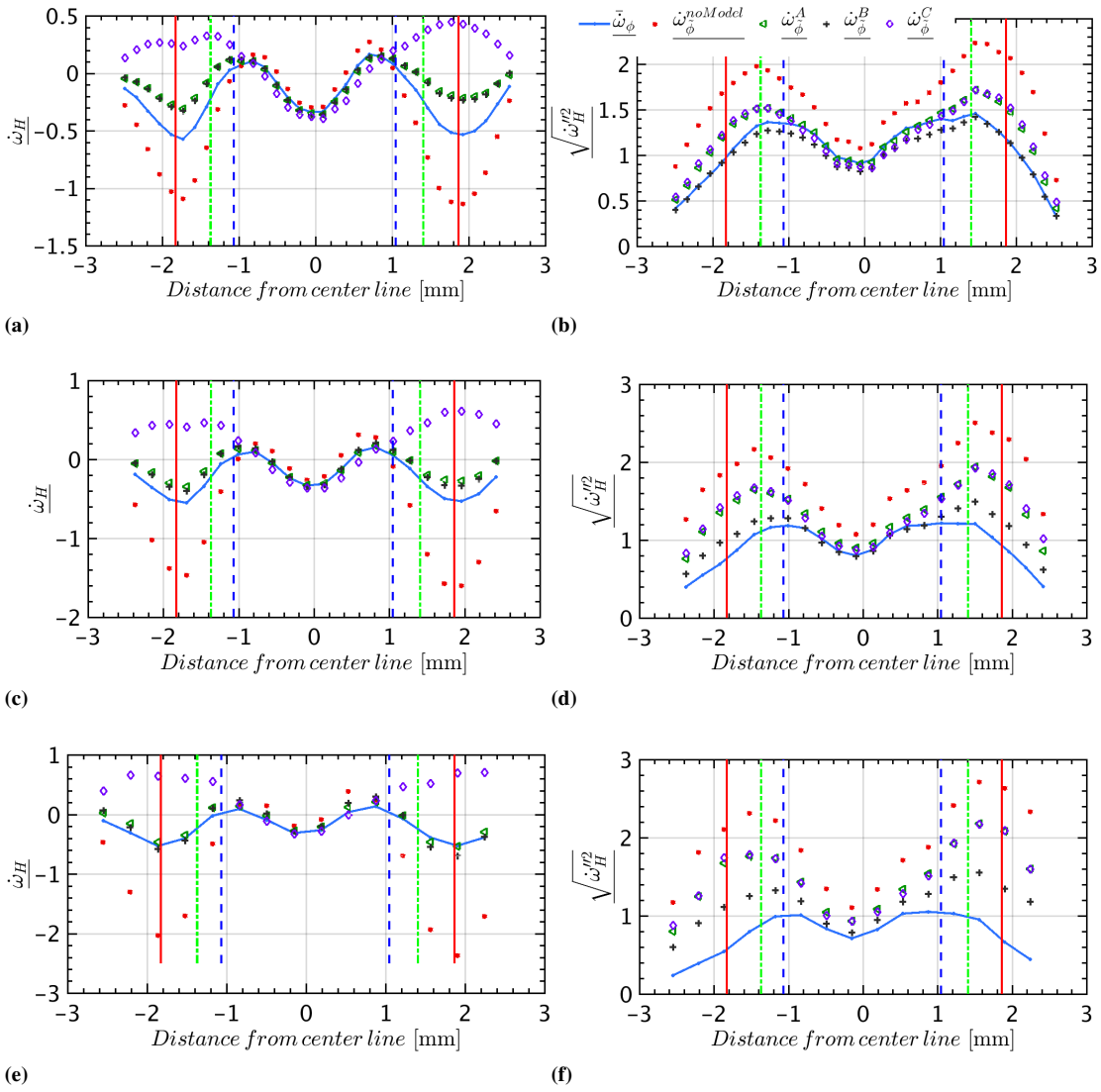


**Figure 5.43:** *Production/consumption rate of* H *with units* $[kg/(m^3 s)]$, ***(a,c,e)*** *Mean;* ***(b,d,f)*** *RMS. Different filter widths are applied: (up)* $\overline{\Delta}/\Delta_{\mathrm{DNS}} = 8$*; (middle)* $\overline{\Delta}/\Delta_{\mathrm{DNS}} = 12$*; (down)* $\overline{\Delta}/\Delta_{\mathrm{DNS}} = 18$*. The data are extracted at t=20*$t_j$*.Vertical lines are the same as in Fig. 5.42.*

model A predicts the mean with a good accuracy (see e.g. Fig. 5.42) and the lowest local errors, this model is preferable for major species.

Looking at radicals, this is model B with the least local error. Considering that model B has a high accuracy in predicting mean of the radicals net formation rates, it can be concluded that model B is a better model to capture radical net production/-consumption rates. Detailed analysis of the rate of reactions (Eq. 2.95) involved in the syngas mechanism shows that $O_2$ is mainly consumed through $H + O_2 = O + OH$ and $H + O_2(+M) = HO_2(+M)$ reactions. The contribution of all other reactions is very small. As a result, $O_2$ net consumption rate is linked to radicals formation rates. Since model B is the best model to capture radicals net formation rates, the same is true for $O_2$. Further, in Figs. 5.44d-5.44f the performances of different SS models are compared with the "no model" approach by dividing their cumulative local errors to the one of "no model" approach. The value of 1 in this figure shows that the models have the same cumulative local error as the "no model" approach. It is now clearly seen that models B and C are filter dependent, i.e. increasing the filter width decreases their local error values compared to the "no model" approach. However, the relative performance of model A remains approximately constant. It is observed that the sum of local errors approximately improved by $25\%$ using model A. For radicals, it is evident that model B has the best performance by decreasing the errors more than $50\%$ compared to using no SGS model for combustion.

#### Heat Release Rates Predictions in Extinction Regime

Concentrating now on the filtered heat release rate in the energy equation, Fig. 5.45 depicts the mean and RMS of filtered heat release rates per unit volume (Eq. 4.9) computed using different models and filter widths. It should be noted that to compute $\overline{\dot{Q}}$ (mean of the filtered heat release rate), from DNS, $\dot{Q}$ is first directly filtered and afterwards the mean is determined using Eq. 2.14. To get the heat release rates from the models, the related modeled $\overline{\dot{\omega}}_k$ respectively, from Eq. 3.66, Eq. 3.68 and Eq. 3.70), are inserted in Eq. 4.9. In Figs. 5.45a-5.45c, the failure of the "no model" approach to predict the correct mean heat release rate is observed. Higher prediction of heat release rate means that the lower number of computational cells are predicted to be in extinction mode. On the contrary, models A and B can predict the mean filtered heat release rates with a very good accuracy. As expected, the predictions of model C are not satisfactory.

#### Combustion Rates Predictions in Re-Ignition Regime

The same analysis presented in the previous sections is repeated here for the time at which the flame experiences re-ignition from the core region of the jet. The flame interacts with fully developed decaying turbulence at this time instant [188].

In Fig. 5.46 the modeled filtered rates of consumption of $H_2$ (fuel) are compared with the exact value obtained by filtering the DNS data. From Figs. 5.46a and 5.46d, it is evident that for a small filter width ($\overline{\Delta}/\Delta_{\mathrm{DNS}} = 8$) all models predict almost the same mean and RMS. By using $\overline{\Delta}/\Delta_{\mathrm{DNS}} = 8$ and looking at mean filtered fuel net formation rate (Fig. 5.46a) one can only conclude that the SGS combustion models which are tested can adapt themselves to the condition that there is no need to do SGS

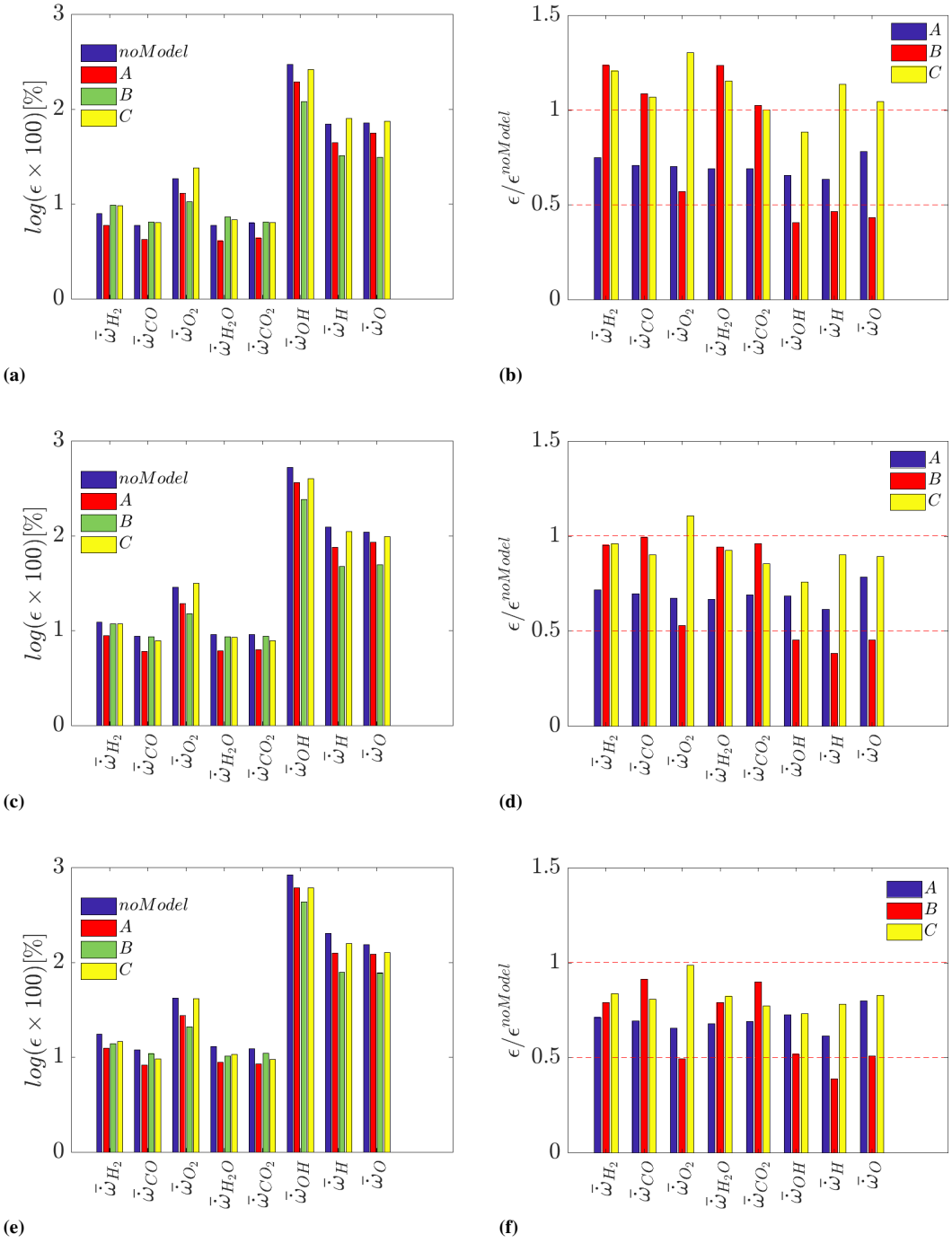


**Figure 5.44:** *Cumulative local errors incurred using different models in prediction of different species net formation rates:* ***(a,c,e)*** *logarithm of errors for all models;* ***(b,d,f)*** *The errors are divided by the "no model" approach error. Different filter widths are applied: (up)* $\overline{\Delta}/\Delta_{\mathrm{DNS}} = 8$*; (middle)* $\overline{\Delta}/\Delta_{\mathrm{DNS}} = 12$*; (down)* $\overline{\Delta}/\Delta_{\mathrm{DNS}} = 18$*. The data are extracted at t=20$t_j$. Vertical lines are the same as in Fig. 5.42.*

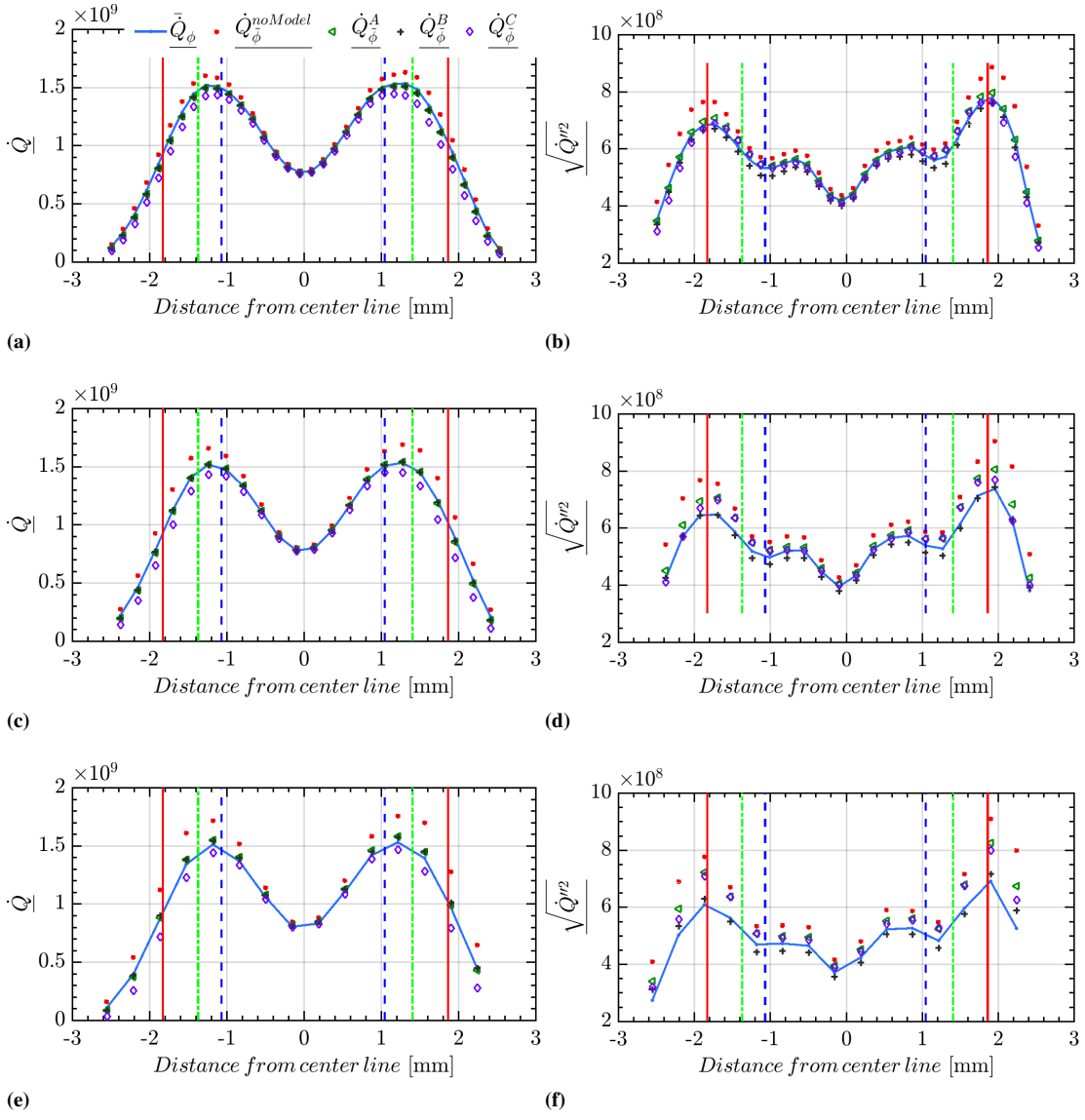


**Figure 5.45:** *Heat release rates, (**a,c,e**) Mean; (**b,d,f**) RMS. Different filter widths are applied: (up)* $\overline{\Delta}/\Delta_{\mathrm{DNS}} = 8$*; (middle)* $\overline{\Delta}/\Delta_{\mathrm{DNS}} = 12$*; (down)* $\overline{\Delta}/\Delta_{\mathrm{DNS}} = 18$*. The data are extracted at t=20$t_j$. Vertical lines are the same as in Fig. 5.42.*

modeling. In other words, they can switch themselves off automatically. In the current study two larger filter widths are also applied. By increasing the filter width, the "no model" approach error increases in both mean and RMS (see Figs. 5.46c and 5.46f). This is also true for other three models however the increase of the error is less for SS models. It should be mentioned that for other major species, like $CO$, $O_2$, $CO_2$ and $H_2O$, the similar performance as described in Fig. 5.46 for $H_2$ is observed. So, for the sake of brevity, only the results for $\dot{\omega}_{H_2}$ are presented.

Filtered H radical production/consumption rate is analyzed in Fig. 5.47. Compared to Fig. 5.43, it is evident that the flame is in re-ignition phase, where the rate of production of $H$ radical increased in the core of the jet. The maximum error of the "no model" approach is around the mean stoichiometric plane and the region between this plane and the maximum of mean temperature fluctuations. In the core of the jet, the "no model" approach can predict the true mean regardless of the applied filter width. It seems that in the core jet region, due to perfect mixing and the lack of gradients, the flame is in "perfectly stirred reactor" regime [56].

Contrary to the "no model" approach, the SS models A and B predict the mean formation rate $\dot{\omega}_H$ with good accuracy regardless of the applied filter width. Similar to Fig. 5.43, model C fails to predict the mean with good accuracy.

In terms of the second moment, all models predict the qualitative behavior. The deviation from the exact RMS increases by increasing the filter width. Similar to previous observations with respect to radicals in the current study, model B better predicts the RMS of $H$ radical compared to other models.

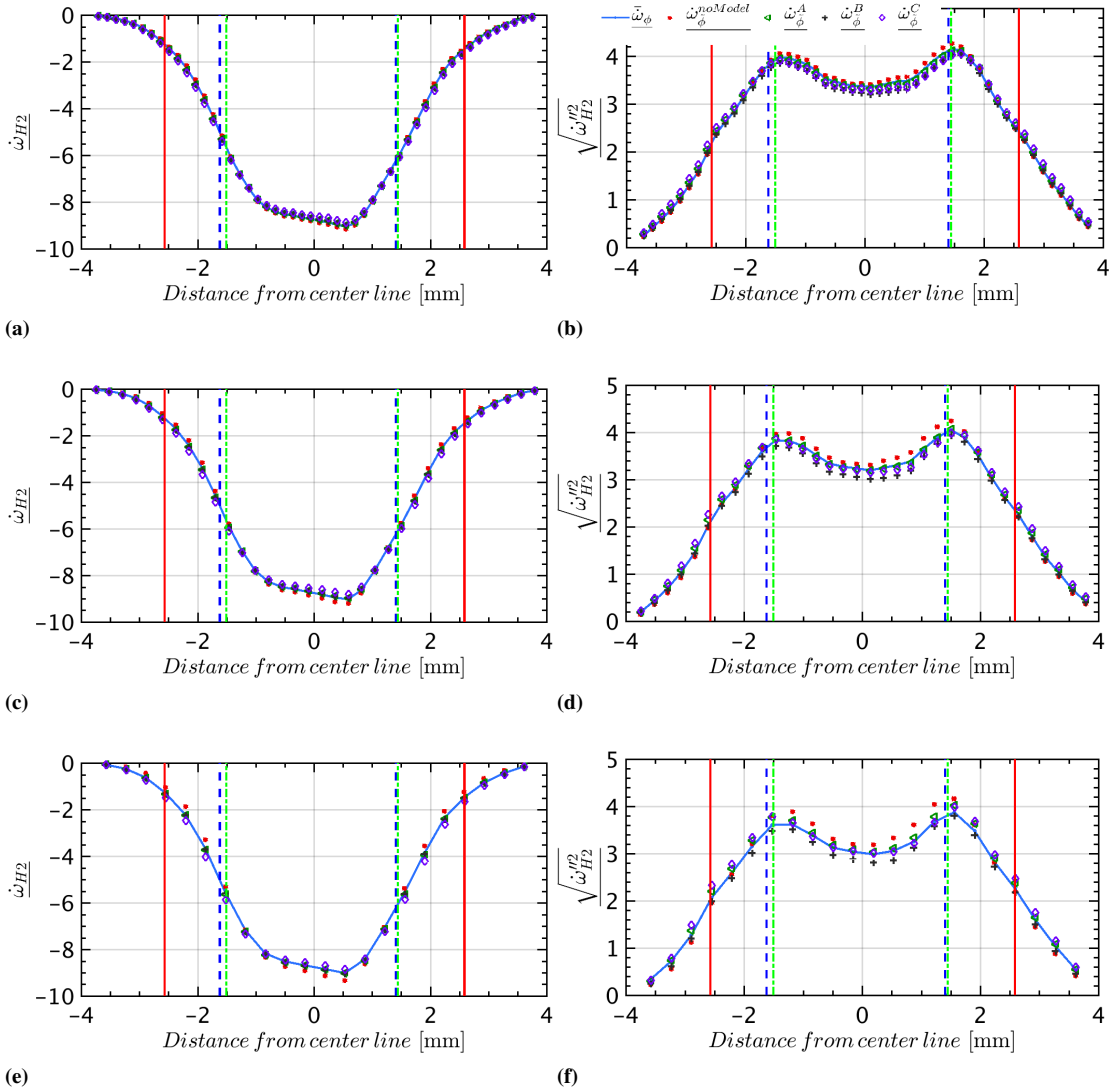


**Figure 5.46:** *Production/consumption rate of* $H_2$ *with units* $[kg/(m^3 s)]$, ***(a,c,e)*** *Mean;* ***(b,d,f)*** *RMS. Different filter widths are applied: (up)* $\overline{\Delta}/\Delta_{\mathrm{DNS}} = 8$*; (middle)* $\overline{\Delta}/\Delta_{\mathrm{DNS}} = 12$*; (down)* $\overline{\Delta}/\Delta_{\mathrm{DNS}} = 18$*. The data are extracted at re-ignition time, t=35*$t_j$*. vertical dashed-blue lines: planes of maximum mean turbulent kinetic energy; vertical dot-dashed green lines: planes of mean stoichiometric mixture fraction; vertical red lines: planes of maximum mean temperature fluctuations.*

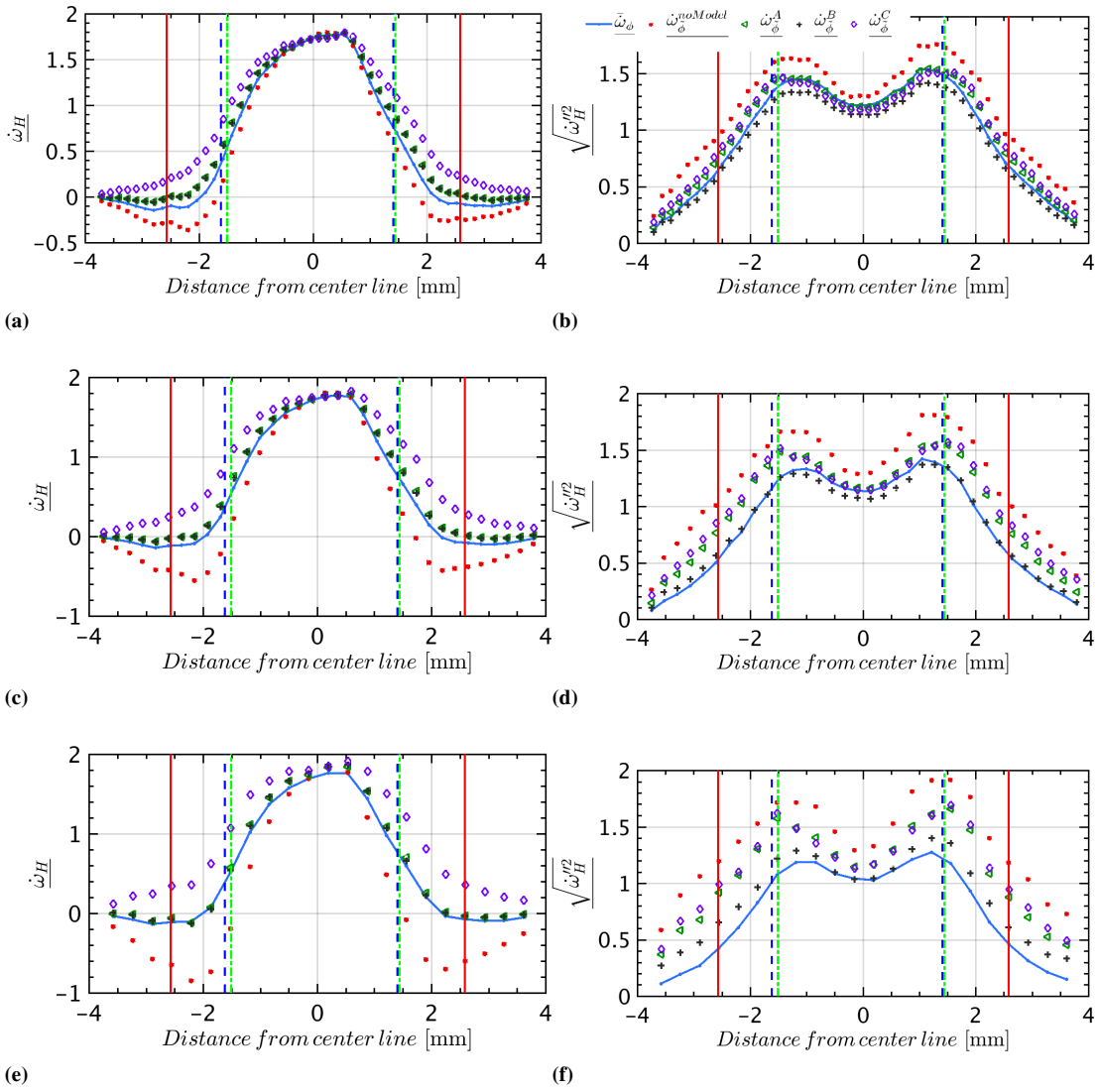


**Figure 5.47:** *Production/consumption rate of* H *with units* $[kg/(m^3 s)]$, ***(a,c,e)*** *Mean;* ***(b,d,f)*** *RMS. Different filter widths are applied: (up)* $\overline{\Delta}/\Delta_{\mathrm{DNS}} = 8$*; (middle)* $\overline{\Delta}/\Delta_{\mathrm{DNS}} = 12$*; (down)* $\overline{\Delta}/\Delta_{\mathrm{DNS}} = 18$*. The data are extracted at at re-ignition time, t=35*$t_j$*.Vertical lines are the same as in Fig. 5.46.*

**Heat Release Rates Predictions in Re-Ignition Regime**

In Fig. 5.48 the filtered heat release rates are depicted. It is observed that using $\overline{\Delta}/\Delta_{\mathrm{DNS}} = 8$, the "no model" approach can predict the mean filtered heat release rate with a good accuracy compared to the filtered DNS data. However, it should be again mentioned that "mean" results suffer from error cancellation. The RMS shown in Fig. 5.48d is a bit higher in the outer flame region which can be corrected by using SS models A and B. It should be noted that the flame re-ignites from the center of the jet (regions between two vertical green lines). This is evident in the high heat release rates in this region. Increasing the filter width increases the error of the "no model" approach (compare Figure Figs. 5.48b and 5.48c with 5.48a). However, SS models A and B correctly predict the mean filtered heat release rates. In RMS results, discrepancies exist compared to the exact filtered DNS data, however, as can be seen in Figs. 5.48d-5.48f, SS models effectively try to decrease the error.

As it can be inferred from the results of the two previous subsections, both SS models A and B can predict well the mean filtered production/consumption rate of major species and radicals compared to the "no model" approach, both in extinction and re-ignition times. The RMS is captured with a reasonable accuracy by both models. It is found that SS models are able to detect the locations where SGS effects prevail in the flame. As an example, Fig. 5.49 shows the exact SGS or residual scalar field for the production/consumption rate of $\mathrm{H_2O}$ at time $t = 20t_j$ in the $Oxy$ plane at $z = 0$. The SGS field is obtained by subtracting $\dot{\omega}_{H_2O}\left(\overline{\boldsymbol{\varphi}}^f\right)$ from $\overline{\dot{\omega}}^A_{H_2O}\left(\boldsymbol{\varphi}\right)$ where $\overline{\Delta}/\Delta_{\mathrm{DNS}} = 12$ is used as the filter width. The performance of SS model A is assessed by comparing the exact SGS field with $\mathcal{L}_{\dot{\omega}^A}$. Note that $\mathcal{L}_{\dot{\omega}^A}$ is the residual field predicted by model A and is defined in Eq. 3.67. From Fig. 5.49, it is evident that the SGS structures are captured. The locations of the predicted peak residual field (Fig. 5.49b) are in agreement with the exact residual field (Fig. 5.49a).

**Summary and Conclusions**

In this section, the finite-rate SGS non-dynamic Scale Similarity (SS) combustion models have been used to calculate the filtered combustion and heat release rates of a non-premixed jet flame exhibiting a high level of local extinction and re-ignition. Thereby, the performance of three SS type combustion models for LES have been evaluated by means of an *a priori* assessment using numerical experiment from the DNS database of a temporally evolving syngas jet flame (case H) [6]. Two SS models, namely the scale similarity resolved reaction rate model (SSRRRM) [17], called model A, and the scale similarity filtered reaction rate model (SSFRRM) [17], called model B, were considered, together with a third model, called model C, which was derived following the Germano's/Liu's approach [122, 128]. To summarize, the following conclusions could be drawn:

- When looking at the mean profiles, it was found that, regardless of the filter width ($\overline{\Delta}$) applied and the flame regime, models A and B predicts nearly similar results with a good accuracy for both major and minor species. On the contrary, the predictions of model C for major species have larger errors, especially when using larger $\overline{\Delta}$. Moreover, for radicals, model C fails to predict the correct mean (see Figs. 5.43 and 5.47). However, by increasing $\overline{\Delta}$ the error becomes less than the so

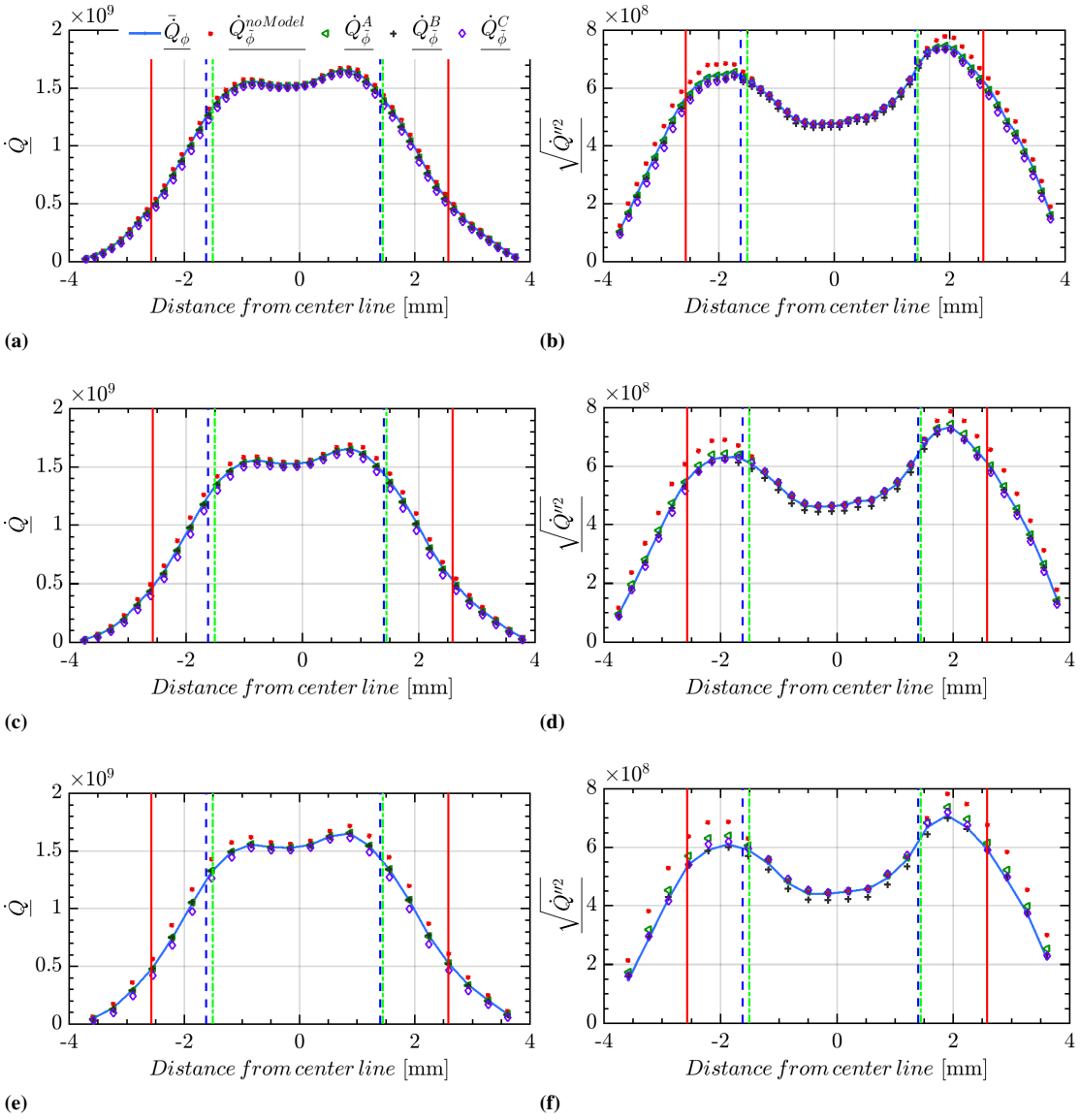


**Figure 5.48:** *Heat release rates, (**a,c,e**) Mean; ( **b,d,f**) RMS. Different filter widths are applied: (up)* $\overline{\Delta}/\Delta_{\mathrm{DNS}} = 8$*; (middle)* $\overline{\Delta}/\Delta_{\mathrm{DNS}} = 12$*; (down)* $\overline{\Delta}/\Delta_{\mathrm{DNS}} = 18$*. The data are extracted at t=35*$t_j$*. Vertical lines are the same as in Fig. 5.46.*

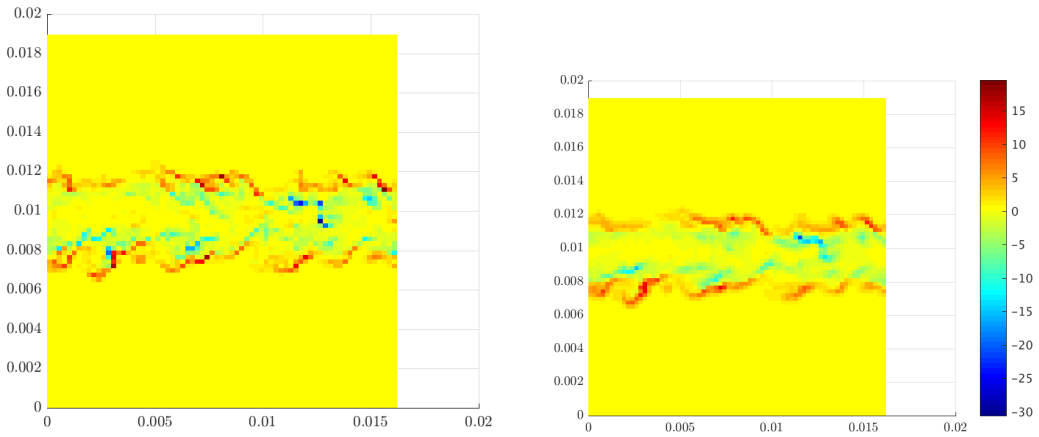


**(a)** **(b)**

**Figure 5.49:** *Residual $\dot{\omega}_{H_2O}$ with units $[kg/(m^3 s)]$ when DNS is filtered by using at : (**a**) Exact; (**b**) Predicted by model A. Cutted plane is the central $Oxy$ plane.*

called "quasi laminar" or "no model" approach,

- In terms of the Root Mean Square (RMS) and local errors, model A performs better than model B, with smaller local errors for major species like $CO$, $H_2$, $CO_2$ and $H_2O$. However, for radicals, the performances of model B are locally better,
- It was found that SS models are able to detect the locations where SGS effects prevail in the flame. This is the advantage of SS models which can accurately detect the locations where SGS effects are high and a model for the residual field is needed. The differences in predicting the mean and RMS of the filtered combustion and heat release rates among the adopted models result from the way that they compute the residual field at the same detected locations. In the current study, it was found that the SS type models which are derived according to the "double filtering" approach of Bardina et al. [120] (i.e. models A and B) have the capability to predict the mean profiles with a good accuracy at the instant of extinction and re-ignition of the flame. A good agreement is observed even when large filter widths (compared to the previous works) are applied.

### 5.4.3 New Dynamic Scale Similarity Models

From the previous section, following inferences can be drawn:

- Finite-rate SS SGS non-dynamic combustion models found to yield good predictions for the direct closure of filtered species production/consumption and heat release rates [17, 123]. One way to improve the results is a dynamic evaluation of SS coefficients. However, the first version of Jaberi and James [18] (the dynamic SSRRRM or DA2 discussed in Sec. 3.3) was tested in an ideal test case of homogeneous isotropic turbulence with one step reaction. There is no comprehensive study of the performance of this type of dynamic model in practical combustion regimes like jets with multi species/multi reactions,
- Of particular interest is the assessment of dynamic B model since the non-dynamic B was found to predict well minor species [123].
- Since dynamic SS models include explicit filtering (sometimes up to 4 stages), which is computationally not easy to implement and also time consuming in LES, it is important to understand whether dynamic procedures are effective or not.

The present section aims therefore at assessing the prediction capability of existing dynamic SS model (DA2) and the newly developed dynamic versions of finite-rate SS SGS models B and C (explained in details in Sec. 3.4), by using 3 DNS databases of a complex 3D temporal non-premixed jets in which the flames experience a high level of local extinction (introduced in Sec. 4.5). A skeletal mechanism with 11 species and 21 reactions [6] is used in the current study, which made possible the direct assessment on major species as well as radicals.

For comparison purposes, three classical non-dynamic finite-rate SS SGS combustion models are selected: the two proposed in [17] (i.e. SSRRRM and SSFRRM) and the one developed according to on Germano's test filtering approach [123, 128]. In particular, the effect of Reynolds number on the models performances are studied. This is done by using three similar DNS databases of the same configurations with the only difference of initial jet Reynolds number.

#### Performance of Different Variants of Dynamic Models

As stated before, there are two procedures to compute dynamically the similarity coefficients of models A, B and C. The two procedures explained in Section 3.2 result in the two versions of dynamic models for each SS model, namely models DA1 and DA2 for model A, models DB1 and DB2 for model B, and models DC1 and DC2 for model C. In Fig. 5.50 the mean and RMS of specie $H_2O$ is depicted. Also in Fig. 5.51 their relative errors compared to the exact filtered DNS for two versions of model A at t=20$t_j$ for the highest Reynolds number (case H) using $\overline{\Delta} = 12\Delta_{DNS}$. The $x$ axis is the distance of statistically homogeneous planes, used to compute mean and RMS, from the center of the jet ($y$=0). As it can be clearly seen in Fig. 5.51a and 5.51b, the error remains almost similar for both models in the shear layers. However, the error of model DA1 is much higher than model DA2 in the core of the jet (the region between two vertical blue lines) and outside of the jet (the regions with distance more than 2 mm from the center of the jet). The same behaviour is observed for all the species in the mechanism and for the purpose of brevity only the results for $H_2O$ is shown. Moreover

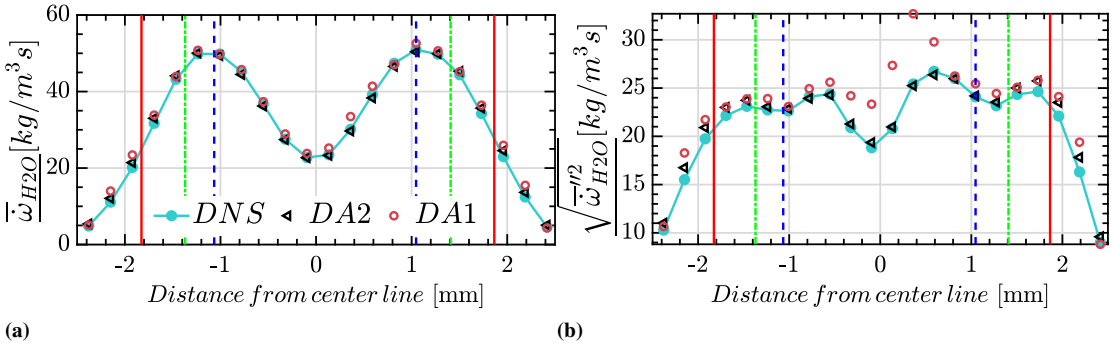


(a) (b)

**Figure 5.50:** *Case H, at t=20$t_j$ using $\overline{\Delta}/\Delta_{\mathrm{DNS}}$=12: comparison of dynamic models DA1 and DA2 performance with exact filtered $\dot{\omega}_{\mathrm{H_2O}}$ extracted from DNS database. (**a**) mean, (**b**) RMS. The vertical blue lines are the location of the planes of maximum mean turbulent kinetic energy ($TKE$). Vertical green lines represent the plane of mean stoichiometric mixture fraction, while the vertical red lines show the planes in which the maximum mean fluctuations of density occurs*

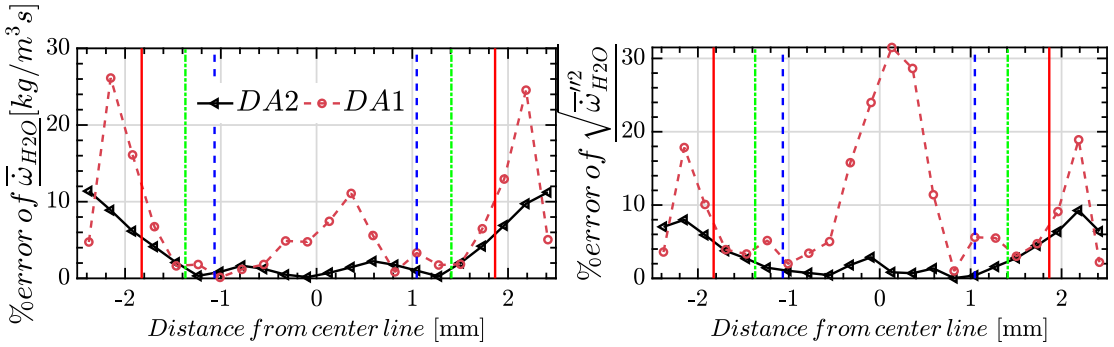


(a) (b)

**Figure 5.51:** *Case H, at t=20$t_j$ using $\overline{\Delta}/\Delta_{\mathrm{DNS}}$=12: comparison of dynamic models DA1 and DA2 performance with exact filtered $\dot{\omega}_{\mathrm{H_2O}}$ extracted from DNS database. (**a**) relative error of mean profiles and **b**) relative error of RMS profiles.*

in mean, DB1 and DB2 show similar results. However, for model C it is found that DC1 produces better results (see Appendix B).

It is also useful to look at the mean local errors in predictions using the two versions of dynamic models. The RMSE is plotted in Fig. 5.52. As it can be seen, the RMSE of DA1 in Fig. 5.52a and DB1 in Fig. 5.52b is higher than DA2 and DB2 respectively. However, DC1 has lower locally incurred error than DC2. The behaviour of two dynamic versions of models A, B and C is the same for all the species and cases studied in the present work. So in the following only the results of the dynamic models, DB2, DA2 and DC1 will be presented.

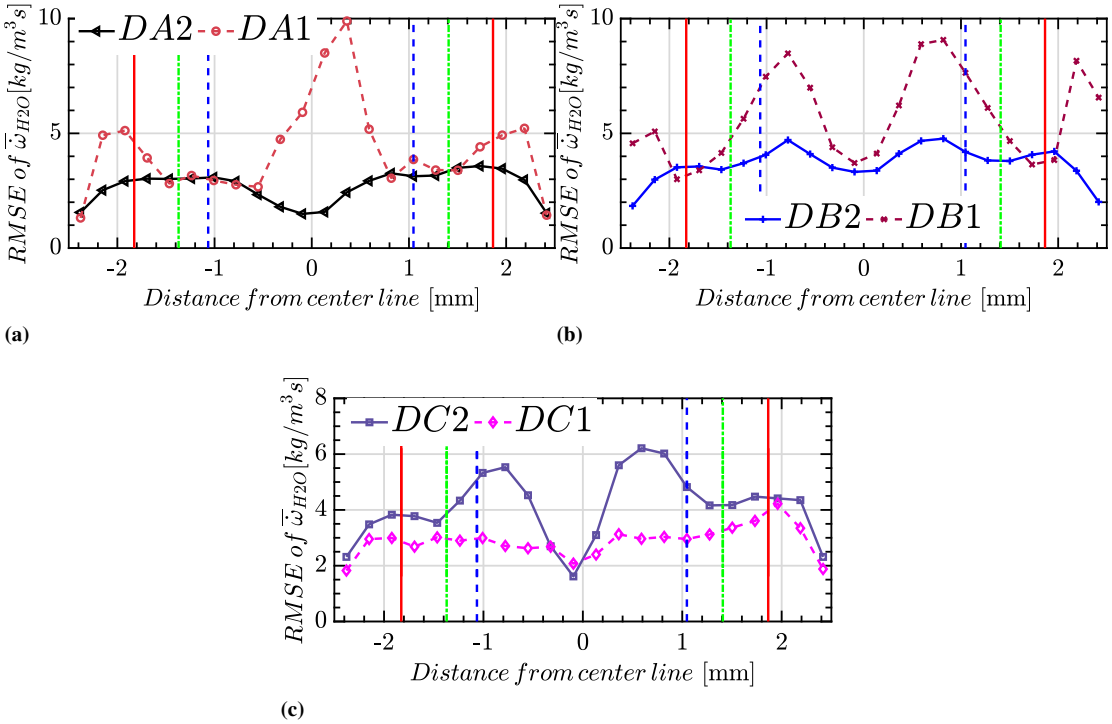


**Figure 5.52:** *Case H, at t=20$t_j$ using $\overline{\Delta}/\Delta_{\mathrm{DNS}}$=12: comparison of dynamic models performance using RMSE metric in predicting locally exact filtered $\dot{\omega}_{\mathrm{H_2O}}$ extracted from DNS database. (**a**) DA1 and DA2, (**b**) DB1 and DB2 and (**c**) DC1 and DC2 dynamic scale similarity models*

**Comparison of Different SS-SGS Combustion Models for Flows with Different Re**

In this section, the data of three flames at t=20$t_j$ with different Reynolds numbers are used to assess the performance of dynamic and non-dynamic scale similarity models introduced in Table 3.5 to model filtered production/consumption rate of species. The analysis is the *a priori* testing of models using $\overline{\Delta}/\Delta_{\mathrm{DNS}}$=12. The filter width is kept constant to see the effect of Reynolds number on the model predictions. The time instant for cases H and M corresponds to the maximum local extinction instant and for case L is close to it. The flames at this time instant are in the fully turbulent, self-similar regime [188].

In Figs. 5.53, scatter plots are depicted in which the modeled source terms for $\mathrm{H_2}$ are plotted versus the exact filtered source terms from the three DNS databases. From left to right, by increasing the Re, improvements are observed by the decreased scatter. The improvement is more pronounced in major species than radicals (see also the scatter plots for different species in Appendix B. The improvement is also evident in the correlation coefficients in the inset of the figures. Comparing the model C and its dynamic version, DC1, improvements in the correlation coefficient can be observed.

In Fig. 5.54, the conditional means of $\mathrm{H_2}$ and $\mathrm{H}$ conditioned on the mixture fraction are plotted. The results for other species can be found in Appendix B. The failure of the "no model" approach is obvious for $\mathrm{H}$ radical.

In Fig. 5.55, the conditional mean of $\mathrm{O_2}$ (conditioned on the mass fraction of $\mathrm{O_2}$ ) and $\mathrm{O}$ (conditioned on the temperature) are plotted. The results for other species can be found in Appendix B. It should be mentioned that since the flames are in extinction mode, the lack of data was observed in high temperatures. So the last bins of the joint histograms were omitted in the final plots of conditional means. The improvements compared to the "no model" approach can be observed. Moreover, all models can capture the trends in the composition space, especially in higher Reynolds cases M and H.

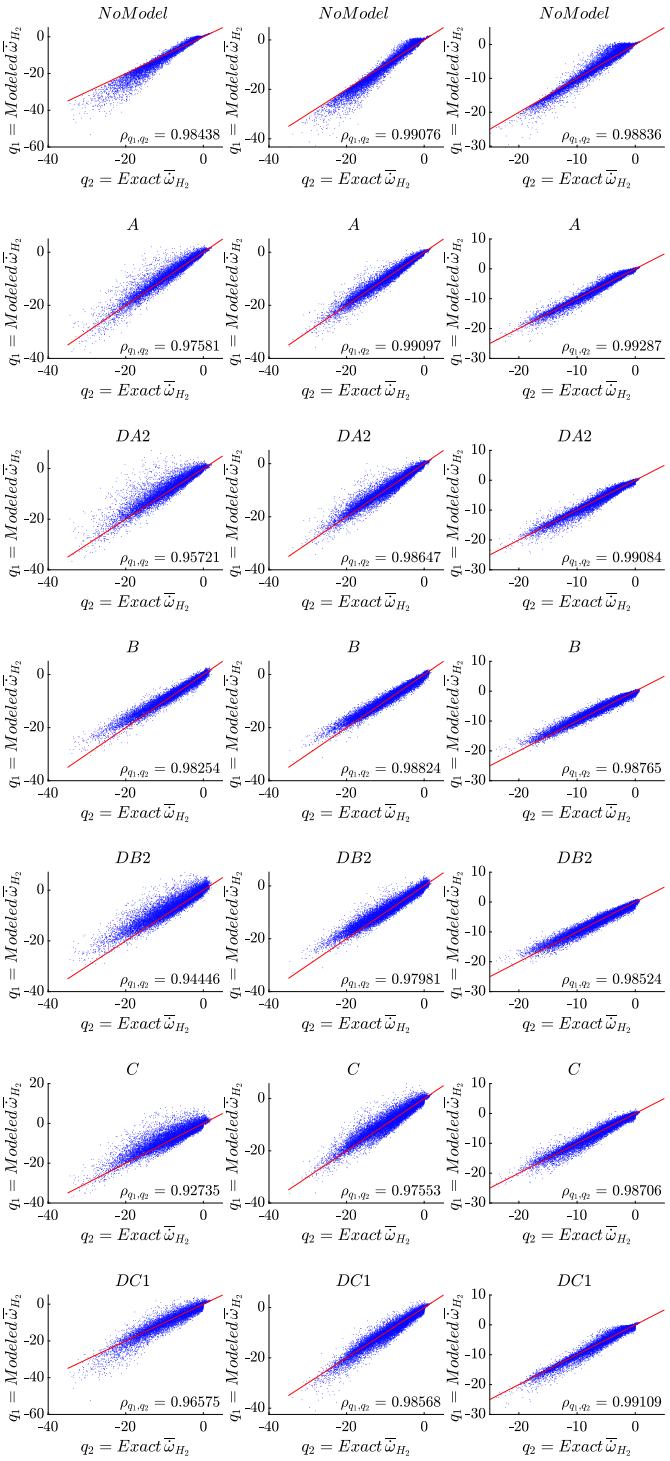


**Figure 5.53:** *Scatter plots of modeled versus exact filtered source terms of* $H_2$. *Extracted from DNS databases L (left), M (middle) and H (right) at t=20$t_j$ using* $\overline{\Delta}/\Delta_{\mathrm{DNS}}$=*12*

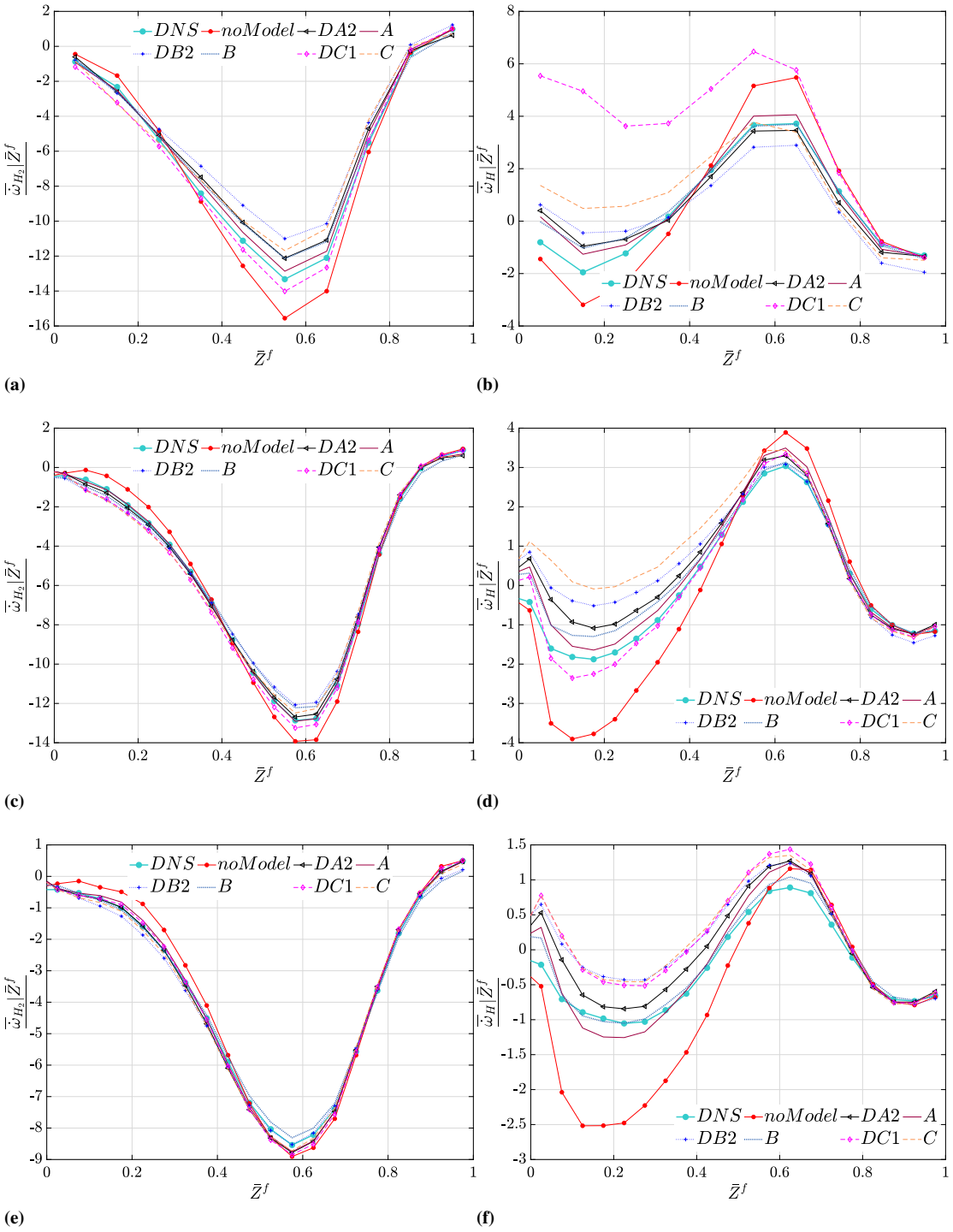


**Figure 5.54:** *Comparison of dynamic and non-dynamic models performances in predicting conditional mean filtered source terms of* $H_2$ *(left), and* H *(right), conditioned on the mixture fraction at t=20t$_j$ using* $\overline{\Delta}/\Delta_{\mathrm{DNS}}$*=12. (Top:) case L, (Middle:) case M and (Bottom:) case H*

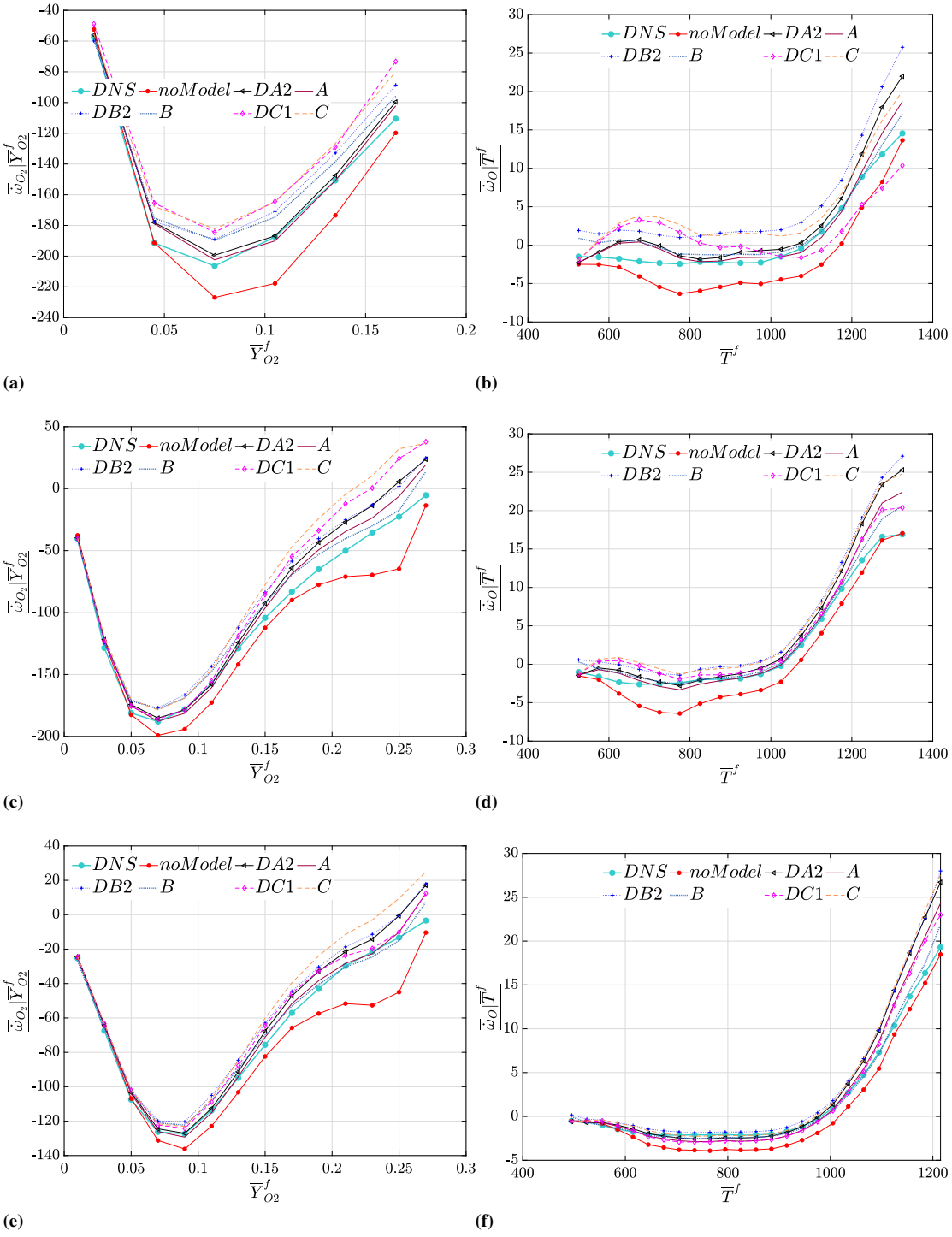


**Figure 5.55:** *Comparison of dynamic and non-dynamic models performances in predicting conditional mean filtered source terms of* $O_2$ *conditioned on the mass fraction of* $O_2$ *(left), and conditional mean filtered source terms of* O *conditioned on the temperature (right), at t=20*$t_j$ *using* $\overline{\Delta}/\Delta_{\mathrm{DNS}}$*=12 for case L (top), case M (middle), and case H (bottom)*

In Fig. 5.56, the conditional mean heat release rates (conditioned on mixture fraction) are plotted and compared with the exact filtered values from DNS databases. Since the heat release rate contains the contributions of all species production rates, this is a good measure for the overall effect of SGS combustion models. It is clearly seen that the “no model" approach overpredicts the heat release rates. On the other hand SS models A and B improved the results in the whole composition space. It is observed that model C and its dynamic version have very high error in low Reynolds number case (Fig. 5.56a); by increasing the Reynolds number the error of both become lower. Further, it is seen that for the medium and high Reynolds number cases (Fig. 5.56a and 5.56b) model C results are improved by using the dynamic coefficient. This is not the case for other two models. Model DB2 has a higher error than model B and model DA2 produces almost similar results compared to its non-dynamic version A.

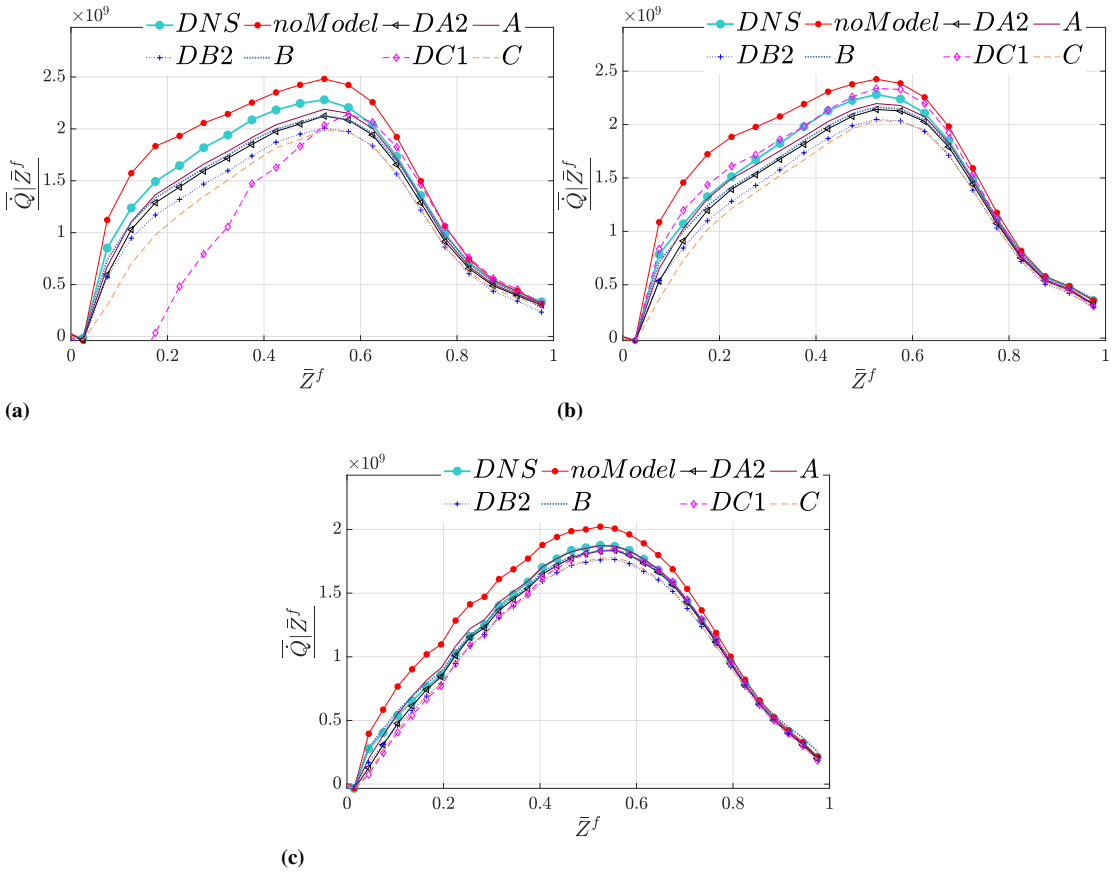


**Figure 5.56:** *Comparison of dynamic and non-dynamic models performance in predicting conditional mean heat release rate (conditioned on mixture fraction) at t=20$t_j$ using $\overline{\Delta}/\Delta_{\mathrm{DNS}}$=12. (**a**) case L, (**b**) case M and (**c**) case H*

**Summary and Conclusions**

In this section the finite-rate dynamic Scale Similarity (SS) SGS combustion models for LES were developed and *a priori* tested using the DNS of non-premixed turbulent syngas jet flames with a high level of local extinction and different Reynolds numbers. Explicit top-hat filter with relatively large filter width ($\overline{\Delta}/\Delta_{\mathrm{DNS}}$=12), compared to previous studies, was applied to compute exact LES-like filtered quantities from the DNS databases to be used in the *a priori* analysis. Two variants of dynamic versions for each existing non-dynamic model were derived. In particular, three classical non-dynamic models were: (i) the SS models derived following Bardina's grid filtering approach [120], namely the scale similarity resolved reaction rate model (model A), (ii) the scale similarity filtered reaction rate model (model B) proposed in [17], and (iii) a SS model derived using the test filtering approach of Germano [123, 128] (model C). Two versions of dynamic models (DA1,DA2; DB1,DB2 and DC1,DC2) resulted from application of different filtering levels in the mathematical formulations. Comparing the two dynamic versions of each SS model, it was found that models DA2, DB2 and DC1 produce better results. This demonstrates that the mathematically consistent formulation [125] of SS models for combustion does not always improve the results like what was seen before for the SGS stress field [125]. It should be mentioned that only DC1 was derived using the mathematically consistent formulation of Vreman [125].

Comparisons were made with non-dynamic models as well as an existing dynamic one (model DA2) [18]. The focus was on the assessment of the ability of different SS models in the prediction of filtered net formation rates of major species, radicals and also the filtered heat release rates in flames with extinction.

Considering the conditional mean heat release rates (see Fig. 5.56), the SS models could predict correctly (in mean) the filtered heat release rates, while in all three flames, the "no model" approach predicted higher heat release rates. It was observed that by increasing the Re (increasing $\overline{\Delta}/\lambda_f$), the error of both dynamic and non-dynamic models decreased. DC1 produced better results than the non-dynamic C for case H (see e.g. Fig. 5.56b and 5.56c). However, for the other two models, in the best case the dynamic procedure produced results similar to their non-dynamic counterparts. It should be mentioned that in these DNS cases, there is more extinction in the higher Re conditions with the lower Re one, showing progressively more flamelet-like behavior. So it is possibly the case that it is the flamelet-like behavior that is more challenging rather than lower Re. This needs to be further studied in the future. It seems that the specific test cases considered here are not suitable to reveal the true potentials of the new dynamic procedures. One may conclude that the dynamic models can at least converge to the best predictions which here resulted from the default similarity coefficient of 1. The optimal estimators concept [190] can be exploited to find the minimum achievable error by the SS models for these specific databases. By the observed dependency of the performance of dynamic models on Reynolds number:

- It is expected that the dynamic procedures presented in the current study, produce acceptable results in higher Reynolds than the ones considered here. The highest Re in this study is around 9000. One may argue that the encouraging results of the SS SGS combustion models observed in the current study may be due to the specific DNS test cases in which the scales are overlapped and there is possibly not enough scale separation. It is true that these DNS databases lack a distinct

scale separation, however, one should also take this into account that in this study it was observed that the performance of the models are better in higher Reynolds cases M and H. Furthermore, by increasing the Re, the $\overline{\Delta}/\underline{\lambda}_f$ is also increasing. So it is reasonable to expect better performances in higher Reynolds numbers. It is so suggested doing this analysis to draw a solid conclusion on the effect of the Re on the performance of the new models.

- The application of Germano's identity for pure SS models seems to be unsuccessful in improving the performance in low Re flames. It will be interesting to use a combination of mixed models and Germano's identity to compute the similarity coefficient dynamically like what is done for flame surface density closure in [186].

CHAPTER 6

# Conclusions and Future Works

## 6.1 Summary and Conclusions

The activities presented in this dissertation can be divided into two parts, both sharing the same idea and goal. The goal was the assessment and development of sub-grid scale (SGS) combustion models (turbulence-chemistry interaction models) for non-premixed flames capable of handling detailed chemistry in Large Eddy Simulation (LES) of reactive flows. The idea was to use fully resolved numerical experiments (DNS) as a representation of reality.

The first part was devoted to gain more physical insights, from the statistical point of view, on reactive turbulent flow fields using DNS databases, mainly on the second order velocity structure functions (velocity spectrum in Fourier space) and the fourth order moment of velocity gradients (the internal intermittency). These two specific statistical quantities are of great importance in turbulence-chemistry interaction models both in RANS and LES, although the fundamental analyses carried out in this work have more applications. The second part was devoted to the application of the new findings and development of new the finite-rate (FR) combustion models. Moreover, the assessment of existing and developed finite-rate combustion models (specifically EDC and non-dynamic Scale Similarity models) was carried out to fulfill the goals of the project. The methodology for the assessment of FR combustion models was *a priori* DNS analysis. LES like quantities extracted from DNS do not contain additional error associated with the modeling of turbulent fields. The idea was to use these quantities to model/close the unclosed non-linear species source term in the governing equation of reactive LES Navier-Stokes equations. The unclosed source terms are already available from the explicitly filtered DNS data, to be compared with the model predictions. Three sets of DNS databases were selected, all experiencing high level of local extinctions with different initial Reynolds numbers (the so called cases **H**, **M**, and **L**, with the highest,

moderate and lowest Reynolds number, respectively) so that the effect of bulk Reynolds number of the flow can also be studied.

In summary, following topics were covered in the dissertation:

- **The scalings of the velocity spectra and adaptation of the model dissipation spectrum**: The velocity and its dissipation spectra in non-premixed jets were analyzed using the 3 above mentioned DNS databases. In each database, 3 different time instants are selected (9 in total) corresponding to the events of maximum local extinction and re-ignition phases. It was observed that using Favre averaged Kolmogorv's length scale ($\underline{\eta}_f$) and Favre averaged Turbulent Kinetic Energy (TKE) dissipation rate ($\underline{\varepsilon}_f$) for normalization, the spectra extracted in different planes across the shear layers, different flame dynamics, and different Reynolds numbers are collapsed on a single curve very well in the inertial range. In the dissipation range, the collapse was very well up to $\kappa\underline{\eta}_f \approx 0.6$ for case H, with $\kappa$ the wavenumber. The range of the collapse of the spectra is wider in cases M and L (up to $\kappa\underline{\eta}_f \approx 1$) in which the resolution is higher. In general in all the cases, the collapse can be observed in the dissipation spectra up to the wavenumber at which 98% of the dissipation happens. This was verified by using a cut-off scale defined by the inverse of wavenumber corresponding to $2\%$ of the dissipation spectra peaks ($\lambda_\beta$). $\kappa^{-5/3}$ scaling was observed in the inertial range with a constant of proportionality of $C_K = 2.3$ in all three cases. In the dissipation range, the exponential drop-off of all velocity spectra was steeper than the corresponding non-reactive flows. It was observed that the $\exp(\beta\kappa)$ scaling exists with the value of $\beta = 7.2$ instead of non-reactive flows value of $\beta = 5.2$ for the exponential roll-off range of the spectra. Finally, the 1D model spectrum of Pope [38] for non-reacting flows was adapted to the spectra from reactive DNS cases. If the values of $C_K$ and $\beta$ mentioned above, along with a fitting value of $c_{eta} = 0.28$ are used in the model, the model can correctly predict the reactive dissipation spectra from DNS.

- **The scalings of the normalized dissipation fluctuations; studies on the external and internal intermittency phenomena**: Both external and internal intermittency phenomena in non-premixed flames were studied. The conditional statistics on turbulent regions were calculated by excluding the irrotational laminar regions from the database. These regions were identified based on the threshold on vorticity magnitude commonly used to identify Turbulent-Non Turbulent (T-NT) interfaces. The flatness of the longitudinal gradient of Favre fluctuations of streamwise velocity, viz. $\mathcal{F}_{\frac{\partial u_t''}{\partial x}}$, and in general the internal intermittency factor in turbulent regions were analyzed. It was found that on the central plane of the reactive jets, $\mathcal{F}_{\frac{\partial u_t''}{\partial x}}$, and $\underline{\varepsilon}^2_{f,t}/\left(\underline{\varepsilon}_{f,t}\right)^2$ (the averaged square of local/instantaneous dissipation fluctuations divided by the square of Favre averaged dissipation or inverse of the internal intermittency factor) scales with $Re_\lambda$ as $Re_\lambda^{0.28}$. This is consistent with the scaling found in different types of non-reactive flows with low $Re_\lambda$ ($Re_\lambda < 300$), namely on the centerline behind the wake, behind the grid generated turbulence and forced periodic box turbulence. The power law ($\approx 0.28$), however, is much weaker than the one predicted by the phenomenological models

of Corrsin [111] ($= 1.5$) and Tennekes [103] ($= 1$). A perfect agreement found for the three DNS cases with the theory proposed by Yakhot [36]. Interestingly, on the central plane of the reacting jets, $\underline{\varepsilon}^2_{f,t}/\left(\underline{\varepsilon}_{f,t}\right)^2$ found to scale very well with large scale Reynolds number ($Re^{0.152}$ [36]). Large scale Reynolds number defined as $Re = u_{rms}L/\nu$, with $u_{rms}$ two times TKE and $L$ here taken to be the initial width of the fuel jet. This is very interesting since both extinction and re-ignition time instants' statistics collapsed to the theoretical curve of Yakhot [36] which is for non-reactive HIT flows. At the extinction time, there is approximately no reactivity on the central plane of the jets however, at re-ignition times, the jets are mainly re-ignited from the central planes. Although a very good scalings with both types of Reynolds numbers were observed on the center of the jets, it was observed that across the shear layers the behavior of $\underline{\varepsilon}^2_{f,t}/\left(\underline{\varepsilon}_{f,t}\right)^2$ is more complex than to be solely described by kind of Reynolds number scalings.

- **New EDC models for LES**: The findings from the two above fundamental analyses were applied to modify the EDC combustion model. Two modifications were carried out. The first modification was based on mathematical relations found between the two EDC coefficients, viz. $CD_2 = (3/2)^{8/3}(1/3)^{1/3}\dfrac{CD_1^2}{\left(\kappa_*^-\underline{\eta}\right)^{4/3}}C_K^2$. This means that $CD_2$ found to be a function of $CD_1$, the Kolmogorov constant ($C_K$) and a normalized cut-off wavenumber from which the integral of normalized model dissipation spectrum is $3/4$ ($\kappa_*^-\underline{\eta}$). The normalized model dissipation spectrum discussed above used to find the cut-off wavenumber ($\kappa_*^-\underline{\eta} \approx 0.15$) and create a final relation between the two coefficients, viz. $CD_2 \approx 135.7CD_1^2$. The second modification was based on the internal intermittency factor scaling laws, discussed above. $\gamma^*$ in EDC was redefined to comply with the new scalings, viz. $\gamma^* = \gamma_{int} = \left(u^*/u'\right)^{2\times 0.28}$. These two modifications and new ways to evaluate $CD_1$ resulted in variants of EDC-RANS and EDC-LES models (see Tables3.1 and 3.2, respectively).

- **New dynamic Scale Similarity combustion models for LES**: The finite-rate dynamic Scale Similarity (SS) SGS combustion models were developed by applying the Germano identity on non-dynamic SS models. Two variants of dynamic versions for each existing non-dynamic model were derived (see Table 3.5).

- **An *a priori* DNS assessment of EDC-LES combustion models**: The new EDC-LES models were *a priori* assessed using the DNS databases. The first modification found to improve the results specifically when the filter width is relatively large. For example, using $\overline{\Delta}/\Delta_{\mathrm{DNS}} = 18$ compared to $\overline{\Delta}/\Delta_{\mathrm{DNS}} = 8$, it was observed that the original EDC-LES models failed to predict the correct conditional means (conditioned on mixture fraction, temperature and species mass fractions). Modification in $\gamma^*$ shows its improving effects when $Re_{\lambda_{SGS}}$ is below the saturation threshold (see Table5.3 and the definitions therein).

- **An *a priori* DNS assessment of SS combustion models**: The developed dynamic SS combustion models and the existing non-dynamic ones were *a priori* assessed using the DNS databases. Explicit top-hat filter with relatively large filter width ($\overline{\Delta}/\Delta_{\mathrm{DNS}}$=12) was applied to compute the LES-like filtered quantities from the

DNS databases. Comparing the two dynamic versions of each SS model, it was found that the mathematically consistent formulation [125] of SS models for combustion does not always improve the results like what was seen before for the SGS stress field [125]. Considering conditional mean heat release rates (see Fig. 5.56), the SS models could predict correctly (in mean) the filtered heat release rates, while in all three flames, the “no model" approach predicted higher rates. It was observed that by increasing Re, the error of both dynamic and non-dynamic models decreased. By the observed dependency of the performance of dynamic models on Reynolds number, It is expected that the dynamic procedures presented in the current study produce acceptable results in higher Re than the ones considered. The highest Re in this study is around 9000. For detailed conclusions regarding specific models see Sec.5.4.3.

## 6.2 Future Works

The results obtained during the PhD. course work can be extended in different aspects which are summarized in the following.

### 6.2.1 Proposals for Future Works on the Theory

In this dissertation, fundamental analyses carried out on the dissipation spectrum of turbulent kinetic energy in non-premixed jet flames. Although the modified model spectrum proposed in Sec.5.3 was tested using the three DNS databases, more work is needed to systematically evaluate the model for non-premixed flames. Further, the analysis can be extended to premixed flames databases. We are aware that the identification of Kolmogorov constant using compensated spectra plots needs databases with very high Reynolds (based on $Re_\lambda$, say $Re_\lambda > 200$). The existence of a sufficiently wide inertial subrange is a prerequisite to analyzing such plots [70]. We were confined to such low Reynolds databases and hope that the study can be extended using much higher Reynolds. However, consider that the theory developed in Sec.3.2.3, is general. The Kolmogorov constant introduced in the final relation for $CD_2$, i.e. Eq. 3.45, can be changed if better DNS databases of reactive flows is provided. Moreover, unlike the value of $C_K = 2.3$ used in the current study, one may rely on well resolved DNS data of non-reactive flows and uses the value of $C_K = 1.5 - 1.7$ [70]. DNS databases specifically designed for this purpose are needed. The DNS databases should have the below specifications:

- As mentioned before, the separation of scales is required. So the highest Reynolds number is desired. However, the conventional resolution of $\kappa\underline{\eta}_f \geq 1$ or 2, is sufficient because we are not interested in the far dissipation range.

- To this end, it is not needed for the DNS case to contain detailed kinetics since and inclusion of heat release rate suffices. Single or two steps kinetics are sufficient.

- Both temporal and spatial jet configurations can be used. In the specific case of spatial jets, since the turbulence is not decaying, the temporal averaging can be done to increase the convergence of the spectra.

Using the above DNS databases, the same analysis carried out in Sec.5.3 should be repeated.

The second fundamental study in this dissertation was devoted to statistics of velocity gradients, namely the flatness of velocity gradient. Specifically, the analysis was carried out on the scaling of normalized Favre fluctuation of dissipation in turbulent regions, viz., $\underline{\varepsilon^2}_{f,t}/\left(\underline{\varepsilon}_{f,t}\right)^2$. The analysis should be extended in different manners. All need specifically designed DNS cases with below specifications:

- Unlike the analysis of spectra discussed before, here, there is no need for the Reynolds number to be as high as possible. The most demanding requirement is the resolution of the DNS. Since we are dealing with $4^{th}$ order statistics, for them to be converged, we need a high-resolution DNS. An acceptable resolution is $\kappa\underline{\eta}_f \approx 3$ [29, 30].
- As stated above, the focus must be on a well-resolved DNS which means that cases with low to medium Reynolds number based on $Re_\lambda$ are sufficient. $Re_\lambda$ should be below a threshold where the flatness becomes independent of $Re_\lambda$ which is $Re_\lambda < 300$. Also, it is suggested to study higher $Re_\lambda$ compared to the ones in the current study. The suggested range is $100 < Re_\lambda < 300$.
- As before, it is not needed for the DNS case to contain detailed kinetics and single or two-step kinetics are sufficient.
- The double shear layers configuration similar to what was used in this thesis seems to be fine and data on the central plane of the jet must be used. In the case of premixed flames in HIT configurations, one can use the advantage of larger produced dataset free from inhomogeneity and external intermittency effects induced by shears. However, in some references, it is suggested to calculate conditional statistics, conditioned on reacting scalars, to avoid inhomogeneity caused by the wrinkled flame [191].

Using the above produced databases one can add more data points on Fig.5.13 to see if the same scaling holds for either the flatness of velocity gradients or $\underline{\varepsilon^2}_{f,t}/\left(\underline{\varepsilon}_{f,t}\right)^2$.

In Sec.5.2.2 no systematic relation could be found between $\underline{\varepsilon^2}_{f,t}/\left(\underline{\varepsilon}_{f,t}\right)^2$ and $Re_\lambda$ across the jet. It is suggested to do the analysis in simpler cases of reacting homogeneous turbulent shear flows. This means reducing the complexity of the problem to be between very complex jet flows and simple homogeneous isotropic flows. An example is the case used in [192]. Analyses of this type have been already carried out for non-reacting constant density flows (see e.g., [163, 193, 194]).

The other extension of the current work is to do the same analysis as was done in Sec.5.2.2 for the sub-grid viscous dissipation. For example, it can follow the work in [195], however, for reacting flows. The final goal is to search for any relation between $\underline{\varepsilon_{\nu,SGS}{}^2}_f/\left(\underline{\varepsilon_{\nu,SGS}}_f\right)^2$, or even the flatness of high-pass filtered velocity gradients, and large scales related quantities like $Re_{\lambda,SGS}$. The scaling can be applied in combustion modeling like what was done in Eq. 3.58.

In the current dissertation, no study was done on fractal theory [51] and its application in turbulent combustion modeling. Fractals and multi-fractals were found to be able to correctly predict the high order structure functions. In particular, they are able

to define scaling laws for the flatness of velocity gradients. A separate project can be defined based on the application of the theory in the evaluation of $\gamma^*$ in the EDC. The starting points can be either an *a priori* DNS assessment of the fractal type model developed by Giacomazzi [196, 197] and searching further possible developments or direct application of fractal and multifractal cascade models [109, 110] on the evaluation of $\gamma^*$.

### 6.2.2 Proposals for Future Works on the Applications

The models developed in this thesis must be assessed in *a posteriori* analyses and also LES of experimental setups for the assessment to be complete. In this thesis, it was shown that the developed EDC-LES models work well in the *a priori* DNS analysis. This means that if filtered quantities which the models required are exact, the models will work. These include for example the sub-grid kinetic energy or its dissipation rate. However, in LES, these quantities also need modeling. So it is interesting to see the performance of the models while the inputs have errors. For the new dynamic Scale Similarity (SS) models, it was found that the proposed models work much better in the highest Reynolds DNS (case H) compared to cases with the medium (M) and Lowest (L) Reynolds numbers. Since the production of high Reynolds numbers DNS databases is computationally very expensive, one can either choose to perform a high Reynolds DNS with single/two-step chemistry or to test the models in LES of real burners.

In summary, below future investigations can be considered:

- ***a posteriori* DNS analysis of the EDC-LES and SS models:** The current DNS databases of temporally evolving jet flames can be used as test cases. The temporal jets have an advantage over spatial jets; the computational load is much lower in the case of temporal jets. Initial conditions of DNS must be filtered and interpolated to LES grid. This will be the initial condition of LES. A crucial issue in LES of temporal jets (or their disadvantage compared to spatial jets) is that the LES model (for the flow field) should be able to capture the temporal transition from the initially perturbed condition to the fully developed jet. This is not an easy task.
- **LES of experimental setups using the EDC-LES and SS models**: To finalize the assessment, the developed model in this dissertation should be assessed in LES of experimental setups in high Reynolds numbers. The Adelaide Jet in Hot Co-flow (AJHC) burner [198], which has been studied extensively using FR-TCI models (see e.g. [199]) can be an ideal choice.

# Bibliography


[1] J.A. Wünning and J.G. Wünning, "Flameless oxidation to reduce thermal NO-formation," *Progress in Energy and Combustion Science*, vol. 23, no. 1, pp. 81 – 94, 1997.

[2] A. Cavaliere and M. de Joannon, "Mild combustion," *Progress in Energy and Combustion Science*, vol. 30, no. 4, pp. 329 – 366, 2004.

[3] A. A. Perpignan, A. G. Rao, and D. J. Roekaerts, "Flameless combustion and its potential towards gas turbines," *Progress in Energy and Combustion Science*, vol. 69, pp. 28 – 62, 2018.

[4] A. Parente, M. R. Malik, F. Contino, A. Cuoci, and B. B. Dally, "Extension of the Eddy Dissipation Concept for turbulence/chemistry interactions to MILD combustion," *Fuel*, vol. 163, pp. 98 – 111, 2016.

[5] M. J. Dunn, A. R. Masri, R. W. Bilger, and R. S. Barlow, "Finite Rate Chemistry Effects in Highly Sheared Turbulent Premixed Flames," *Flow, Turbulence and Combustion*, vol. 85, pp. 621–648, Dec 2010.

[6] E. R. Hawkes, R. Sankaran, J. C. Sutherland, and J. H. Chen, "Scalar mixing in direct numerical simulations of temporally evolving plane jet flames with skeletal CO/H2 kinetics," *Proceedings of the combustion institute*, vol. 31, no. 1, pp. 1633–1640, 2007.

[7] Y. Yang, H. Wang, S. B. Pope, and J. H. Chen, "Large-eddy simulation/probability density function modeling of a non-premixed CO/H2 temporally evolving jet flame," *Proceedings of the Combustion Institute*, vol. 34, no. 1, pp. 1241–1249, 2013.

[8] E. Fedina, C. Fureby, G. Bulat, and W. Meier, "Assessment of Finite Rate Chemistry Large Eddy Simulation Combustion Models," *Flow, Turbulence and Combustion*, vol. 99, no. 2, pp. 385–409, 2017.

[9] S. B. Pope, "PDF methods for turbulent reactive flows," *Progress in energy and combustion science*, vol. 11, no. 2, pp. 119–192, 1985.

[10] D. Haworth, "Progress in probability density function methods for turbulent reacting flows," *Progress in Energy and Combustion Science*, vol. 36, no. 2, pp. 168–259, 2010.

[11] V. Sabelnikov and C. Fureby, "LES combustion modeling for high Re flames using a multi-phase analogy," *Combustion and Flame*, vol. 160, no. 1, pp. 83–96, 2013.

[12] V. Golovitchev and J. Chomiak, "Numerical modeling of high temperature air flameless combustion," in *Proceedings of the 4th International Symposium on High Temperature Air Combustion and Gasification (HiTACG)*, pp. 27–30, 2001.

[13] B. Magnussen, "On the structure of turbulence and a generalized eddy dissipation concept for chemical reaction in turbulent flow," in *19th Aerospace Sciences Meeting*, p. 42, 1981.

[14] B. F. Magnussen, "The Eddy Dissipation Concept-A Bridge Between Science and Technology," in *ECCOMAS thematic conference on computational combustion*, pp. 21–24, 2005.

[15] I. S. Ertesvåg and B. F. Magnussen, "The eddy dissipation turbulence energy cascade model," *Combustion science and technology*, vol. 159, no. 1, pp. 213–235, 2000.

[16] D. A. Lysenko, I. S. Ertesvåg, and K. E. Rian, "Numerical simulation of non-premixed turbulent combustion using the eddy dissipation concept and comparing with the steady laminar flamelet model," *Flow, turbulence and combustion*, vol. 93, no. 4, pp. 577–605, 2014.

[17] P. E. DesJardin and S. H. Frankel, "Large eddy simulation of a nonpremixed reacting jet: Application and assessment of subgrid-scale combustion models," *Physics of Fluids*, vol. 10, no. 9, pp. 2298–2314, 1998.

[18] F. Jaberi and S. James, "A dynamic similarity model for large eddy simulation of turbulent combustion," *Physics of fluids*, vol. 10, no. 7, pp. 1775–1777, 1998.

[19] M. Ihme and H. Pitsch, "Prediction of extinction and reignition in nonpremixed turbulent flames using a flamelet/progress variable model: 1. A priori study and presumed PDF closure," *Combustion and flame*, vol. 155, no. 1-2, pp. 70–89, 2008.

[20] D. O. Lignell, J. C. Hewson, and J. H. Chen, "A-priori analysis of conditional moment closure modeling of a temporal ethylene jet flame with soot formation using direct numerical simulation," *Proceedings of the Combustion Institute*, vol. 32, no. 1, pp. 1491–1498, 2009.

[21] M. Ameen and J. Abraham, "A priori evaluation of subgrid-scale combustion models for diesel engine applications," *Fuel*, vol. 153, pp. 612–619, 2015.

[22] S. Lapointe and G. Blanquart, "A priori filtered chemical source term modeling for LES of high Karlovitz number premixed flames," *Combustion and Flame*, vol. 176, pp. 500–510, 2017.

[23] U. Allauddin, M. Klein, M. Pfitzner, and N. Chakraborty, "A priori and a posteriori analyses of algebraic flame surface density modeling in the context of Large Eddy Simulation of turbulent premixed combustion," *Numerical Heat Transfer, Part A: Applications*, vol. 71, no. 2, pp. 153–171, 2017.

[24] S. Vo, O. Stein, A. Kronenburg, and M. Cleary, "Assessment of mixing time scales for a sparse particle method," *Combustion and Flame*, vol. 179, pp. 280–299, 2017.

[25] H. S. Shafi, Y. Zhu, and R. A. Antonia, "Statistics of $\partial$u/$\partial$y in a turbulent wake," *Fluid Dynamics Research*, vol. 19, pp. 169–183, mar 1997.

[26] R. A. Antonia, S. L. Tang, L. Djenidi, and L. Danaila, "Boundedness of the velocity derivative skewness in various turbulent flows," *Journal of Fluid Mechanics*, vol. 781, pp. 727–744, 2015.

[27] S. Tang, R. Antonia, L. Djenidi, L. Danaila, and Y. Zhou, "Finite Reynolds number effect on the scaling range behaviour of turbulent longitudinal velocity structure functions," *Journal of Fluid Mechanics*, vol. 820, pp. 341–369, 2017.

[28] K. R. Sreenivasan and R. Antonia, "The phenomenology of small-scale turbulence," *Annual review of fluid mechanics*, vol. 29, no. 1, pp. 435–472, 1997.

[29] D. Donzis, P. Yeung, and K. Sreenivasan, "Dissipation and enstrophy in isotropic turbulence: resolution effects and scaling in direct numerical simulations," *Physics of Fluids*, vol. 20, no. 4, p. 045108, 2008.

[30] J. Schumacher, J. D. Scheel, D. Krasnov, D. A. Donzis, V. Yakhot, and K. R. Sreenivasan, "Small-scale universality in fluid turbulence," *Proceedings of the National Academy of Sciences*, vol. 111, no. 30, pp. 10961–10965, 2014.

[31] K. Sreenivasan, "Possible effects of small-scale intermittency in turbulent reacting flows," *Flow, Turbulence and Combustion*, vol. 72, no. 2-4, pp. 115–131, 2004.

[32] P. E. Hamlington, D. Krasnov, T. Boeck, and J. Schumacher, "Local dissipation scales and energy dissipation-rate moments in channel flow," *Journal of Fluid Mechanics*, vol. 701, pp. 419–429, 2012.

[33] Z. Pouransari, L. Biferale, and A. V. Johansson, "Statistical analysis of the velocity and scalar fields in reacting turbulent wall-jets," *Physics of Fluids*, vol. 27, no. 2, 2015.

[34] B. Coriton and J. H. Frank, "High-speed tomographic PIV measurements of strain rate intermittency and clustering in turbulent partially-premixed jet flames," *Proceedings of the Combustion Institute*, vol. 35, no. 2, pp. 1243–1250, 2015.

[35] S. Tang, R. Antonia, L. Djenidi, L. Danaila, and Y. Zhou, "Reappraisal of the velocity derivative flatness factor in various turbulent flows," *Journal of Fluid Mechanics*, vol. 847, pp. 244–265, 2018.

[36] V. Yakhot, "Probability densities in strong turbulence," *Physica D: Nonlinear Phenomena*, vol. 215, no. 2, pp. 166–174, 2006.

[37] G. Wang, A. N. Karpetis, and R. S. Barlow, "Dissipation length scales in turbulent nonpremixed jet flames," *Combustion and Flame*, vol. 148, no. 1-2, pp. 62–75, 2007.

[38] S. Pope, *Turbulent Flows*. Cambridge University Press, 2000.

[39] K. R. Sreenivasan, "On the universality of the Kolmogorov constant," *Physics of Fluids*, vol. 7, no. 11, pp. 2778–2784, 1995.

[40] P. Yeung and Y. Zhou, "Universality of the Kolmogorov constant in numerical simulations of turbulence," *Physical Review E*, vol. 56, no. 2, p. 1746, 1997.

[41] Y. Kaneda, T. Ishihara, M. Yokokawa, K. Itakura, and A. Uno, "Energy dissipation rate and energy spectrum in high resolution direct numerical simulations of turbulence in a periodic box," *Physics of Fluids*, vol. 15, no. 2, pp. L21–L24, 2003.

[42] T. Ishihara, K. Morishita, M. Yokokawa, A. Uno, and Y. Kaneda, "Energy spectrum in high-resolution direct numerical simulations of turbulence," *Physical Review Fluids*, vol. 1, no. 8, p. 082403, 2016.

[43] S. G. Saddoughi and S. V. Veeravalli, "Local isotropy in turbulent boundary layers at high Reynolds number," *Journal of Fluid Mechanics*, vol. 268, pp. 333–372, 1994.

[44] J. H. Frank and S. A. Kaiser, "High-resolution imaging of dissipative structures in a turbulent jet flame with laser rayleigh scattering," *Experiments in Fluids*, vol. 44, no. 2, pp. 221–233, 2008.

[45] G.-H. Wang, R. S. Barlow, and N. T. Clemens, "Quantification of resolution and noise effects on thermal dissipation measurements in turbulent non-premixed jet flames," *Proceedings of the Combustion Institute*, vol. 31, no. 1, pp. 1525–1532, 2007.

[46] R. Knaus and C. Pantano, "On the effect of heat release in turbulence spectra of non-premixed reacting shear layers," *Journal of Fluid Mechanics*, vol. 626, pp. 67–109, 2009.

[47] H. Kolla, E. Hawkes, A. Kerstein, N. Swaminathan, and J. Chen, "On velocity and reactive scalar spectra in turbulent premixed flames," *Journal of Fluid Mechanics*, vol. 754, pp. 456–487, 2014.

[48] H. Kolla, X.-Y. Zhao, J. H. Chen, and N. Swaminathan, "Velocity and reactive scalar dissipation spectra in turbulent premixed flames," *Combustion Science and Technology*, vol. 188, no. 9, pp. 1424–1439, 2016.

[49] Q. Wang and M. Ihme, "Regularized deconvolution method for turbulent combustion modeling," *Combustion and Flame*, vol. 176, pp. 125–142, 2017.

[50] H. Tennekes and J. Lumley, *A First Course in Turbulence*. MIT Press, 1972.

[51] U. Frisch, *Turbulence: The Legacy of A. N. Kolmogorov*. Cambridge University Press, 1995.

[52] A. Monin and A. Yaglom, *Statistical fluid mechanics: mechanics of turbulence*. No. v. 1 in Statistical Fluid Mechanics: Mechanics of Turbulence, MIT Press, 1971.

[53] H. A. Sturges, "The Choice of a Class Interval," *Journal of the American Statistical Association*, vol. 21, no. 153, pp. 65–66, 1926.

[54] M. R. Overholt and S. B. Pope, "A deterministic forcing scheme for direct numerical simulations of turbulence," *Computers & Fluids*, vol. 27, no. 1, pp. 11–28, 1998.

[55] W. K. George, "Lectures in Turbulence for the 21st Century," *Chalmers University of Technology*, 2013.

[56] T. Poinsot and D. Veynante, *Theoretical and numerical combustion*. RT Edwards, Inc., 2005.

[57] R. BILGER, "A note on Favre averaging in variable density flows," *Combustion Science and Technology*, vol. 11, no. 5-6, pp. 215–217, 1975.

[58] J. M. McDonough, "Introductory lectures on turbulence: physics, mathematics and modeling," 2007.

[59] A. Oboukhov, "On the distribution of energy in the spectrum of turbulent flow," *CR Acad. Sci. URSS*, vol. 32, p. 19, 1941.

[60] A. Obukhov, "Spectral energy distribution in a turbulent flow," *Izv. Akad. Nauk. SSSR. Ser. Geogr. i. Geofiz*, vol. 5, pp. 453–466, 1941.

[61] M. Van Dyke and F. M. White, "An album of fluid motion," 1982.

[62] J. Schumacher, K. R. Sreenivasan, and P. Yeung, "Very fine structures in scalar mixing," *Journal of Fluid Mechanics*, vol. 531, pp. 113–122, 2005.

[63] J. Schumacher, K. R. Sreenivasan, and V. Yakhot, "Asymptotic exponents from low-Reynolds-number flows," *New Journal of Physics*, vol. 9, no. 4, p. 89, 2007.

[64] J. Jiménez, A. A. Wray, P. G. Saffman, and R. S. Rogallo, "The structure of intense vorticity in isotropic turbulence," *Journal of Fluid Mechanics*, vol. 255, pp. 65–90, 1993.

[65] J. Boschung, F. Hennig, M. Gauding, H. Pitsch, and N. Peters, "Generalised higher-order Kolmogorov scales," *Journal of Fluid Mechanics*, vol. 794, pp. 233–251, 2016.

[66] J. Hinze, *Turbulence*. McGraw-Hill classic textbook reissue series, McGraw-Hill, 1975.

[67] J. OBrien, J. Urzay, M. Ihme, P. Moin, and A. Saghafian, "Subgrid-scale backscatter in reacting and inert supersonic hydrogen–air turbulent mixing layers," *Journal of Fluid Mechanics*, vol. 743, pp. 554–584, 2014.

[68] M. Nelkin, "Universality and scaling in fully developed turbulence," *Advances in physics*, vol. 43, no. 2, pp. 143–181, 1994.

[69] Y. Kaneda and T. Ishihara, "High-resolution direct numerical simulation of turbulence," *Journal of Turbulence*, no. 7, p. N20, 2006.

[70] T. Ishihara, T. Gotoh, and Y. Kaneda, "Study of high–Reynolds number isotropic turbulence by direct numerical simulation," *Annual Review of Fluid Mechanics*, vol. 41, pp. 165–180, 2009.

[71] S. Khurshid, D. A. Donzis, and K. Sreenivasan, "Energy spectrum in the dissipation range," *Physical Review Fluids*, vol. 3, no. 8, p. 082601, 2018.

[72] D. Martinez, S. Chen, G. Doolen, R. Kraichnan, L.-P. Wang, and Y. Zhou, "Energy spectrum in the dissipation range of fluid turbulence," *Journal of plasma physics*, vol. 57, no. 1, pp. 195–201, 1997.

[73] T. Ishihara, Y. Kaneda, M. Yokokawa, K. Itakura, and A. Uno, "Energy spectrum in the near dissipation range of high resolution direct numerical simulation of turbulence," *Journal of the Physical Society of Japan*, vol. 74, no. 5, pp. 1464–1471, 2005.

[74] P. Orlandi, "Energy spectra power laws and structures," *Journal of Fluid Mechanics*, vol. 623, pp. 353–374, 2009.

[75] C. Bailly and G. Comte-Bellot, *Turbulence*. Experimental Fluid Mechanics, Springer International Publishing, 2015.

[76] K. Lilly, "The representation of small-scale turbulence in numerical simulation experiments," 1966.

[77] P. Sagaut, *Large eddy simulation for incompressible flows: an introduction*. Springer Science & Business Media, 2006.

[78] W. Jones and B. E. Launder, "The prediction of laminarization with a two-equation model of turbulence," *International journal of heat and mass transfer*, vol. 15, no. 2, pp. 301–314, 1972.

[79] J. R. Cho and M. K. Chung, "A k-$\epsilon$-$\gamma$ equation turbulence model," *Journal of Fluid Mechanics*, vol. 237, pp. 301–322, 1992.

[80] B. E. Launder, G. J. Reece, and W. Rodi, "Progress in the development of a Reynolds-stress turbulence closure," *Journal of fluid mechanics*, vol. 68, no. 3, pp. 537–566, 1975.

[81] L. Davidson, *Fluid mechanics, turbulent flow and turbulence modeling*. 1997.

[82] A. Saghafian, *High-fidelity simulations and modeling of compressible reacting flows*. PhD thesis, Stanford University, 2014.

[83] R. S. Rogallo and P. Moin, "Numerical simulation of turbulent flows," *Annual review of fluid mechanics*, vol. 16, no. 1, pp. 99–137, 1984.

[84] C. B. da Silva and O. Métais, "On the influence of coherent structures upon interscale interactions in turbulent plane jets," *Journal of Fluid Mechanics*, vol. 473, pp. 103–145, 2002.

[85] J. Smagorinsky, "General circulation experiments with the primitive equations: I. The basic experiment," *Monthly weather review*, vol. 91, no. 3, pp. 99–164, 1963.

[86] A. Yoshizawa, "Statistical theory for compressible turbulent shear flows, with the application to subgrid modeling," *The Physics of fluids*, vol. 29, no. 7, pp. 2152–2164, 1986.

[87] M. Germano, "Turbulence: the filtering approach," *Journal of Fluid Mechanics*, vol. 238, pp. 325–336, 1992.

[88] J. Janicka and A. Sadiki, "Large eddy simulation of turbulent combustion systems," *Proceedings of the Combustion Institute*, vol. 30, no. 1, pp. 537–547, 2005.

[89] B. Fiorina, O. Gicquel, L. Vervisch, S. Carpentier, and N. Darabiha, "Approximating the chemical structure of partially premixed and diffusion counterflow flames using FPI flamelet tabulation," *Combustion and flame*, vol. 140, no. 3, pp. 147–160, 2005.

[90] E. Knudsen and H. Pitsch, "A general flamelet transformation useful for distinguishing between premixed and non-premixed modes of combustion," *Combustion and flame*, vol. 156, no. 3, pp. 678–696, 2009.

[91] C. Fureby, "LES of a multi-burner annular gas turbine combustor," *Flow, turbulence and combustion*, vol. 84, no. 3, pp. 543–564, 2010.

[92] O. Colin, F. Ducros, D. Veynante, and T. Poinsot, "A thickened flame model for large eddy simulations of turbulent premixed combustion," *Physics of fluids*, vol. 12, no. 7, pp. 1843–1863, 2000.

[93] F. Charlette, C. Meneveau, and D. Veynante, "A power-law flame wrinkling model for LES of premixed turbulent combustion part II: dynamic formulation," *Combustion and Flame*, vol. 131, no. 1-2, pp. 181–197, 2002.

[94] F. Charlette, C. Meneveau, and D. Veynante, "A power-law flame wrinkling model for LES of premixed turbulent combustion part I: non-dynamic formulation and initial tests," *Combustion and Flame*, vol. 131, no. 1-2, pp. 159–180, 2002.

[95] A. Cuoci, A. Frassoldati, T. Faravelli, and E. Ranzi, "OpenSMOKE++: An object-oriented framework for the numerical modeling of reactive systems with detailed kinetic mechanisms," *Computer Physics Communications*, vol. 192, pp. 237–264, 2015.

[96] E. Baudoin, R. Yu, Bai, K. J. Nogenmur, X.-S. Bai, and C. Fureby, "Comparison of LES models applied to a bluff body stabilized flame," in *47th AIAA Aerospace Sciences Meeting Including The New Horizons Forum and Aerospace Exposition*, p. 1178, 2009.

[97] C. Fureby, "Large eddy simulation modelling of combustion for propulsion applications," *Philosophical Transactions of the Royal Society A: Mathematical, Physical and Engineering Sciences*, vol. 367, no. 1899, pp. 2957–2969, 2009.

[98] E. Fedina and C. Fureby, "A comparative study of flamelet and finite rate chemistry LES for an axisymmetric dump combustor," *Journal of Turbulence*, no. 12, p. N24, 2011.

[99] C. Fureby, "A comparative study of flamelet and finite rate chemistry LES for a swirl stabilized flame," *Journal of Engineering for Gas Turbines and Power*, vol. 134, no. 4, p. 041503, 2012.

[100] C. Fureby, "A Comparative Study of Large Eddy Simulation (LES) Combustion Models applied to the Volvo Validation Rig," in *55th AIAA Aerospace Sciences Meeting*, p. 1575, 2017.

[101] D. A. Lysenko and I. S. Ertesvåg, "Reynolds-Averaged, Scale-Adaptive and Large-Eddy Simulations of Premixed Bluff-Body Combustion Using the Eddy Dissipation Concept," *Flow, Turbulence and Combustion*, vol. 100, no. 3, pp. 721–768, 2018.

[102] D. A. Lysenko, I. S. Ertesvåg, and K. E. Rian, "Numerical simulations of the Sandia flame d using the eddy dissipation concept," *Flow, turbulence and combustion*, vol. 93, no. 4, pp. 665–687, 2014.

[103] H. Tennekes, "Simple model for the small-scale structure of turbulence," *The Physics of Fluids*, vol. 11, no. 3, pp. 669–671, 1968.

[104] A. W. Vreman, *Direct and large-eddy simulation of the compressible turbulent mixing layer*. PhD thesis, 1995.

[105] S. Ghosal, T. S. Lund, P. Moin, and K. Akselvoll, "A dynamic localization model for large-eddy simulation of turbulent flows," *Journal of fluid mechanics*, vol. 286, pp. 229–255, 1995.

[106] C. B. da Silva and J. C. Pereira, "On the local equilibrium of the subgrid scales: The velocity and scalar fields," *Physics of Fluids*, vol. 17, no. 10, p. 108103, 2005.

[107] G. K. Batchelor, A. A. Townsend, and H. Jeffreys, "The nature of turbulent motion at large wave-numbers," *Proceedings of the Royal Society of London. Series A. Mathematical and Physical Sciences*, vol. 199, no. 1057, pp. 238–255, 1949.

[108] A. Tsinober, *An informal conceptual introduction to turbulence*, vol. 483. Springer, 2009.

[109] U. Frisch, P.-L. Sulem, and M. Nelkin, "A simple dynamical model of intermittent fully developed turbulence," *Journal of Fluid Mechanics*, vol. 87, no. 4, pp. 719–736, 1978.

[110] C. Meneveau and K. Sreenivasan, "Simple multifractal cascade model for fully developed turbulence," *Physical review letters*, vol. 59, no. 13, p. 1424, 1987.

[111] S. Corrsin, "Turbulent dissipation fluctuations," *Physics of Fluids*, vol. 5, no. 10, pp. 1301–1302, 1962.

[112] A. Y. Kuo and S. Corrsin, "Experiments on internal intermittency and fine-structure distribution functions in fully turbulent fluid," *Journal of Fluid Mechanics*, vol. 50, no. 2, pp. 285–319, 1971.

[113] R. A. Antonia, L. Djenidi, L. Danaila, and S. L. Tang, "Small scale turbulence and the finite Reynolds number effect," *Physics of Fluids*, vol. 29, no. 2, p. 020715, 2017.

[114] M. Meldi, L. Djenidi, and R. Antonia, "Reynolds number effect on the velocity derivative flatness factor," *Journal of Fluid Mechanics*, vol. 856, pp. 426–443, 2018.

[115] O. L. Gulder, "Contribution of small scale turbulence to burning velocity of flamelets in the thin reaction zone regime," *Proceedings of the Combustion Institute*, vol. 31, no. 1, pp. 1369–1375, 2007.

[116] P. Davidson, *Turbulence: an introduction for scientists and engineers*. Oxford University Press, 2015.

[117] A. De, E. Oldenhof, P. Sathiah, and D. Roekaerts, "Numerical simulation of delft-jet-in-hot-coflow (DJHC) flames using the eddy dissipation concept model for turbulence–chemistry interaction," *Flow, Turbulence and Combustion*, vol. 87, no. 4, pp. 537–567, 2011.

[118] E. Garnier, N. Adams, and P. Sagaut, *Large eddy simulation for compressible flows*. Springer Science & Business Media, 2009.

[119] P. Domingo and L. Vervisch, "DNS and approximate deconvolution as a tool to analyse one-dimensional filtered flame sub-grid scale modelling," *Combustion and Flame*, vol. 177, pp. 109–122, 2017.

[120] J. Bardina, J. Ferziger, and W. Reynolds, "Improved subgrid-scale models for large-eddy simulation," in *13th Fluid and PlasmaDynamics Conference*, p. 1357, 1980.

[121] M. Germano, "A proposal for a redefinition of the turbulent stresses in the filtered Navier–Stokes equations," *The Physics of fluids*, vol. 29, no. 7, pp. 2323–2324, 1986.

[122] S. Liu, C. Meneveau, and J. Katz, "On the properties of similarity subgrid-scale models as deduced from measurements in a turbulent jet," *Journal of Fluid Mechanics*, vol. 275, pp. 83–119, 1994.

[123] A. Shamooni, A. Cuoci, T. Faravelli, and A. Sadiki, "Prediction of Combustion and Heat Release Rates in Non-Premixed Syngas Jet Flames Using Finite-Rate Scale Similarity Based Combustion Models," *Energies*, vol. 11, no. 9, p. 2464, 2018.

[124] C. Meneveau, "Germano identity-based subgrid-scale modeling: A brief survey of variations on a fertile theme," *Physics of Fluids*, vol. 24, no. 12, p. 121301, 2012.

[125] B. Vreman, B. Geurts, and H. Kuerten, "On the formulation of the dynamic mixed subgrid-scale model," *Physics of Fluids*, vol. 6, no. 12, pp. 4057–4059, 1994.

[126] Y. Zang, R. L. Street, and J. R. Koseff, "A dynamic mixed subgrid-scale model and its application to turbulent recirculating flows," *Physics of Fluids A: Fluid Dynamics*, vol. 5, no. 12, pp. 3186–3196, 1993.

[127] J.-F. Vinuesa and F. Porté-Agel, "Dynamic models for the subgrid-scale mixing of reactants in atmospheric turbulent reacting flows," *Journal of the Atmospheric Sciences*, vol. 65, no. 5, pp. 1692–1699, 2008.

[128] M. Germano, A. Maffio, S. Sello, and G. Mariotti, "On the extension of the dynamic modelling procedure to turbulent reacting flows," in *Direct and Large-Eddy Simulation II*, pp. 291–300, Springer, 1997.

[129] P. Trisjono and H. Pitsch, "Systematic analysis strategies for the development of combustion models from DNS: a review," *Flow, Turbulence and Combustion*, vol. 95, no. 2-3, pp. 231–259, 2015.

[130] C. Argyropoulos and N. Markatos, "Recent advances on the numerical modelling of turbulent flows," *Applied Mathematical Modelling*, vol. 39, no. 2, pp. 693 –732, 2015.

[131] C. B. da Silva and J. C. Pereira, "Analysis of the gradient-diffusion hypothesis in large-eddy simulations based on transport equations," *Physics of Fluids*, vol. 19, no. 3, p. 035106, 2007.

[132] S. Yang, R. Ranjan, V. Yang, W. Sun, and S. Menon, "Sensitivity of predictions to chemical kinetics models in a temporally evolving turbulent non-premixed flame," *Combustion and Flame*, vol. 183, pp. 224–241, 2017.

[133] S. B. Pope, "A model for turbulent mixing based on shadow-position conditioning," *Physics of Fluids*, vol. 25, no. 11, p. 110803, 2013.

[134] S. Vo, A. Kronenburg, O. T. Stein, and M. J. Cleary, "MMC-LES of a syngas mixing layer using an anisotropic mixing time scale model," *Combustion and Flame*, vol. 189, pp. 311–314, 2018.

[135] A. Scholtissek, F. Dietzsch, M. Gauding, and C. Hasse, "In-situ tracking of mixture fraction gradient trajectories and unsteady flamelet analysis in turbulent non-premixed combustion," *Combustion and Flame*, vol. 175, pp. 243–258, 2017.

[136] B. A. Sen, E. R. Hawkes, and S. Menon, "Large eddy simulation of extinction and reignition with artificial neural networks based chemical kinetics," *Combustion and Flame*, vol. 157, no. 3, pp. 566–578, 2010.

[137] N. Punati, J. C. Sutherland, A. R. Kerstein, E. R. Hawkes, and J. H. Chen, "An evaluation of the one-dimensional turbulence model: Comparison with direct numerical simulations of CO/H2 jets with extinction and reignition," *Proceedings of the Combustion Institute*, vol. 33, no. 1, pp. 1515–1522, 2011.

[138] C. B. da Silva and J. C. Pereira, "Invariants of the velocity-gradient, rate-of-strain, and rate-of-rotation tensors across the turbulent/nonturbulent interface in jets," *Physics of fluids*, vol. 20, no. 5, p. 055101, 2008.

[139] J. Philip and I. Marusic, "Large-scale eddies and their role in entrainment in turbulent jets and wakes," *Physics of Fluids*, vol. 24, no. 5, p. 055108, 2012.

[140] J. Mathew and A. J. Basu, "Some characteristics of entrainment at a cylindrical turbulence boundary," *Physics of Fluids*, vol. 14, no. 7, pp. 2065–2072, 2002.

[141] H. Z. Baumert, J. Simpson, J. Sundermann, and J. Sündermann, *Marine turbulence: theories, observations, and models*, vol. 1. Cambridge University Press, 2005.

[142] S. Corrsin, "Investigation of flow in an axially symmetrical heated jet of air," techreport NACA WR W-94, NACA, Washington DC, 1943.

[143] S. Corrsin and A. L. Kistler, "Free-stream boundaries of turbulent flows," techreport NACA TR 1244, NACA, Washington DC, 1955.

[144] M. Gampert, V. Narayanaswamy, P. Schaefer, and N. Peters, "Conditional statistics of the turbulent/non-turbulent interface in a jet flow," *Journal of Fluid Mechanics*, vol. 731, pp. 615–638, 2013.

[145] C. B. da Silva and R. R. Taveira, "The thickness of the turbulent/nonturbulent interface is equal to the radius of the large vorticity structures near the edge of the shear layer," *Physics of Fluids*, vol. 22, no. 12, p. 121702, 2010.

[146] D. K. Bisset, J. C. Hunt, and M. M. Rogers, "The turbulent/non-turbulent interface bounding a far wake," *Journal of Fluid Mechanics*, vol. 451, pp. 383–410, 2002.

[147] M. Gampert, J. Boschung, F. Hennig, M. Gauding, and N. Peters, "The vorticity versus the scalar criterion for the detection of the turbulent/non-turbulent interface," *Journal of Fluid Mechanics*, vol. 750, pp. 578–596, 2014.

[148] R. Schefer and R. Dibble, "Mixture fraction field in a turbulent nonreacting propane jet," *AIAA journal*, vol. 39, no. 1, pp. 64–72, 2001.

[149] R. R. Taveira, J. S. Diogo, D. C. Lopes, and C. B. da Silva, "Lagrangian statistics across the turbulent-nonturbulent interface in a turbulent plane jet," *Physical Review E*, vol. 88, no. 4, p. 043001, 2013.

[150] A. Townsend, "Local isotropy in the turbulent wake of a cylinder," *Australian Journal of Chemistry*, vol. 1, no. 2, pp. 161–174, 1948.

[151] T. Watanabe, Y. Sakai, K. Nagata, Y. Ito, and T. Hayase, "Vortex stretching and compression near the turbulent/non-turbulent interface in a planar jet," *Journal of Fluid Mechanics*, vol. 758, pp. 754–785, 2014.

[152] I. Wygnanski and H. E. Fiedler, "The two-dimensional mixing region," *Journal of Fluid Mechanics*, vol. 41, no. 2, pp. 327–361, 1970.

[153] J. Jimenez, "Turbulent velocity fluctuations need not be gaussian," *Journal of Fluid Mechanics*, vol. 376, pp. 139–147, 1998.

[154] P. Vaishnavi, A. Kronenburg, and C. Pantano, "On the spatial length scales of scalar dissipation in turbulent jet flames," *Journal of Fluid Mechanics*, vol. 596, pp. 103–132, 2008.

[155] P. Vedula, P. Yeung, and R. Fox, "Dynamics of scalar dissipation in isotropic turbulence: a numerical and modelling study," *Journal of Fluid Mechanics*, vol. 503, pp. 377–377, 2004.

[156] Z. Warhaft, "Passive scalars in turbulent flows," *Annual Review of Fluid Mechanics*, vol. 32, no. 1, pp. 203–240, 2000.

[157] A. N. Kolmogorov, "A refinement of previous hypotheses concerning the local structure of turbulence in a viscous incompressible fluid at high Reynolds number," *Journal of Fluid Mechanics*, vol. 13, no. 1, pp. 82–85, 1962.

[158] A. Townsend, "On the fine-scale structure of turbulence," *Proc. R. Soc. Lond. A*, vol. 208, no. 1095, pp. 534–542, 1951.

[159] P. Tabeling and H. Willaime, "Transition at dissipative scales in large-Reynolds-number turbulence," *Physical Review E*, vol. 65, no. 6, p. 066301, 2002.

[160] A. Gylfason, S. Ayyalasomayajula, and Z. Warhaft, "Intermittency, pressure and acceleration statistics from hot-wire measurements in wind-tunnel turbulence," *Journal of Fluid Mechanics*, vol. 501, pp. 213–229, 2004.

[161] T. Ishihara, Y. Kaneda, M. Yokokawa, K. Itakura, and A. Uno, "Small-scale statistics in high-resolution direct numerical simulation of turbulence: Reynolds number dependence of one-point velocity gradient statistics," *Journal of Fluid Mechanics*, vol. 592, pp. 335–366, 2007.

[162] A. Vreman and J. G. Kuerten, "Statistics of spatial derivatives of velocity and pressure in turbulent channel flow," *Physics of fluids*, vol. 26, no. 8, p. 085103, 2014.

[163] J. Schumacher, K. Sreenivasan, and P. Yeung, "Derivative moments in turbulent shear flows," *Physics of Fluids*, vol. 15, no. 1, pp. 84–90, 2003.

[164] J. Jimenez and A. A. Wray, "On the characteristics of vortex filaments in isotropic turbulence," *Journal of Fluid Mechanics*, vol. 373, pp. 255–285, 1998.

[165] L. Djenidi, L. Danaila, R. Antonia, and S. Tang, "A note on the velocity derivative flatness factor in decaying HIT," *Physics of Fluids*, vol. 29, no. 5, p. 051702, 2017.

[166] L. Djenidi, R. A. Antonia, M. K. Talluru, and H. Abe, "Skewness and flatness factors of the longitudinal velocity derivative in wall-bounded flows," *Physical Review Fluids*, vol. 2, no. 6, p. 064608, 2017.

[167] S. Corrsin, "On the spectrum of isotropic temperature fluctuations in an isotropic turbulence," *Journal of Applied Physics*, vol. 22, no. 4, pp. 469–473, 1951.

[168] G. K. Batchelor, "Small-scale variation of convected quantities like temperature in turbulent fluid part 1. general discussion and the case of small conductivity," *Journal of Fluid Mechanics*, vol. 5, no. 1, pp. 113–133, 1959.

[169] R. H. Kraichnan, "Small-scale structure of a scalar field convected by turbulence," *The Physics of Fluids*, vol. 11, no. 5, pp. 945–953, 1968.

[170] C. Gibson and W. Schwarz, "The universal equilibrium spectra of turbulent velocity and scalar fields," *Journal of Fluid Mechanics*, vol. 16, no. 3, pp. 365–384, 1963.

[171] K. R. Sreenivasan, "The passive scalar spectrum and the Obukhov–Corrsin constant," *Physics of Fluids*, vol. 8, no. 1, pp. 189–196, 1996.

[172] P. A. Davidson, Y. Kaneda, and K. R. Sreenivasan, *Ten chapters in turbulence*. Cambridge University Press, 2012.

[173] D. A. Donzis, K. Sreenivasan, and P. Yeung, "The Batchelor spectrum for mixing of passive scalars in isotropic turbulence," *Flow, turbulence and combustion*, vol. 85, no. 3-4, pp. 549–566, 2010.

[174] A. Attili and F. Bisetti, "Fluctuations of a passive scalar in a turbulent mixing layer," *Phys. Rev. E*, vol. 88, p. 033013, Sep 2013.

[175] D. Donzis and K. Sreenivasan, "The bottleneck effect and the Kolmogorov constant in isotropic turbulence," *Journal of Fluid Mechanics*, vol. 657, pp. 171–188, 2010.

[176] Y. Tsuji, "High-Reynolds-number experiments: the challenge of understanding universality in turbulence," *Fluid dynamics research*, vol. 41, no. 6, p. 064003, 2009.

[177] A. Praskovsky and S. Oncley, "Measurements of the Kolmogorov constant and intermittency exponent at very high Reynolds numbers," *Physics of Fluids*, vol. 6, no. 9, pp. 2886–2888, 1994.

[178] B. Petersen and J. Ghandhi, "High-resolution turbulent scalar field measurements in an optically accessible internal combustion engine," *Experiments in fluids*, vol. 51, no. 6, pp. 1695–1708, 2011.

[179] F. Fuest, R. S. Barlow, G. Magnotti, and J. A. Sutton, "Scalar dissipation rates in a turbulent partially-premixed dimethyl ether/air jet flame," *Combustion and Flame*, vol. 188, pp. 41–65, 2018.

[180] G. Wang and R. S. Barlow, "Spatial resolution effects on the measurement of scalar variance and scalar gradient in turbulent nonpremixed jet flames," *Experiments in Fluids*, vol. 44, no. 4, pp. 633–645, 2008.

[181] R. H. Kraichnan, "The structure of isotropic turbulence at very high Reynolds numbers," *Journal of Fluid Mechanics*, vol. 5, no. 4, pp. 497–543, 1959.

[182] K. Sreenivasan, "On the fine-scale intermittency of turbulence," *Journal of Fluid Mechanics*, vol. 151, pp. 81–103, 1985.

[183] B. Ganapathisubramani, K. Lakshminarasimhan, and N. Clemens, "Investigation of three-dimensional structure of fine scales in a turbulent jet by using cinematographic stereoscopic particle image velocimetry," *Journal of fluid mechanics*, vol. 598, pp. 141–175, 2008.

[184] J. Meyers and C. Meneveau, "A functional form for the energy spectrum parametrizing bottleneck and intermittency effects," *Physics of Fluids*, vol. 20, no. 6, p. 065109, 2008.

[185] A. Potturi and J. R. Edwards, "Investigation of subgrid closure models for finite-rate scramjet combustion," in *43rd AIAA Fluid Dynamics Conference*, p. 2461, 2013.

[186] R. Knikker, D. Veynante, and C. Meneveau, "A priori testing of a similarity model for large eddy simulations of turbulent premixed combustion," *Proceedings of the combustion institute*, vol. 29, no. 2, pp. 2105–2111, 2002.

[187] R. Knikker, D. Veynante, and C. Meneveau, "A dynamic flame surface density model for large eddy simulation of turbulent premixed combustion," *Physics of Fluids*, vol. 16, no. 11, pp. L91–L94, 2004.

[188] M. Gauding, F. Dietzsch, J. H. Goebbert, D. Thévenin, A. Abdelsamie, and C. Hasse, "Dissipation element analysis of a turbulent non-premixed jet flame," *Physics of Fluids*, vol. 29, no. 8, p. 085103, 2017.

[189] C. Pantano, "Direct simulation of non-premixed flame extinction in a methane–air jet with reduced chemistry," *Journal of Fluid Mechanics*, vol. 514, pp. 231–270, 2004.

[190] L. Berger, K. Kleinheinz, A. Attili, F. Bisetti, H. Pitsch, and M. E. Mueller, "Numerically accurate computational techniques for optimal estimator analyses of multi-parameter models," *Combustion Theory and Modelling*, vol. 22, no. 3, pp. 480–504, 2018.

[191] P. E. Hamlington, A. Y. Poludnenko, and E. S. Oran, "Intermittency in premixed turbulent reacting flows," *Physics of Fluids*, vol. 24, no. 7, p. 075111, 2012.

[192] D. Livescu, F. Jaberi, and C. Madnia, "The effects of heat release on the energy exchange in reacting turbulent shear flow," *Journal of Fluid Mechanics*, vol. 450, pp. 35–66, 2002.

[193] J. Schumacher and B. Eckhardt, "On statistically stationary homogeneous shear turbulence," *EPL (Europhysics Letters)*, vol. 52, no. 6, p. 627, 2000.

[194] P. Gualtieri, C. Casciola, R. Benzi, G. Amati, and R. Piva, "Scaling laws and intermittency in homogeneous shear flow," *Physics of Fluids*, vol. 14, no. 2, pp. 583–596, 2002.

[195] S. Cerutti and C. Meneveau, "Intermittency and relative scaling of subgrid-scale energy dissipation in isotropic turbulence," *Physics of Fluids*, vol. 10, no. 4, pp. 928–937, 1998.

[196] E. Giacomazzi, C. Bruno, and B. Favini, "Fractal modelling of turbulent combustion," *Combustion Theory and Modelling*, vol. 4, no. 4, pp. 391–412, 2000.

[197] E. Giacomazzi, V. Battaglia, and C. Bruno, "The coupling of turbulence and chemistry in a premixed bluff-body flame as studied by LES," *Combustion and Flame*, vol. 138, no. 4, pp. 320–335, 2004.

[198] B. B. Dally, A. Karpetis, and R. Barlow, "Structure of turbulent non-premixed jet flames in a diluted hot coflow," *Proceedings of the combustion institute*, vol. 29, no. 1, pp. 1147–1154, 2002.

[199] Z. Li, A. Cuoci, and A. Parente, "Large Eddy Simulation of MILD combustion using finite rate chemistry: Effect of combustion sub-grid closure," *Proceedings of the Combustion Institute*, 2018.

# Glossary

$CD_1$ The first proportionality constant in the EDC model. 43

$CD_2$ The first proportionality constant in the EDC model. 43

$c_\eta$ The coefficient of the model spectrum function. 25

$C_K$ Kolmogorov's constant. 24

$c_L$ The coefficient of the model spectrum function. 25

**CFD** Computational Fluid Dynamics. 1

**CDF** Cumulative Distribution Function. 10

**DNS** Direct Numerical Simulation. VII

**DFT** The Discrete Fourier Transgerform. 26

$D(\kappa)$ Turbulent kinetic energy dissipation spectrum. 25

$D_{Normal}$ The 3D normalized turbulent kinetic energy dissipation spectrum. 26

$E_{Compensated}$ Compensated turbulent kinetic energy spectrum function. 24

**EDC** Eddy Dissipation Concept. 2

$E_{f,j}$ forward activation energy of reactions $j$. 29

$E(\kappa)$ Turbulent kinetic energy spectrum function. 23

$E^{3D}(\kappa)$ 3D turbulent kinetic energy spectrum function. 23

$E_{11}^{1D}(\kappa)$ 1D velocity spectrum in longitudinal direction. 24

$E_{ii}^{1D}(\kappa_x)$ 1D velocity spectrum in $i^th$ direction as a function of the longitudinal wavenumber. 27

$E_{22}^{1D}(\kappa)$ 1D velocity spectrum in transversal direction. 24

$E$ Total energy. 28

$E_{Normal}$ Normalized turbulent kinetic energy spectrum function. 24

**FR** finite-rate. 1

$f_L$ The integral range multiplier for Pope's model spectrum function. 25

$\mathcal{F}$ Flatness. 13

$h_k$ Sensible enthalpy of species $k$. 28

**HIT** Homogeneous Isotropic Turbulence. 3

$\mathcal{I}_{LES}$ The prefactor of the EDC model related to the internal intermittency factor in LES. 41

$\mathcal{I}_{RANS}$ The prefactor of the EDC model related to the internal intermittency factor in RANS. 40

$\mathcal{I}$ The prefactor of the EDC model related to the internal intermittency factor. 41

**JPDF** Joint Probability Density Function. 14

$k_{f,j}$ Forward rate of reactions $j$. 29

$k_n$ The kinetic energy of the turbulent flow in the cascade model at $n^{th}$ level. 41

$k_r$ Large scale (resolved) kinetic energy. 37

$k_{r,j}$ Backward rate of reactions $j$. 29

$k_{SGS}$ Sub-grid kinetic energy. 37

**LES** Large Eddy Simulation. VII

$l_{int}$ Integral length scale. 21

$L_n$ The length scale of the turbulent flow in the cascade model at $n^{th}$ level. 41

$L_x$ The length of the computational domain in x (streamwise) direction. 26

$L_y$ The length of the computational domain in y (crosswise) direction. 26

$L_z$ The length of the computational domain in z (span-wise) direction. 26

**Ma** Mach number. 32

**NS** Navier Stokes. 9

$N_r$ Number of reactions in the chemical mechanism. 29

$N_s$ Number of species in the chemical mechanism. 28

$N_x$ The number of the computational cells in x (streamwise) direction. 12

$N_y$ The number of the computational cells in y (crosswise) direction. 12

$N_z$ The number of the computational cells in z (span-wise) direction. 12

$P_0$ The coefficient of the model spectrum function. 25

**PDF** Probability Density Function. 10

$\Pi$ Pressure-dilatation term in exact large-scale kinetic energy transport equation. 37

$P$ Mean production of turbulent kinetic energy. 33

$Pr_t$ Tutbulent Prandtl number. 32

$p$ Pressure. 28

$P_{ij}$ Mean production of Reynolds stresses. 33

$P_{SGS}$ grid-scale to sub-grid scale energy transfer. 37

$\dot{Q}$ Net heat release rate. 29

$q_i$ Heat flux. 28

$q_n$ The part of the kinetic energy which is dissipated to heat in the cascade model at $n^{th}$ level. 42

**R** Universal gas constant. 30

**RMS** Root Mean Square. 13

$Re_{int}$ Integral Reynolds number. 22

$Re_\lambda$ Taylor scale Reynolds number. 3

**Re** Reynolds number. 9

**RANS** Reynolds Average Navier-Stokes Simulation. VII

$R_{ij}$ Two point correlation function. 15

$\dot{r}_j$ Net reaction rate of reactions $j$. 29

**RSM** Reynolds Stress equation Model. 32

**SS** Scale Similarity. 2
Sc Schmidt number. 107
$Sc_{kt}$ Turbulent Schmidt number. 32
$S_{ij}$ Strain rate tensor. 28
$\mathcal{S}$ Skewness. 13
**SGS** Sub Grid Scale. 2

**TCI** Turbulence-Chemistry Interaction. 1
$t_\eta$ Local Kolmogorov's time scale. 23
$T_{ij}$ Transport of mean Reynolds stress. 33
$t_{int}$ Integral time scale. 22
**TKE** Turbulent Kinetic Energy. 3
**T-NT** Turbulent-Non Turbulent. 170

$u_\eta$ Instantaneous or local Kolmogorov's velocity scale. 23
$u_i$ Velocity components. 28
$u_{int}$ Integral velocity scale. 21
$u_n$ The velocity scale of the turbulent flow in the cascade model at $n^{th}$ level. 41
**URANS** Unsteady Reynolds Average Navier-Stokes Simulation. VII

$V_{i,k}$ Diffusion velocity of species $k$ in direction $i$. 28

$W_k$ Molecular weight of species $k$. 29
$w_n$ The vorticity scale of the turbulent flow in the cascade model at $n^{th}$ level. 41
$W^n$ The rate of the mechanical energy transferred to the $n^{th}$ level in the cascade model. 42

$Y_k$ The mass fraction of species $k$. 28

$\alpha$ Redistribution term in exact large-scale kinetic energy transport equation. 37
$\alpha_{SGS}$ Sub-grid redistribution. 38
$\beta_P$ The exponential drop-off factor for Pope's model spectrum function. 25
$\Delta\hat{S}^0_j$ Enthalpy change in reactions $j$ in conversion from reactants to products. 29
$\Delta\hat{H}^0_j$ Entropy change in reactions $j$ in conversion from reactants to products. 29
$\Delta H^0_{f,k}$ Enthalpy of formation of species $k$. 30
$\Delta_i$ The grid spacing in $i^{th}$ direction. 26
$\delta_{ij}$ Kronecker delta. 28
$\delta_L$ Laminar flame thickness. 108
$\Delta_v$ Flow dilatation. 28
$\varepsilon$ Turbulent kinetic energy dissipation rate. 22
$\varepsilon_{ij}$ Mean dissipation of Reynolds stresses. 33
$\varepsilon$ Mean dissipation of turbulent kinetic energy. 33
$\varepsilon_\nu$ Viscous dissipation term in exact large-scale kinetic energy transport equation. 37
$\varepsilon_{\nu,SGS}$ Sub-grid viscous dissipation. 38
$\varepsilon^s$ Pseudo dissipation. 22
$\eta$ Instantaneous or local Kolmogorov's length scale. 23

## Glossary

$\Gamma_{k,mix}$ Mass diffusion coefficient of species $k$ into the mixture. 29

$\gamma_{ext}$ External intermittency factor. 84

$\gamma_{int}$ Internal intermittency factor. 13

$\kappa_n$ The wavenumber associated to the scales of the turbulent flow in the cascade model at $n^{th}$ level. 41

$\boldsymbol{\kappa}$ Wave number vector. 23

$\kappa$ Wave number magnitude. 23

$\kappa_x$ The streamwise component of the wavenumber vector. 24

$\kappa_y$ The crosswise component of the wavenumber vector. 26

$\kappa_z$ The span-wise component of the wavenumber vector. 26

$\lambda$ Thermal conductivity. 28

$\lambda_\beta$ cut-off length scale. 107

$\lambda$ Taylor length scale. 22

$\mu$ Viscosity. 21

$\nu'_{k,j}$ Molar stoichiometric coefficients of species $k$ in forward reaction $j$. 29

$\nu''_{k,j}$ Molar stoichiometric coefficients of species $k$ in backward reaction $j$. 29

$\nu_{SGS}$ Subgrid Viscosity. 37

$\nu_t$ Turbulent viscosity. 32

$\boldsymbol{\varphi}$ The composition vector. 39

$\Phi_{ij}$ Velocity spectrum tensor. 23

$\Pi_{ij}$ Mean pressure-strain term in transport equation for the Reynolds stress tensor. 33

$\rho$ Density. 28

$\rho_{q_1 q_2}$ Correlation coefficient. 15

$\sigma$ Standard deviation. 13

$\tau_{ij}$ Viscous stress tensor. 28

$\tau_{ij}^R$ Residual Stress Tensor. 36

$\dot{\omega}_k$ Net formation rate of species $k$. 28

$\chi$ scalar dissipation rate. 40

$\Pi_{SGS}$ Sub-grid pressure-dilatation. 38

$\Phi_k$ Symbol for species $k$ in the chemical kinetics mechanism. 29

$\zeta$ The proportionality constant in the EDC model by Magnussen. 44

## Mathematical operators

| | |
|---|---|
| $\langle q \rangle$ | Probability mean of quantity $q$. Eq. 2.14 has been used unless otherwise mentioned. |
| $\underline{q}$ | Average of $q$. Eq. 2.14 has been used unless otherwise mentioned. |
| $q'$ | Fluctuation of $q$. $q' = q - \underline{q}$, unless otherwise mentioned. |
| $\underline{q}_f$ | Favre average of $q$. Eq. 2.35 has been used unless otherwise mentioned. |
| $q''$ | Favre Fluctuation of $q$. Eq. 2.36 has been used unless otherwise mentioned. |
| $\underline{q}_t$ | average of $q$ only in turbulent regions (turbulent average). |
| $\underline{q}_{f,t}$ | Favre average of $q$ only in turbulent regions (Favre turbulent average). |
| $q'_t$ | Fluctuation of $q$ based on turbulent average. $q'_t = q - \underline{q}_t$, unless otherwise mentioned. |
| $q''_t$ | Favre fluctuation of $q$ based on Favre turbulent average. $q''_t = q - \underline{q}_{f,t}$, unless otherwise mentioned. |
| $\overline{q}$ | Filtered $q$. The equation in Tab. 4.1 has been used unless otherwise mentioned. |
| $\overline{q}^f$ | Favre filtered $q$. $\overline{q}^f = \frac{\overline{\rho q}}{\overline{\rho}}$. |
| $\overline{\overline{q}}$ | Grid filtering operator. The equation in Tab. 4.1 has been used unless otherwise mentioned. |
| $\widehat{q}$ | Test filtering operator with filter size of 2 times the grid size.<br>The equation in Tab. 4.1 has been used unless otherwise mentioned. |
| $\widehat{\widehat{q}}$ | Second test filtering operator with filter size of 4 times the grid size.<br>The equation in Tab. 4.1 has been used unless otherwise mentioned. |

# Appendices

APPENDIX $\mathcal{A}$

# Extra Results for Spectral Analysis

In this appendix the supplementary plots are presented for the spectral analysis of cases L and M (see Sec. 4.5).

## Appendix A. Extra Results for Spectral Analysis

**Table A.1:** *DNS parameters of the cases on selected planes of DNS case M for which spectra are studied*

.

| Time | Plane | $\underline{\eta}_f \times 10^5[m]$(Eq.2.63) | $\underline{\lambda}_f \times 10^4[m]$ (Eq.2.62) | $Re_\lambda$ (Eq.2.61) | $u_{int}[m/s]$ (Eq.2.51) | $Re_t$ (Eq.2.57) | $\underline{Z}_f$ (Eq.2.35) |
|---|---|---|---|---|---|---|---|
| $20t_j$ | $P_0$ | 1.7483 | 2.135 | 38.530 | 20.810 | 98.975 | 0.821 |
| | $P_1$ | 1.5672 | 1.948 | 39.929 | 13.180 | 106.291 | 0.1154 |
| | $P_2$ | 1.7022 | 2.297 | 47.032 | 18.197 | 147.468 | 0.2175 |
| | $P_3$ | 1.8233 | 2.634 | 53.909 | 26.437 | 193.745 | 0.4695 |
| | $P_4$ | 1.691 | 2.514 | 57.082 | 29.652 | 217.229 | 0.5602 |
| | $P_5$ | 1.783 | 2.577 | 53.897 | 27.628 | 193.664 | 0.7028 |
| | $P_6$ | 1.810 | 2.591 | 52.874 | 25.4836 | 186.382 | 0.4225 |
| | $P_7$ | 1.846 | 1.822 | 25.162 | 5.805 | 42.210 | 0.0194 |
| $30t_j$ | $P_0$ | 2.584 | 2.952 | 33.692 | 17.929 | 75.680 | 0.7217 |
| | $P_1$ | 1.848 | 2.4293 | 44.614 | 11.950 | 132.697 | 0.1009 |
| | $P_2$ | 1.936 | 2.8544 | 56.122 | 18.477 | 209.985 | 0.2110 |
| | $P_3$ | 2.213 | 3.199 | 53.956 | 24.520 | 194.087 | 0.5101 |
| | $P_4$ | 2.0336 | 3.081 | 59.274 | 25.161 | 234.231 | 0.4031 |
| | $P_5$ | 2.401 | 2.970 | 39.497 | 21.014 | 104.001 | 0.6259 |
| | $P_6$ | 2.051 | 3.064 | 57.629 | 25.058 | 221.408 | 0.4202 |
| | $P_7$ | 2.068 | 2.198 | 29.166 | 5.913 | 56.711 | 0.0245 |

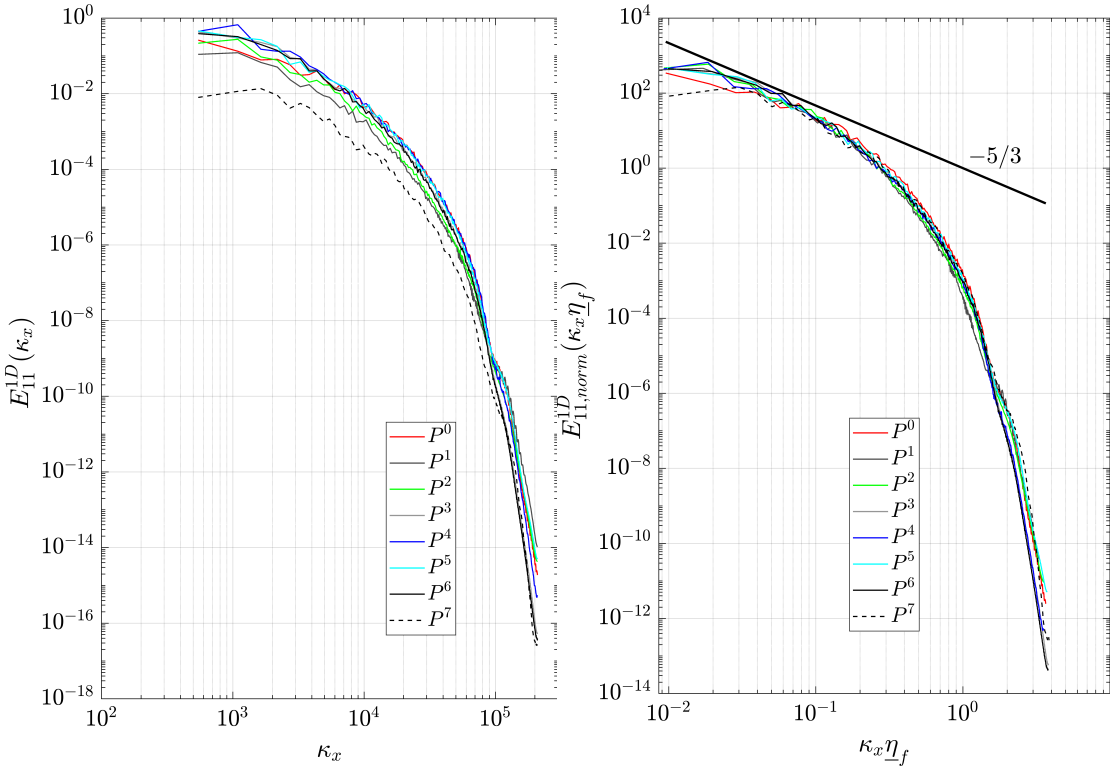


**(a)** **(b)**

**Figure A.1:** *The 1D longitudinal spectra on different planes across the reacting shear layer at maximum extinction time, t=20$t_j$ extracted from M case DNS, (**a**) Non-normalized; (**b**) Normalized using Favre averaged $\eta$ and $\varepsilon$.*

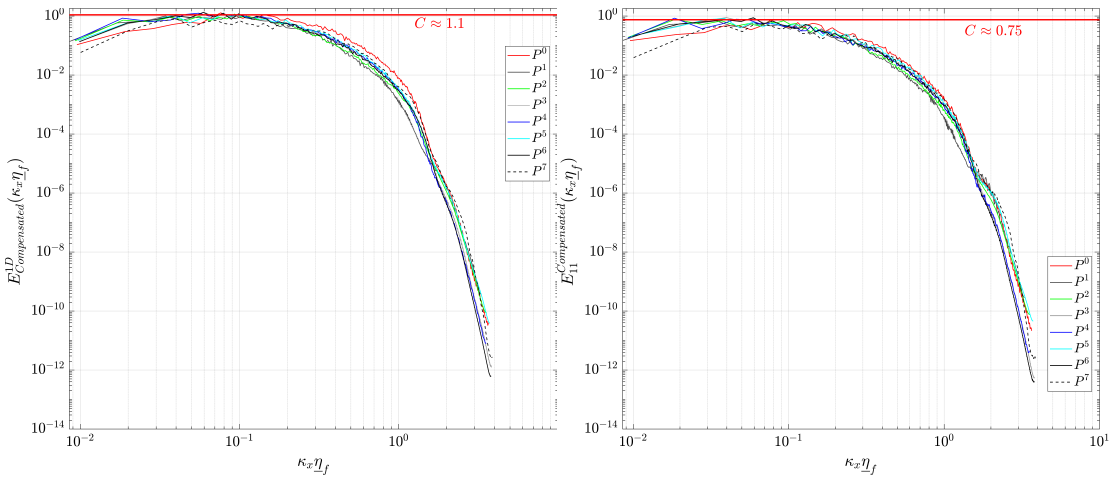


**(a)** **(b)**

**Figure A.2:** *1D compensated spectra on different planes across the reacting shear layer at maximum extinction time, t=20$t_j$ extracted from M case DNS, (**a**) 1D compensated energy spectra; (**b**) 1D compensated longitudinal spectra. The horizontal lines show the constant in Kolmogorov's spectrum.*

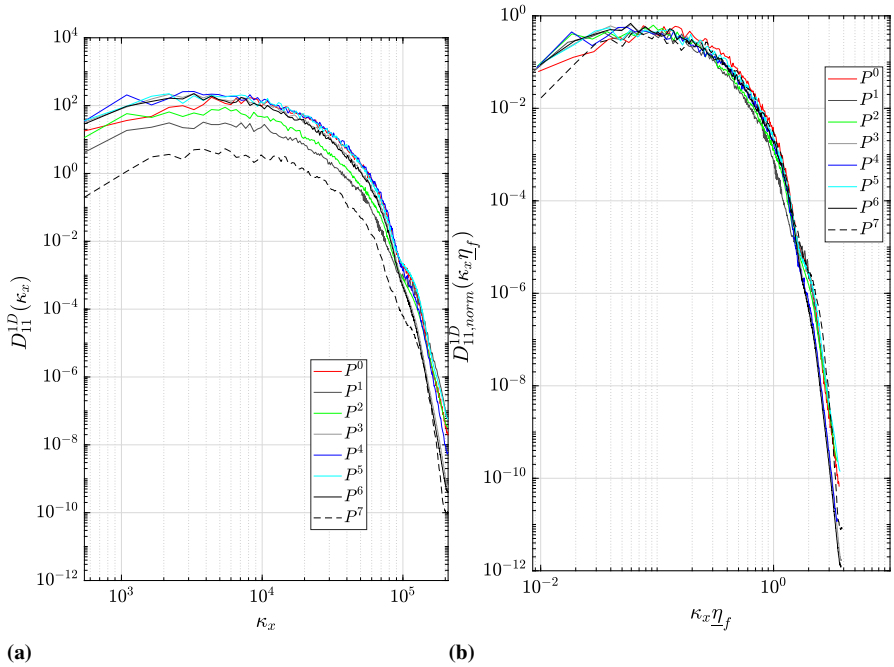


**Figure A.3:** *1D longitudinal dissipation spectra across the reacting shear layer at maximum extinction time, t=20$t_j$ extracted from M case DNS, (**a**) Non-normalized; (**b**) Normalized using Favre averaged $\eta$ and $\varepsilon$.*

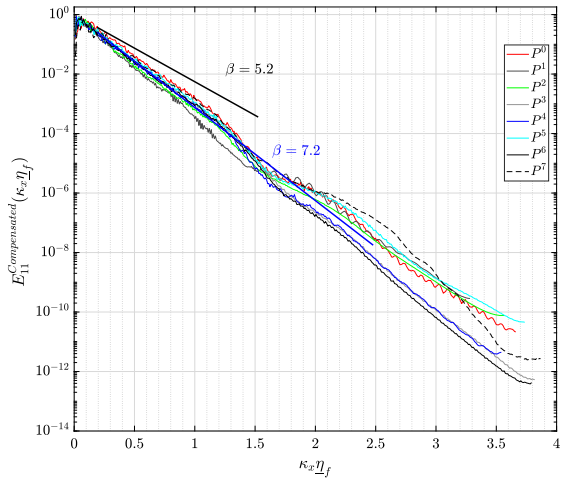


**Figure A.4:** *1D compensated longitudinal spectra on different planes across the reacting shear layer at maximum extinction time, t=20$t_j$ extracted from M case DNS with slopes of exponential drop-off.*

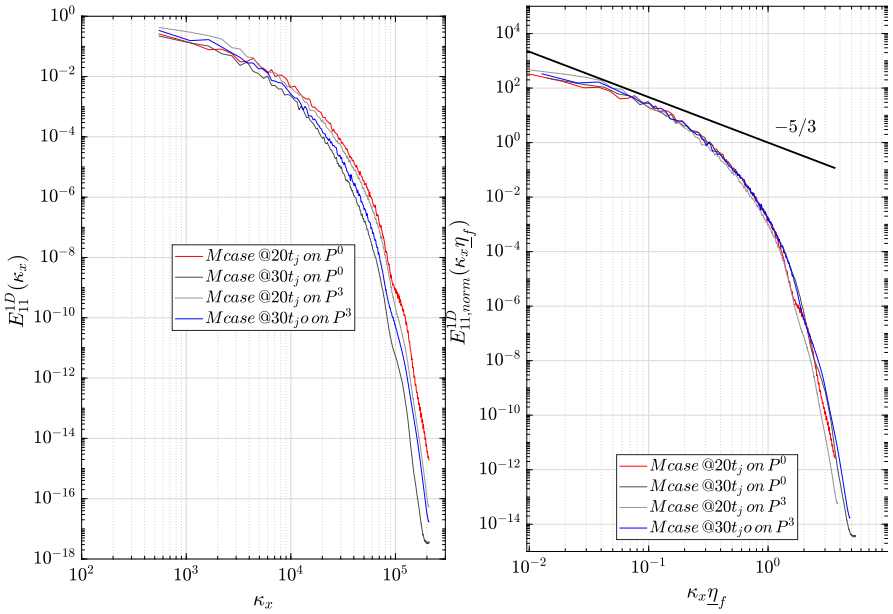


**Figure A.5:** *1D longitudinal velocity spectra across the reacting shear layer at maximum extinction, t=20$t_j$ and re-ignition time t=30$t_j$ extracted from M case DNS on the central plane, $P^0$ and the maximum of mean OH mass fraction plane, $P^3$ (**a**) Non-normalized; (**b**) Normalized using Favre averaged $\eta$ and $\varepsilon$.*

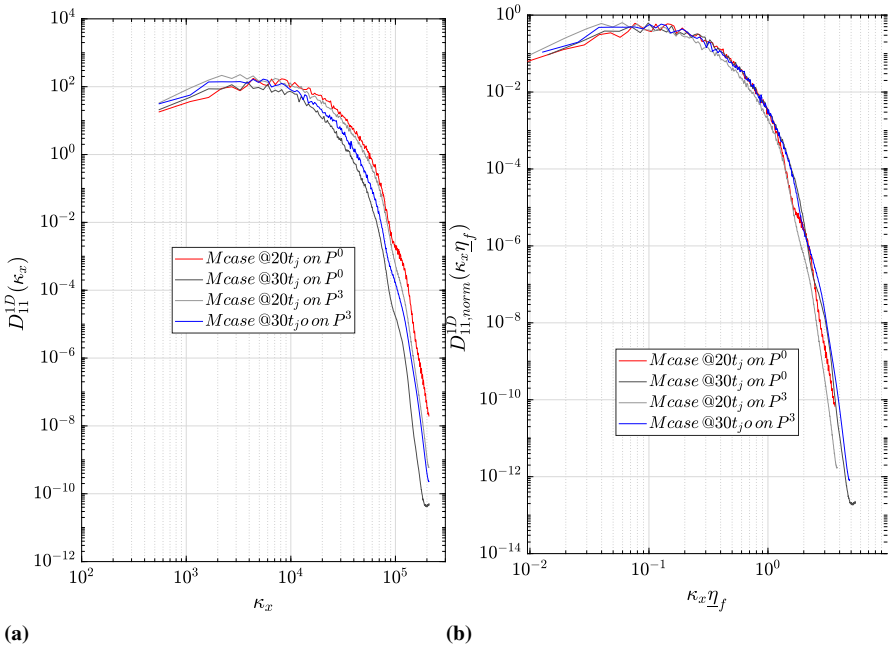


**Figure A.6:** *1D longitudinal dissipation spectra across the reacting shear layer at maximum extinction, t=20$t_j$ and re-ignition time t=30$t_j$ extracted from M case DNS on the central plane, $P^0$ and the maximum of mean OH mass fraction plane, $P^3$ (**a**) Non-normalized; (**b**) Normalized using Favre averaged $\eta$ and $\varepsilon$.*

**Table A.2:** *DNS parameters of the cases on selected planes of DNS case L for which spectra are studied*
.

| Time | Plane | $\underline{\eta}_f \times 10^5[m]$(Eq.2.63) | $\underline{\lambda}_f \times 10^4[m]$ (Eq.2.62) | $Re_\lambda$ (Eq.2.61) | $u_{int}[m/s]$ (Eq.2.51) | $Re_t$ (Eq.2.57) | $\underline{Z}_f$ (Eq.2.35) |
|---|---|---|---|---|---|---|---|
| $20t_j$ | $P_0$ | 2.158 | 2.333 | 30.180 | 15.985 | 60.723 | 0.8181 |
| | $P_1$ | 1.934 | 1.766 | 21.52 | 7.9446 | 30.888 | 0.0950 |
| | $P_2$ | 2.05 | 2.043 | 25.65 | 11.488 | 43.865 | 0.2026 |
| | $P_3$ | 2.289 | 2.635 | 34.223 | 19.388 | 78.08 | 0.5413 |
| | $P_4$ | 2.32 | 2.87 | 39.497 | 20.706 | 104.001 | 0.6778 |
| | $P_5$ | 2.203 | 2.562 | 34.927 | 19.977 | 81.32 | 0.6993 |
| | $P_6$ | 2.3220 | 2.741 | 36.003 | 17.702 | 86.414 | 0.4207 |
| | $P_7$ | 2.021 | 1.644 | 17.07 | 4.576 | 19.445 | 0.0231 |
| $30t_j$ | $P_0$ | 3.188 | 3.190 | 25.858 | 13.578 | 44.576 | 0.7299 |
| | $P_1$ | 2.241 | 2.577 | 34.13 | 8.930 | 77.67 | 0.1097 |
| | $P_2$ | 2.455 | 3.232 | 44.720 | 12.550 | 133.330 | 0.1902 |
| | $P_3$ | 3.009 | 3.761 | 40.325 | 18.411 | 108.410 | 0.5465 |
| | $P_4$ | 2.940 | 3.895 | 45.320 | 18.695 | 136.929 | 0.4794 |
| | $P_5$ | 3.141 | 3.246 | 27.575 | 14.701 | 50.693 | 0.701 |
| | $P_6$ | 2.899 | 3.97 | 48.545 | 18.218 | 157.113 | 0.421 |
| | $P_7$ | 2.409 | 2.126 | 20.124 | 4.1871 | 27.000 | 0.021 |

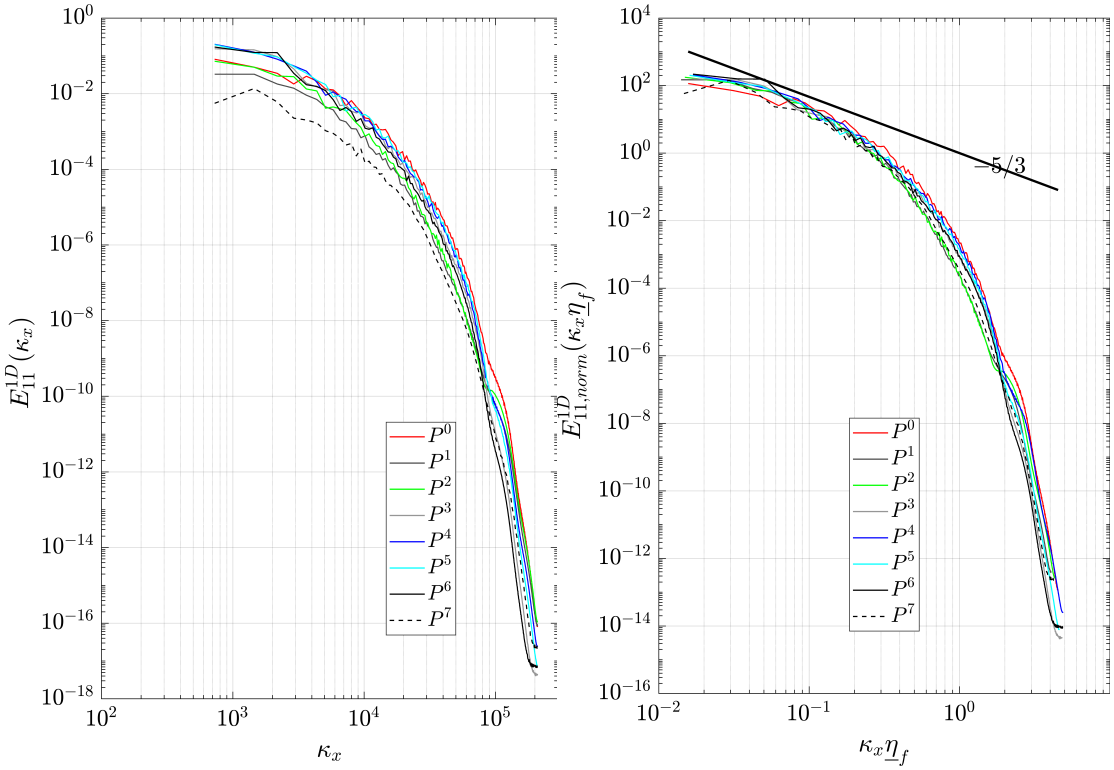


**(a)** **(b)**

**Figure A.7:** *The 1D longitudinal spectra on different planes across the reacting shear layer at maximum extinction time, t=20$t_j$ extracted from L case DNS, (**a**) Non-normalized; (**b**) Normalized using Favre averaged $\eta$ and $\varepsilon$.*

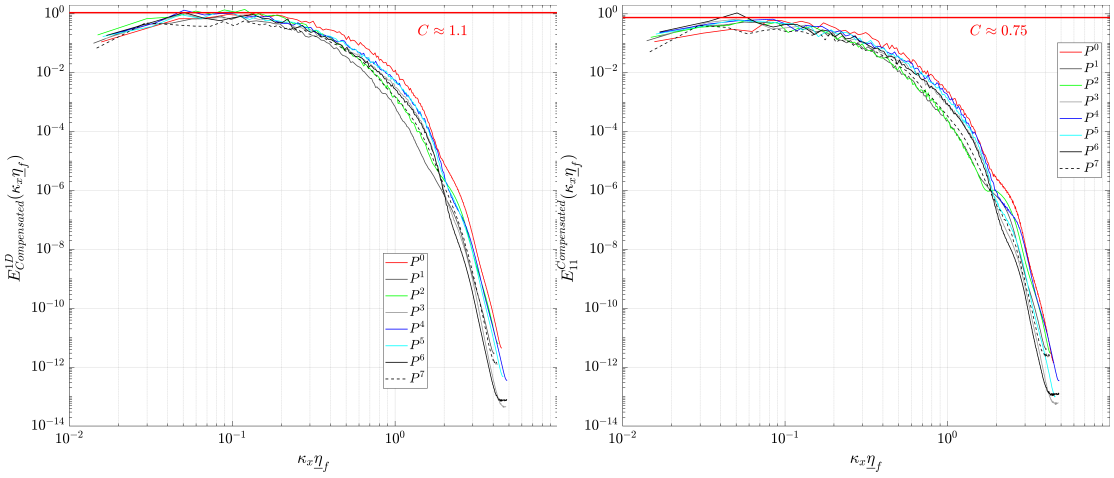


**(a)** **(b)**

**Figure A.8:** *1D compensated spectra on different planes across the reacting shear layer at maximum extinction time, t=20$t_j$ extracted from L case DNS, (**a**) 1D compensated energy spectra; (**b**) 1D compensated longitudinal spectra.*

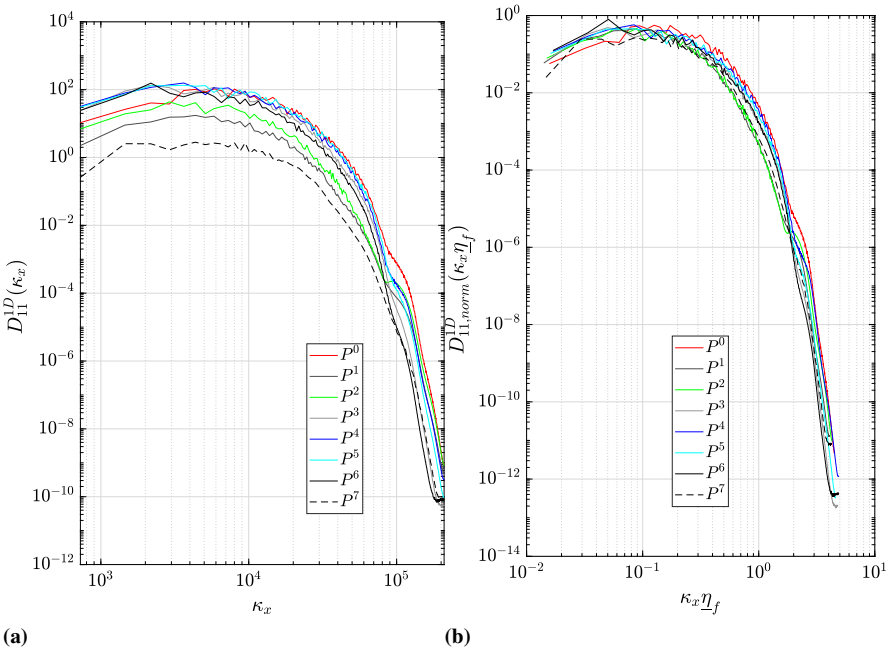


**Figure A.9:** *1D longitudinal dissipation spectra across the reacting shear layer at maximum extinction time, t=20$t_j$ extracted from L case DNS, (**a**) Non-normalized; (**b**) Normalized using Favre averaged $\eta$ and $\varepsilon$.*

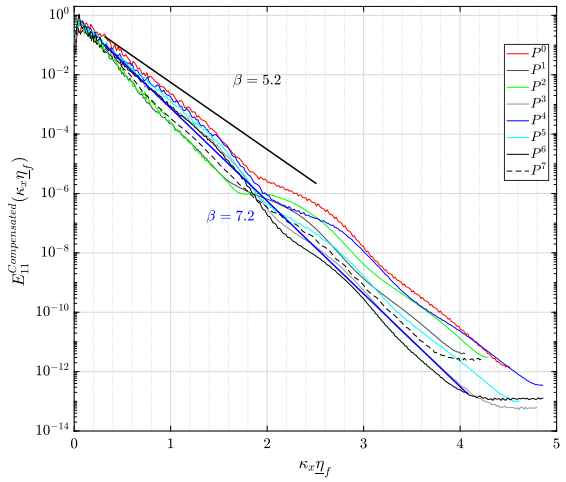


**Figure A.10:** *1D compensated longitudinal spectra on different planes across the reacting shear layer at maximum extinction time, t=20$t_j$ extracted from L case DNS with slopes of exponential drop-off.*

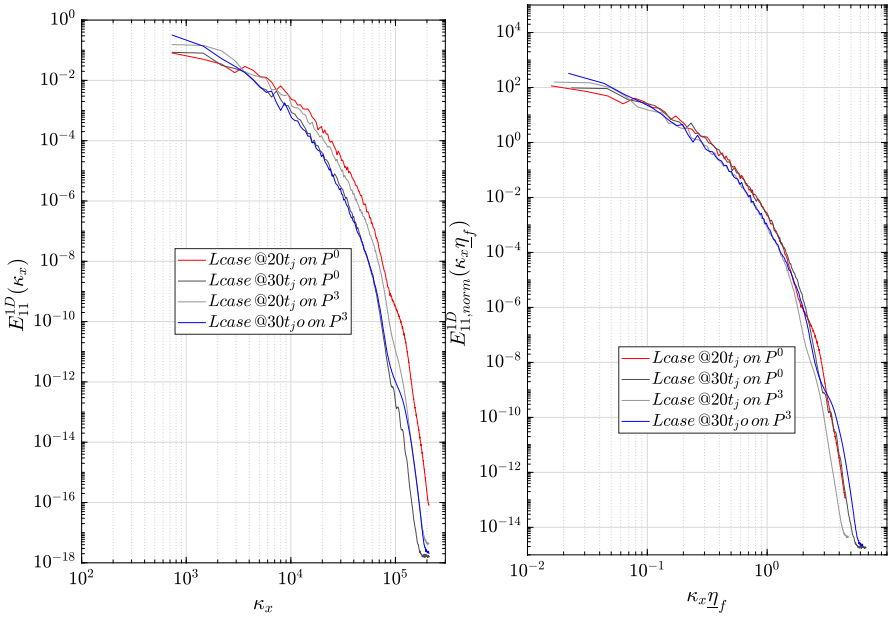


**(a)** **(b)**

**Figure A.11:** *1D longitudinal velocity spectra across the reacting shear layer at maximum extinction, t=20$t_j$ and re-ignition time t=30$t_j$ extracted from L case DNS on the central plane and the maximum of Favre mean OH mass fraction plane, (**a**) Non-normalized; (**a**) Non-normalized; (**b**) Normalized using Favre averaged $\eta$ and $\varepsilon$.*

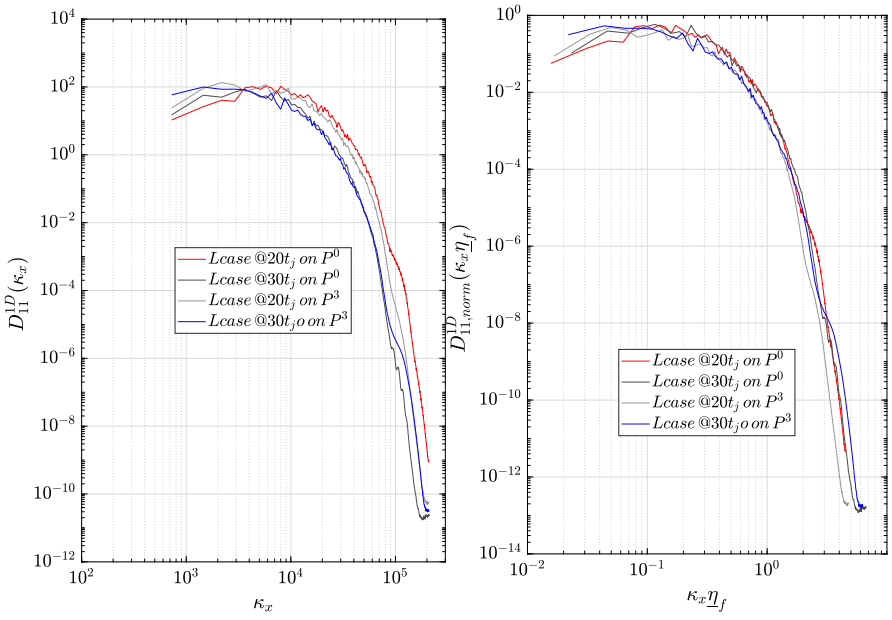


**(a)** **(b)**

**Figure A.12:** *1D longitudinal dissipation spectra across the reacting shear layer at maximum extinction, t=20$t_j$ and re-ignition time t=30$t_j$ extracted from L case DNS on the central plane and the maximum of Favre mean OH mass fraction plane, (**a**) Non-normalized; (**b**) Normalized using Favre averaged $\eta$ and $\varepsilon$.*

APPENDIX B

# Extra Results for Dynamic SS models

**The Comparison of the variants of dynamic models B and C**

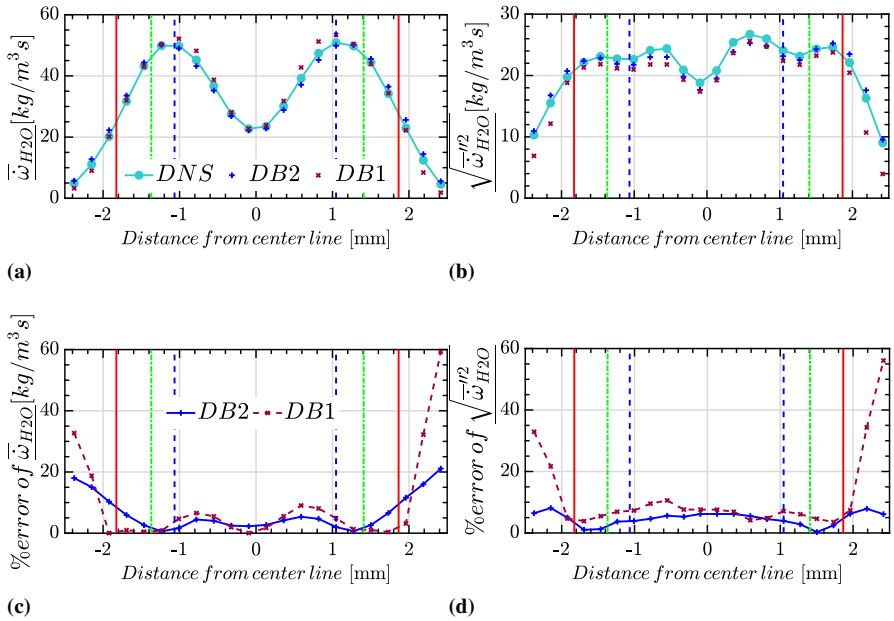


**Figure B.1:** *Case H, at t=20$t_j$ using $\Delta/\Delta_{\mathrm{DNS}} = 12$: comparison of dynamic models DB1 and DB2 performance with exact filtered $\dot{\omega}_{\mathrm{H_2O}}$ extracted from DNS database. (**a**) mean, (**b**) RMS, (**c**) relative error of mean profiles and (**d**) relative error of RMS profiles*

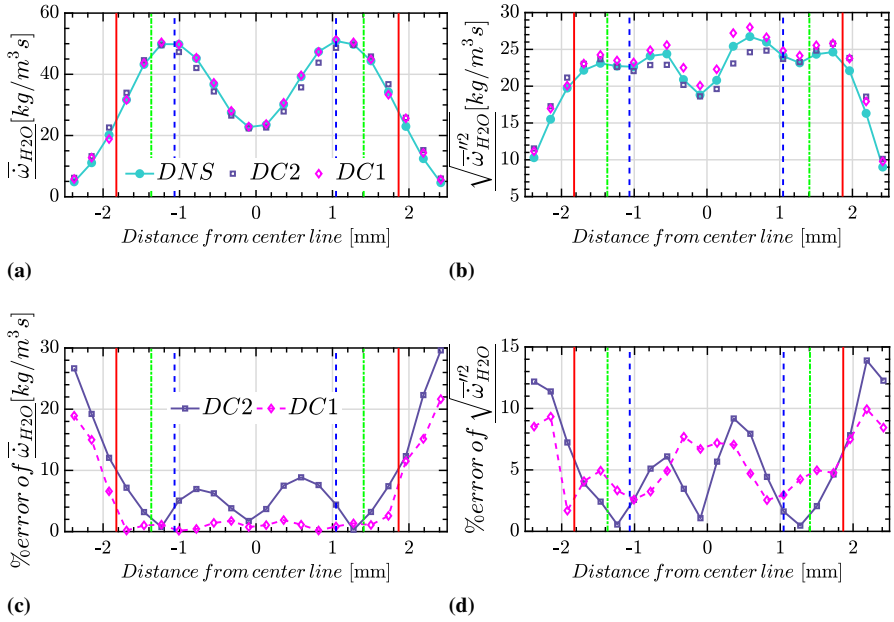


**Figure B.2:** *The same as in Fig. B.1 but for dynamic models DC1 and DC2*

## Scatter plots

## Appendix B. Extra Results for Dynamic SS models

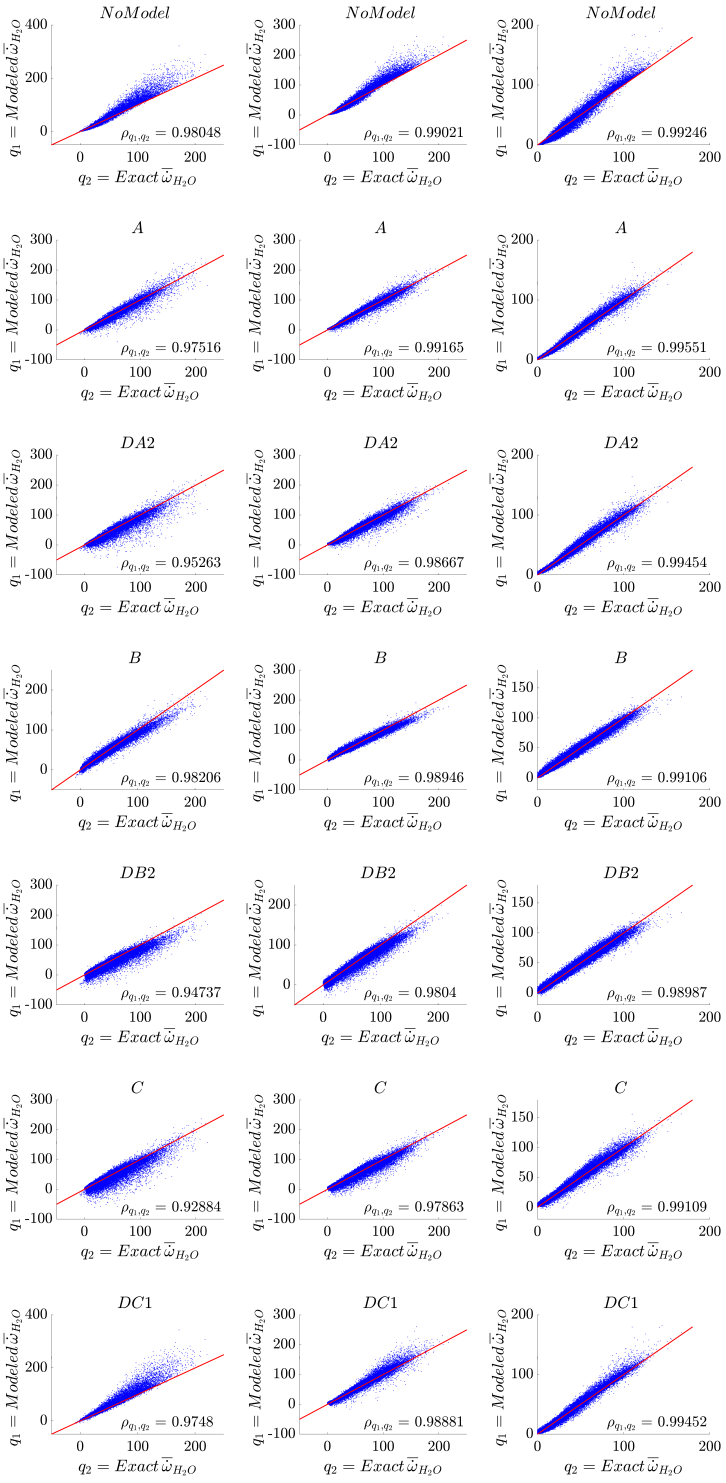


**Figure B.5:** *Scatter plots of the modeled versus the exact filtered source terms of* $H_2O$ *using different SS models. Extracted from the DNS databases L (left), M (middle) and H (right) at t=20*$t_j$ *using* $\overline{\Delta}/\Delta_{\mathrm{DNS}} = 12$.

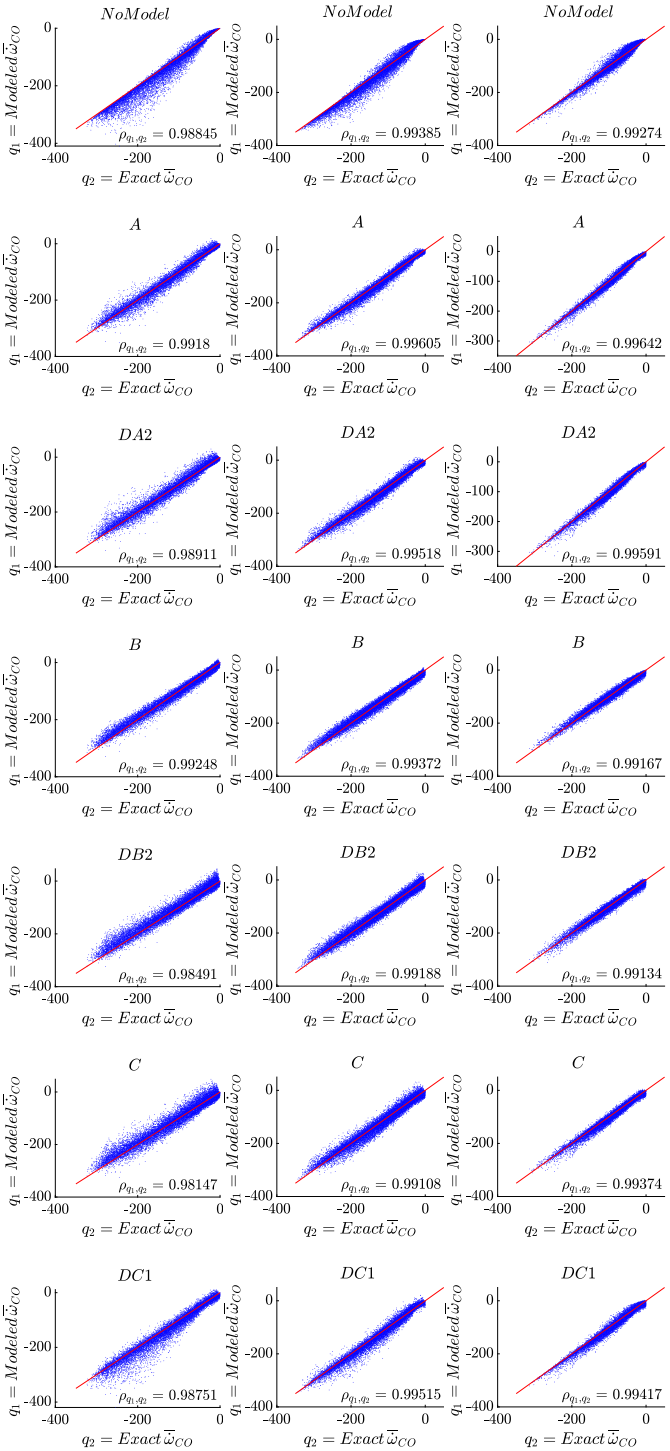


**Figure B.3:** *Scatter plots of modeled versus exact filtered source terms of* CO. *Extracted from DNS databases L (left), M (middle) and H (right) at t=20$t_j$ using $\overline{\Delta}/\Delta_{\mathrm{DNS}}$=12*

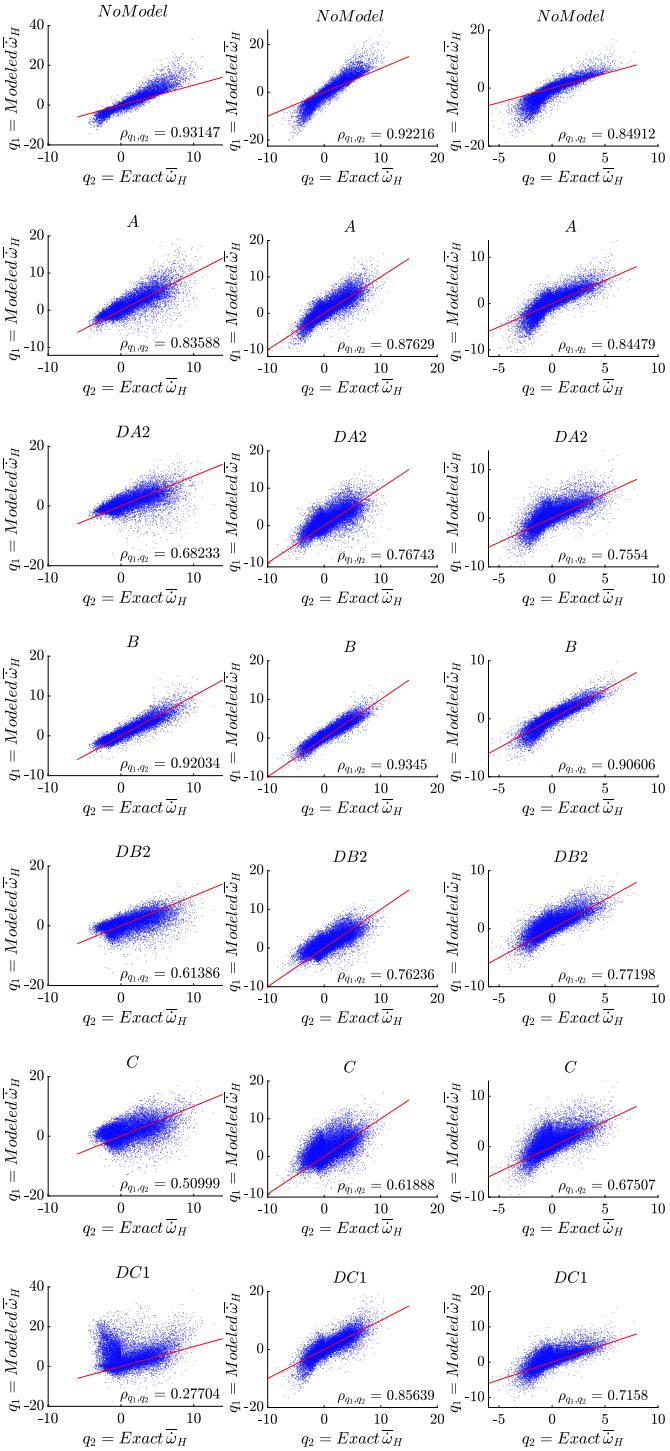


**Figure B.4:** *Scatter plots of modeled versus exact filtered source terms of* H. *Extracted from DNS databases L (left), M (middle) and H (right) at t=20$t_j$ using $\overline{\Delta}/\Delta_{\mathrm{DNS}}$=12*

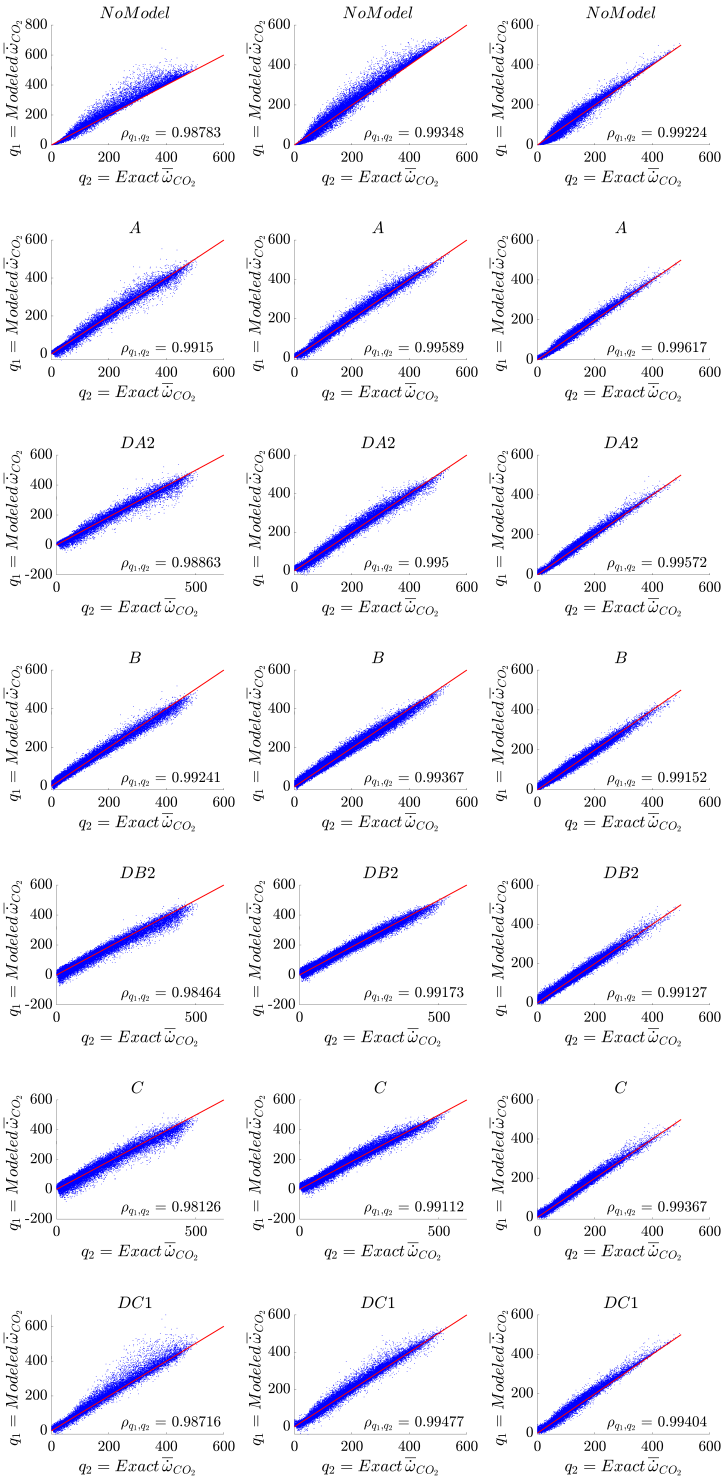


**Figure B.6:** *Scatter plots of the modeled versus the exact filtered source terms of* $CO_2$ *using different SS models. Extracted from the DNS databases L (left), M (middle) and H (right) at t=20*$t_j$ *using* $\overline{\Delta}/\Delta_{\mathrm{DNS}} = 12$.

## Appendix B. Extra Results for Dynamic SS models

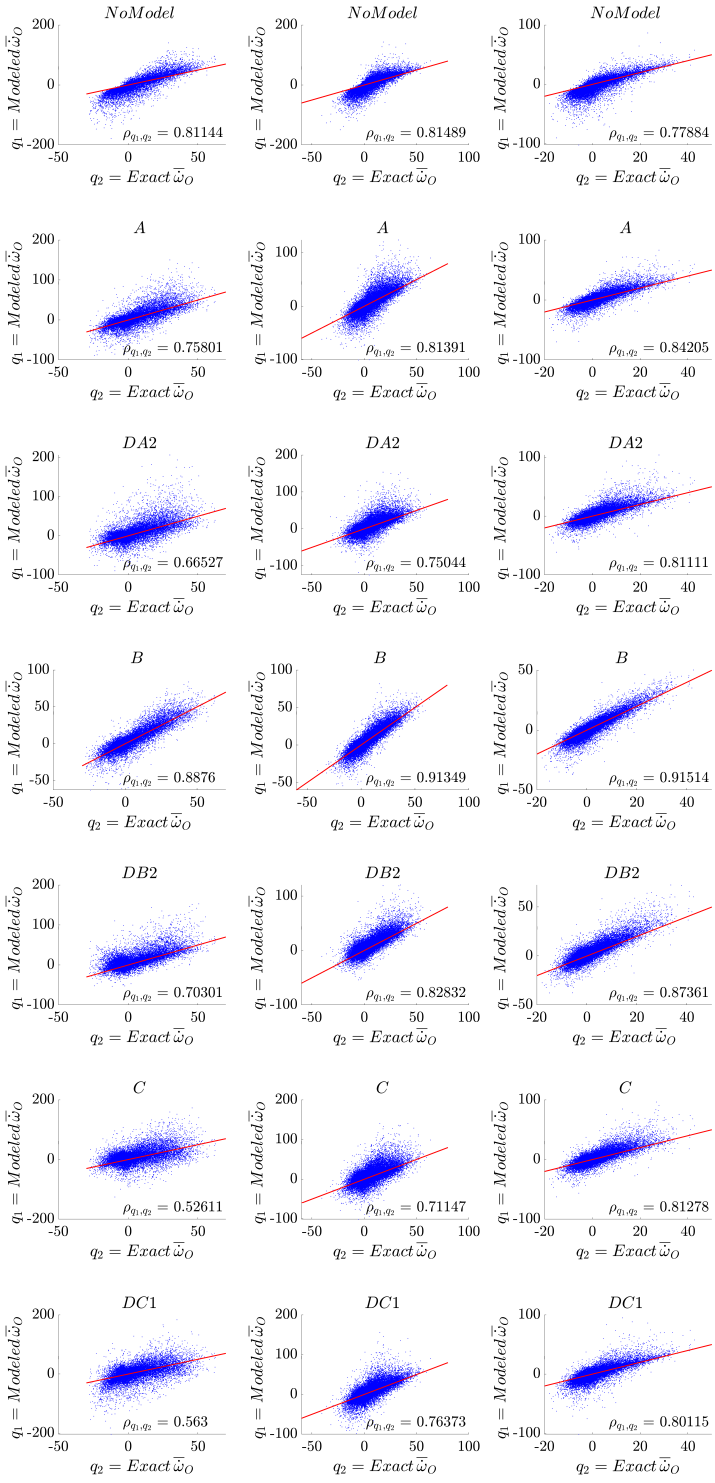


**Figure B.7:** *Scatter plots of the modeled versus the exact filtered source terms of* O *using different SS models. Extracted from the DNS databases L (left), M (middle) and H (right) at t=20$t_j$ using* $\overline{\Delta}/\Delta_{\mathrm{DNS}} = 12$.

## Conditional plots

In this section the conditional averages of the modeled filtered source terms conditioned on the mixture are plotted and compared with the conditional averages of the exact filtered source terms from the DNS databases. The conditional averages are computed using the joint PDFs (histograms).

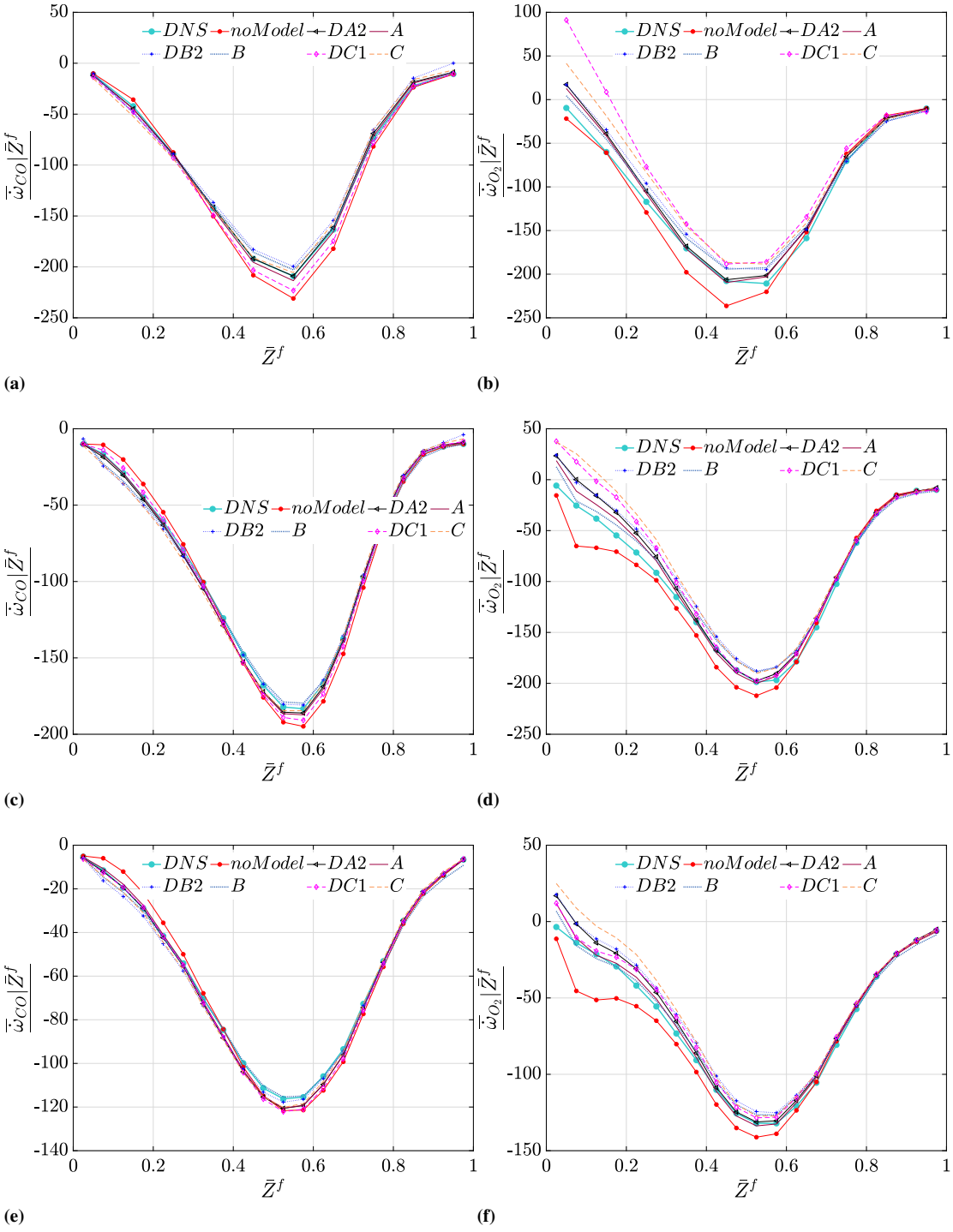


**Figure B.8:** *Comparison of dynamic and non-dynamic SS models performances in predicting the conditional mean filtered source terms of (**left**)* CO *and (**right**)* $O_2$ *(conditioned on mixture fraction) at t=20$t_j$ using* $\overline{\Delta}/\Delta_{\mathrm{DNS}} = 12$. *(**top**) case L, (**middle**) case M and (**bottom**) case H*

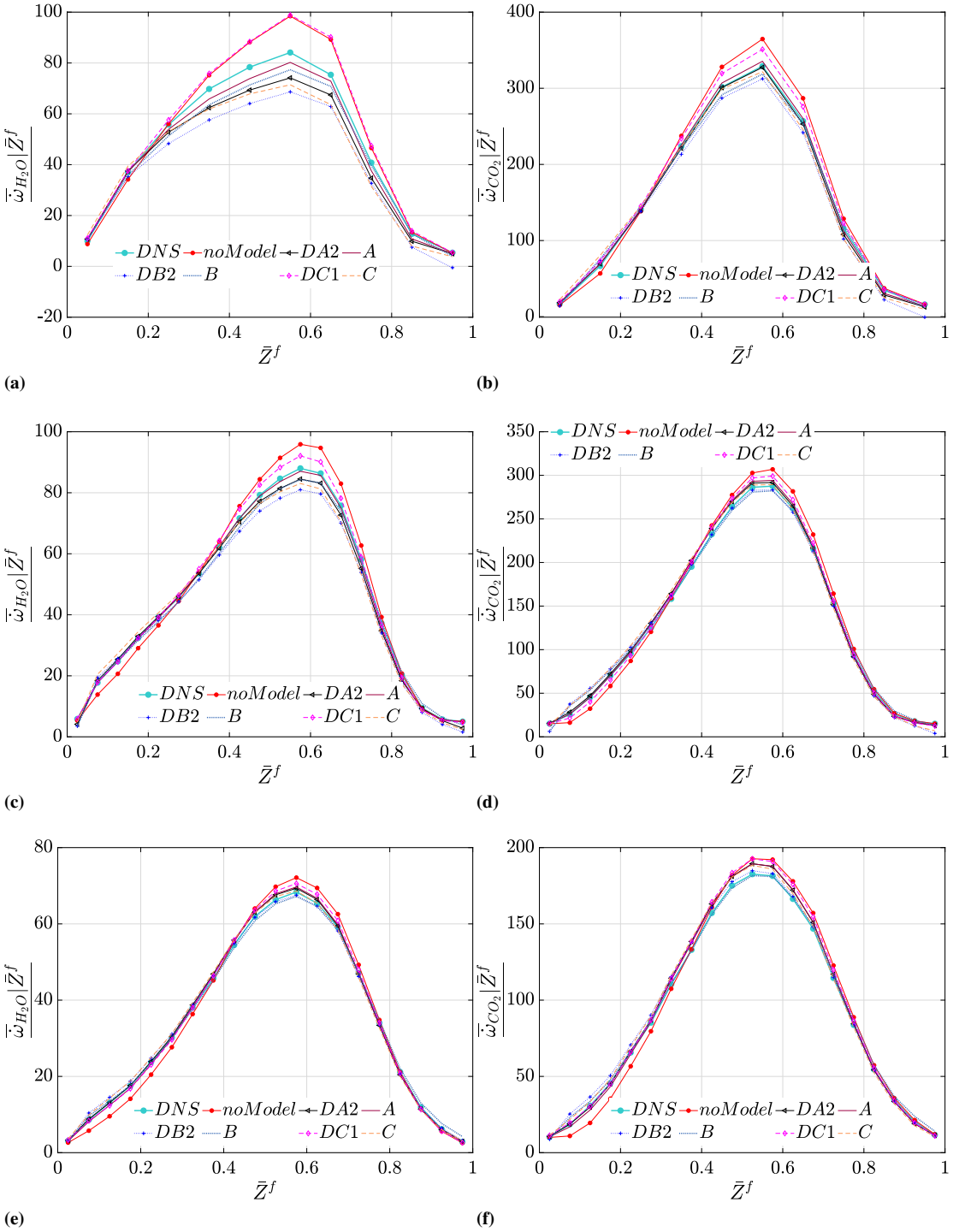


**Figure B.9:** *Comparison of dynamic and non-dynamic SS models performances in predicting the conditional mean filtered source terms of* (***left***) $H_2O$ *and* (***right***) $CO_2$ *(conditioned on mixture fraction) at t=20$t_j$ using* $\overline{\Delta}/\Delta_{\mathrm{DNS}} = 12$. (***top***) *case L,* (***middle***) *case M and* (***bottom***) *case H*

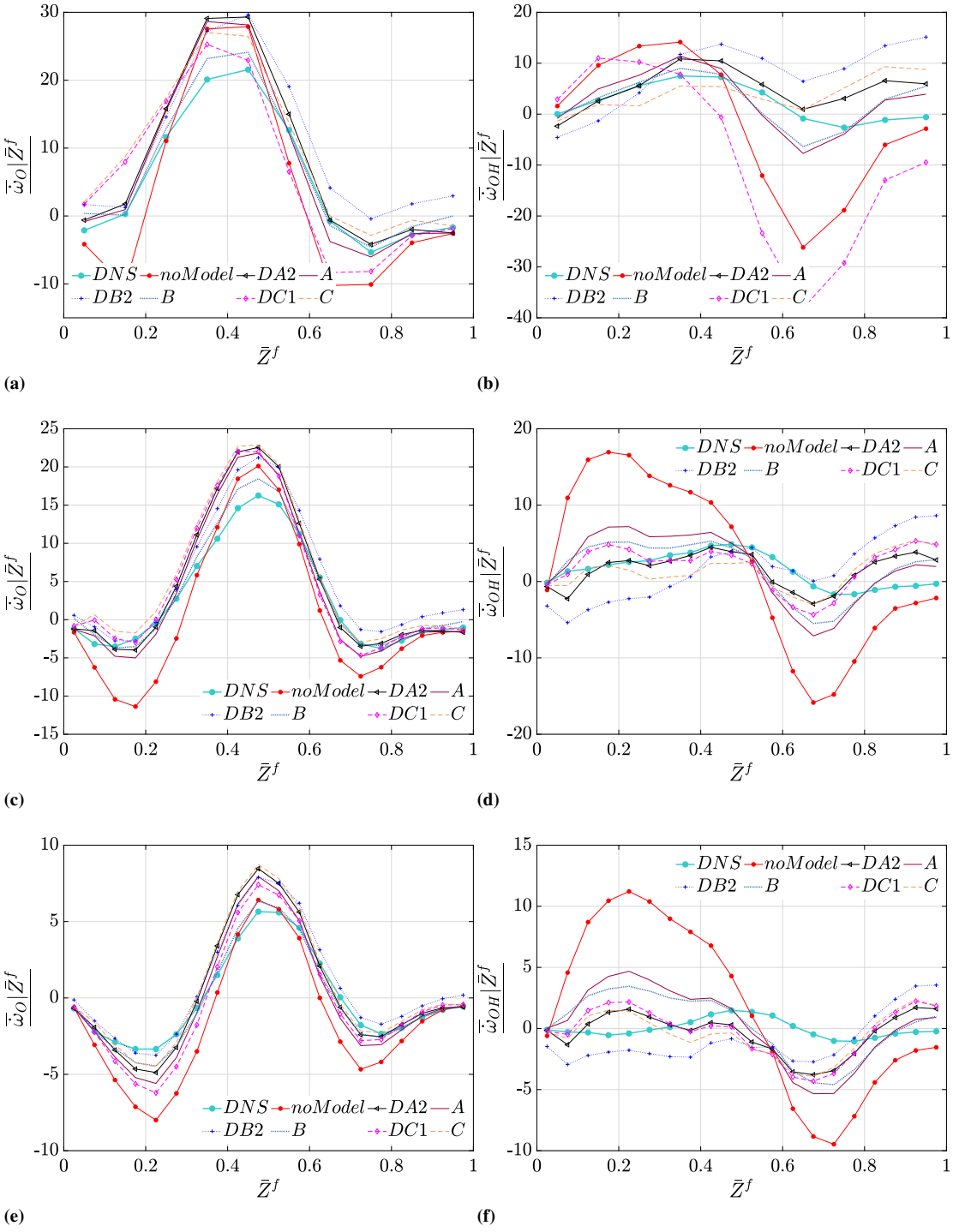


**Figure B.10:** *Comparison of dynamic and non-dynamic SS models performances in predicting the conditional mean filtered source terms of* (***left***) O *and* (***right***) OH *(conditioned on mixture fraction) at* $t$=20$t_j$ *using* $\overline{\Delta}/\Delta_{\mathrm{DNS}} = 12$. (***top***) *case L,* (***middle***) *case M and* (***bottom***) *case H*

## Conditional plots: conditioned on the species mass fractions

In this section the conditional averages of the modeled filtered source terms of species $k$ conditioned on the mass fraction of species $k$ are plotted and compared with the conditional averages of the exact filtered source terms from the DNS databases. The conditional averages are computed using the joint PDFs (histograms).

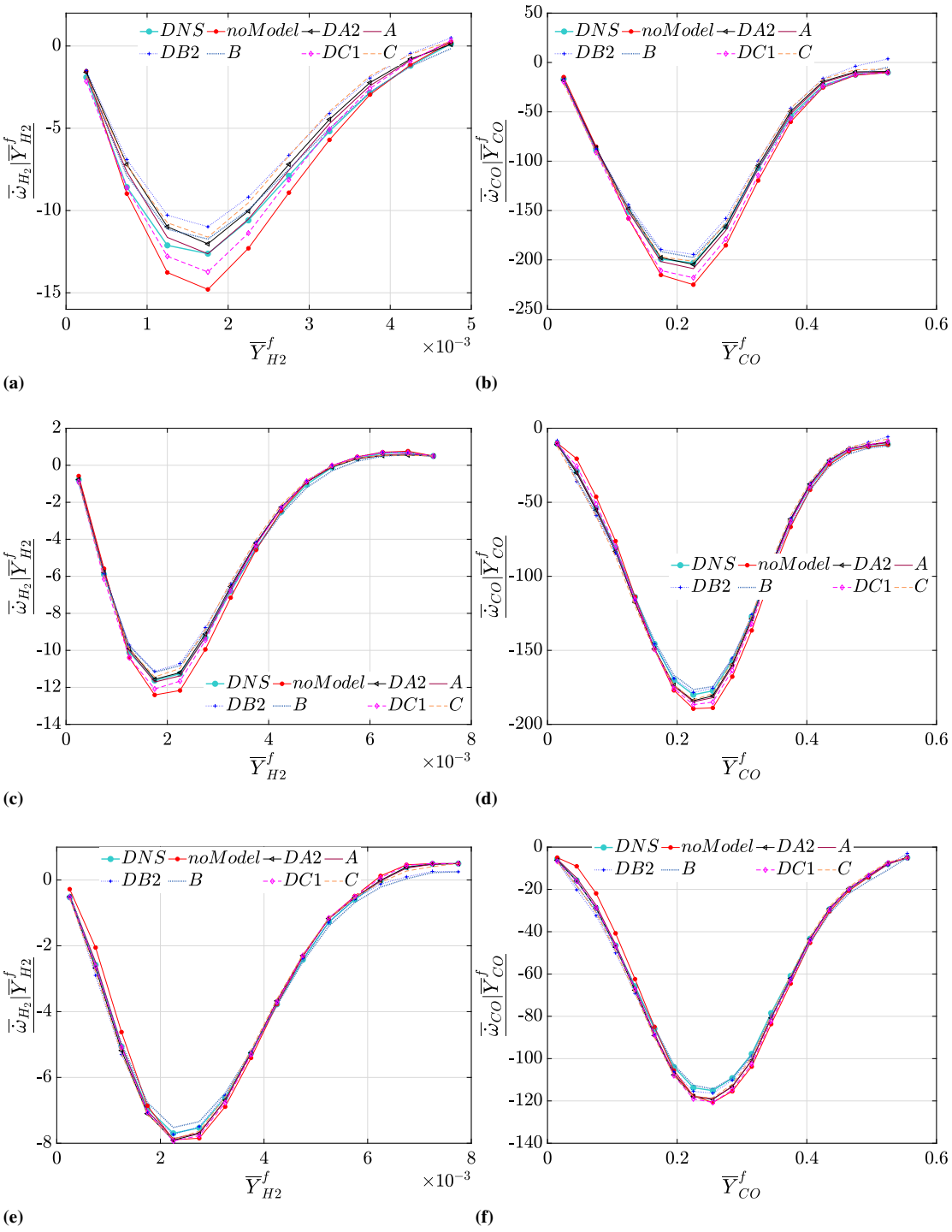


**Figure B.11:** *Comparison of dynamic and non-dynamic SS models performances in predicting the conditional mean filtered source terms of (**left**)* $H_2$ *and (**right**)* CO *(conditioned on the species mass fraction) at t=20$t_j$ using* $\overline{\Delta}/\Delta_{\mathrm{DNS}} = 12$*. (**top**) case L, (**middle**) case M and (**bottom**) case H*

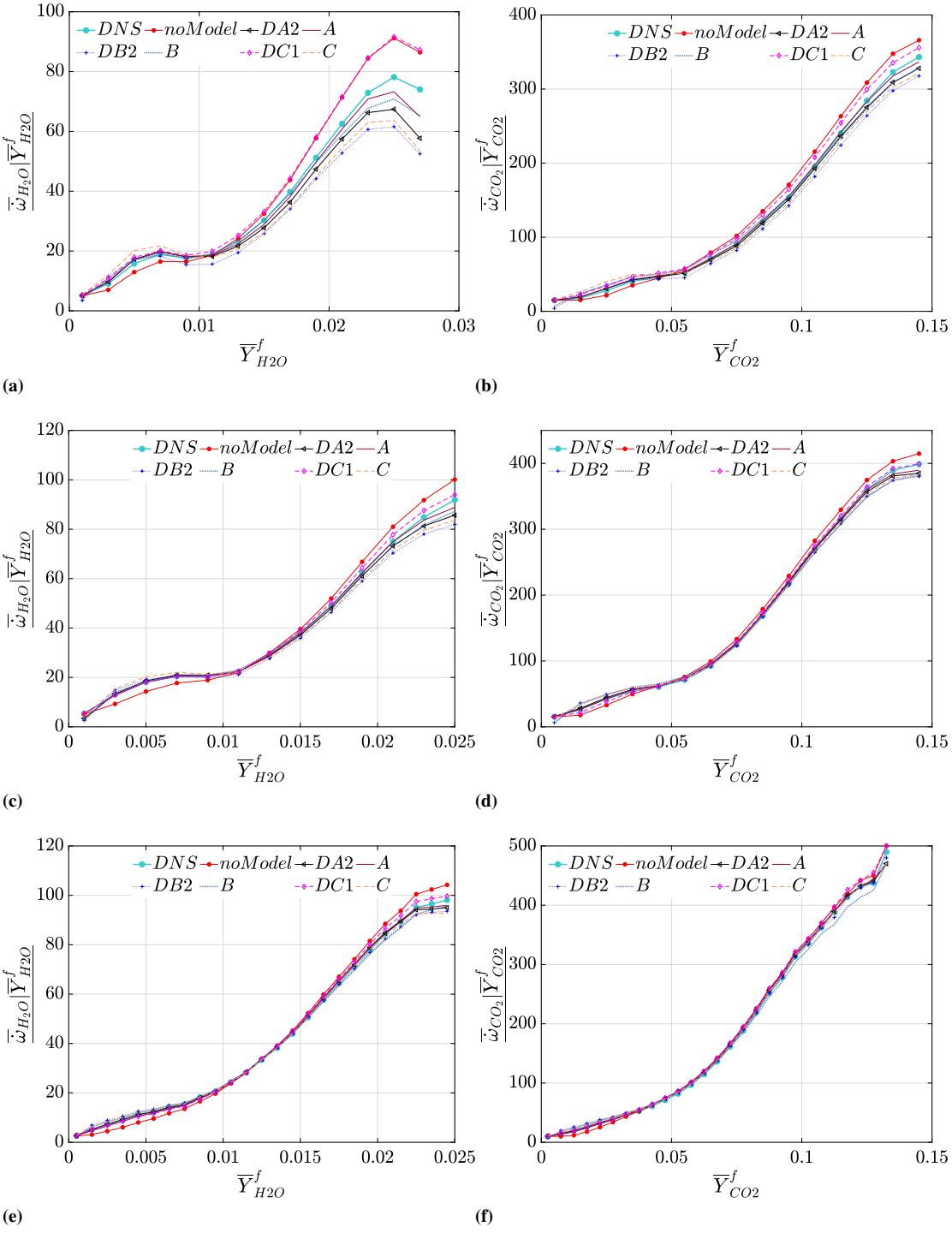


**Figure B.12:** *Comparison of dynamic and non-dynamic SS models performances in predicting the conditional mean filtered source terms of (**left**)* $H_2O$ *and (**right**)* $CO_2$ *(conditioned on the species mass fraction) at t=20$t_j$ using* $\overline{\Delta}/\Delta_{\mathrm{DNS}} = 12$*. (**top**) case L, (**middle**) case M and (**bottom**) case H*

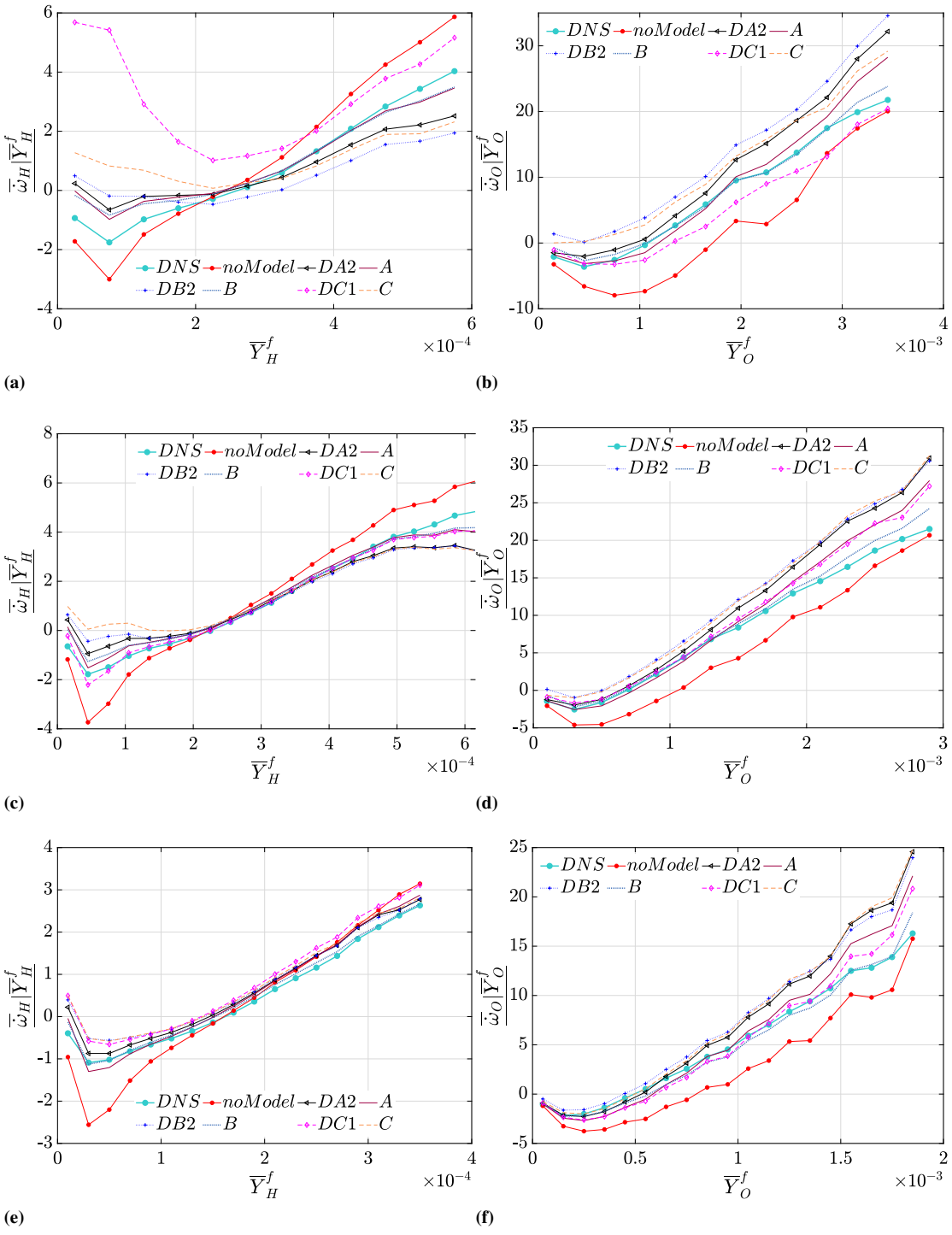


**Figure B.13:** *Comparison of dynamic and non-dynamic SS models performances in predicting the conditional mean filtered source terms of* (***left***) H *and* (***right***) O *(conditioned on the species mass fraction) at t=20$t_j$ using* $\overline{\Delta}/\Delta_{\mathrm{DNS}} = 12$. (***top***) *case L,* (***middle***) *case M and* (***bottom***) *case H*

## Conditional plots: conditioned on temperature

In this section the conditional averages of the modeled filtered source terms conditioned on temperature are plotted and compared with the conditional averages of the exact filtered source terms from the DNS databases. The conditional averages are computed using the joint PDFs (histograms). Since the flames are in extinction mode, the lack of data was observed in high temperatures. So the last bins of the joint histograms were omitted in the final plots of conditional means.

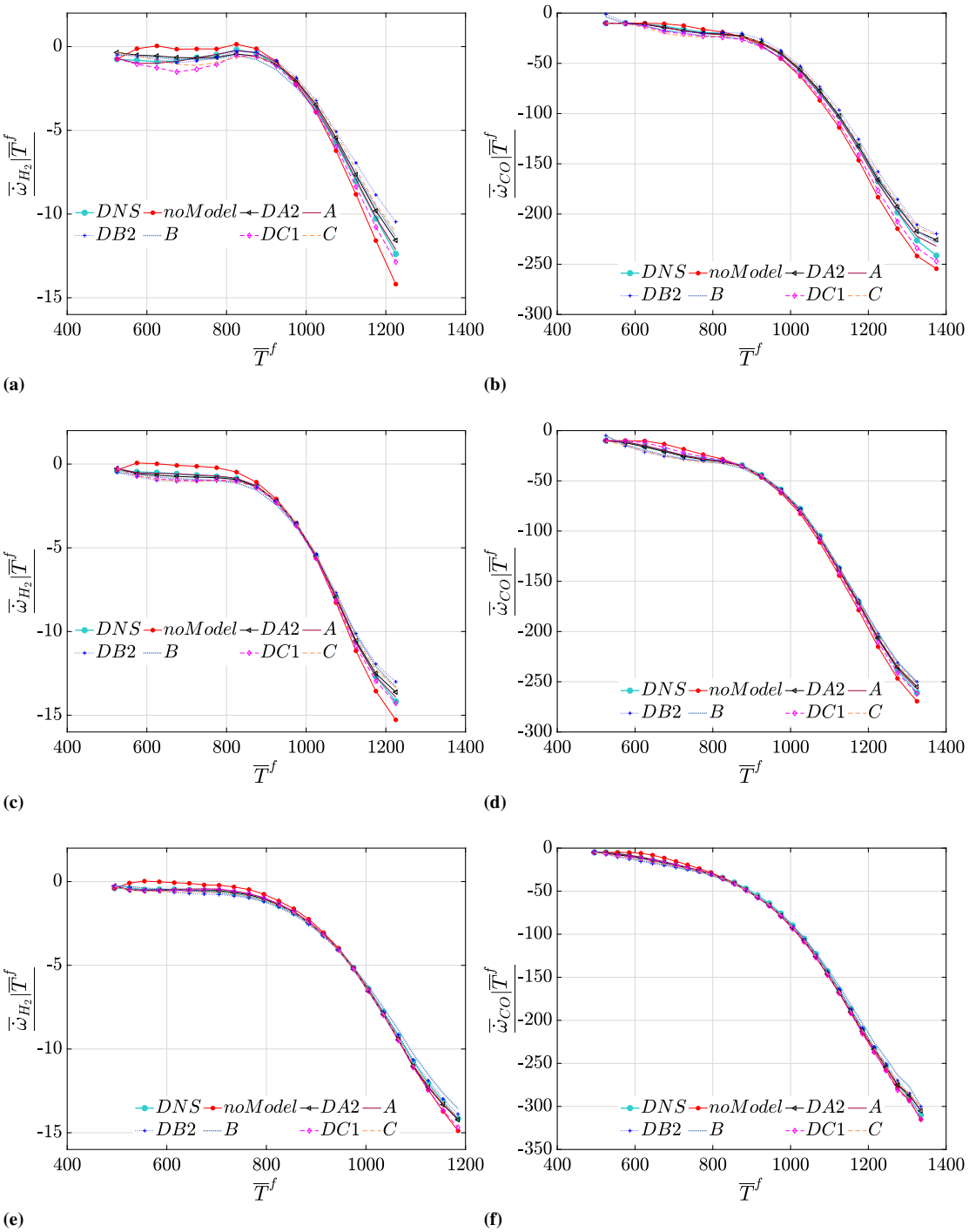


**Figure B.14:** *Comparison of dynamic and non-dynamic SS models performances in predicting the conditional mean filtered source terms of* (***left***) $H_2$ *and* (***right***) CO *(conditioned on temperature) at t=20$t_j$ using* $\overline{\Delta}/\Delta_{\mathrm{DNS}} = 12$. (***top***) *case L,* (***middle***) *case M and* (***bottom***) *case H*

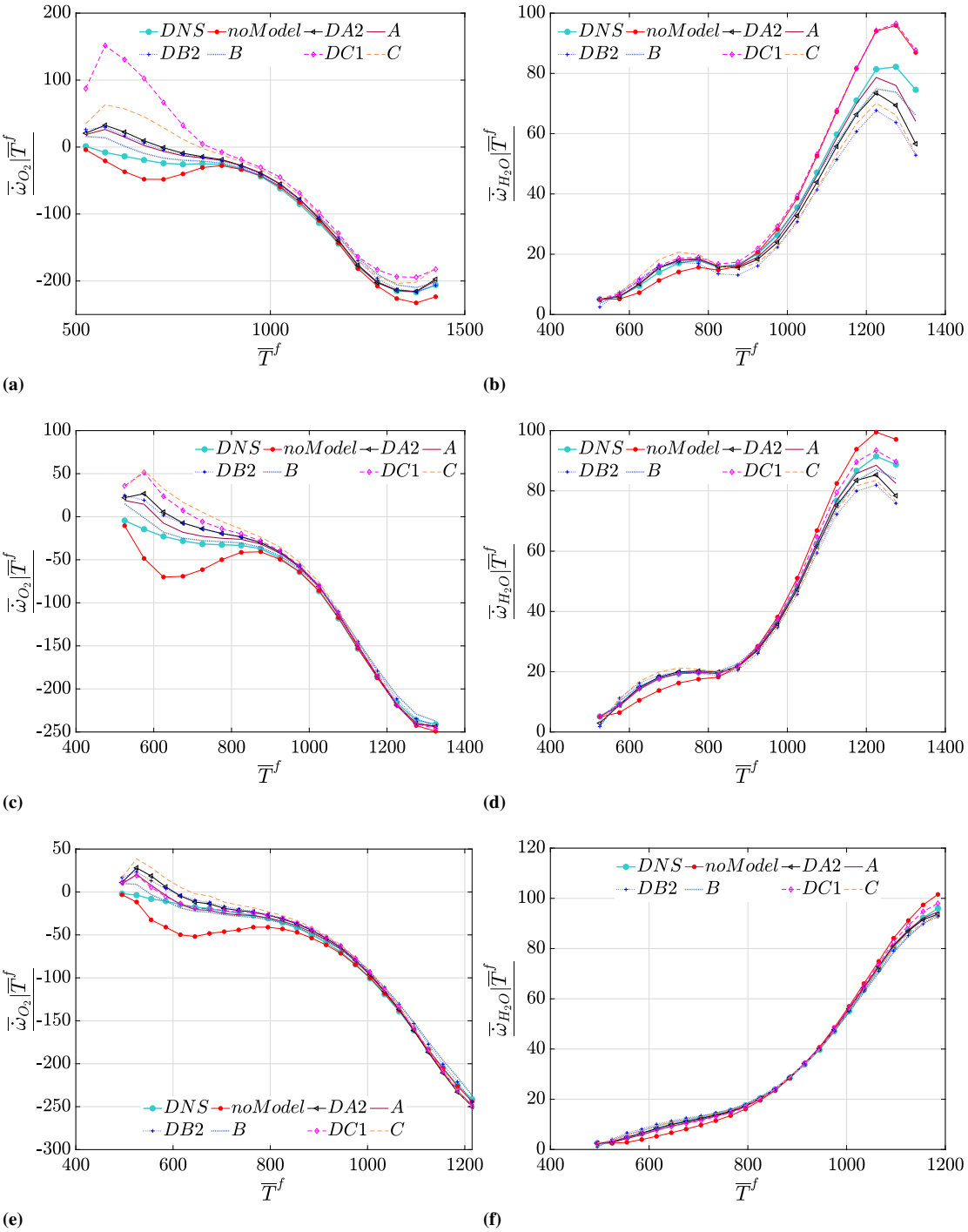


**Figure B.15:** *Comparison of dynamic and non-dynamic SS models performances in predicting the conditional mean filtered source terms of* (***left***) $O_2$ *and* (***right***) $H_2O$ *(conditioned on temperature) at t=20$t_j$ using* $\overline{\Delta}/\Delta_{\mathrm{DNS}} = 12$. (***top***) *case L,* (***middle***) *case M and* (***bottom***) *case H*